# Development and characterisation of a copper-based oxygen carrier for chemical-looping with oxygen uncoupling (CLOU)

Wenting Hu

Selwyn College

A Dissertation submitted for the degree of

Doctor of Philosophy

Department of Chemical Engineering and Biotechnology

University of Cambridge

September 2015

Revised November 2015[1]

[1] The document was last updated in September 2016 to change the format and correct some typographical errors for online deposition. No changes to the content of this Dissertation were made after the original revision date stated (November 2015).

# Preface

This Dissertation is the result of my own work and includes nothing which is the outcome of work done in collaboration except as declared in the Preface and specified in the text.

It is not substantially the same as any that I have submitted, or, is being concurrently submitted for a degree or diploma or other qualification at the University of Cambridge or any other University or similar institution except as declared in the Preface and specified in the text. I further state that no substantial part of my dissertation has already been submitted, or, is being concurrently submitted for any such degree, diploma or other qualification at the University of Cambridge or any other University of similar institution except as declared in the Preface and specified in the text.

It does not exceed the prescribed word limit for the relevant Degree Committee.

This Dissertation contains approximately 54000 words, 8 tables and 76 figures.

Wenting Hu
Department of Chemical Engineering and Biotechnology
University of Cambridge
September 2015
Revised November 2015

# Acknowledgements

First, I would like to thank my supervisor, Prof. John Dennis, for his immeasurable support and guidance throughout my PhD. I would also like to thank my project advisor, Dr. Stuart Scott from the Department of Engineering, for his generous provision of the laboratory space and equipment, as well as many helpful discussions and suggestions along the way. It has been my pleasure to collaborate with Felix Donat on this project. Felix has been so meticulous about almost every aspect of his work and I have learnt much through working with him. I wish him all the best with his Dissertation which should come to a finish in a few months' time.

As every experimentalist knows, the work carried out during a PhD would not have been possible without the help of many supporting staff members. My gratitude goes to Ms Weiyao Ma, John Gannon, Kevin Swann, John Hitchin, Lee Pratt, Andy Hubbard, Gary Chapman, Peter Claxton and Zlatko Saracevic from the Department of Chemical Engineering and Biotechnology as well as Mick Underwood, Roy Slater, Robert Leroy, John Harvey and Ken Griggs from the Department of Engineering for their help in one way or another.

I would like to thank my colleagues who have kept me sane in times of difficulty and shared my joy when the occasion called for it: Drs. Christopher Boyce, Belen Gonzalez, Cindy Lau, Jin Yang Lim, Wen Liu, Ewa Marek, Robert Pott, Saquib Sultan, Marco Saucedo and Pieterjan Van Uytvanck; Martin Chan, Peng Dai, Richard Goerke, Paul Hodgson, Lei Hu, Ross Hubble, Mohammad Ismail, Manny Kemp, Ruinan Mao, Matthias Schnellmann, Jose Velazquez, Ning Xiao and Yaoyao Zheng.

I am extremely grateful to Selwyn College, Cambridge and the Cambridge Overseas Trust for their financial support during my PhD and The Engineering and Physical Sciences Research Council for funding the project (grant EP/I010912/1).

Finally, my most sincere thanks to all my friends from the college, the department and the university as well as my family, for my life outside work would fall apart miserably if not for all of you.

And I shall always remember, *Hinc lucem et pocula sacra*, a place where I spent eight years of my life (although it might be difficult for me to pronounce properly).

# Abstract

In chemical-looping, a fuel is oxidised by a solid metal oxide, MeO, in one reactor: $(2n+m)MeO+C_nH_{2m}\rightarrow(2n+m)Me+mH_2O+nCO_2$. The exit gas yields pure $CO_2$ after the steam has been condensed. The reduced metal oxide, Me, is transferred to an oxidation reactor and regenerated: Me+air$\rightarrow$MeO. Adding these reactions, the fuel has been combusted, but the $CO_2$ has been separated from the nitrogen in air. In fact, it is in a suitable form for sequestration in the Earth where prevention of greenhouse gas emissions to the atmosphere is desired. Generally, Me is a transition metal and, to withstand many such redox cycles, it has to be supported on a suitable refractory oxide, with particles of the resulting construct being termed the “oxygen carrier”.

This Dissertation is concerned with the release and uptake of gaseous oxygen when Me is copper. In particular, the interest is in the following reaction at temperatures exceeding ~900°C undertaken in a fluidised bed reactor:

$$4CuO_{(s)} \rightleftharpoons 2Cu_2O_{(s)}+O_{2(g)}. \quad (1)$$

The value of this reaction is that the oxygen released as part of a chemical looping scheme is important in combusting unreactive solid fuels, *e.g.* coal chars, whilst the $Cu_2O$ could, in principle, be further reduced to Cu by the more reactive components of the fuel. This Dissertation investigates the development and characterisation of suitable, Cu-based oxygen carriers, which must (i) be inexpensive and easy to produce at a large scale and (ii) remain stable in prolonged operation in terms of mechanical integrity and chemical reactivity when fluidised. Here, a suitable oxygen carrier was developed, satisfying the above criteria, using a wet-mixing method and containing nominally 60 wt% CuO, 23 wt% $Al_2O_3$ and 17 wt% CaO. In particular, it was found that this oxygen carrier could operate between CuO and $Cu_2O$ without problem in a circulating fluidised bed but agglomeration and de-fluidisation was observed when the carrier was re-oxidised from the Cu form.

For design, it is important to understand the thermodynamics and kinetics of the release of gaseous $O_2$ from the oxygen carrier, because the combustion of the solid fuel depends critically on this reaction. A novel method was developed to measure experimentally the thermodynamics of reaction (1) for the supported copper oxide. It was found that the thermodynamic equilibrium deviated slightly from that of the pure $CuO/Cu_2O$ system reported in the literature and that the enthalpy of reaction was lower by ~ 15%; the reasons for this are discussed. The rate of release of $O_2$ from the oxygen

carrier was investigated using a thermogravimetric analyser and the activation energy for the forward reaction of (1) was found to be 59.7±5.6 kJ/mol, obtained after appropriate modelling of the external mass transfer resistances present in the experimental apparatus. A critical analysis of the seemingly disparate activation energies reported in the literature revealed that the activation energy of the forward step in reaction (1) was, in fact, similar for many CuO-based oxygen carriers supported on different materials. The associated pre-exponential factor for the forward rate constant was also determined in the present research, and the kinetic parameters were used in a numerical model to predict the behaviour of the oxygen carriers in a fluidised bed reactor. Excellent agreement between theory and experiment was found, confirming that the kinetic parameters obtained in this work reflect the intrinsic chemical kinetics of the oxygen carrier, rather than being totally dominated by transport effects.

# Contents

# 1. Introduction

## *1.1. Background*

The most recent assessment report (AR5) by the Intergovernmental Panel on Climate Change (IPCC) has found that each of the last three decades has been successively warmer at the Earth's surface than any preceding decade since 1850 and that by 2012, the surface temperature had risen by an average of 0.85°C since 1880 (IPCC, 2014). This significant rise in surface temperature has been accompanied by a sharp increase in the atmospheric content of greenhouse gases, which interact with infra-red radiation and help retain heat in the troposphere and below. IPCC (2014) concluded that over half the temperature increase from 1951 to 2010 was a result of

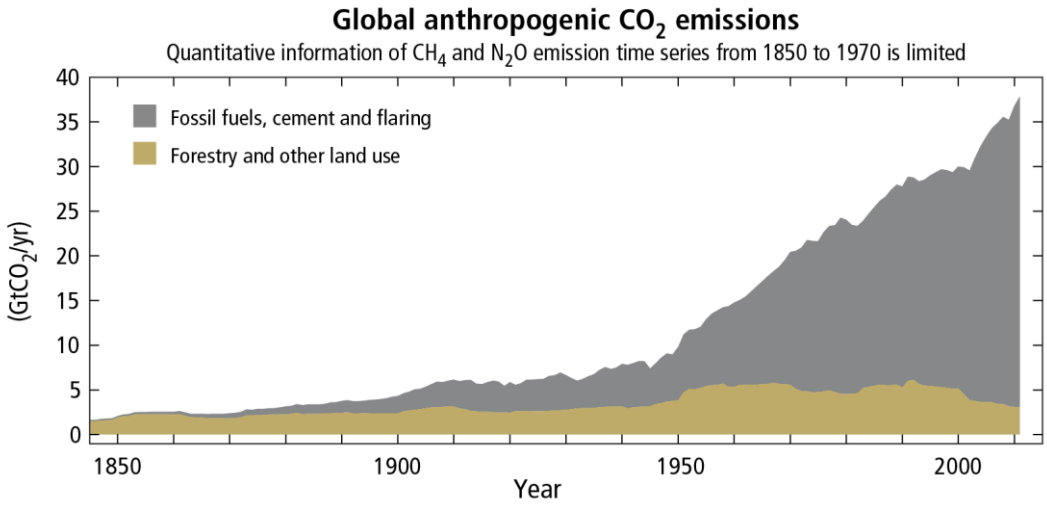


Figure 1-1 Annual global anthropogenic $CO_2$ emissions between 1850 and 2012. Figure adapted from IPCC AR5 (IPCC, 2014).

emissions from anthropogenic activities. This is exemplified by Figure 1-1 where it can be seen that the emission of $CO_2$, as the most influential species, has increased by approximately five-fold since 1950 and its rate of increase is currently fast and steady. In fact, the monthly global average concentration of $CO_2$ in the atmosphere exceeded 400 ppm for the first time in recent geological history in March 2015 (Dlugokencky and Tans, 2015), the value before the Industrial Revolution being ~280 ppm. The IPCC report (IPCC, 2014) pointed out that to meet the target of limiting the temperature rise to 2°C set out in the Copenhagen Accord, a total cumulative amount of approximately 2900 Gt of $CO_2$ could be emitted, starting from the year 1870, corresponding to an atmospheric $CO_2$ concentration of ~500 ppm. In fact, by 2011, 1900 Gt had already been emitted.

It can be estimated from Figure 1-1 that the target would be exceeded by ~2040 if the emissions are maintained at the same level as of 2010, about 35 Gt/year, without further increase. If the emissions continue to increase year on year following the current trend, the time frame would be even shorter.

Since most of the anthropogenic $CO_2$ originates from the use of fossil fuels, one important strategy for reducing carbon emissions is to replace fossil fuels by renewable energy sources (*e.g.* wind, hydro, solar, geothermal, or biofuel) or by nuclear energy. However, the share of fossil fuels in the total, global supply of primary energy had, by 2012, only deceased by 5 percentage points to 81.7%, compared to the percentage in 1973, whilst the total amount of primary energy used had doubled during the same period (IEA, 2014a). In fact, it is predicted that fossil fuels will still account for about 75% of the total supply of primary energy by 2040, approximately equally divided among oil, gas and coal (IEA, 2014b). It is therefore evident that the rate of introduction of carbon-free energy sources is far outmatched by the rate of growth of total energy supply and cannot be the sole means of controlling emissions of carbon. A further complication is that certain industrial sectors contribute to substantial $CO_2$ emissions. For example, about 50% of the $CO_2$ generated from cement production can be attributed to the use of fossil fuels to generate heat for the production of clinkers whereas the other 50% of the $CO_2$ is released from the calcinations of limestone in the production process itself (Worrell *et al.*, 2001) and cannot be avoided by switching to a different source of energy. Hence, active capture and subsequent storage of $CO_2$ from the source of emission, such as power stations or process industries, must be implemented along with the phasing out of fossil fuels in order to meet the challenging 2°C target. The approach is termed carbon Capture and Storage (CCS).

Carbon Capture and Storage consists of three separate activities: capture, transport and storage (*e.g.* reviews by Bode and Jung, 2006; Boot-Handford *et al.*, 2014; IPCC, 2007; Pires *et al.*, 2011). Basically, the carbon dioxide must first be separated in pure form from flue gas. The compressed gas is then transported by pipelines, or by ship, to a suitable reservoir within the Earth, where it is stored for all time. The cost of transport is ~ 1-8 US$/t of $CO_2$ transported over 250 km and geological storage and monitoring of the stored $CO_2$ incurs a cost of the same order (IPCC, 2007). However, as noted by Boot-Handford *et al.* (2014), the storage of $CO_2$ presents great uncertainties in terms of capacity and the probability of leakage over time. That aside, the most expensive part of CCS is the capture of $CO_2$ from its sources,

ranging from ~5 to 115 US$/t (IPCC, 2007): much effort has been directed towards reducing this cost, as discussed below.

Since most $CO_2$ is associated with the combustion of carbonaceous fuels, the technologies for carbon capture are categorised as *pre-combustion capture*, *post-combustion capture* and *oxy-fuel combustion*. In pre-combustion and post-combustion capture, the objective is to separate $CO_2$ either from the fuel or from the flue gas, respectively. To separate the $CO_2$, contact of the flue gas with solvents (*e.g.* monoethanolamine (MEA), SELEXOL™), solid sorbents (*e.g.* zeolite, calcined limestone, dolomite), or selective membranes have been variously proposed.

Pre-combustion capture can be employed when synthesis gas is involved, generated from the gasification of coal or steam reforming of natural gas. The resulting mixture, rich in CO and $H_2$, can be further conditioned *via* the water-gas shift reaction and simultaneous removal of $CO_2$ to yield a stream of almost pure $H_2$, which can then be fed to a combined cycle for power generation or otherwise utilised. Post-combustion capture separates $CO_2$ from the flue gas generated from the combustion process. The flue gas from combustion in air typically contains about 80 vol% of $N_2$ and a few percent of $O_2$, depending on the air to fuel ratio. The remaining 10-15 vol% of gas primarily consists of $CO_2$ and $H_2O$, which need to be separated.

On the other hand, oxy-fuel combustion does not remove $CO_2$ from gas streams directly. In this process, pure $O_2$ mixed with $CO_2$ serves as the oxidant instead of air so that the flue gas is almost pure $CO_2$, with some steam and other minor contaminants. This flue gas can be directly compressed for subsequent storage with minimal treatment, eliminating the need of separation. The required $O_2$ can be obtained from standard cryogenic distillation of air. Alternatively, the $O_2$ can be supplied as lattice oxygen bound in solid. This forms the basis of an emerging technology termed chemical-looping combustion (CLC), discussed in Section 1.2.

As noted above, the additional energy required for the separation of $CO_2$ is responsible for the high cost of carbon capture. For pre and post-combustion systems, the carbon capture medium must be regenerated and reused for better economy but the regeneration process normally involves temperature swing or pressure swing, both of which are energy intensive and costly. In the case of oxy-fuel combustion, the air separation unit is the main contributor to the additional cost. It is estimated that these operations account for ~60% of the total energy penalty (*i.e.* the percentage reduction

in power output given the same energy input) associated with current carbon capture technologies (Rubin *et al.*, 2012). The remaining 40% of energy penalty is due to the compression of $CO_2$ for subsequent transportation and storage, along with other pumping costs and cannot be easily avoided. Chemical-looping combustion, described in Section 1.2, has been studied in this Dissertation because it has the potential to reduce, substantially, the amount of energy needed to separate $CO_2$ from flue gases.

## *1.2. Chemical-looping combustion*

Chemical-looping combustion was initially proposed by Richter and Knoche (1983) to improve the exergy efficiency of gas turbine power generation systems and the concept was later expanded by Ishida *et al.* (1987). It was proposed that instead of utilising fuels such as methane directly in a combustion process, the fuel could be used to reduce a solid metal oxide (known as an oxygen carrier, OC), typically that of a Period 4 transition metal, and the reduced metal or its lower oxide could be re-oxidised in air. The separate reactions are shown below, with methane ($CH_4$) as the fuel and M representing some suitable metal species.

$$CH_4 + 4M_xO_y \rightarrow CO_2 + 2H_2O + 4M_xO_{y-1} \qquad 1\text{-}1$$

$$4M_xO_{y-1} + 2O_2 \rightarrow 4M_xO_y \qquad 1\text{-}2$$

Although the overall reaction of the above scheme is the same as the direct combustion of methane, the enthalpy of reaction of reaction 1-2 can be much higher, if the reaction 1-1 is considerably endothermic. As a result, the CLC scheme can achieve higher output efficiency by producing more heat at high temperature from reaction 1-2 and recovering some of the waste heat at a low temperature to drive reaction 1-1. Ishida *et al.* (1987) found that 50.4% of the lower heating value of methane could be converted into shaft work for a CLC scheme, compared to 45.9% for a combined cycle system or 47.0% for a multi-phase and multi-component system. Unfortunately the proposed system largely remained a theoretical concept probably because it was much more complicated than conventional combustion schemes.

However, CLC is capable of capturing almost pure $CO_2$ from power plants with little energy penalty compared to other methods such as amine scrubbing or oxy-fuel combustion. This is because the exhaust from reaction 1-1 would consist of only $CO_2$ and water vapour, which could be easily condensed to yield a pure stream of $CO_2$ for storage. There would be no need for cryogenic separation of air (Ishida and Jin, 1994, 1997). Accordingly, it is now a very active area of research, roughly divided into two

themes: the design and operation of CLC reactor systems at various scales and the development of novel materials to be used as oxygen carriers.

## *1.3. The chemical-looping combustion reactor system*

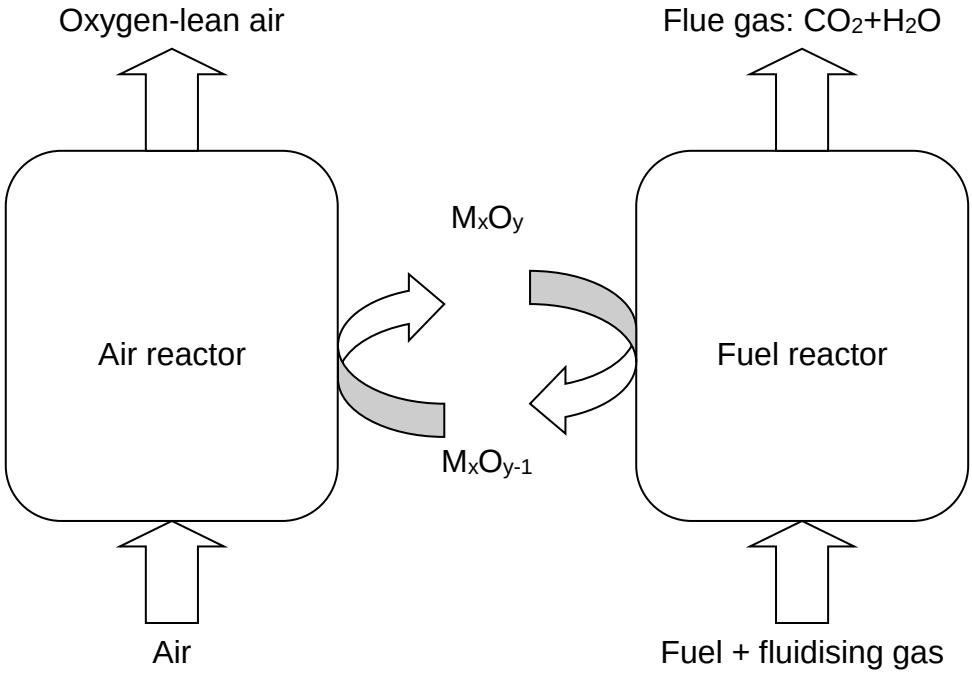


Figure 1-2 A schematic diagram of a typical CLC process.

As shown in Figure 1-2, in a typical CLC process, two reactors are required for continuous operation: in the fuel reactor, the carbonaceous fuel reacts with the oxygen carriers in a similar manner as reaction 1-1 and produces a mixture of $CO_2$ and $H_2O$. The flue gas leaving the fuel reactor is suitable for compression and storage after the removal of water and other minor contaminants and the reduced OCs are transported to the air reactor for re-oxidation. At the same time, re-oxidised OCs from the air reactor are fed back to the fuel reactor continuously as a source of oxygen for reaction with the fuel and the oxygen-lean air leaving the air reactor can be vented directly into the atmosphere after cooling, without the emission of $CO_2$. In this way, combustion of the fuel is achieved through the looping of the OC within the system and hence the name chemical-looping combustion. In order to capture the $CO_2$ efficiently, it is crucial that the flue gases from each reactor do not cross contaminate each other – air leaking into the fuel reactor would introduce non-condensable $N_2$ and $O_2$ which would need to be separated at a later stage, increasing the cost of separation; $CO_2$ leaking into the air reactor would result in direct emission of $CO_2$ to the atmosphere, reducing the carbon

capture efficiency. Thus it is necessary to install loop seals between the two reactors in the solid transfer lines to ensure that gases do not enter the other reactor. Such devices are commonly employed in, for example, fluidised catalytic cracking (FCC) processes, where separation between the gases in the cracking reactor and the air in the regenerating reaction is essential (Fan and Zhu, 2005).

In the past decade, more than 10 pilot facilities for CLC have been constructed and operated for over 4000 hours cumulatively, across the world (Lyngfelt, 2011). Most notably, the 10 kW unit at Chalmers University of Technology has been operated for more than 1000 hours, using either gaseous fuels (natural gas) or solid fuels (coal, petcoke) with different oxygen carriers (*e.g.* Berguerand and Lyngfelt, 2008a, 2008b; Linderholm *et al.*, 2012, 2009, 2008). The largest CLC pilot plant to date is located at Technische Universität Darmstadt with a capacity of 1 $MW_{th}$ (Ströhle *et al.*, 2014).

Large scale units tend to consist of two interconnected fluidised beds when operating with gaseous fuels, as reviewed by Lyngfelt (2011). The popularity of interconnected fluidised beds systems can be attributed to the fact that fluidised beds offer good mass and heat transfer characteristics so that hot-spots in the reactor can be avoided and the combustion can take place at a relatively low and uniform temperature, around 900°C. Furthermore, the rate of heat transfer from the bed to the surface is comparatively higher than that of, for example, a packed bed so that less surface area is required for heat exchange. Another important reason for the choice is that such systems are very similar to commercially available CFB boilers and this offers additional confidence to the emerging technology.

CLC with solid fuels is more challenging than with gaseous fuels - whilst gaseous fuels can reduce the OCs directly in the fuel reactor, it is unlikely for solid fuels to react with OCs *via* solid-solid reactions. Hence the fuels must first be gasified into synthesis gas, primarily $H_2$ and CO, using a gasifying agent such as steam or $CO_2$. The gasification reactions can be represented by reactions 1-3 and 1-4 to a first approximation as carbon is the major constituent in most solid fuels. Although the solid fuels can be gasified separately before being fed into the CLC combustor (Jin and Ishida, 2004), the process is highly endothermic and partial combustion with oxygen may be required to maintain the heat balance. Since air separation will be required to avoid contamination by $N_2$, the advantage of CLC is lost in this configuration and it may be more sensible to employ one of the pre-combustion capture techniques instead.

$$C + CO_2 \rightarrow 2CO \qquad \Delta H_r^\circ = 172.46\ \text{kJ/mol} \qquad 1\text{-}3$$

$$C + H_2O \rightarrow H_2 + CO \qquad \Delta H_r^\circ = 175.30\ \text{kJ/mol} \qquad 1\text{-}4$$

It is possible to gasify the solid fuels *in situ* in a bed of OCs (Dennis *et al.*, 2006; Scott *et al.*, 2006). While the volatile matter in the solid fuels reacts readily with the OCs either directly or as it gasifies, the gasification of the remaining char (fixed carbon) is generally slow and rate limiting, even though the presence of OCs somewhat increases the rate of gasification (Leion *et al.*, 2007; Saucedo *et al.*, 2014). It is therefore possible for the unconverted char to enter the air reactor together with the circulated OCs and give rise to a significant concentration of $CO_2$ in the flue gas of the air reactor, resulting in a decrease of the efficiency of carbon capture (Cuadrat *et al.*, 2011). To minimise the undesirable transport of solid fuels to the air reactor, a third fluidised bed, termed a carbon stripper, can be installed between the two reactors to separate the solid fuel particles from the OCs and return them to the fuel reactor (Markström *et al.*, 2013; Ströhle *et al.*, 2014). Markström *et al.* (2013) achieved a carbon capture efficiency of 95.5%-98.5% in a 100 kW unit operating with bituminous coal as the fuel. Numerical simulations attempting to optimise the 1 MW unit at Darmstadt also reported a similar carbon capture efficiency (Gayán *et al.*, 2013) although experimental results from the pilot plant are not available in the literature. One possible way of eliminating the carbon stripper when using solid fuels, hence reducing the complexity of the design of the reactor system, would be to utilise a special class of OCs able to release gaseous oxygen in oxygen deficient environment such as in the fuel reactor so that the char can undergo direct combustion rather than gasification and be consumed much faster. This is termed chemical-looping with oxygen uncoupling (CLOU) and will be discussed separately in Section 1.5.

## *1.4. Development of oxygen carriers*

### *1.4.1. Requirements for potential OCs*

The choice of oxygen carrier is critical in the CLC process. An ideal OC should be chemically active in both reduction and oxidation with a high rate of reaction. However, it is also desirable that the OC is otherwise inert so that its activity is not degraded by other species present, such as CO and $CO_2$ in the flue gas or contaminants such as sulphurous compounds and ash from solid fuels. In addition, the OC particles must be mechanically robust so that they do not break up inside a fluidised system. Significant break up of particles, by attrition (loss of material due to grinding

between particles), abrasion (loss of material due to grinding between particles and other structures such as the wall of the reactor) or fragmentation, causes the particle size to decrease and the very fine solids produced will be elutriated from the reactor, resulting in the loss of active material and a dusty flue gas which may require further cleaning downstream. The attrition of particles can be due to the internal stress of the particles induced by thermal expansion if the temperature of the particles changes rapidly, *e.g.* when the fuel reactor and air reactor have a large temperature difference. Such stress can also arise from chemical reactions, especially if the molar volume of the OC differs significantly in the oxidised and reduced forms. Lastly, impacts between particles and the reactor are frequent in a fluidised bed and sometimes at very high relative velocity, *e.g.* in the transport section of a circulating bed, effectively crushing the particles if they are not mechanically strong.

Opposite to attrition, agglomeration of carrier particles must be avoided in fluidised beds. Here, several particles may form an aggregate of a larger size. Whilst this might not necessarily be problematic for packed bed operations, the particle size influences the heat and mass transfer characteristics to and from particles significantly in a fluidised bed. More importantly, large aggregates cannot be transported pneumatically due to their much higher terminal velocity compared to individual, smaller particles. In extreme cases where very large aggregates form, fluidisation cannot be maintained and the reactors would slump to a packed bed, resulting in certain operational failure. Even if agglomeration does not pose problems in the operation of the fluidised bed systems, it is commonly accompanied by material sintering where grains within a single particle merge to form larger grains. The sintering of material increases the size of the grains and therefore the mass transfer resistance within a particle. Thus the apparent chemical activity of the OC will decrease significantly. The effect of both agglomeration and sintering becomes more significant as the operating temperature approaches the melting point of the material.

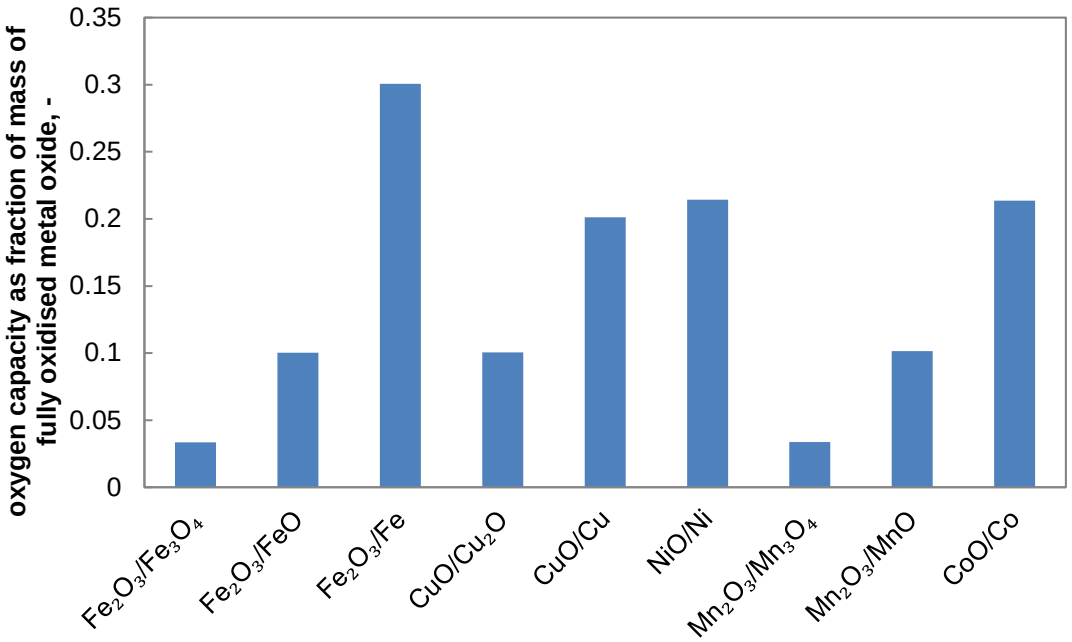


Figure 1-3 Theoretical oxygen capacity for selected metal oxides, from the reduction of the species preceding the forward slash to the species after

Another factor for consideration is the amount of oxygen that can be transferred between the air and fuel reactors per unit mass of the OC. Clearly, if an OC has a very low oxygen capacity, more material must be circulated per unit time in the system to supply the same amount of oxygen for fuel conversion compared to an OC with high oxygen capacity. This means that larger reactors must be built for the same power output and therefore the capital cost will be higher. The oxygen capacities of some metal oxides commonly considered as potential oxygen carriers are presented in Figure 1-3. It should be emphasised that even though all the transitions listed are thermodynamically feasible at ~ 900°C (Adánez *et al*., 2012), some transitions occur with equilibrium conditions such that the fuel gas may not combust completely. For example, for the oxidation of CO with Fe-based materials, the equilibrium $CO_2$/CO ratio for the transition from $Fe_3O_4$ to FeO is close to 1 at 900°C, depending on the extent of non-stoichiometry of FeO (Liu, 2013). Although such equilibrium can be exploited for the production of $H_2$, for the purpose of CLC, only the $Fe_2O_3/Fe_3O_4$ transition ensures the complete conversion of the fuel and further reduction will lead to incomplete combustion.

Lastly, since chemical and mechanical degradation of materials is inevitable in practice, it is always necessary to replenish OCs during operation to compensate for the loss of materials through attrition and the decrease in chemical reactivity of the bed

material. Therefore the cost of the OC materials should be as low as possible for the process to be economical.

### *1.4.2. Overview of potential OCs*

Taking all the factors into account, it is clear that many potential OCs will be based on Period 4 transition metals for their ease of reduction and oxidation, compared to main group elements. Also, their relatively low atomic masses, give a reasonable oxygen capacity per unit mass of material. Indeed, the initial investigations by Ishida and co-workers in the 1990s were based on $Fe_2O_3$, NiO and CoO and a mixture of NiO and CoO as active materials (Ishida and Jin, 1994; Ishida *et al.*, 1998; Jin *et al.*, 1998). It should be noted that all the particles investigated were supported on other ceramic materials, such as alumina ($Al_2O_3$), titania ($TiO_2$), or yttrium stabilised zirconia (YSZ) to improve the mechanical stability. Later, synthetic OCs based on the oxides of *e.g.* Cu, Fe, Mn, Ni were studied, synthesised using a variety of methods (*e.g.* Adánez *et al.*, 2004; Cho *et al.*, 2004; Chuang *et al.*, 2008; de Diego *et al.*, 2004; Ryu *et al.*, 2003; Scott *et al.*, 2006; Shen *et al.*, 2009a, 2009b). The major means of synthesis include mechanical mixing, spray drying, freeze granulation, co-precipitation and impregnation. The resulting particles are usually calcined at a high temperature, typically above 900°C, before use to improve the mechanical strength. In addition, several minerals, such as haematite and ilmenite, have been studied as candidate OCs for CLC (Adánez *et al.*, 2010; Arjmand *et al.*, 2012c; Gu *et al.*, 2011; Leion *et al.*, 2009, 2008a, 2008b; Mattisson *et al.*, 2001; Wen *et al.*, 2012; Xiao *et al.*, 2010). Such natural ores are generally considerably cheaper than synthetic oxygen carriers. Some effort has also been directed to doping such ores with carbonate or nitrate salts of Group 1 (alkaline metals) and 2 (alkaline earth metals) elements such as K, Na and Ca, to enhance their performance (Bao *et al.*, 2013; Gu *et al.*, 2012).

More recently, the focus on the development of OCs has shifted towards more complicated systems involving mixed oxides as the active material, usually spinels and perovskites. Spinels are a group of materials with the same lattice structure as the mineral “spinel”, $MgAl_2O_4$ with a general formula of $A^{2+}B^{3+}{}_2O_4$, where A and B are generic terms for divalent and trivalent species. Many spinels have been used as a support material, rather than the active species, for OCs and some are formed during the synthesis of carriers. For example, Adánez *et al.* (2006) found that NiO formed the spinel $NiAl_2O_4$ with $\gamma$-$Al_2O_3$ which led to a lowered reactivity during reduction, compared with carriers made with $\alpha$-$Al_2O_3$ in which some NiO was retained as the simple oxide.

De Diego *et al.* (2005) concluded that OCs made by supporting CuO on $Al_2O_3$ formed the spinel $CuAl_2O_4$ at temperatures above 850°C during calcination, but after 100 redox cycles of the OCs, some free CuO was detected even if none was present in the virgin particles. Other researchers have deliberately synthesised spinels and spinel solutions to be used as OCs. Lambert *et al.* (2011) synthesised 17 different OCs containing various spinels with or without simple oxides (NiO or CuO). The 8 OCs without any active simple oxides were found to be less reactive in both reduction and oxidation than the reference material (60%NiO-40%$NiAl_2O_4$ by weight) although the compound $Cu_{0.95}Fe_{1.05}AlO_4$ exhibited a comparable rate of oxidation to the reference material. Yang *et al.* (2012) found that the spinel solid solution $Ni(Al,Fe)_2O_4$ prepared from the spray drying of ball-milled constituent oxides in the mass ratio $NiO:Fe_2O_3:Al_2O_3$ = 22.5:47.5:30 and calcined at 1100°C for 4 hours can be used as an economic alternative for $NiO/NiAl_2O_4$.

Perovskites are mixed oxides with the general formula $A^{2+}B^{4+}O_3$, named after the natural mineral $CaTiO_3$. The perovskite structure can exhibit non-stoichiometry, especially through the partial substitution of A and, or, B sites by ions of a lower valency. The oxygen vacancies facilitate the diffusion of lattice oxygen within the solid and are partially responsible for the activity of such compounds (Teraoka *et al.*, 1985). In particular, perovskites in the form of $La_xSr_{1-x}Co_yFe_{1-y}O_{3-\delta}$ are known to be capable of absorbing and desorbing significant amounts of oxygen depending on the partial pressure of $O_2$ of the environment and thus can be used as membranes for oxygen transport. Readman *et al.* (2005) examined the above perovskites with different stoichiometry and suggested that variants with low Co content, in particular, $La_{0.8}Sr_{0.2}Co_{0.2}Fe_{0.8}O_{3-\delta}$, can be used for CLC with a change in $\delta$ up to approximately 0.1 between reduction and oxidation. Importantly, this material did not experience a significant phase change during the redox cycle, evident from *in-situ* XRD experiments, and the authors argued that this would be advantageous since potential internal stresses due to phase change were avoided so that the OCs were less prone to mechanical degradation. Perovskites based on Ca and Mn have been shown to release $O_2$ (Abad *et al.*, 2015; Arjmand *et al.*, 2013; Galinsky *et al.*, 2015; Källén *et al.*, 2013; Rydén *et al.*, 2011) around 900°C, depending on the partial pressure of oxygen in the surrounding gas, and can be used for CLOU, a process discussed in Section 1.5.

$CaSO_4$, although not a transition metal oxide, is also a potential OC and can be reduced to CaS under reducing conditions (Wang and Anthony, 2008). However, several studies have reported that $CaSO_4$ gradually loses sulphur and releases $SO_2$ and $H_2S$ due to undesirable side reactions, especially at high temperatures (Song *et al.*, 2008a, 2008b; Tian *et al.*, 2008). Such side reactions result in the deactivation of the carrier as the product, CaO, cannot function as an OC and the sulphurous compounds can be problematic for flue gas processing when burning gaseous fuels where normally no such compounds are to be expected.

### *1.4.3. Common methods for preparing OCs*

The preparation of OCs broadly follows two steps: homogeneous mixing of the precursors and the formation of particles. Intimate mixing of the precursors can be achieved by several means. A popular method is mechanical mixing, which is largely a physical process. In this method, powdered solid precursors, normally having a particle size of the order of 10 μm or below, are mixed *e.g.* in a ball mill or a high shear mixer, to create a homogeneous mix. Sometimes water or other liquids are added to the mixture to improve the cohesion of the powders for better results (see, for instance, de Diego *et al.,* 2004 and Xu *et al.*, 2013). On the other hand, chemical processes such as co-precipitation can also be used for mixing. In this method, soluble precursors are first dissolved in a solution in the desired ratio. For the preparation of OCs, this typically involves the nitrate salts of various metals to be dissolved in water, although other soluble salts and solvents can also be used. A titrating agent, normally hydroxides or carbonates of an alkali metal, is then slowly added to the stirred solution or *vice versa*. If the appropriate titrating agent is used, the desired metals will form insoluble salts or hydroxides in the designed ratio throughout the solution, thus ensuring a uniform mixing. The precipitates are subsequently recovered by filtration and washed several times to remove any soluble contaminants before further processing (*e.g.* Chuang *et al.*, 2008; Imtiaz *et al*., 2012). Precipitation can also be achieved through evaporation although this process removes the solvent gradually and there is a risk of different species crystallising at different stages of the evaporation, leading to segregation and therefore inhomogeneity in the final mix. Hybrid physical and chemical methods can also be used. For example, the wet mixing method used in this work, as described in Section 2.2.2, relies on the hydration of the hydroxides to form gels which prevents the premature sedimentation of the CuO powder during drying.

Once a homogeneous mixture of the precursors is prepared, it can be further processed to form particles. The simplest method is granulation, in which a small amount of liquid is added to the dry mixture followed by agitation to form granules of various sizes. Granules of the desired size, typically with diameter between 75 and 500 μm, can be separated by sieving and the remaining material recycled (Bohn *et al.*, 2008). In an alternative method, the mixture can be made into a paste, either through the controlled addition of liquid to a dry mix or partial drying if a wet method was used, and extruded through a die of a chosen diameter by the application of high pressure. The extrudates can be cut to a prescribed length or broken up in a rotating device, known as the spheroniser, to form spheres with a rather uniform size, comparable to the die diameter. Conventionally extrudates on the order of mm are produced and further crushing and sieving is required to reduce the size of particles (Gayán *et al.*, 2012), however, it is possible to synthesis ceramic paste extrudates with diameter as thin as 100 μm with current technology (Grida and Evans, 2003; Yang *et al*., 2006) so that further processing can be avoided. Since high pressures are used in extrusion, it is expected that the particles formed are denser and therefore stronger than those formed by granulation. It is also possible to produce particles by atomisation, which is the process where slurry of the mixture is forced through a nozzle to produce droplets. The droplets can either be dried in flight (known as spray drying), before coming into contact and merging with other droplets, under ambient pressure or vacuum (Linderholm *et al.*, 2009), or injected into liquid nitrogen for instantaneous freezing followed by the sublimation of ice in vacuum, known as freeze drying or freeze granulation (*e.g.* Cho *et al.*, 2004; Mattisson *et al.*, 2009a). Lastly, some mixtures behave similarly to clays and set to form cakes rather than powders when dried. These cakes can be crushed directly to the desired size and do not require advanced processing techniques described above (Xu *et al.*, 2013).

Particles can also be produced from a different route, using the method of impregnation. In this method, the support material or its precursor is pre-formed into porous particles rather than mixed with the active material. A solution containing the precursor of the active component is introduced to fill the pores of the support particles and then dried, so that the active component can be evenly distributed onto the inner surface of the particles (Adánez *et al.*, 2006b; de Diego *et al.*, 2004; Shen *et al.*, 2009a). This procedure can be repeated several times to increase the loading of the active component.

Generally the particles are calcined at a temperature higher than the normal operating temperature for an extended period of time before use. This is done partly to sinter the material for higher mechanical strength and stability and partly to ensure that the particles will not undergo unexpected changes such as melting at the operating temperature.

## *1.5. Chemical-Looping with Oxygen Uncoupling (CLOU)*

Mattisson *et al.* (2009b) examined OC systems with an equilibrium partial pressure of $O_2$ near 0.01 bar around 900°C, namely $Co_3O_4$/CoO, $Mn_2O_3$/$Mn_3O_4$ and CuO/$Cu_2O$. In the fuel reactor, such OCs are able to release gas phase $O_2$ (termed Chemical-looping with oxygen uncoupling, or CLOU) so that the solid fuels can undergo direct combustion rather than gasification. Mattisson *et al.* (2009b) compared the average rate of conversion of petroleum coke in the presence of CuO supported on $ZrO_2$ with the rate obtained by Leion *et al.* (2007) from similar experiments conducted with $Fe_2O_3$ supported on $MgAl_2O_4$ and demonstrated that the rate was ~50 times faster using CuO, due to the “oxygen uncoupling” from the solid.

Subsequent investigations by Mattisson *et al.* (2009a) using petroleum coke with 40wt% CuO supported on $ZrO_2$ in a bubbling fluidised bed showed that the time required for 95% conversion of the coke ranged from just over 2 minutes at 885°C to about 20 s at 985°C. The relatively short time required for reaction of the latter material means that it is possible to convert all of the fuel within the fuel reactor, provided that the solid residence time of the fuel reactor is sufficiently long, of the order of a few minutes, thus eliminating the need for the carbon stripper and reducing the complexity of the CLC system for solid fuels. Indeed, Abad *et al.* (2012) demonstrated that full combustion of a bituminous coal with a carbon capture efficiency between 94.1% and 99.3% was possible without a carbon stripper, in a 1.5 $kW_{th}$ continuous apparatus using Cu-based OC with a solid inventory of 235 kg/$MW_{th}$ in the fuel reactor. As a first approximation, the results translate to an inventory requirement of 94 tonnes of OC for a 400 $MW_{th}$ boiler, which could be contained in a vessel with an i.d. of 10 m and a bed height about 1 m. Granted that on scaling up, the system can be expected to be less efficient and thus require more OC for the same performance, but even so, the size of the boiler would not be excessive compared to conceptual designs of large modern CFB boilers (Hotta, 2010; Robertson *et al.*, 2010). It should also be noted that larger

units have less specific surface area so that the heat loss would be smaller, which could compensate for the loss in efficiency.

A further advantage of CLOU is that the overall reaction is moderately exothermic in both the air reactor and the fuel reactor when using Mn- and Cu-based OCs while the fuel reactor would be almost thermally neutral when using Co-based OCs (Mattisson *et al.*, 2009b). In comparison, the fuel reactor is moderately endothermic for Fe- and Ni-based systems used in conventional CLC but, correspondingly, the air reactor is much more exothermic (Siriwardane *et al.*, 2009). As a result, the operating temperatures in the air and fuel reactors can be very close to each other or identical for CLOU whereas a difference in temperature about 50°C (depending on the solid inventory and circulation rate in the system) may be required for CLC with other OCs so that the OCs can supply the surplus sensible heat to sustain the endothermic reaction in the fuel reactor (Fennell and Anthony, 2015). It has been recognised that a temperature difference as high as possible is desired to improve the overall exergy efficiency of the system (Ishida *et al.*, 1987; Zhang *et al.*, 2009) when gas turbines are used, however if steam cycle is the primary means to generate energy rather than gas turbines, the high exergy stream generated at high temperature does not improve the overall efficiency since the limiting factor is the relatively low operating temperature of the steam cycle at ~620°C at best (Fennell and Anthony, 2015). On the other hand, for carrier materials experiencing relatively high degrees of thermal expansion, the cyclic temperature swing during continuous operation could cause internal stresses within the OCs, eventually leading to mechanical failure and attrition, reducing the lifetime of the carriers and in such cases CLOU processes can be more favourable.

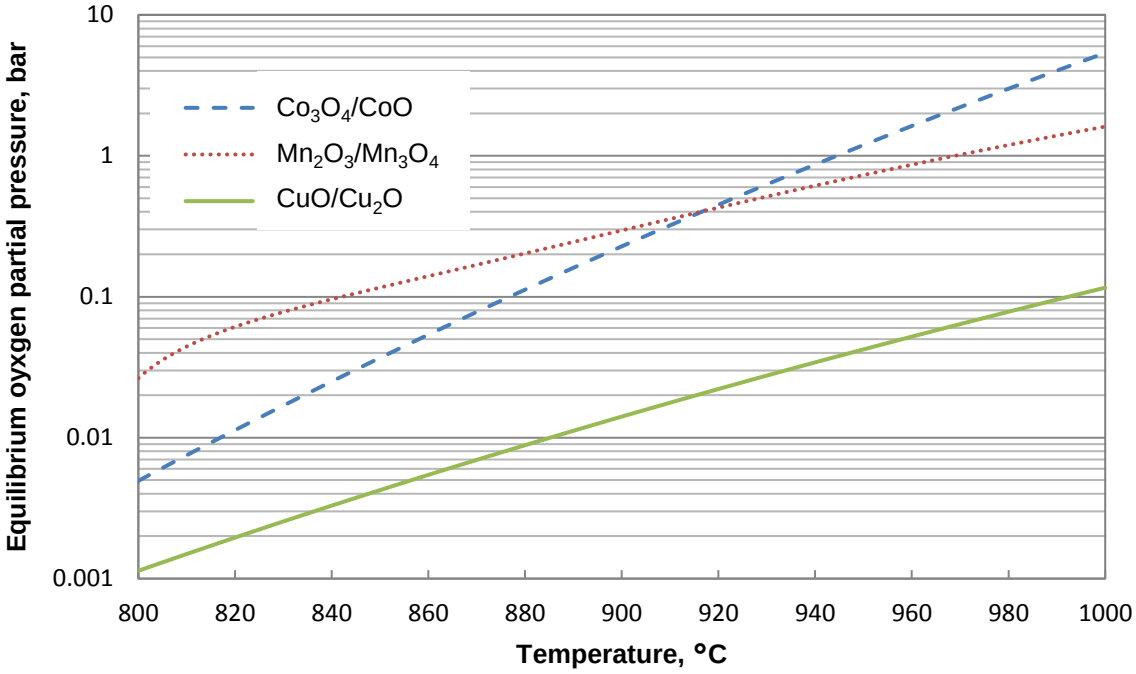


Figure 1-4 Calculated $P_{eq}$ for different CLOU systems between 800°C and 1000°C, data for the Co and Cu systems were generated from NIST WebBook (NIST, 2011) and data for the Mn system were generated using MTDATA from the national physical laboratory (NPL) (Davies *et al.*, 2002).

A defining feature of CLOU is the existence of a moderate equilibrium partial pressure or $O_2$, $P_{eq}$, so that the OC can spontaneously release appreciable amounts of $O_2$ in the fuel reactor for combustion and regain the lost $O_2$ from the air reactor in a timely manner. If reactions are carried out at ambient pressure, the $P_{eq}$ of a suitable carrier must be below 0.21 bar, the partial pressure of $O_2$ in air, so that the oxygen uncoupling can be reversed in the air reactor, although a much higher limit applies to pressurised systems. However, a high $P_{eq}$ can lead to a significant loss of $O_2$ in the fuel reactor or even the loop seals during transport (Abad *et al.*, 2012). This is undesirable because the effective oxygen capacity of the OC is lowered and the lost $O_2$ needs to be removed from the flue gas before the transport and sequestration of the $CO_2$, incurring additional cost. The lower limit of $P_{eq}$ for CLOU is a complicated trade-off and the rate of combustion of the particular solid fuel as well as the OC to fuel ratio and the rate of release of $O_2$ from the OC can influence the minimum value of $P_{eq}$ to some extent. Generally, the $P_{eq}$ needs to be greater than 0.005 bar or even 0.01 bar for the process to be practical. It can be seen from Figure 1-4 that assuming a feasible

range of $0.005 \leq P_{eq} \leq 0.05$ bar for CLOU, the operating temperature can vary from as low as 800°C to ~950°C for three common candidate oxides.

The kinetics of the thermal decomposition of the OC is also important for design and operation. For instance, Terayama and Ikeda (1983) investigated the rate of thermal decomposition of $Mn_2O_3$ using thermogravimetric analysis (TGA) and complete conversion of the sample at 800°C was achieved in 25 minutes. Although complete reaction was possible within ~9 minutes at 900°C, the $P_{eq}$ of the reaction would have been too high (~ 0.3 bar) for the material to be regenerated in air at this temperature. In comparison, Gayán *et al.* (2012) conducted TGA experiments with Cu-based materials and the thermal decomposition completed in ~ 1 minute at 900°C. Clearly, in a reactor system that is largely limited by chemical reaction of the OC, a larger solid inventory is required for OCs with a slower rate of oxygen release to maintain the same rate of consumption of fuel and in the above example, the Cu-based materials would be more favourable in this respect.

However, it is possible to tune $P_{eq}$ by using mixed oxides such as perovskites, partly due to the fact that the value of $P_{eq}$ of such systems depend on the oxygen vacancy, $\delta$, in addition to temperature (Mantzavinos *et al.*, 2000; Mizusaki *et al.*, 2000). Arjmand *et al.* (2013) examined the feasibility of several Mn-based perovskites as OCs and found that several modified materials based on $CaMnO_3$ (doped with La at the A site and Mg, Ti, Fe or Cu at the B site) could be oxidised by 5% $O_2$ at 900°C. Unlike simple metal oxides, the degree of oxygen deficiency in the lattice of the perovskites can influence the $P_{eq}$ for the release and uptake of $O_2$ (Leonidova *et al.*, 2011) so that the oxygen carrying capacity of such OCs would be dependent on the difference in the partial pressure of $O_2$ between the air and fuel reactors.

## *1.6. Objectives and Structure of the Dissertation*

The initial objective was to develop and characterise Cu-based OCs with a high oxygen capacity suitable for CLOU at a large scale. The aim was at finding OCs which

- could be readily, and economically, scaled up in production for industrial application,
- maintained high reactivity over repeated use,
- did not agglomerate under CLOU conditions and
- did not attrit excessively.

The next objective was to study the thermodynamics and chemical kinetics of the CLOU reaction with the chosen carriers using a series of carefully-designed experiments, as well as to investigate factors influencing their chemical and mechanical stability.

The final objective was to develop a suitable model, based on the thermodynamic and kinetic results, to describe the behaviour of the OC in a fluidised bed reactor.

This Dissertation is structured as follow. Chapter 2 describes the methods used for the development and characterisation of the OCs. Chapter 3 presents the effect of different support materials and preparation methods on the reactivity and stability of the prepared carriers while Chapter 4 focuses on the characterisation of the most suitable carrier based on the results from Chapter 3, with a particular emphasis on the attrition and agglomeration of the carrier in a fluidised bed. Chapter 5 focuses on the experimental determination of the thermodynamic equilibrium of the chosen OC in the temperature range relevant to CLOU and compares the results with the literature. In particular, potential factors influencing the equilibrium are studied and discussed. In Chapter 6, the kinetics of the thermal decomposition of the OC is investigated. The contribution to the apparent rate of decomposition measured experimentally from mass transfer and thermodynamic limitations was carefully analysed to extract the intrinsic chemical kinetics. Chapter 7 presents a mathematical model describing the behaviour of the OC in a fluidised bed environment with the aid of the thermodynamic and kinetic results obtained from previous chapters, as well as correlations available from literature to describe the characteristics of the bubbling fluidised bed. The model was validated using experimental results from a laboratory-scale fluidised bed reactor. Finally, conclusions from the current work and recommendations for future work are presented in Chapters 8 and 9, respectively.

# 2. Experimental Methods

## 2.1. Introduction

The experimental procedures and apparatus employed for the current work are described in this chapter, together with the methods for preparation and characterisation of the oxygen carriers. The principal types of apparatus used to investigate the synthesised OCs are described, together with typical operating conditions. However, since a wide range of experimental conditions were explored in this work, more details of individual, specific investigations are presented in appropriate chapters.

## 2.2. Preparation of oxygen carriers

### 2.2.1. Source of Materials

The chemicals used for this work are listed in Table 2-1. In addition to the chemicals, de-ionised water was available with conductivity $\leq$ 1 µS/cm; various gases used for experiments (air, ≥99.995%; $N_2$, ≥99.998%; Ar, ≥99.998%; 5 vol% $H_2$ in $N_2$, ≥99.999%) were supplied by BOC.

**Table 2-1 List of chemicals used with specifications from suppliers**

| *Molecular Formula* | *Supplier* | *Product SKU* | *Specifications* |
|---|---|---|---|
| $Al(NO_3)_3 \cdot 9H_2O$ | Fisher Scientific | A/2200/65 | ≥98% |
| $Al(OH)_3$ | Sigma-Aldrich | 239186 | 50-57% $Al_2O_3$ basis, <5 µm |
| $\alpha$-$Al_2O_3$ | Sigma-Aldrich | 11028 | ≥98%, <5 µm |
| $Ca(CH_3COO)_2 \cdot H_2O$ | Sigma-Aldrich | 402850 | ACS reagent, ≥99.0% |
| $Ca(OH)_2$ | Fisher Scientific | 219180010 | ≥98%, <5 µm |
| CaO | Fisher Scientific | C/2120/60 | Reagent grade, powder |
| $CH_3CH(OH)CH_3$ (2-propanol) | Fisher Scientific | 10173240 | 99.5+% |
| $Cu(NO_3)_2 \cdot 2.5H_2O$ | Sigma-Aldrich | 12837 | ≥98%, ≥26% Cu basis |
| CuO | Sigma-Aldrich | 208841 | 98%, powder, <10 µm |
| $NH_4HCO_3$ | Fisher Scientific | 393210010 | 99% |

### 2.2.2. Preparation of Oxygen Carriers

The primary method used for the synthesis of oxygen carriers was mechanical mixing.

In the *dry mixing* procedure, a mixture of dry powders (~150 ml of each) of the active material, CuO (70 wt%), and support, either $Al_2O_3$ or mayenite ($Ca_{12}Al_{14}O_{33}$, or $12CaO{\cdot}7Al_2O_3$), were ground in a planetary ball mill (MTI, model MSK-SFM-1) for 2 hours at a speed of 25 revolutions per second. The mayenite was synthesised separately *via* a sol-gel method, described below. The resulting powder from the ball milling was calcined in air in a box furnace at 1000°C for 6 hours preceded by a heating period with rate 20°C/min. The process of milling and calcination was performed successively up to 4 times to investigate the effect of repeated processing. As noted above, the mayenite was prepared separately using a sol-gel method, largely following the protocol of Li *et al.* (2005) and Dennis and Pacciani (2009). The precursors, CaO and $Al(NO_3)_3{\cdot}9H_2O$, in the appropriate molar ratio of 6:7, were dissolved in a 75:25 by volume solution of de-ionised water and 2-propanol. The mixture was stirred on a hotplate at 70°C for 6 hours to form a gel, which was subsequently dried in an oven overnight, at 120°C. The resulting cake was then crushed into fine powder and calcined at 1000°C for 4 hours to yield the desired mayenite.

In the *wet mixing* method, 11.23 g of $Ca(OH)_2$ and 17.60 g of $Al(OH)_3$ powders were mixed with 400 ml of de-ionised water in a 1 L beaker. The resulting slurry was maintained at 40°C and continuously stirred on a hotplate for 2 hours, at which point 30.00 g of CuO powder was added to the mixture. After further mixing for 20 hours, the slurry was dried in a ventilated oven for 48 hours at 80°C. The cake obtained from drying was crushed and calcined at 1000°C for 6 hours and finally sieved to the desired size fraction, typically between 300 and 425 µm, for subsequent use. The majority of investigations in this Dissertation used this wet method. For experiments requiring large quantities of the carrier, the above process was repeated several times under the same conditions to ensure consistency between batches.

A gel method was also used to produce the reference material – $CuAl_2O_4$. Here, $Cu(NO_3)_2{\cdot}2.5H_2O$ and $Al(NO_3)_3{\cdot}9H_2O$ were dissolved in de-ionised water to form 200 ml of aqueous solution consisting of 0.10 M of $Cu^{2+}$ and 0.20 M of $Al^{3+}$. The solution was titrated against 1.0 M $NH_4HCO_3$ solution until the pH of the mixture reached 4.00. At this final condition, a light blue gel was formed, which was then oven dried at 80°C and calcined at 1000°C for 6 hours to form the desired $CuAl_2O_4$.

## 2.3. Characterisation of the Oxygen Carriers

### 2.3.1. Analysis by X-Ray Powder Diffraction (XRD)

In this work, XRD analysis was performed using an Empyrean PANalytical diffractometer with Cu as the anode material. The X-ray generator was operating at 40 kV with a tube current of 40 mA, producing X-rays with characteristic wavelengths at 1.5406 Å and 1.5444 Å with an intensity ratio of 2:1. These two wavelengths correspond to the $K_{\alpha 1}$ and $K_{\alpha 2}$ emissions of Cu atoms, *i.e.* the emission of photons due to the relaxation of electrons from 2p orbitals to 1s orbital. The slight difference in energy is due to spin-orbit interaction. In a typical scan, fine powder (<50 μm, the smallest test sieve size available) of the materials of interest was prepared by manual grinding with a mortar and pestle. The powder was carefully packed into a sample holder disc to produce a flat finish and loaded into the diffractometer using an automatic sampling robot. The diffractometer was set up in a typical Bragg-Brentano geometry where both the source and detector moved along the goniometer circle synchronously, each making an angle $\theta$ (known as the Bragg angle) to the sample. The scan range used was from $2\theta = 5°$ to 80° with a step size of 0.0167°. The scan type was set to continuous at a speed of 0.125°/s. The spectra obtained were compared with the Inorganic Crystal Structure Database (ICSD) embedded within the software, X'pert HighScore Plus, accompanying the system for phase identification.

Estimates of crystallite size were performed for selected samples alongside the phase identification, using the Scherrer equation (Patterson, 1939), *viz.*

$$d_{grain} = \frac{K_{Sh}\lambda}{\beta \cos\theta} \qquad 2\text{-}1$$

where $d_{grain}$ denotes the average diameter of the crystallite; $K_{Sh}$ is the shape factor, taken to be the typical value of 0.9; $\lambda$ is the wavelength of the incoming radiation, taken as the weighted average of the two $K_{\alpha}$ radiations, 1.5418 Å. This is acceptable since the diffraction angles involved were sufficiently small and with the relatively fast scan rate used, the separation of the doublet was not significant. The parameter $\beta$ is the full width at half maximum (FWHM) of the diffraction peak at the corresponding Bragg angle $\theta$. Since the calculation was only meant to be an order-of-magnitude analysis to assess whether the crystallite size had changed significantly between treatments (of both physical and chemical nature), it was assumed that the broadening of the diffraction peak was due entirely to the size of crystallite. Instrumental broadening, which would lead to an underestimation of $d_{grain}$, was not taken into account. However,

this effect should be constant across different samples so that when comparing the crystallite size, this systematic error would diminish and not affect the conclusion.

### *2.3.2. Nitrogen adsorption analysis*

The surface area and pore size distribution of the OC particles were measured using a TriStar 3000 (Micrometrics, Serial No. 1001) gas adsorption analyser. In a typical analysis, particles were first degassed *in vacuo* at room temperature to remove contaminants adsorbed on the internal surface. After degassing, $N_2$ was introduced into the sampling chamber isothermally at 77 K, in small increments so that the absolute pressure of the chamber increased from ~0.01 bar to 1 bar and then gas was withdrawn to a pressure of ~0.14 bar. The amount of $N_2$ adsorbed and desorbed during the pressure swing was recorded and used to calculate the surface area of the sample using the Brunauer–Emmett–Teller (BET) theory (Brunauer *et al.*, 1938). The pore size distribution and pore volume (for pore sizes smaller than 200 nm) were calculated from the Barrett-Joyner-Halenda (BJH) model (Barrett *et al.*, 1951).

### *2.3.3. Optical microscopy*

Cross sections of the OC particles were examined using a Leica DM LM microscope (Leica Microsystems) equipped with objective lenses of magnifications 2.5x, 5x, 10x, 20x and 50x and an ocular lens of magnification 10x. The samples were mounted in a clear acrylic resin and polished using SiC paper up to a grit size of P4000 (mean diameter 2.5 µm) and finished in an alumina suspension with a mean particle size of 0.3 µm (all materials were acquired from MetPrep). The microscope was also coupled with a Leica EC3 digital colour camera to digitalise the obtained micrograph and the micrograph was further processed within the accompanying Leica LAS EZ software to produce scale bars.

## 2.4. Thermogravimetric analysis

A thermogravimetric analyser (TGA) (TGA/DSC1, Mettler Toledo) was used to investigate the thermodynamic and kinetic properties of materials. The analyser consists of a microbalance accurate to 1 µg and an electrically-heated horizontal tube

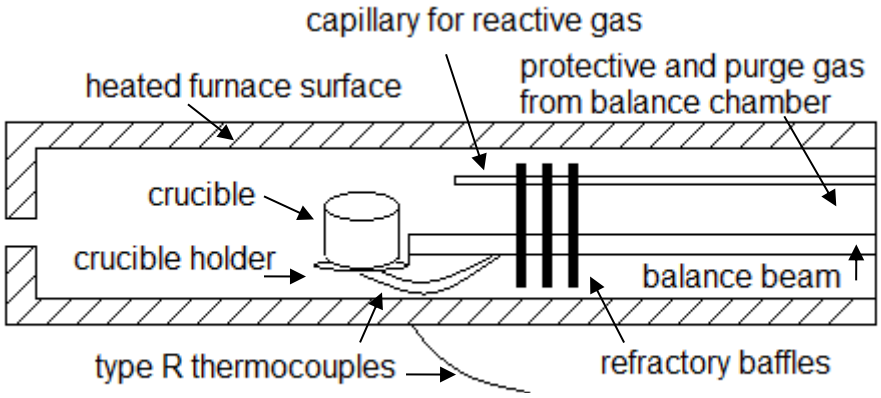


Figure 2-1 Schematic diagram of the furnace of TGA/DSC1 with annotated features.

furnace (Figure 2-1) of internal diameter 12 mm and heated length ~150 mm (the total volume of the furnace is 16 ml). The microbalance extends a ceramic balance beam into the furnace as shown in Figure 2-1 but the balance chamber is water cooled to maintain a temperature of 22°C. A crucible holder made of an alloy of platinum and rhodium is attached to the end of the balance beam and two type R thermocouples are welded to the back of the crucible holder to measure the temperature of the sample. Two types of crucibles were used for the investigations: 70 µL alumina crucibles with an internal diameter of 4.90 mm and depth 4.00 mm and 30 µL platinum crucibles with an i.d. of 5.48 mm and depth 2.11 mm. The furnace wall is heated electrically with a cooling jacket on the outside for fast heating and cooling. To illustrate this, the rate of heating was investigated, with results in Figure 2-2.

It can be seen from Figure 2-2 that, at the maximum heating rate, the furnace could reach 900°C from 50°C in 2 minutes and settle to a steady condition within 10 minutes. If a smaller step change in temperature set point, *e.g.* from 875°C to 925°C, were implemented, the sample temperature was found to settle at the new value within 2 minutes if no reaction were taking place.

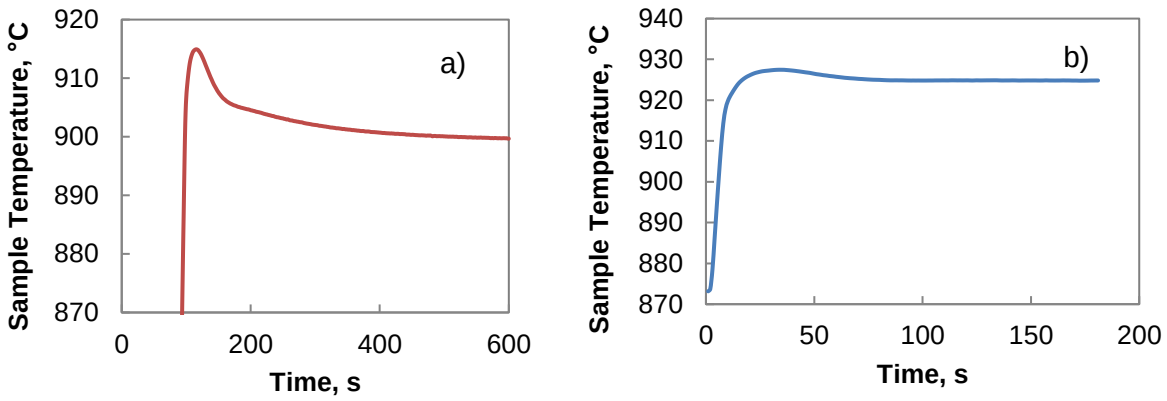


Figure 2-2 Typical temperature response of the TGA to a step change. a) For a large step change, 50°C-900°C. b) For a small step change, 875°C-925°C. The set point changed at $t = 0$ in both cases.

In addition to measuring the change in mass of a specimen, the TGA performs simultaneous differential thermal analysis (SDTA) using the difference between the measured sample temperature and furnace temperature, measured by another type R thermocouple embedded in the wall of the furnace. The temperature difference is subsequently used to calculate the heat flow from the sample to the environment such that a negative heat flow represents an endothermic process. The SDTA measurements can sometimes be more useful than the weight measurement, for example, to determine the onset of significant reaction, as illustrated in Figure 2-3, or to identify events without mass change such as change of phase. However, SDTA measurements are less reliable than differential scanning calorimetry (DSC) measurements because the temperature of the environment in the vicinity of the sample is not measured simultaneously in the SDTA method, and conclusions drawn from the quantitative analysis of the heat flow measurements should be treated with extreme caution.

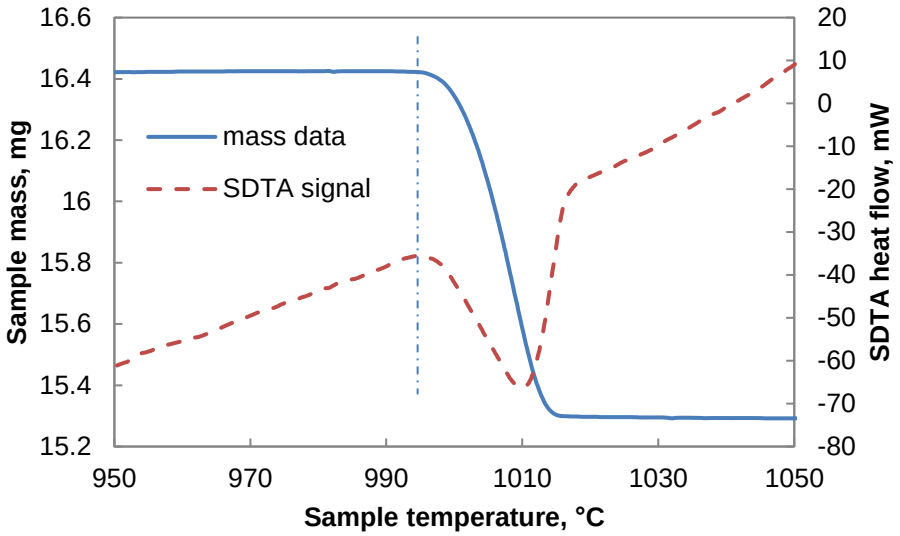


Figure 2-3 Sample mass measurement (solid curve) and SDTA measurement (dashed curve), taken from the temperature programmed reduction of 70 wt% CuO supported with mayenite (dry mixing) in diluted air with a heating rate of 5°C/min. The onset of reduction at ~993°C (dash-dot vertical line) can be seen clearly from the sharp change in the SDTA signal whereas the mass change at the same temperature is less obvious.

To prevent any hot gas from entering the balance chamber and affecting the performance of the balance, ~70 ml/min of inert gas (measured at 20°C and 1 bar, same for all flowrates stated hereafter, unless otherwise specified), known as the protective gas, flows through the balance chamber into the furnace constantly during operation. Most of the experiments were conducted using Ar as the protective gas but some were done in $N_2$. It was confirmed that the calibration of the TGA was not affected by the choice of the protective gas and either could be used interchangeably for convenience. A second stream of gas, known as the purge gas, is introduced into the furnace from the same position as the protective gas. However, the purge gas bypasses the balance chamber and only serves to sweep any gas in the furnace downstream to protect the wall of the furnace, in addition to the protective gas. Typically, the purge gas was set to ~ 50 ml/min and had the same composition as the protective gas. Occasionally, other gases were blended into the purge gas intentionally to produce an oxidising or reducing atmosphere in the furnace chamber. Lastly, a reactive gas could be supplied through a capillary with exit located 9 mm from the centre of the crucible. The capillary is designed such that the reactive gas is well dispersed across the crucible so that the sample experiences a uniform environment.

Since the reactive gas is introduced near the sample, dilution of the gas by the purge and protective gas is limited.

The TGA could be programmed to operate either isothermally or with a constant rate of heating or cooling (with typical rates between 1-20°C/min) or a combination of the two. Particular protocols used for individual investigations will be described later in the respective chapters.

## 2.5. Fluidised bed reactors

### 2.5.1. Batch fluidised bed reactor

A batch fluidised bed reactor was used to measure the rate of release of oxygen from the OC particles. The fluidised bed was made of an alumina tube with an i.d. of 17 mm. A distributor of sintered alumina was fixed inside the reactor tube with calcium aluminate cement at the interface between the distributor and the inner surface of the reactor. The typical pressure drop across the distributor was approximately 2000 Pa, while the pressure drop across the fluidised bed was less than 1000 Pa, measured using an omega PX-138 differential pressure transducer. In a typical experiment, approximately 8 g of silica sand in the size fraction 300-355 µm was added to the reactor and fluidised by $N_2$ at a constant flowrate. To investigate the effect of fluidisation velocity on the overall reaction, a range of flowrates of $N_2$ was used, between 0.6 and 2.2 l/min, as measured at 20°C and 1 bar. The flowrates correspond to superficial velocities between 4.8 and 18 times the minimum fluidisation velocity at 900°C and the ratio only changes slightly at 850°C and 950°C, the other two temperatures where experiments were conducted. The fluidised bed is expected to operate in the bubbling regime at the lower end of the flowrates used and in the slugging regime at the higher end. The minimum fluidisation velocity of the bed, $U_{mf}$, based on the cross-sectional area of the reactor, was estimated using the correlation of Wen and Yu, (1966) *viz.*

$$Re_{mf} = \sqrt{1135.7 + 0.0408 Ar_p} - 33.7 \qquad 2\text{-}2$$

where the Reynolds number, $Re_{mf}$ depends on the minimum fluidisation velocity, $U_{mf}$, the particle diameter, $d_p$, the dynamic viscosity of the fluidising gas, $\mu$ and the density of the gas, $\rho$ by

$$Re_{mf} = \frac{\rho U_{mf} d_p}{\mu} \qquad 2\text{-}3$$

and the Archimedes number is,

$$Ar_p = \frac{g d_p{}^3 \rho\left(\rho_p - \rho\right)}{\mu^2} \qquad 2\text{-}4$$

with the gravitational acceleration being $g$ and the density of the particles, $\rho_p$. The density of the sand particles was calculated to be 2510 kg/m$^3$, by measuring the volume of a known mass of the particles under water. The diameter of the particles, $d_p$, used for the above calculations was taken to be the arithmetic average of the upper and lower limit of the particle sieve size fraction. The dynamic viscosity of $N_2$ at atmospheric pressure up to 1100°C was obtained from the NIST database and the density of the gas was calculated using the ideal gas law. The viscosity data can be parameterised for algebraic manipulation using Sutherland's formula (Sutherland, 1893), *i.e.*

$$\mu = \frac{C_{\mu,1} T^{3/2}}{T + C_{\mu,2}} \qquad 2\text{-}5$$

with $C_{\mu,1}$ = 1.519×10$^{-5}$ Pa s K$^{-1/2}$ and $C_{\mu,2}$ = 151 K. Here, $T$ is the temperature of the gas expressed in kelvin.

In a typical experiment, the fluidised bed was maintained at a steady temperature with a fixed flowrate of $N_2$. Then, a small amount of OCs, up to about 20 mg, was tipped into the fluidised bed of sand from the top and the gas emerging from the reactor was sampled by a universal exhaust gas oxygen (UEGO) sensor to measure the concentration of $O_2$. The UEGO sensor was modified from the Bosch LSU 4.2 sensor and optimised for fast response. The time constant of the response to a step change (time taken for the signal to change from 10% to 90% of the total response) was ~20 ms and steady state could be achieved within 100 ms (Collings *et al.*, 2012; Regitz and Collings, 2008). The short response time makes the UEGO sensor most suitable for measuring fast reactions. In this case, the time taken for complete reaction was of the order of 10-20 s, as seen in the typical experimental response in Figure 2-4. It would not have been possible to obtain reliable results from the more commonly used paramagnetic analyser (ABB, Magnos 206) because of its long response time. The 90% response time of the paramagnetic $O_2$ analyser is specified as 4 s with a sampling rate

of 90 l/h, or 1.5 l/min, by the manufacturer and the response time will be even longer with lower sampling rates.

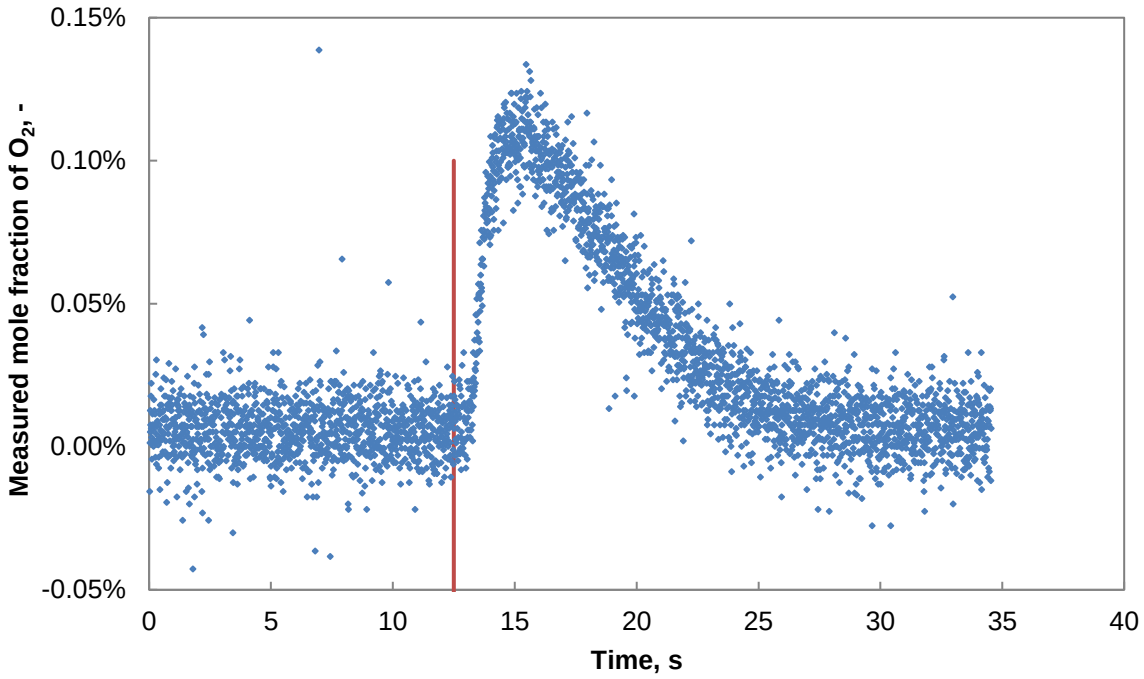


Figure 2-4 The concentration profile of $O_2$ as measured by the UEGO sensor during a typical experiment conducted in the fluidised bed at 900°C with a $N_2$ flowrate of 1.8 l/min and a sample mass of 4.7 mg. The time at which the sample was dropped into the bed is marked by the red vertical line ($t$ = 12.5 s).

### 2.5.2. *Fluidised bed with internal circulation*

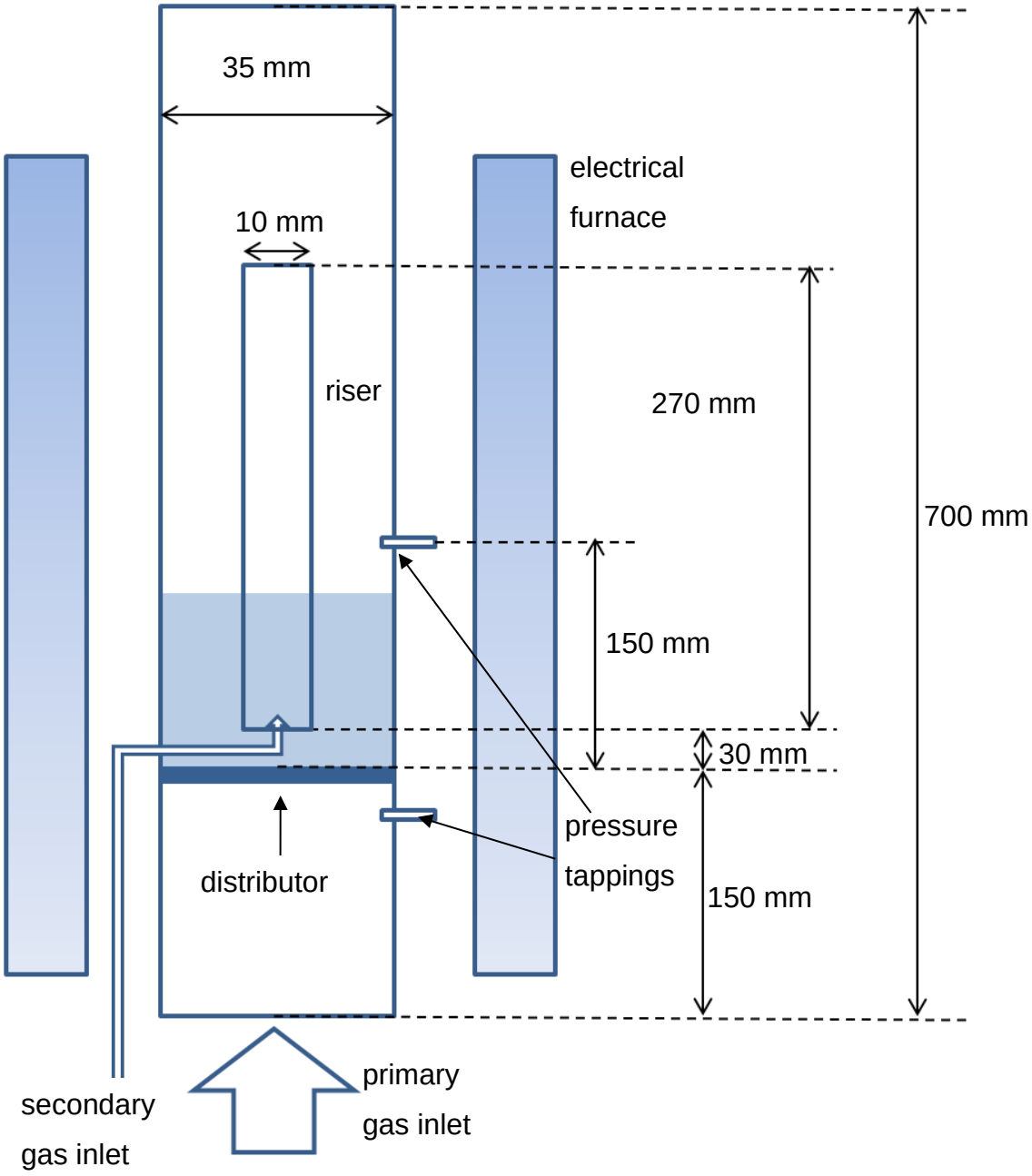


Figure 2-5 Schematic diagram of the fluidised bed with internal circulation.

An electrically-heated, stainless-steel (grade 316) circulating fluidised bed reactor was used to investigate the agglomeration and attrition of the oxygen carrier at high temperatures; a schematic diagram of the reactor is shown in Figure 2-5. A draft tube (riser) was fixed inside the reactor by set screws so that its lower end was 30 mm above the distributor. The main reactor was fluidised by air, $N_2$ or 5 vol% $H_2$ in $N_2$ with a typical flow rate of ~ 2.0 l/min measured at 20°C and 1 bar, corresponding to a superficial velocity ~ 4 times that of the minimum fluidisation velocity. The distributor was made of stainless steel (grade 316) with 15 holes each having a diameter of

0.3 mm. The holes were evenly spaced on two concentric circles with 6 on the inner circle with a radius of 7.5 mm and 9 on the outer circle with a radius of 12.5 mm, as shown in Figure 2-6.

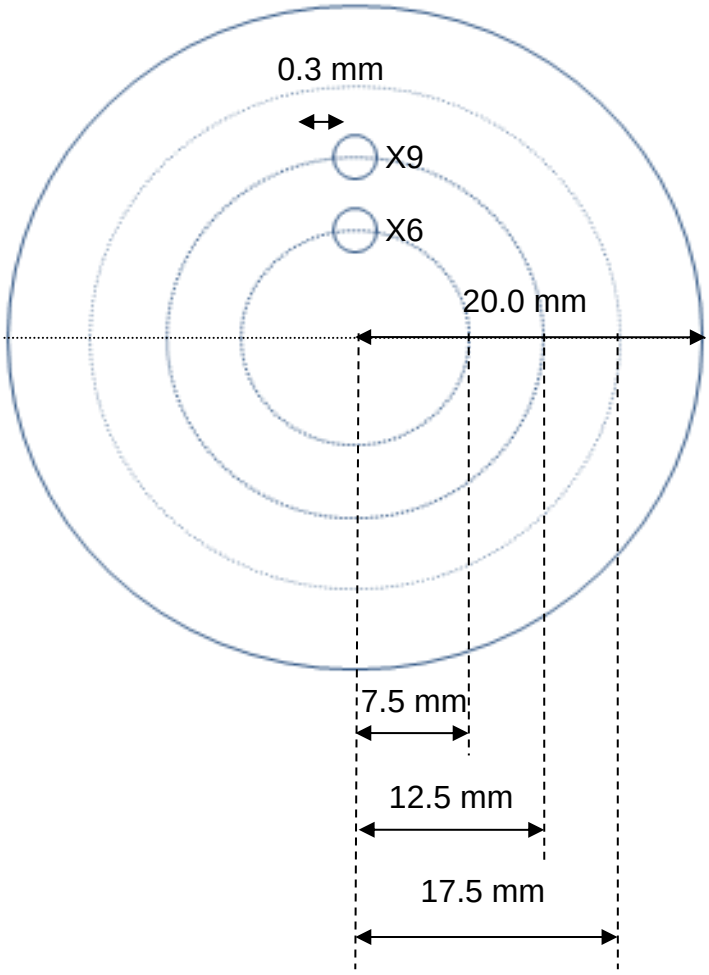


Figure 2-6 Principal dimensions of the distributor consisting of 15 holes, 6 of which were evenly distributed on a circle with a radius 7.5 mm from the centre and 9 were evenly distributed on a circle with a radius 12.5 mm from the centre. The i.d. of the reactor was 35 mm.

In a typical experiment, approximately 100 g of the OC particles were fluidised in the reactor and the height of the bubbling fludised bed was ~ 100 mm. A separate gas supply (air, $N_2$ or 5 vol% $H_2$ in $N_2$) was introduced directly into the draft tube with a flowrate ~ 2.4 l/min (20°C and 1 bar) through a stainless steel (grade 316) tube with a nominal diameter of 1/8 inch (Swagelok®), shown as the secondary gas inlet in Figure 2-5, to enable transport of solids from the fluidised bed upwards *via* the draft tube and the solid emerging from the top of the draft tube would fall back to the bed, forming a circulation loop. Two type-K thermocouples were used to monitor the temperature within the reactor, one located in the bubbling bed outside the draft tube, ~ 5 cm above

the distributor and the other located at the middle of the inside of the draft tube. The typical temperature difference between the two thermocouples was 5-10°C at steady state. The pressure drop across the bubbling section was measured using an Omega PX-138 pressure transducer operating in differential mode between just below the distributor plate and 150 mm above the distributor. The total differential pressure measured during operation was approximately 3450 Pa when the particles were present and ~2500 Pa for an empty reactor. The mass of the particles before and after being fluidised between 850°C-900°C for an extended period of time, up to 100 hours, was measured to assess the attrition of the particles.

# 3. The influence of the support on the reactivity and stability of OCs

## *3.1. Introduction*

As outlined in Chapter 1, the OC is central to chemical-looping processes. In addition to the chemical activity and stability required for long term operation, the OC must be resistant to agglomeration and attrition. While some natural minerals, most notably ilmenite, can be used directly as the OC, most synthetic carriers are made from powdered precursors. Consequently, the method of preparation of synthetic OCs may influence the chemical and mechanical stability of the final product. Furthermore, when the OC is composed of more than one substance, reactions between the substances may also affect the behaviour of the carrier.

This chapter presents the work undertaken to investigate the effect of support on the chemical properties of OCs.

### *3.1.1. Background*

CuO is an attractive candidate as an OC because it has a high capacity for donating oxygen per unit mass of oxidised material – 20 wt% for CLC *via* the transition CuO/Cu and 10 wt% for CLOU *via* CuO/$Cu_2O$. However, pure CuO sinters heavily at temperatures as low as 800°C. De Diego *et al.* (2004), on the basis of investigations in a TGA, reported that pure extrudates of CuO lost 90% of their oxygen capacity after a mere 3 cycles of reduction by $CH_4$ followed by re-oxidation in air at 800°C, whereas extrudates containing 60 wt% of other materials, known as supports, could retain their activity for up to 100 cycles. However, some of the extrudates degraded significantly and turned into powders after the cycling in a TGA where, of course, the samples remained stationary throughout. Follow up studies showed that particles where the CuO was supported on $Al_2O_3$ displayed various degrees of agglomeration in a fluidised bed when the CuO content exceeded 10 wt% (de Diego *et al.*, 2005) but for CLOU operations, agglomeration was not observed with particles containing 40 wt% CuO on $ZrO_2$ or 60 wt% CuO on $MgAl_2O_4$ (Gayán *et al.*, 2012).

From the evidence presented in previous research, it is clear that pure CuO must be supported on, *e.g.* a refractory oxide, for stable performance in terms of chemical activity. Even so, the mechanical stability varies widely depending on the proportion of CuO present, supporting materials used as well as the method of preparation. In this Dissertation, various Ca- and Al-based supports have been used for the synthesis

because the precursors are cheap and readily available, hence suitable for large scale production.

### *3.1.2. Interactions between the support and active material*

The Ca-Cu-O system has been studied by many authors (*e.g.* Roth *et al.*, 1991; Suzuki *et al.*, 1994; Tsang *et al.*, 1995), partly because of interest in high-temperature superconductors such as the quaternary oxides of Bi-Sr-Ca-Cu or Hg-Ba-Ca-Cu (Schilling *et al.*, 1993; Subramanian *et al.*, 1988). The ternary Ca-Cu-O compounds have rather low melting points just above 1000°C (Roth *et al.*, 1991). This is even lower than the melting point of metallic Cu, the sintering of which is believed to be the cause of de-fluidisation and agglomeration of Cu-based OCs for CLC with $CH_4$ (de Diego *et al.*, 2005). Furthermore, Suzuki *et al.* (1994) found that the equilibrium partial pressure of $O_2$ in the system CaO-$Ca_2CuO$-$Cu_2O$ is considerably lower than in the CuO-$Cu_2O$ system. This implies that the viable temperature for CLOU will have to be higher if CaO and $Ca_2CuO$ are present in the OC, making the OC more susceptible to agglomeration. Moreover, CaO is able to react with $CO_2$ to form $CaCO_3$ if the partial pressure of $CO_2$ is sufficiently high. This would normally be of no concern because, at 900°C, the required partial pressure of $CO_2$ is slightly above 1 bar for the carbonation to be feasible. However, if the combustion were carried out at elevated pressure, it would be possible for the partial pressure of $CO_2$ to exceed the equilibrium value in the fuel reactor causing some $CO_2$ to be transferred to the air reactor in the form of $CaCO_3$, reducing the carbon capture efficiency. Thus it is imperative to avoid either free CaO or the mixed oxides in any potential Cu-based OCs.

Jacob and Alcock (1975) used an electrochemical method to investigate the equilibria of the Al-Cu-O system between 700°C and 1100°C. The feasible equilibria are

$$4CuO \rightleftharpoons 2Cu_2O + O_2 \qquad 3\text{-}1$$

$$CuO + Al_2O_3 \rightleftharpoons CuAl_2O_4 \qquad 3\text{-}2$$

$$Cu_2O + Al_2O_3 \rightleftharpoons 2CuAlO_2 \qquad 3\text{-}3$$

$$2CuO + 2CuAl_2O_4 \rightleftharpoons 4CuAlO_2 + O_2 \qquad 3\text{-}4$$

$$4CuAl_2O_4 \rightleftharpoons 4CuAlO_2 + 2Al_2O_3 + O_2 \qquad 3\text{-}5$$

and the measured values of Gibb's free energy of reactions, $\Delta G$, decrease with temperature for all the reactions apart from that of reaction 3-3.

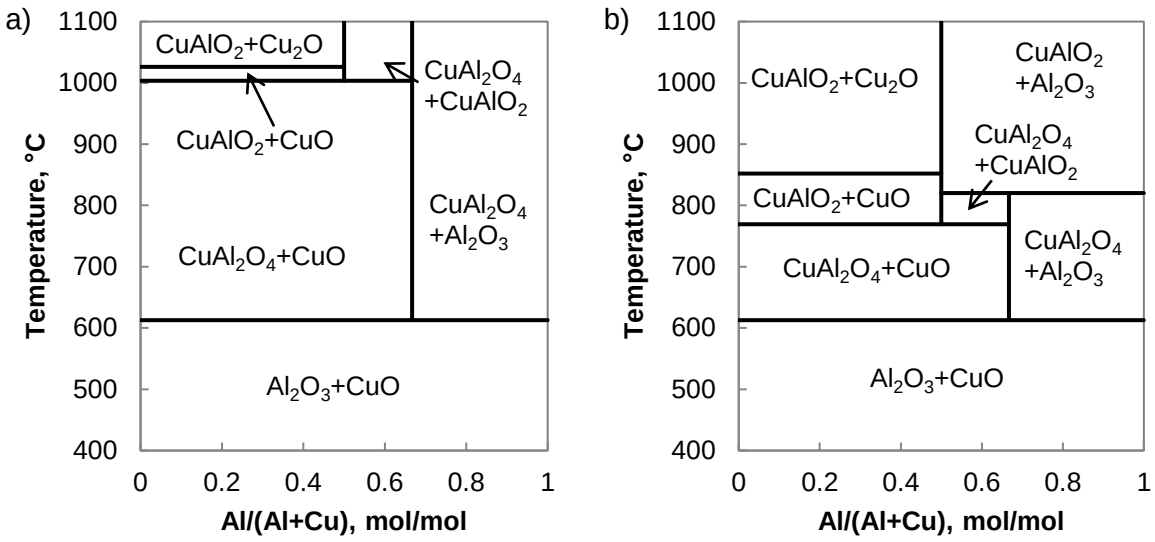


Figure 3-1 Sections of the phase diagram of the Al-Cu-O system at different partial pressures of $O_2$, based on the results of Jacob and Alcock (1975). The thermodynamically stable phases in each region are annotated accordingly. a) $P_{O2}$ = 0.21 bar. b) $P_{O2}$ = 0.005 bar.

Using the thermodynamic data measured in their work, two sections of the phase diagram of the system have been calculated and are presented in Figure 3-1, at different but fixed partial pressures of $O_2$ ($P_{O2}$). From these sections, it is evident that at temperatures relevant to CLOU, *i.e*. between 800°C and 1000°C, $CuAl_2O_4$ is expected to form *via* reaction 3-2 and this spinel can decompose to the delafossite phase $CuAlO_2$ in the presence of CuO at a lower temperature than the thermal decomposition of CuO alone. When excess $Al_2O_3$ is present, the conversion from the spinel to the delafossite can occur at a much higher temperature but the equilibrium is strongly dependent on $P_{O2}$, more so than reactions 3-1 and 3-4. At extremely low $P_{O2}$, of the order $10^{-10}$ bar, $CuAlO_2$ and $Cu_2O$ can be further reduced to metallic Cu. Such levels of $P_{O2}$ are normally only achieved in a reducing environment in which any residual $O_2$ in the gas phase is removed by the reducing agent, *e.g*. $CH_4$, CO or $H_2$. The melting points of the ternary compounds $CuAlO_2$ and $CuAl_2O_4$ were not explicitly reported but the phase diagrams presented in the work of Jacob and Alcock (1975) suggested that a eutectic mixture of $CuAlO_2$ and $Cu_2O$ may melt just above 1100°C whereas the spinel and the delafossite do not melt at 1200°C. In comparison, the eutectic mixture of CuO and $Cu_2O$ melts at 1075°C with a $P_{O2}$ of 0.53 bar but $Cu_2O$ has a melting point as high as 1235°C at a low $P_{O2}$ of $8\text{x}10^{-4}$ bar (Schmidt-Whitley *et*

*al.*, 1974). In conclusion, the formation of copper aluminates can be beneficial for CLOU in terms of chemical equilibrium. However the melting temperature of the mixture is comparable to that of the pure Cu-O system so that particles based on the Al-Cu-O system may suffer similar problems of agglomeration to the Cu-O system.

The Al-Ca-O system has been studied extensively and different calcium aluminates (from $CaO{\cdot}6Al_2O_3$ to $3CaO{\cdot}Al_2O_3$, expressed in pseudo binary form) can be formed depending on the ratio of Al to Ca present in the precursor. The melting temperatures of various calcium aluminates are rather high, all above 1400°C (Hallstedl, 1990). As the main ingredients in high alumina cement, calcium aluminates exhibit relatively high mechanical strength, too, making them suitable candidates as the support material for OCs. However, when CuO is introduced to the system, the constituents CaO and $Al_2O_3$ in the system might react preferentially with CuO depending on the equilibria of the respective systems involving Cu as discussed earlier, and the rate of formation of any intermediates. In addition, quaternary compounds may also be formed. However, insufficient information is generally available regarding this quaternary system. Donat *et al*. (2015a) did investigate such possible interactions using a theoretical approach by means of thermodynamic calculations using the software MTDATA, utilising the NPL materials database (Davies *et al.*, 1990). Experimental verification was also undertaken. The calculations showed that $CuAl_2O_4$ is thermodynamically favourable over $CaO{\cdot}6Al_2O_3$ whereas all other calcium aluminate phases are more favourable than the ternary compounds of Cu. However, XRD analysis of samples containing nominally 60 wt% CuO and supports prepared with different Al:Ca ratios using the wet mixing method showed that trace amounts of $CuAl_2O_4$ were present over a wider range than predicted from the calculations. Furthermore, as the fraction of Ca approached the stoichiometry of $12CaO{\cdot}7Al_2O_3$, the compound $Ca_3Cu_7O_{10}$ started to form instead of $3CaO{\cdot}Al_2O_3$, which resulted in the severe sintering of the particles after calcination in air for 6 hours at 1000°C.

## *3.2. Experimental methods*

### *3.2.1. Preparation of OCs*

Two different supported OCs were prepared to investigate the effect of support on the carriers. Pure CuO powder was used as a reference material for comparison and all the supported OCs were manufactured using the same CuO powder. Carriers containing 70 wt% CuO supported on $Al_2O_3$ and mayenite, respectively, were prepared

using a ball mill, as described in Section 2.2.2. The powders were subjected to the grinding-calcination process for up to 4 times and samples were taken after each calcination for XRD analysis. Pure $CuAl_2O_4$ was also synthesised, using the gel method, also described in Section 2.2.2.

### *3.2.2. Methods of characterisation*

The phases present in the calcined OCs were determined using XRD analysis whilst the chemical reactivity and stability of the OCs were examined using the TGA.

To investigate the CLOU properties, approximately 6 mg of a powdered sample ($\leq$ 50 µm) were subjected to a temperature swing under a constant atmosphere with $P_{O2} \approx 0.02$ bar. The samples were held at 850°C for 20 minutes before the temperature was increased to 1000°C at a constant rate of 5°C/min, followed by a decrease back to 850°C at the same rate. Upon completion of the temperature swing, the samples were held at 850°C for 20 minutes before the start of the next temperature cycle over the same temperatures and at the same rates as the first cycle. Three cycles of the temperature programme were performed for each sample to assess the stability of the OCs.

A second set of experiments was performed isothermally at 900°C. In these experiments, the reactive gas used was changed sequentially from air to $N_2$ and then to 5%$H_2$ in $N_2$, repeated five times. The flowrate of each reactive gas was approximately 50 ml/min (measured at 20°C and 1 bar) and each gas was supplied for 20 minutes before switching to the next. A relatively large amount of sample, about 25 mg was used for each experiment so that the mass change in each segment was large compared to the background noise and the difference in buoyancy in different atmospheres. This was so that the oxygen capacity could be measured accurately.

## *3.3. Results*

### *3.3.1. Phase identification*

The phases present in each of the OCs investigated were identified using X-ray powder diffraction and the results are summarised in Table 3-1.

The XRD results confirmed that pure $Al_2O_3$ can react with CuO to form the spinel $CuAl_2O_4$ whereas calcium aluminates, mayenite in particular, do not react with CuO. The presence of $\alpha$-$Al_2O_3$ in Sample 2 is an indication that the ball milling method used

cannot guarantee micro mixing, which is the homogenisation of the precursor to the molecular level, and the individual particles of CuO and $Al_2O_3$ remained relatively large after the grinding so that the formation of $CuAl_2O_4$ was not complete due to the heterogeneity. This observation is further supported by the fact that variants of Sample 2 subjected to additional grinding (for 2 hours) and calcination (1000°C, 6hours) showed a decrease in the amount of $\alpha$-$Al_2O_3$.

**Table 3-1 Phase identification for the main OCs investigated**

| *Sample number* | *Nominal composition of OC* | *Phases present from XRD analysis* |
|---|---|---|
| 1 | Pure CuO as received | CuO |
| 2 | 70 wt% CuO 30 wt% $Al_2O_3$ | CuO, $\alpha$-$Al_2O_3$, $CuAl_2O_4$ |
| 3 | 70 wt% CuO 30 wt% mayenite | CuO, mayenite ($12CaO \cdot 7Al_2O_3$) |

### *3.3.2. The effect of support on the stability of carriers*

A sample of the reference material, 5.453 mg of pure CuO, was subjected to the temperature programme as outlined in Section 3.2.2, and the results are shown in Figure 3-2.

The figure shows the following features. The decomposition of CuO occurred at a measurable rate to form $Cu_2O$ at ~931°C and is clearly marked by the strong endothermic peak. The mass of the sample stabilised at 4.925 mg after the temperature reached ~950°C. Detectable re-oxidation of the sample only started at ~909°C but the reaction was slow with a mild exothermic signal from the SDTA measurement compared to the decomposition. The loss of mass during the decomposition was 9.68% of the sample mass, in good agreement with the theoretical value of 10.0%, allowing for the sample having a nominal purity of 98%. When the sample temperature was returned to 850°C in the first cycle, the mass was 5.290 mg, corresponding to a conversion of 69.1% for the oxidation. After the temperature programme, the sample was held at 850°C for a further 20 minutes (not shown in the figure) and the sample mass increased further to 5.373 mg during that period, *i.e.* a conversion of 84.8%.

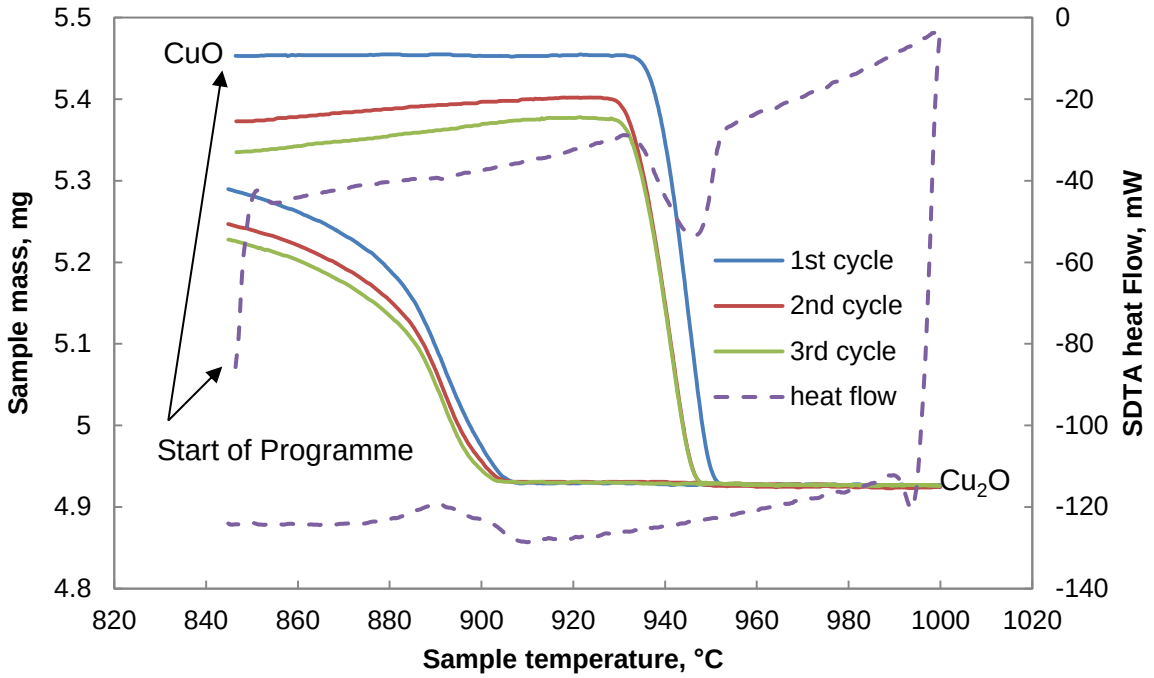


Figure 3-2 Reaction of pure CuO (Sample 1) in the temperature range 850°C-1000°C-850°C with a constant heating/cooling rate of 5°C/min in a fixed atmosphere ($P_{O2}$ ≈ 0.02 bar). The primary axis (left hand side) shows the mass of the sample (solid lines) for 3 successive cycles (blue, red, green) and the secondary axis (right hand side) is the SDTA measurement (dashed line) for the first cycle. The isothermal sections between cycles are omitted for clarity. The starting points of the curves are indicated on the graph by the arrows.

Detectable subsequent decomposition of the re-oxidised sample occurred at a slightly lower temperature of 928°C but the rate of decomposition appeared to be similar to that in the first cycle. On the other hand, subsequent re-oxidation occurred at the same temperature as the first cycle but the rate decreased as the number of cycles increased. By the end of the third cycle, the conversion was only 57.4%. In comparison with the results reported by de Diego *et al.* (2004), it appears that pure CuO deactivated less in CLOU operation compared to CLC where the oxide is reduced to metallic Cu. Nevertheless, deactivation was still significant over only 3 cycles and therefore pure CuO cannot be used directly for CLOU.

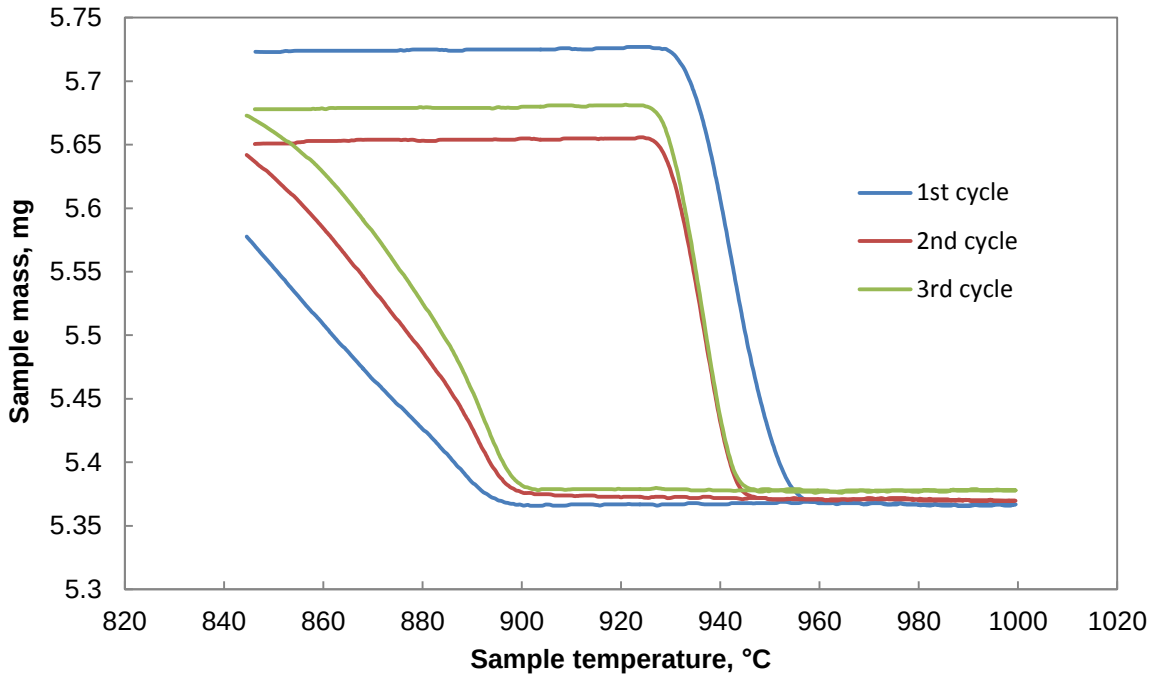


Figure 3-3 Mass change for Sample 2 (70 wt% CuO, 30 wt% $Al_2O_3$: ball milled and calcined at 1000°C once) in the temperature range 850°C-1000°C-850°C with a constant heating and cooling rate of 5°C/min in a fixed atmosphere ($P_{O2}$ ≈ 0.02 bar) for 3 cycles. The isothermal sections between cycles are omitted for clarity.

When 5.725 mg of powder consisting of 70 wt% CuO and 30 wt% $Al_2O_3$ (ball milled and calcined at 1000°C once, Sample 2) was subjected to the same treatment (Figure 3-3), the decomposition and re-oxidation temperatures did not differ significantly from those of the pure CuO sample but there were significant differences in the behaviour of the two samples. In contrast with the sample of pure CuO, the re-oxidation of the decomposed Sample 2 was slowest in the first cycle and the rate improved in subsequent cycles. By the end of the third cycle, the conversion was 85.8%. Most notably, the re-oxidation of the pure CuO slowed down significantly below 880°C whereas although the rate of re-oxidation of the supported also decreased, the change was much less pronounced. It is also worth noting that the mass loss from the decomposition of Sample 2 was only 6.17% compared to the expected value of 7.00%. This discrepancy is much larger than that of the pure CuO and cannot be solely accounted for by the presence of impurities. The decrease in the oxygen capacity for CLOU is most probably due to the formation of $CuAl_2O_4$, which is not easily decomposed; this will be discussed further in the later sections of this chapter.

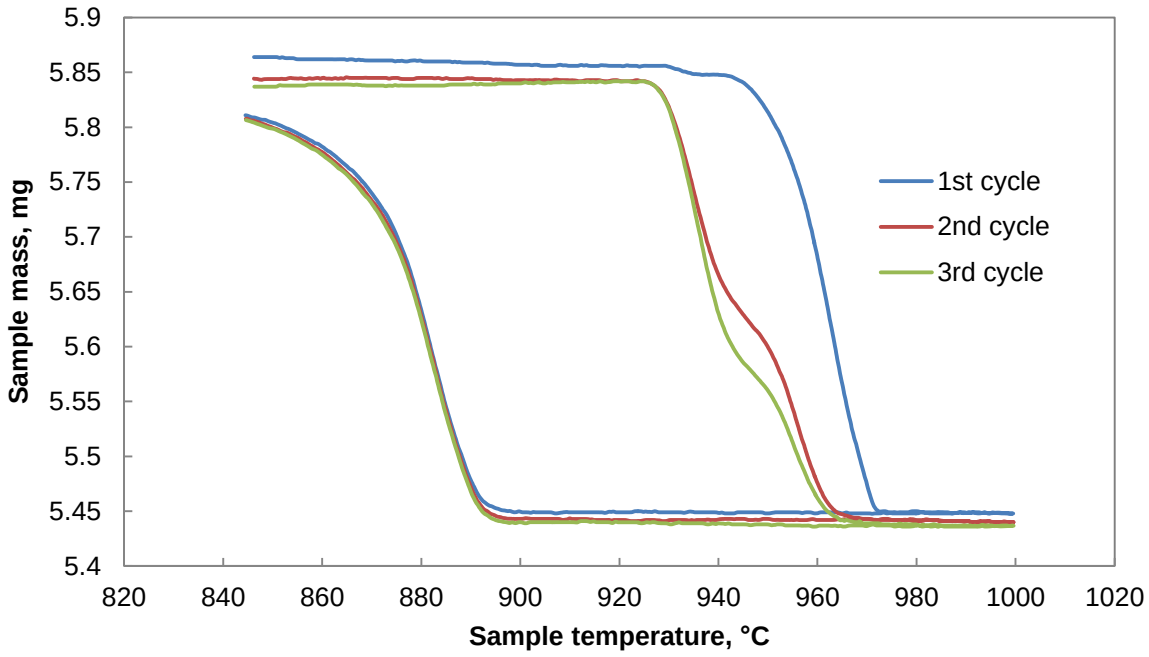


Figure 3-4 Mass change of Sample 3 (70 wt% CuO, 30 wt% mayenite) in the temperature range 850°C-1000°C-850°C with a constant heating and cooling rate of 5°C/min in a fixed atmosphere ($P_{O2} \approx 0.02$ bar) for 3 cycles. The isothermal sections between cycles are omitted for clarity.

Lastly, 5.864 mg of carrier consisting of 70 wt% CuO and 30 wt% mayenite (ball milled and calcined at 1000°C once, Sample 3) was examined. It is clear from Figure 3-4 that the rate of re-oxidation was fast and the profile was consistent across the 3 cycles. The mass of the sample at the start of the first cycle was slightly higher than that in subsequent cycles. It is likely that the difference in mass was due to dehydration of the mayenite rather than the loss in oxygen capacity because mayenite is known to be able to retain hydroxide ions at very high temperatures (Hayashi *et al.*, 2005). The conclusion is also supported by the fact that the difference in mass between the first cycle and the two following cycles just before the decomposition of the OC, at 920°C, was 0.015 mg, very close to the difference in mass of the decomposed sample, 0.011 mg. Furthermore, the mass losses from the decomposition in the second and third cycles were 6.90% and 6.94%, respectively; very close to the expected value of 7.00%. Interestingly, unlike the previous two samples, the decomposition of the oxidised Sample 3 occurs at two distinct temperatures as shown in Figure 3-5. Part of the sample decomposed at a temperature of 925°C (a small fraction of the fresh material decomposed at a slightly higher temperature of ~929°C), similar to the previous samples and the portion of sample decomposing at this temperature

increased significantly over the 3 cycles. The second decomposition occurred at a much higher temperature of 948°C. The sequential decomposition is unexpected since the XRD analysis only identified CuO as the Cu-containing phase in Sample 3. Further investigation into this behaviour was undertaken and is presented in Chapter 5.

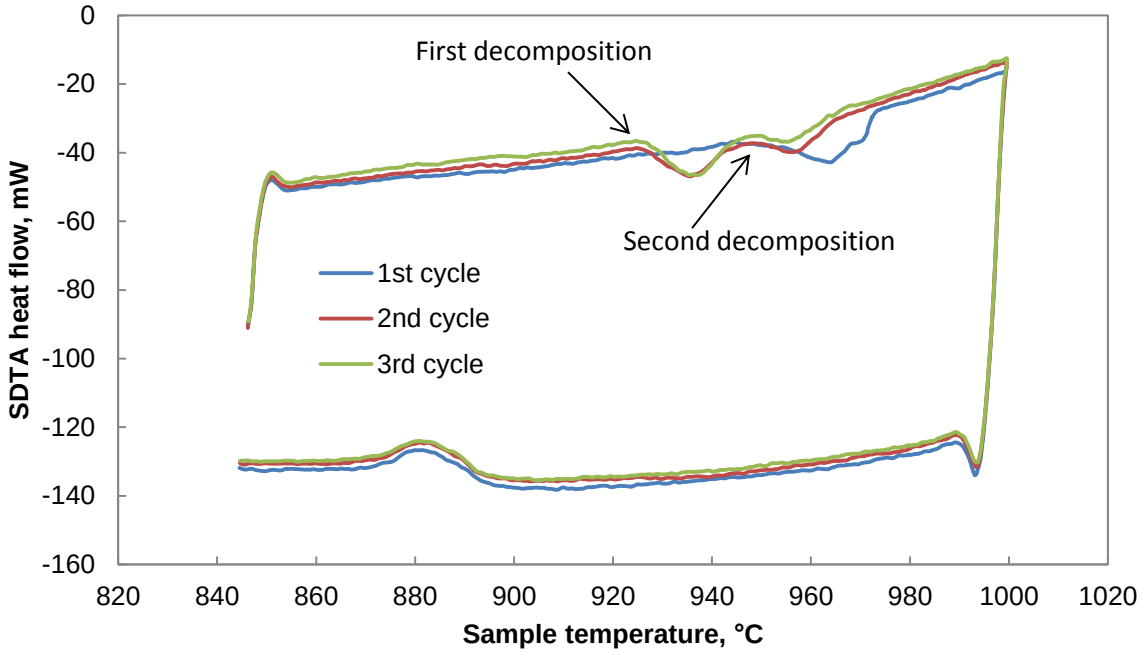


Figure 3-5 SDTA heat curve of Sample 3 (70 wt% CuO, 30 wt% mayenite) in the temperature range 850°C-1000°C-850°C with a constant heating and cooling rate of 5°C/min in a fixed atmosphere ($P_{O2} \approx 0.02$ bar) for 3 cycles. The isothermal sections between cycles are omitted for clarity.

It can be concluded from the comparative investigations above that pure CuO deactivates after only a few cycles when decomposed to $Cu_2O$ and then subsequently re-oxidised. Although the degradation is less severe than that reported in CLC operation, where the CuO is reduced to metallic Cu, the decrease in activity means it is not suitable for use as an OC directly. $Al_2O_3$ is effective in maintaining the activity of the OC but it reacts with the CuO to form a spinel and, or a delafossite phase which is not suitable for CLOU and hence reduces the oxygen capacity of the carrier. Supports based on calcium aluminates, in particular mayenite, appear to be more effective in retaining the activity of the carrier and this support does not form compounds with CuO which, otherwise, are difficult to decompose or re-oxidise.

### 3.3.3. The interaction between CuO and $Al_2O_3$

In order to understand the interaction between CuO and $Al_2O_3$ better, variants of Sample 2 were prepared and examined. Firstly, the process of grinding followed by calcination at 1000°C was repeated for 3 more times for Sample 2 and the materials were examined in the TGA using the isothermal cycling protocol. Secondly, a separate sample was prepared using the same precursors and composition but calcined at a lower temperature, 900°C, to investigate the effect of calcination temperature. In addition, XRD analysis was performed on both the fresh and cycled samples to study the effect of reaction on the interaction.

#### 3.3.3.1. The effect of repeated processing

The results of the isothermal cycling of samples consisting of variants of Sample 2 are presented in Figure 3-6. The original Sample 2 corresponds to the results named “after 1 calcination”. Here, the effect of regrinding and recalcining the original material 1, 2 and 3 times is explored. In each case, a relatively large amount of sample, approximately 28 mg, was used to ensure that the difference in buoyancy arising from the different gases used in the cycling did not have a significant influence on the mass of sample, and therefore the conversion, being measured. The conversion used for the ordinate, $X$, was calculated using the following equation:

$$X = \frac{(m_t - m_{red})}{\Delta m} \qquad 3\text{-}6$$

where $m_t$ is the mass of the sample at time $t$, $m_{red}$ is the mass of the fully reduced sample, taken to be the mass of the sample at $t = 17400$ s, after reduction was complete in the 5$^{th}$ cycle. $\Delta m$ is the expected change in mass of the sample based on the nominal composition of the carrier, assuming that all the $Cu^{2+}$ are reduced to ground state. Using this definition, the fully oxidised sample should have a conversion of 1, the conversion of the sample after CLOU should be 0.5 and that of the fully-reduced sample should be 0.

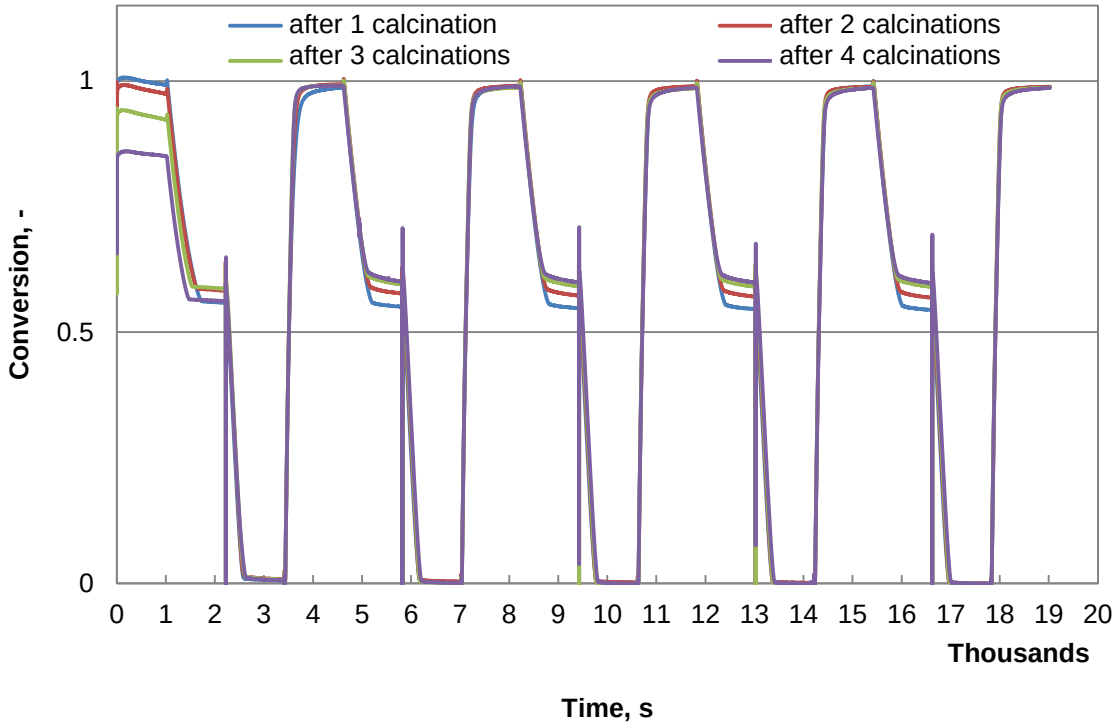


Figure 3-6 The reaction profiles of variants of Sample 2 calcined up to 4 times for five isothermal cycles in $N_2$ - 5% $H_2$ – air starting from $t$ = 1020 s before which time the sample was heated to the reaction temperature of 900°C from room temperature, in air. The spikes at $t$ = 2220 s, 5820 s, 9420 s, 13020 s and 16620 s are experimental artefacts due to gas switching between $N_2$ and 5% $H_2$, rather than mass change due to the reaction.

It can be seen from Figure 3-6 that the effective oxidation state of Cu in the fresh OCs decreased with repeated calcination at 1000°C. For all the 4 variants examined, the oxygen capacity for CLOU of the samples was significantly lower than the expected value and the capacity also decreased with repeated calcination. However, the overall oxygen capacity available for CLC was very close to the expected value, at 98.5% for all the samples by the end of the 5$^{th}$ cycle. Furthermore, the rate of reaction of each segment was found to be identical over the five cycles except for the rate of decomposition (*i.e.* the first segment) in the first cycle which was slightly slower than the rate in the following cycles. On closer examination of the results, it was found that the rate of external mass transfer from the bulk gas to the surface of the OCs had a significant influence on the observed rate of reaction due to the large mass of sample used. Therefore, all that can be concluded here is that the rate of chemical reaction was sufficiently fast during the cycling that no degradation could be observed, the rate

being dominated by external mass transfer. Further investigation of the chemical kinetics of the OCs will be discussed in Chapter 5 with more details.

The decrease of the effective oxidation state of Cu in the fresh samples can be explained by the formation of $CuAlO_2$. Comparing the XRD patterns of the variant samples, shown in Figure 3-8, with standard fingerprints of pure materials obtained from the ICSD database, Figure 3-7, revealed that a significant amount of $CuAlO_2$ was formed on successive calcination at 1000°C, This is seen from the increase in the intensity of peaks at 15.6°, 42.2° and 74.2° which are minor but unique to the delafossite structure. At the same time, the amount of CuO present in the sample declined, evident from the reduction in height of the unique peak at 48.7°. In addition, the amount of $Al_2O_3$ was found to decrease (peaks at 25.6° and 43.4°); that of $CuAl_2O_4$ remained relatively constant after the second calcination (peaks at 44.9°, 55.7° and 59.5°) and no $Cu_2O$ could be detected in any of the samples examined (absence of the unique peak at 73.6°). Combining the XRD evidence with the equilibrium data available, shown in Figure 3-1, it can be concluded that $CuAlO_2$ formed *via* reaction 3-4 during the calcination whereas the $CuAl_2O_4$ consumed was replenished *via* reaction 3-2. Reaction 3-4 was slow, however, probably because the calcination temperature was close to the equilibrium temperature (in fact the equilibrium temperature, according to Jacob and Alcock, (1975) should be 1003°C, slightly higher than the calcination temperature) and equilibrium could not be achieved after calcination for a total of 24 hours.

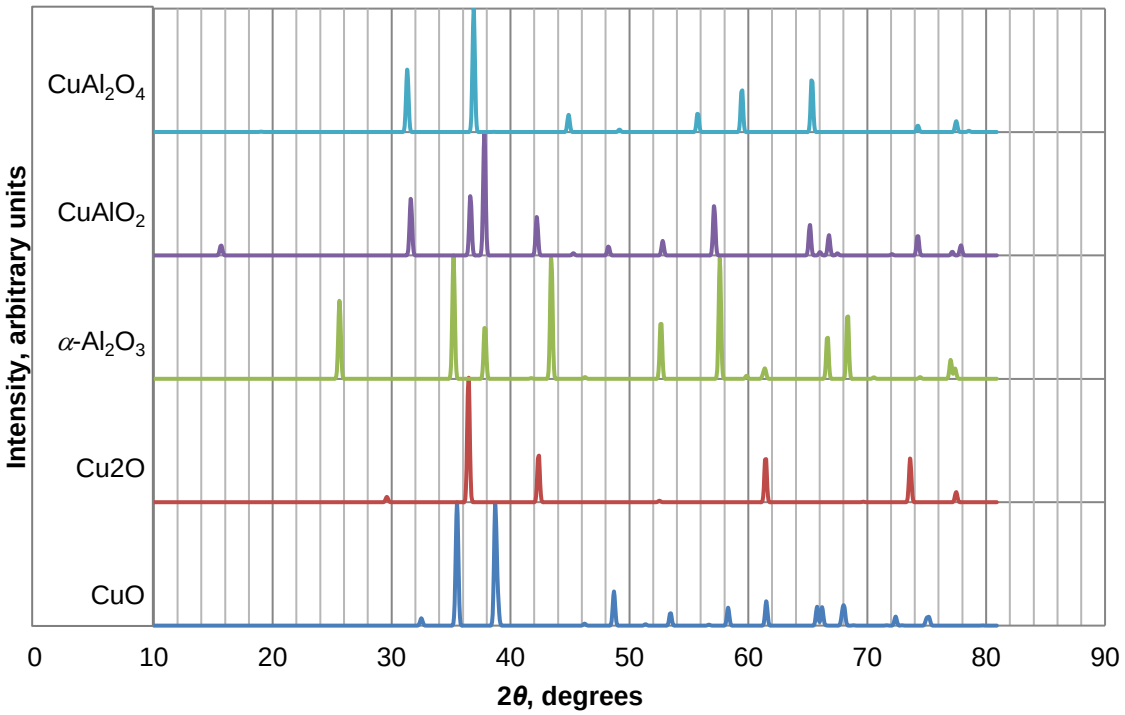


Figure 3-7 Reference XRD patterns for various pure materials calculated from the ICSD database.

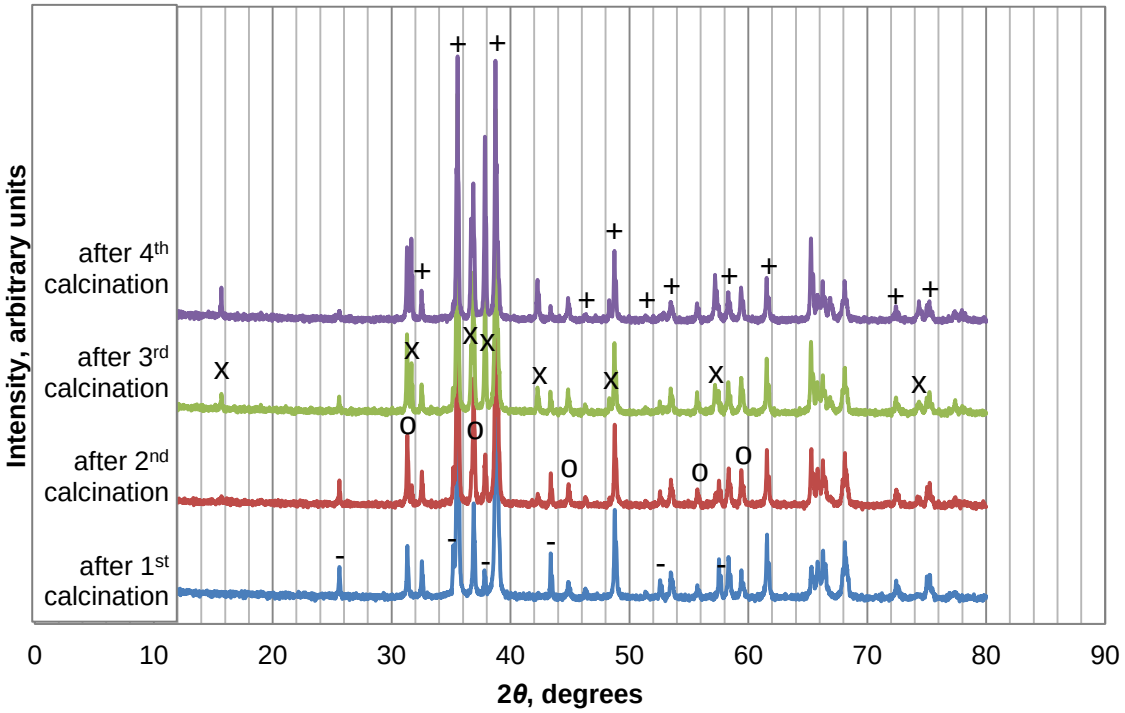


Figure 3-8 XRD patterns of fresh samples of variants of Sample 2 calcined at 1000°C with the major peaks identified and assigned to the respective phases: CuO (+), $\alpha$-$Al_2O_3$ (-), $CuAl_2O_4$ (o), $CuAlO_2$ (x). Some overlapping peaks omitted.

To determine the cause of the decrease in oxygen capacity for CLOU, additional XRD analysis was performed on the recovered samples after the isothermal cycling experiments and the results are shown in Figure 3-9. The reduction in oxygen capacity for CLOU cannot be accounted for based on thermodynamic arguments: both CuO and $CuAl_2O_4$ are thermodynamically unstable at 900°C under $N_2$ and if any $CuAlO_2$ were to be present after the reduction in 5% $H_2$ or oxidation in air, the oxygen capacity for CLC would have been lowered by the same amount but this was not observed experimentally.

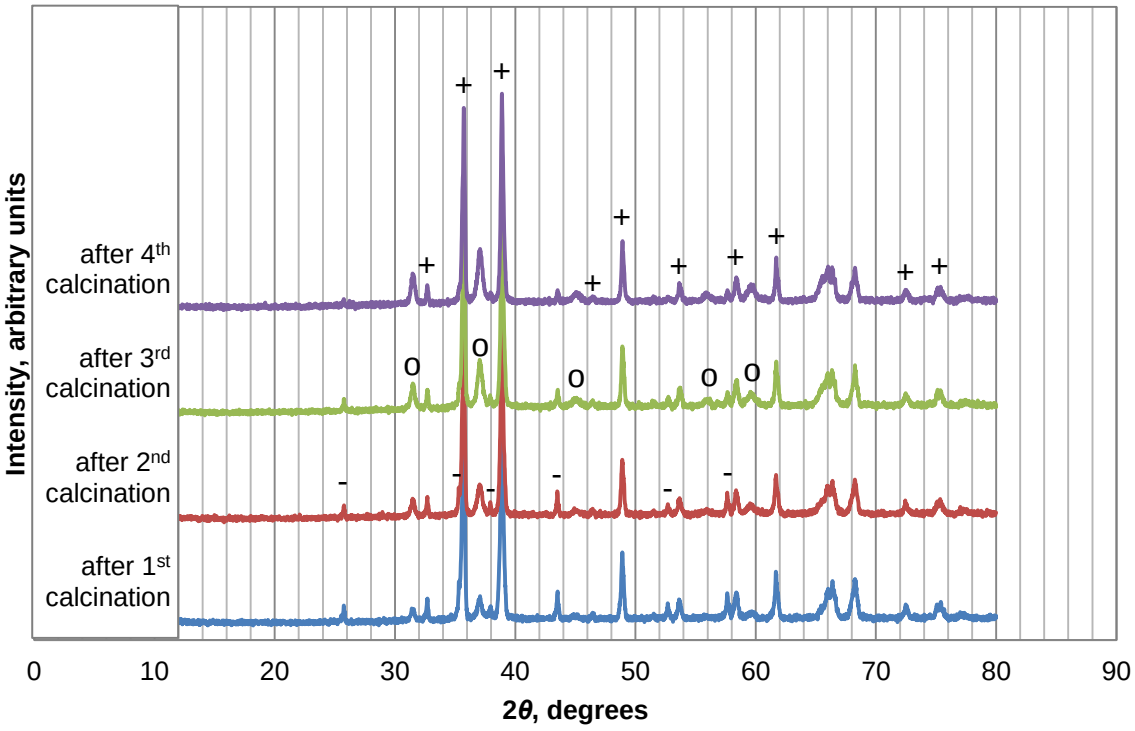


Figure 3-9 XRD patterns of cycled samples of variants of Sample 2 calcined at 1000°C with the major peaks identified and assigned to the respective phases: CuO (+), $\alpha$-$Al_2O_3$ (-) and $CuAl_2O_4$ (o). Assignment of the overlapping peaks around 66° and 68° is omitted for clarity.

Only 3 crystalline phases were detected in all 4 samples, namely CuO, $\alpha$-$Al_2O_3$ and $CuAl_2O_4$. The relative amount of $Al_2O_3$ decreased in the same fashion as the fresh samples whereas the amount of CuO remained approximately constant across all samples. Interestingly, the amount of $CuAl_2O_4$ present in the re-oxidised samples correlated well with the reduction of the oxygen capacity for CLOU observed in cycles 2-5 of the TGA experiment – increasing with the number of calcinations in the first 3 samples and comparable in the 3rd and 4th sample. This correlation implies that

the decomposition of the spinel phase in $N_2$ is slow at 900°C in spite of its being thermodynamically unstable. However, taking into account that the OCs retained almost full oxygen capacity for CLC, it is likely that the spinel can be reduced readily in $H_2$.

Examination of the sizes of crystals of various phases revealed that the repeated processing did not affect the crystal size significantly, as the widths of peaks at the baseline were comparable across the samples. However the crystal size of the $CuAl_2O_4$ phase differed substantially between the fresh and re-oxidised samples. A quantitative comparison of the crystal sizes was undertaken using the Scherrer equation (Patterson, 1939) and the results are presented in Table 3-2.

**Table 3-2 average size of crystals of different phases**

| *Phase* | *Size in fresh samples, nm* | *Size in re-oxidised samples, nm* | *Peak used* |
|---|---|---|---|
| CuO | 42 | 33 | 38.7° |
| $CuAl_2O_4$ | 49 | 20 | 36.9° |
| $Al_2O_3$ | 86 | 71 | 43.4° |

The large difference in the size of $CuAl_2O_4$ crystals seen in Table 3-2 further supports the conclusion that the spinel was completely reduced in 5% $H_2$ and re-formed during the oxidation. The small crystal size in the re-oxidised samples can be attributed to the short oxidation time of only 20 minutes compared with the long duration of the calcinations which lasted at least 6 hours.

Lastly, the absence of a $CuAlO_2$ phase implies that the delafossite can be reduced in 5% $H_2$ very easily and did not re-form on re-oxidation. It is unlikely that the delafossite is an intermediate product in the formation of the spinel phase because if this were the case, oxidation would have been observed during the initial heating up of the fresh sample in air during the TGA experiment.

### *3.3.3.2. The effect of calcination temperature*

When the calcination temperature of the CuO-$Al_2O_3$ powder was lowered to 900°C, the resulting OCs behaved differently from those calcined at 1000°C. It can be seen from the isothermal cycling experiment, results in Figure 3-10, that the oxygen capacities for both CLOU and CLC are close to the expected values and the slight difference between cycles can be attributed to the drift of the TGA balance during the course of the experiment, amounting to < 1% of the full conversion.

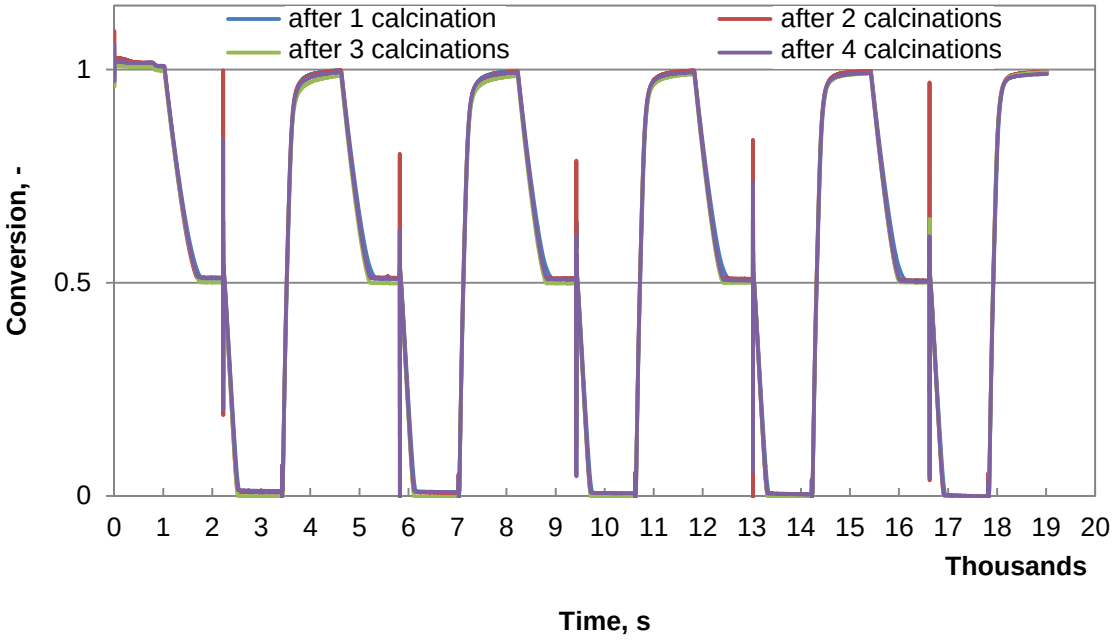


Figure 3-10 Isothermal cycling reaction profiles of variants of Sample 2 calcined at 900°C. The grinding-calcination process was performed up to 4 times. The reaction protocol was the same as that in Figure 3-6.

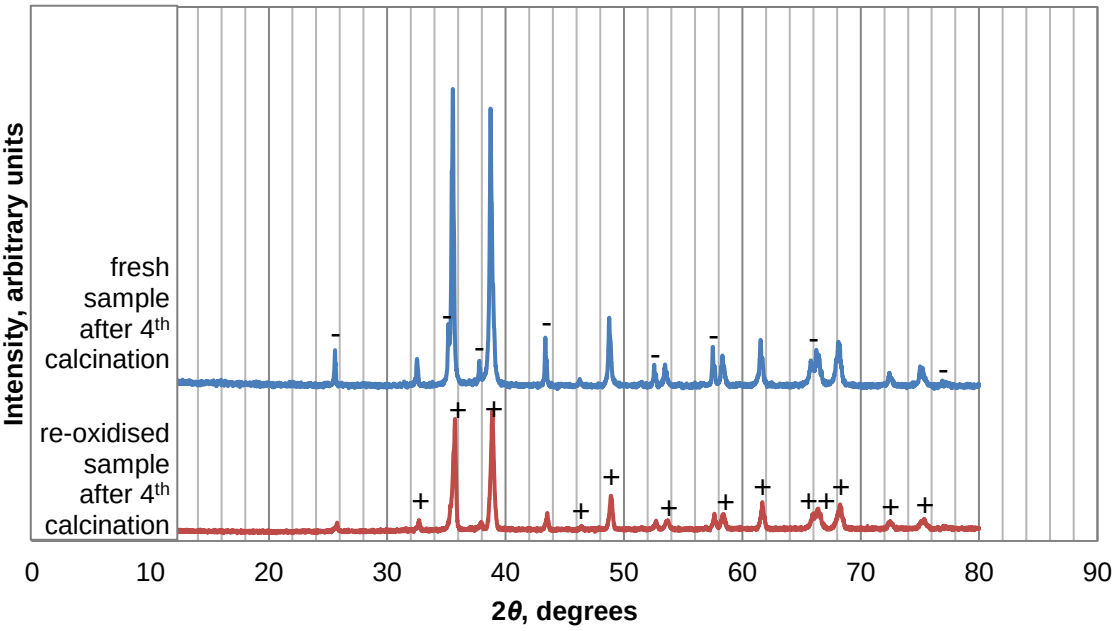


Figure 3-11 XRD patterns of fresh and cycled samples of variants of Sample 2 calcined at 900°C for 4 times, with the major peaks identified and assigned to the respective phases: CuO (+) and $\alpha$-$Al_2O_3$ (-).

XRD analysis performed on the fresh samples as well as the recovered samples after the isothermal cycling showed no trace of the copper aluminates. The only phases

identified were CuO and $\alpha$-$Al_2O_3$ even for the samples calcined 4 times, as shown in Figure 3-11. The results indicate that CuO and $\alpha$-$Al_2O_3$ does not form $CuAl_2O_4$ at an appreciable rate at temperatures up to 900°C during calcination and thus raises questions regarding the origin of the $CuAl_2O_4$ detected in the re-oxidised samples previously calcined at 1000°C.

### *3.3.3.3. The reaction of $CuAl_2O_4$*

It appears that $CuAl_2O_4$ does not decompose at an appreciable rate and is consequently responsible for the reduction of oxygen capacity of Sample 2 for CLOU. To investigate this hypothesis, some sample containing mostly $CuAl_2O_4$ was synthesised using the sol-gel method described in Section 2.2.2. The calcined sample was crushed and sieved to the size fraction 180-355 µm and 28.24 mg of the particles were placed in the TGA at 900°C for 20 hours in Ar. The mass of the sample with time is shown in Figure 3-12. Some fresh samples and the decomposed sample were examined by XRD for further analysis: results are in Figure 3-13.

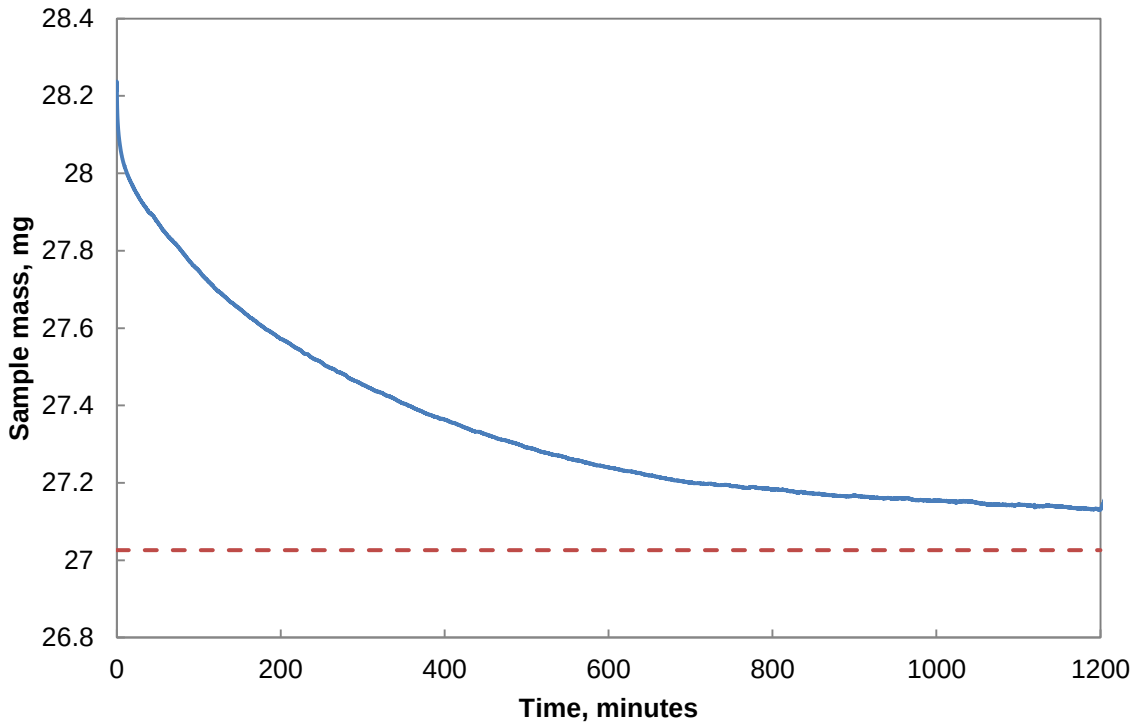


Figure 3-12 The reaction profile of $CuAl_2O_4$ in Ar at 900°C for 20 hours. The dashed line indicates the expected mass of the sample at full conversion.

It can be seen from Figure 3-12 that the decomposition of the spinel is, indeed, very slow and the reaction was not completed after 20 hours. A similar experiment performed at 950°C was able to achieve full conversion after 10 hours. The slow

decomposition of the spinel means that $CuAl_2O_4$ is practically inert with respect to CLOU, considering that the typical residence time of the OCs in the fuel reactor would be of the order of a few minutes. Figure 3-12 also supports the conclusion reached in Section 3.3.3.1 that the reduction in oxygen capacity for CLOU can be attributed to the presence of $CuAl_2O_4$.

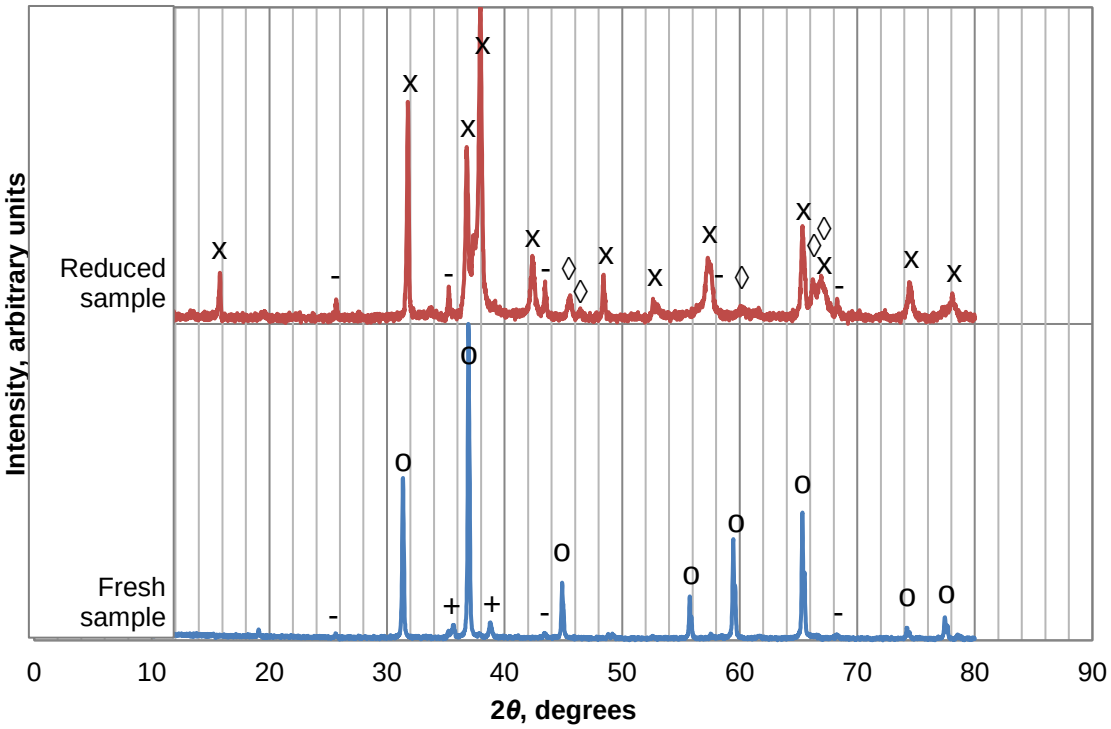


Figure 3-13 XRD patterns of fresh and thermally decomposed samples of $CuAl_2O_4$ prepared by the sol-gel method, with the major peaks identified and assigned to the respective phases: $CuAl_2O_4$ (o), $CuAlO_2$ (x), CuO (+), $\alpha$-$Al_2O_3$ (-) and $\gamma$-$Al_2O_3$ (◊).

The curious case of the formation of $CuAl_2O_4$ in the re-oxidised variants of Sample 2 calcined at 1000°C, but not in the variants calcined at 900°C can be explained with the aid of the XRD analysis of the thermally-decomposed $CuAl_2O_4$ sample shown in Figure 3-13. The XRD pattern of the fresh sample was dominated by the peaks corresponding to $CuAl_2O_4$, as expected, but a small amount of $\alpha$-$Al_2O_3$ and CuO were also detected. In the decomposed sample, the dominant phase was $CuAlO_2$ and the relative amount of $\alpha$-$Al_2O_3$ increased compared to the fresh sample, in agreement with the decomposition reaction 3-5. However, some $Cu_2O$ is also expected, from the decomposition of the CuO, but this cannot be confirmed since most of the major peaks of $Cu_2O$ overlap with those of $CuAlO_2$. Only one peak of $Cu_2O$ is unique

at 73.6° but the absence of this particular peak could arise from the small amount of $Cu_2O$ being present. Interestingly, a different phase of alumina, $\gamma$-$Al_2O_3$, was also observed in the XRD pattern of the decomposed sample, suggesting that at least a part of the product alumina from the decomposition of $CuAl_2O_4$ is in the gamma form. Since $\gamma$-$Al_2O_3$ has a defect spinel structure, which is cubic, whereas $\alpha$-$Al_2O_3$ has a trigonal symmetry (Levin and Brandon, 2005), it is expected that $\gamma$-$Al_2O_3$ can react to form $CuAl_2O_4$ more easily than $\alpha$-$Al_2O_3$ on re-oxidation. Therefore, the presence of $CuAl_2O_4$ in the samples re-oxidised at 900°C depends on the presence of $\gamma$-$Al_2O_3$, which can only exist if some $CuAl_2O_4$ is found in the fresh samples to begin with.

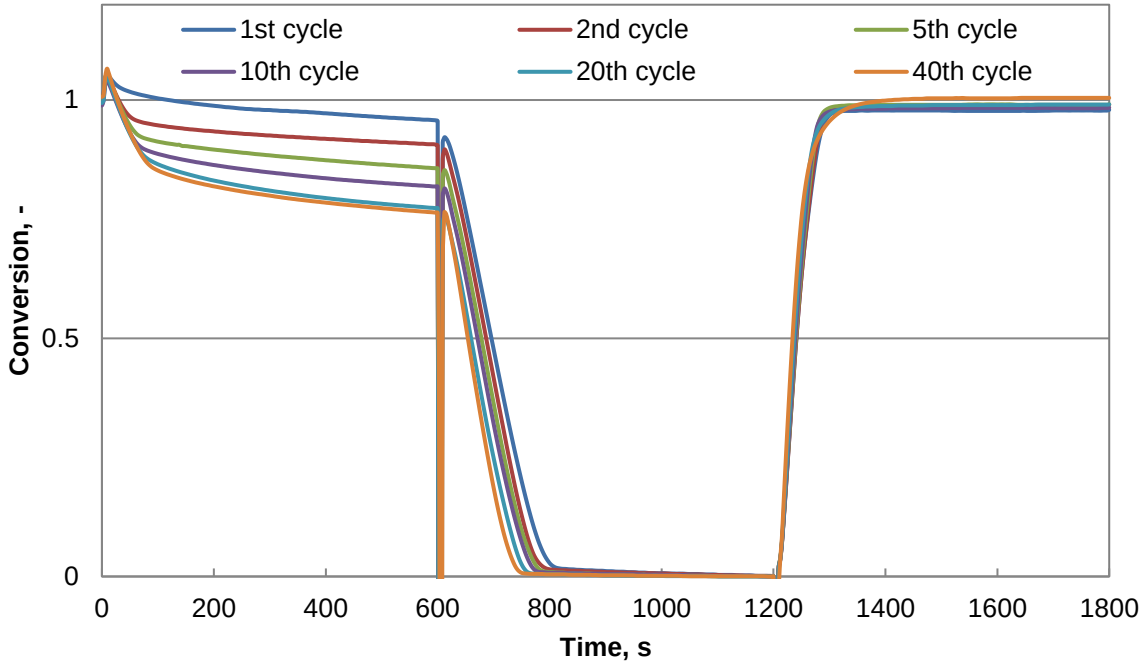


Figure 3-14 Mass change in the isothermal cycling of the $CuAl_2O_4$ sample in Ar (1-600 s), 5% $H_2$ in $N_2$ (601-1200 s) and air (1201-1800 s) for selected cycles. Spikes at $t$ = 600 s are due to gas switching, as are the anomalous increase in mass close to the beginning of each cycle. The mass of sample used was 11.73 mg.

In addition, the full CLC behaviour of $CuAl_2O_4$ was also investigated using the isothermal cycling protocol at 900°C in the TGA for a total of 40 cycles and the results for selected cycles are presented in Figure 3-14. Unsurprisingly the material was easily reduced in $H_2$ and oxidised in air to the full extent. The slight difference of the conversion at $t$ = 1800 s between cycles can be attributed to random experimental error since the deviation was less than 2% in all cases, corresponding to a mass of

0.02 mg, within the range of natural drift of the instrument. Furthermore, the reduction by $H_2$ and oxidation by air was fast throughout the cycles and no significant deactivation could be identified from the results. The CLOU behaviour during the full CLC cycling was perhaps more interesting. It is clear that the rate of decomposition of the material during the CLOU period consisted of a fast initial region, the proportion of which increased with cycling and stabilised after about 20 cycles, and a long tail until the end of the segment. Throughout the 40 cycles, the tail accounted for a conversion of approximately 10% and the increase in the cumulative conversion up to 600 s was probably owing only to the increased proportion of the initial region.

After 40 cycles of reaction, the sample disintegrated into powder and no distinct particles were recovered. Since the oxygen capacity of the material was retained close to unity at the end of the experiment, all the Cu in the material would have been oxidised to either CuO or $CuAl_2O_4$. Comparing the rate of decomposition during the CLOU segment of Sample 2 and its variants, it is most likely that CuO is responsible for the fast decomposition observed initially in Figure 3-14 and $CuAl_2O_4$ for the tail. Since a considerable amount of CuO was present in the oxidised material after 40 cycles, equal amount (in moles) of $Al_2O_3$ must also be formed to maintain material balance. This segregation of phases was the probable cause of the disintegration of the particles.

## *3.4. Discussion*

The evidence available from the experimental results presented in this chapter as well as from the literature (Arjmand *et al.*, 2011; Gayán *et al.*, 2012; Imtiaz *et al.*, 2014) suggests that $Al_2O_3$ has a tendency to form the spinel $CuAl_2O_4$, accompanied by a loss of the oxygen capacity for CLOU. Arjmand *et al.* (2011) identified the delafossite phase in their re-oxidised OCs and concluded that the re-oxidation of $CuAlO_2$ was kinetically hindered so that once $CuAlO_2$ had formed, it would remain essentially inert and result in the reduction of the oxygen capacity of the OCs. Imtiaz *et al.* (2014) invoked the same argument to explain the gradual loss of oxygen capacity in their co-precipitated OCs although no direct evidence was available. On the other hand, the current study has shown that the rate of decomposition of $CuAl_2O_4$ under inert environment is extremely slow as can be seen from Figure 3-12. Indeed, a similar observation was made by Arjmand *et al.* (2011) from their fluidised bed experiments.

Since $CuAlO_2$ forms *via* $CuAl_2O_4$, too, it appears that avoiding the formation of $CuAl_2O_4$ is important for OCs designed for CLOU.

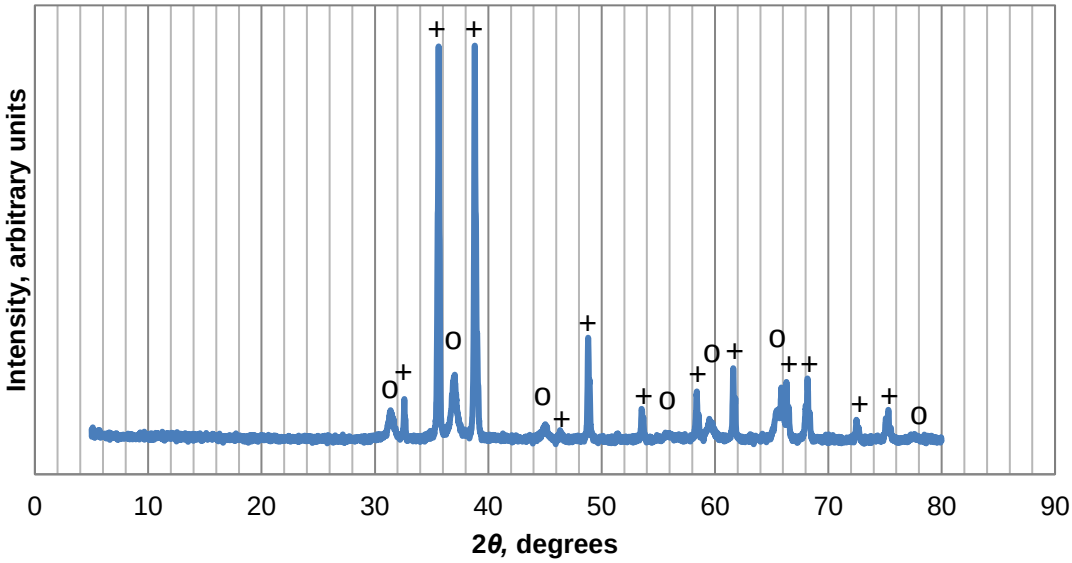


Figure 3-15 XRD patterns of a sample of 70 wt% CuO with $Al_2O_3$, prepared by the dry mixing method with $Al(OH)_3$ instead of $\alpha$-$Al_2O_3$. The sample was calcined at 850°C for 6 hours before the XRD analysis. The major peaks are identified and assigned to the respective phases as: $CuAl_2O_4$ (o), CuO (+).

It has been demonstrated in this study that particles prepared with $\alpha$-$Al_2O_3$ do not form copper aluminates at temperatures around 900°C. Similarly, Arjmand *et al.* (2011) only detected trace amounts of $CuAl_2O_4$ in their particles calcined at 950°C. Therefore, it is possible to synthesise OCs containing CuO and $Al_2O_3$ which can operate at 900°C without losing oxygen capacity over time. $\gamma$-$Al_2O_3$ on the other hand, is much more reactive with respect to the formation of spinel compounds, *e.g.* Bolt *et al.* (1998). For instance, Forero *et al.* (2011) prepared OCs by impregnating $\gamma$-$Al_2O_3$ particles with $Cu(NO_3)_2$. $CuAl_2O_4$ was formed after the particles were calcined at 550°C for 30 min followed by 850°C for 1 hour. Imtiaz *et al.* (2014) reported the formation of $CuAl_2O_4$ in co-precipitated particles calcined at a low temperature of 800°C for 2 hours. Thus, any synthesis route involving $\gamma$-$Al_2O_3$ or its precursor, boehmite ($\gamma$-AlO(OH)), will inevitably lead to the formation of $CuAl_2O_4$ at temperatures suitable for CLOU. In fact, a sample prepared using the dry mixing method with powders of CuO and $Al(OH)_3$ instead of $\alpha$-$Al_2O_3$ formed a significant amount of $CuAl_2O_4$ after being calcined in air at

a relatively low temperature of 850°C for 6 hours, as shown in Figure 3-15, simply because $Al(OH)_3$ dehydrates to from $\gamma$-$Al_2O_3$ instead of $\alpha$-$Al_2O_3$.

As a result, if $Al_2O_3$ were to be used as a support, mechanical mixing or impregnation with $\alpha$-$Al_2O_3$ should be used instead of co-precipitation methods or impregnation with $\gamma$-$Al_2O_3$ but such particles should never be used above 900°C or up to 950°C if some loss in capacity can be tolerated for other reasons such as improved mechanical stability. However, it should be recognised that the formation of $CuAl_2O_4$ in the OC is effectively irreversible in the sense that it cannot be broken down to the constituent CuO and $Al_2O_3$ completely without destroying the particles – a possible route would be to reduce the spinel to metallic Cu and $Al_2O_3$ and calcine the material in the reduced form at high temperature to convert all the $\gamma$-$Al_2O_3$ to $\alpha$-$Al_2O_3$ and then re-oxidise the particle at temperatures below 900°C, however, the temperature required for the transformation of alumina is above the melting point of metallic Cu and therefore infeasible.

In terms of CLC, the formation of $CuAl_2O_4$ or $CuAlO_2$ does not affect the oxygen capacity since both species can be easily reduced by $H_2$. Arjmand *et al.* (2011) obtained similar results with particles consisting of primarily $CuAl_2O_4$, using $CH_4$ as the reducing agent in a fluidised bed. However, the particles made from the sol-gel method in the current work did not retain their mechanical integrity after repeated cycling. Also, $CuAl_2O_4$ particles made from freeze granulation with some excess of $Al_2O_3$ investigated by Arjmand *et al.* (2012a) also exhibited instability after 45 redox cycles in a fluidised bed although to a lesser extent than those made by the sol-gel method. Arjmand *et al.* (2012a) noticed that the bulk density of the cycled particles decreased with cycling and were significantly less than the fresh ones. This observation is consistent with other materials which show phase separation behaviour during cycling. For instance, Adánez *et al.* (2010) observed the segregation of $Fe_2O_3$ from the titanium rich phase in ilmenite after cycling.

Although the interaction between $Al_2O_3$ and CuO to form copper aluminates is undesirable, an Al-based support has advantages in terms of its abundance and low cost. As a result, many Al-based compounds have been studied as supporting materials to date. The original spinel, $MgAl_2O_4$, is one of the most-studied candidates to date. Whilst many studies have shown that CuO supported on $MgAl_2O_4$ do not interact with CuO chemically, so that the full CLOU capacity can be retained and the

particles were able to resist agglomeration and attrition in batch fluidised beds (Adánez-Rubio *et al.*, 2012; Arjmand *et al.*, 2012b; Imtiaz *et al.*, 2014) where the movement of particles was relatively gentle. However, significant attrition was observed for some of the particles in continuous operation using a circulating fluidised bed (Adánez-Rubio *et al.*, 2012). In this work, it has been demonstrated that calcium aluminate, in particular mayenite, is also suitable as support for Cu-based OCs. Although the support material is not completely inert as can be seen from Figure 3-4, no new phases were detected from the XRD analysis of the samples. Moreover, in contrast with the interaction between CuO and $Al_2O_3$, the interaction between CuO and mayenite did not reduce the oxygen capacity of CLOU but only altered the equilibrium slightly. In addition, the OC supported with the same amount of mayenite by weight was able to re-oxidise faster than the OC supported by $Al_2O_3$, making mayenite a better support material. This finding has led to a more thorough investigation into the use of different calcium aluminates as support material (Donat *et al.*, 2015) and the following chapters focus on the characterisation of one particular CuO-based OC supported on calcium aluminates consisting primarily mayenite.

## *3.5. Summary*

The main results from the investigations carried out in this chapter are summarised as follows.

a) $Al_2O_3$ and mayenite can stabilise Cu-based OCs effectively at 30 wt%, producing OCs with relatively high oxygen capacity.
b) $Al_2O_3$ can interact with CuO to form copper aluminates which have a negative impact on the oxygen capacity of CLOU since the decomposition of $CuAl_2O_4$ is too slow to be useful.
c) The interaction between $Al_2O_3$ and CuO depends critically on the form of $Al_2O_3$. In particular, $\alpha$-$Al_2O_3$ does not react with CuO at 900°C in spite of the fact that $CuAl_2O_4$ is thermodynamically favourable at this temperature, whereas $\gamma$-$Al_2O_3$ reacts readily at this temperature, possibly due to its similarity in the crystal structure with $CuAl_2O_4$.
d) Mayenite does not interact with CuO to form new phases and therefore the full oxygen capacity for CLOU can be retained. The OC supported on mayenite is also able to re-oxidise faster than the one supported on $Al_2O_3$.

# 4. Evaluation of wet-mixed oxygen carrier for redox reactions in a circulating fluidised bed

## *4.1. Introduction*

In Chapter 3, it was established that CuO supported on mayenite could be used as a potential OC for CLOU, provided that particles with sufficient mechanical strength could be formed with a mean diameter in the range ~ 40 µm – 500 µm, corresponding to Group A or Group B particles as classified by Geldart (1972), for use in fluidised beds. Attempts to produce such particles from powders investigated in Chapter 3 were made by employing the granulation method of Bohn *et al.* (2008) using different binders such as deionised water, bentonite and alcohol. In this method, the liquid binder was sprayed on to the powder to form agglomerates and the mixture was continuously stirred during the process. The resulting granules were then sieved to a desired size fraction and calcined at a high temperature, *e.g.* 1000°C, for up to 6 hours. Unfortunately, the particles produced in the present work using this method did not possess sufficient mechanical strength and broke up easily after the heat treatment, thus being unsuitable for fluidised bed operations. Hence, a different synthesis route was explored. Since Sample 3 in Chapter 3 was shown to be the most promising candidate, it was decided to synthesise an OC with mayenite as the support using the wet mixing method described in Section 2.2.2. In a preliminary study presented by Donat *et al.* (2015), particles with different compositions of the support were produced using the wet-mixing method. Thus, the ratio of $Ca(OH)_2$ to $Al(OH)_3$ was varied so that the resulting calcium-aluminate support contained CaO and $Al_2O_3$ with a mass ratio between 0.09 to 1.65, covering all possible calcium aluminates. Investigations into the OCs containing 60 wt% CuO and 40 wt% of calcium-aluminate support with the above compositions showed that with a mass ratio of $CaO:Al_2O_3 = 0.94$, the theoretical value for the formation of pure mayenite, trace amounts of $Ca_3Cu_7O_{10}$ were formed. This caused sintering of the OC particles after cycling owing to the low melting point of $Ca_3Cu_7O_{10}$. On the other hand, particles with a low content of CaO content were more susceptible to attrition in a bubbling fluidised bed.

Based on these preliminary experimental results, a support with mass ratio of $CaO:Al_2O_3 = 0.74$, half way between the stoichiometry of $12CaO{\cdot}7Al_2O_3$ and $CaO{\cdot}Al_2O_3$, was chosen as the most suitable candidate. This chapter presents the

characteristics of the OC produced with this support, with a particular emphasis on the chemical and mechanical stability of the OC relevant to the CLOU process.

## *4.2. Experimental methods*

The crystalline phases present in the OC particles prepared by the wet mixing method described in Section 2.2.2 and calcined in air at 1000°C for 6 hours were determined by X-ray powder diffraction. The BET surface area, and BJH pore size distribution for pores < 200 nm diameter, were determined from nitrogen adsorption experiments performed at 77 K. Details of the above experiments are given in Section 2.3.

The chemical stability of the oxygen carrier was investigated in a TGA at 900°C: ~ 20 mg of the OC was examined in a typical experiment. The reactive gas (~50 ml/min, at 20°C, 1 bar) was changed successively from $N_2$ (for oxygen uncoupling) to 5 vol% $H_2$ in $N_2$ (for the reduction of $Cu_2O$ to metallic copper) and finally to air (for complete re-oxidation to CuO) for 10 minutes each. This cycle of gases was repeated 25 times. A background flow of $N_2$ (~130 ml/min at 20°C, 1 bar) was always present to purge the furnace. The OC particles (in fully oxidised form) were recovered after the experiment and the morphology of the cross sections of the particles was examined using an optical microscope and compared with virgin particles.

An electrically-heated stainless steel fluidised bed reactor with internal circulation, as described in Section 0, was used to investigate the agglomeration and attrition resistance of the synthesised particles. In an experiment, 110 g of virgin particles in the sieve size fraction 300-425 µm (54.8 g in the size fraction 300-355 µm and 55.2 g in the size fraction 355-425 µm) was heated from room temperature to 900°C with a rate of heating of 10°C/min with a primary gas flowrate of 2.0 l/min and a secondary gas flowrate of 2.4 l/min, both measured at 20°C and 1 bar. In most cases, compressed air was used as both the primary and secondary gas but other gases such as $N_2$ and 5 vol% $H_2$ in $N_2$ were also used and will be specified as they are discussed later. The mass of the particles used was recorded before and after each experiment to quantify the loss of material due to attrition. The particles were used for 6 such experiments consecutively with each one lasting 24 hours (with the exception of the last experiment, which was 100 hours). The particles recovered after 6 experiments were sieved again to measure their size distribution.

Similar experiments were conducted with a different sample of particles with an initial mass of 98 g, at temperatures between 850°C and 900°C, to investigate the tendency to agglomerate of the particles.

## 4.3. Results

### 4.3.1. Characterisation of the oxygen carrier

The oxygen carrier had a nominal composition of 60 wt% CuO, 23 wt% $Al_2O_3$ and 17 wt% CaO. Analysis of the particles calcined at 1000°C for 6 hours by XRD confirmed that the dominant phases present were CuO and $Ca_{12}Al_{14}O_{33}$. The sample had a BET surface area of 0.99 $m^2/g$ and a BJH pore volume of 2.34 $mm^3/g$ for pore diameters ≤ 200 nm, measured by nitrogen adsorption at 77 K. The bulk density of the sample was found to be 1100 $kg/m^3$ and estimated particle density, assuming the particles formed a close-packed bed with voidage of ~0.36, was 1700 $kg/m^3$. Taking the theoretical density of $Ca_{12}Al_{14}O_{33}$ as 2680 $kg/m^3$ (Ropp, 2013) and that of CuO as 6480 $kg/m^3$ (Eagleson, 1993), the porosity of the particle, $\varepsilon_p$, was calculated to be ~0.66, corresponding to an internal pore volume of 388 $mm^3/g$. Hence, on the basis of this crude calculation, it is likely that virtually all the pores inside the particles are macropores with diameters ≥ 200 nm.

### 4.3.2. Chemical stability of the oxygen carrier

To confirm that the oxygen carrier could retain activity with repeated use, including reduction of the $Cu_2O$ at the end of the thermal decomposition of CuO, 21.05 mg of the particles were investigated at 900°C in the TGA for 25 cycles using the protocol described in Section 4.2. The results are shown in Figure 4-1 as observed rate of change of mass during (a) decomposition in nitrogen, (b) reduction with hydrogen and (c) re-oxidation in air. From Figure 4-1, it was found that the total amount of oxygen available from the carrier, measured by the mass change in the re-oxidation stage, remained consistently at 2.596 ± 0.002 mg, corresponding to 12.4% of the total mass of the carrier, in good agreement with the expected value of 12.0%. Furthermore, the profiles of rate of mass change in each stage were almost identical across cycles with the exception of the first cycle, which showed a slower rate in the oxygen release stage. The anomalous behaviour in the first cycle will be discussed in detail in Chapter 5. The maximum rate of mass transfer was calculated for each stage in the cycle and was found to be of the same order of magnitude as the maximum observed rate of

reaction in these experiments (Donat *et al.*, 2015) but the fact that the rate of reaction in each case varied with conversion at isothermal conditions suggests that the reactions were not entirely controlled by external mass transfer. Thus, the reproducibility of the reaction rate profile over cycles can be attributed to the chemical stability of the particles. In fact, the rate of reaction in cycle 25 was slightly faster than that in cycle 5 during each segment, suggesting that the particles were slightly activated over cycles.

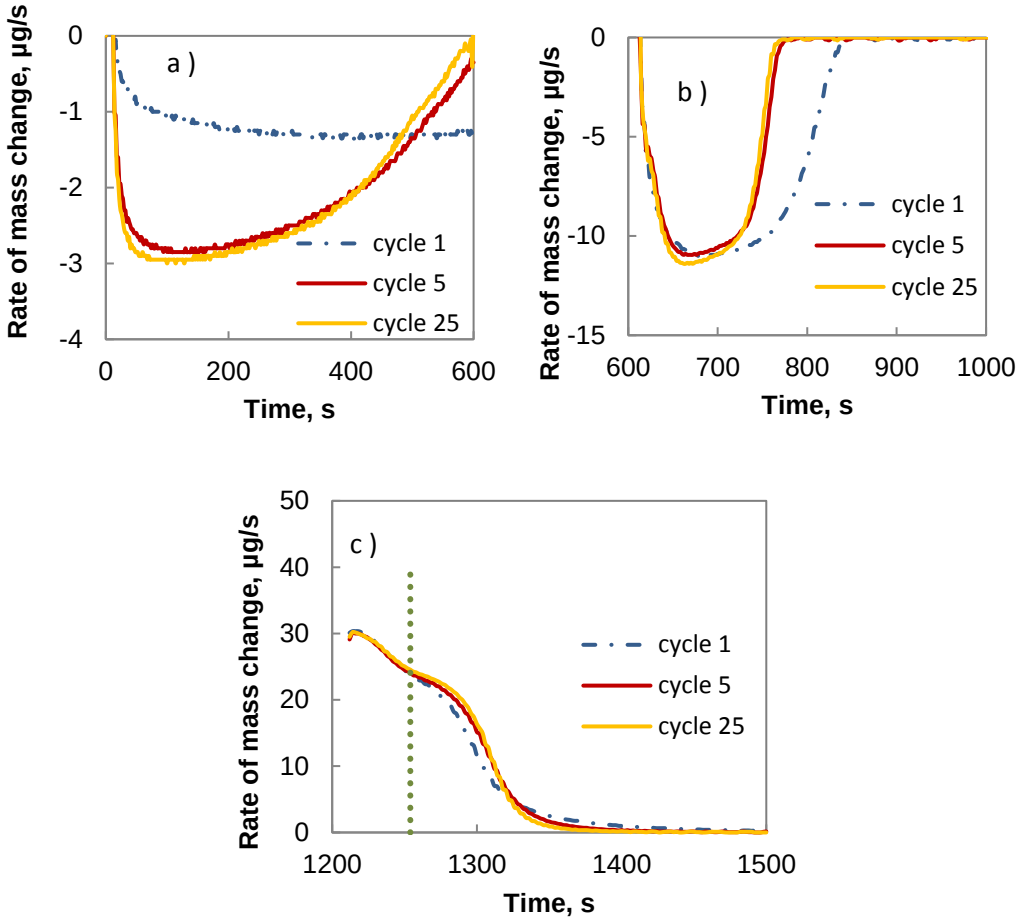


Figure 4-1 Rate of change of mass of sample for selected cycles. a) oxygen release in $N_2$ (0-600 s); b) reduction in 5% $H_2$ (600-1200 s); c) re-oxidation in air (1200-1800 s). The dotted vertical line in graph c) indicates the time when 50% conversion has been reached for the 5$^{th}$ and 25$^{th}$ cycles. The initial 12 s of measurements for each section, because of large mass fluctuations due to gas switching, have been omitted for clarity.

From Figure 4-1, it is also worth noting that the re-oxidation appears to occur via a two-step process, evident from the plateau-like feature of the apparent rate at $t$ ~ 1255 s. This feature coincides with the point of 50% conversion for the 5$^{th}$ and 25$^{th}$ cycles, shown in Figure 4-1 c) by the dotted vertical line. When the experiment was

repeated with a lower bulk oxygen concentration, the feature became more pronounced, owing to a smaller concentration driving force for the oxidation of $Cu_2O$.

The sample was recovered after the experiment and cross sections of the cycled particles were examined using an optical microscope. The micrographs of the cross sections of a) a virgin particle and b) a cycled particle are shown in Figure 4-2. It can be seen from Figure 4-2 that the pores (black regions) in the cycled particle are significantly larger than those present in the virgin particle which could explain the increased reactivity over cycles.

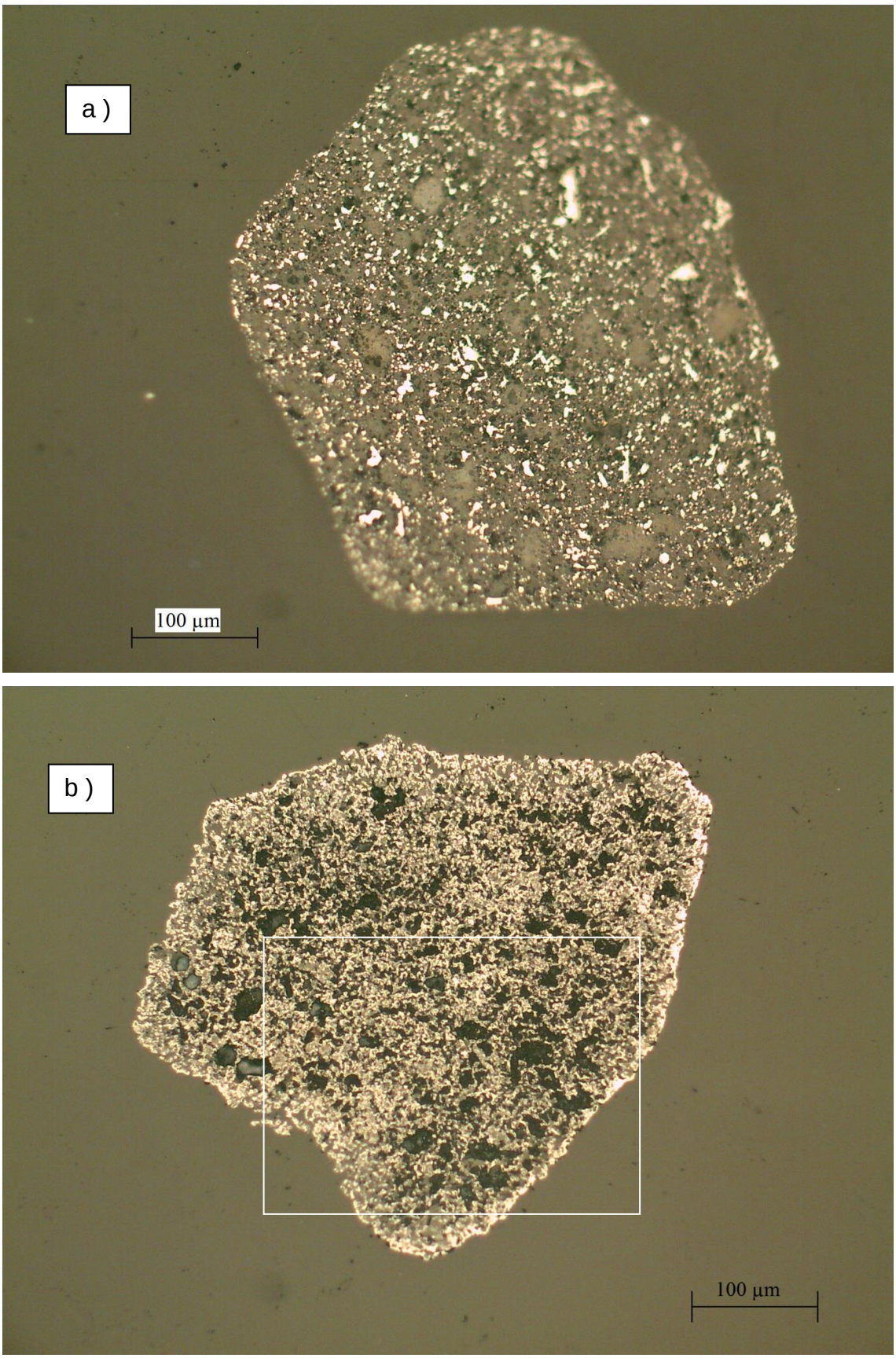


Figure 4-2 Micrographs of a ) virgin particle and b ) cycled particle (after 25 cycles). 200x magnification.

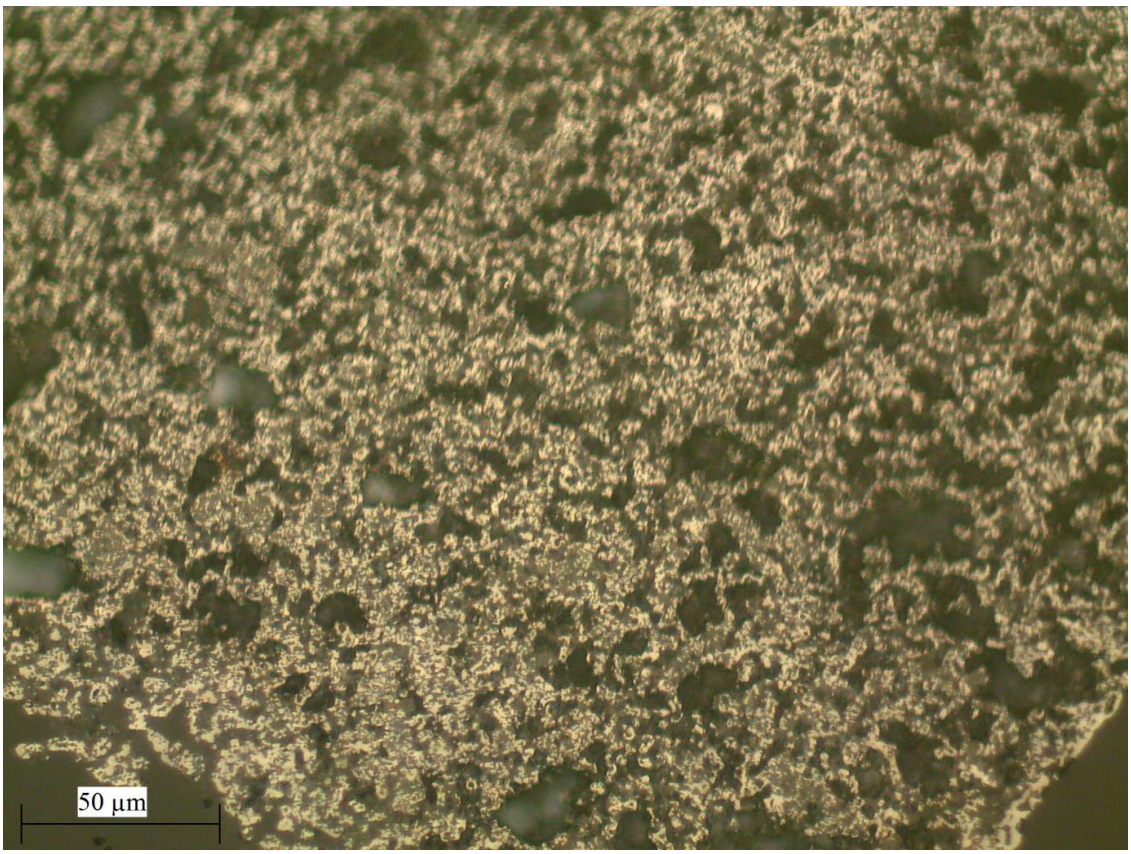


Figure 4-3 Micrograph of part of the cross section of an OC particle cycled 25 times. 500x magnification.

Part of the cycled particle, enclosed in the white rectangle in Figure 4-2 b), was examined with a higher magnification and the micrograph is shown in Figure 4-3. Figure 4-3 shows that the solid part of the particles consists of darker materials (most likely CuO) embedded in a brighter matrix (most likely $Ca_{12}Al_{14}O_{33}$) throughout the particle, suggesting that the active material is well dispersed on the support without significant segregation even after repeated cycling so that the particle could remain reactive.

### *4.3.3. Agglomeration and attrition in fluidised bed*

The outcome of the successive circulation experiments conducted with a batch of virgin OC particles with an initial mass of 110 g and sieve size fraction 300-425 μm is presented in Table 4-1. With the exception of experiment I.5, all experiments were performed with air as the fluidising gas in both the primary (2.0 l/min at 20°C and 1 bar) and secondary (2.4 l/min at 20°C and 1 bar) gas inlet so that the value of $U_0/U_{mf}$ was ~ 4 in the bubbling bed and ~ 45 in the riser section. In experiment 5, the primary gas was a mixture of 0.5 l/min air and 1.5 l/min $N_2$ while the secondary gas was 2.4 l/min of 5 vol% $H_2$ in $N_2$. The gases were chosen such that the OCs would be reduced in the

riser section and re-oxidised in the bubbling bed at the bottom of the reactor. The residence time of the solids in the riser section was estimated as follows:

The terminal velocity of a single particle can be calculated from a simple force balance on the particle, neglecting buoyancy effect:

$$U_t = \sqrt{\frac{4gd_p}{\rho C_d}}, \qquad 4\text{-}1$$

Where $d_p$ is the diameter of the particle, $\rho$ is the density of the fluid and $C_d$ the drag coefficient, which is related to the Reynolds number based on $U_t$ and is given by (Tilton, 2007)

$$C_d = \frac{24}{Re_t}\left(1+0.14Re_t^{0.70}\right) \quad 0.1 < Re_t < 1000, \qquad 4\text{-}2$$

with

$$Re_t = \frac{\rho U_t d_p}{\mu}. \qquad 4\text{-}3$$

Here, $\mu$ is the viscosity of the fluidising gas. Equations 4-1 and 4-2 were solved iteratively to give $U_t$ = 2.1 m/s. The group terminal velocity of the particles was estimated using the correlation of Richardson and Zaki (1954),

$$U_{gr} = U_t \varepsilon^n, \qquad 4\text{-}4$$

$$n = \left(4.45 + \frac{18d_p}{d_{riser}}\right) Re_t^{-0.1} \quad 1 < Re_t < 200 \qquad 4\text{-}5$$

where $\varepsilon$ is the voidage of the group of particles, estimated as 0.95 and $d_{riser}$ is the internal diameter of the riser, 10 mm. Equations 4-4 and 4-5 gave $U_{gr}$ = 1.3 m/s, resulting in a residence time of the solids in the riser section of ~ 0.4 s. Hence the reduction of the OC was not complete in the riser due to this short residence time.

It can be seen from Table 4-1 that the mass loss per unit time of operation was relatively high in experiments I.1 and I.2 but the rate of attrition decreased to a steady value in experiments I.3 –I.5. The redox atmosphere used in experiment I.5 did not appear to affect the rate of attrition. This was expected because the degree of reduction was expected to be low in the experiment. In addition, the molar volumes of CuO and $Cu_2O$ are 12.6 and 11.9 $cm^3$ per mole of Cu atoms, respectively, calculated from their densities. Since the difference is only 5.3%, the reaction should not cause significant expansion or contraction of the material. In comparison, experiment I.6, which lasted a total of 100 hours, resulted in a slightly higher absolute mass loss but significantly

lower mass loss per hour of operation. One possible explanation is that part of the attrition was due to the thermal stress during the heating and cooling period at the beginning and end of each experiment.

**Table 4-1 Duration and mass loss of the OC particles in each successive experiment, all experiments carried out at 900°C in air, with the exception of experiment I.5, where 5 vol% $H_2$ in $N_2$ was used for the secondary gas**

| *Experiment No.* | *Duration, hours* | *Sample mass before experiment, g* | *Mass loss during experiment, g* | *Average mass loss, %/h* |
|---|---|---|---|---|
| I.1 | 24 | 109.95 | 8.67 | 0.33 |
| I.2 | 25 | 101.28 | 1.12 | 0.044 |
| I.3 | 24 | 100.16 | 0.23 | 0.0096 |
| I.4 | 24 | 99.93 | 0.27 | 0.011 |
| I.5 | 25 | 99.66 | 0.26 | 0.010 |
| I.6 | 100 | 99.40 | 0.34 | 0.0034 |

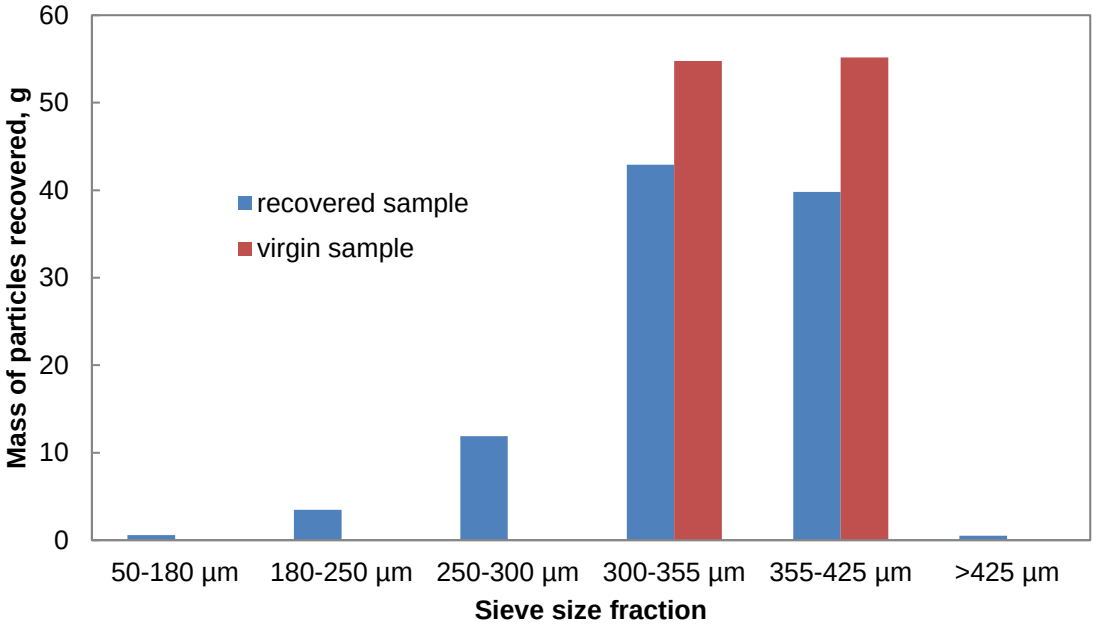


Figure 4-4 the size distribution of the particles recovered after experiment 6 (blue) compared with that of the virgin sample (red).

The size distribution of the particles recovered after experiment I.6 was measured and the results are shown in Figure 4-4. It is clear from Figure 4-4 that the majority of the recovered particles were within the original size of 300-425 µm and only a small portion of particles was below 250 µm. The results suggest that abrasion is likely to be the primary cause of loss of particles with limited contribution from fragmentation.

The tendency for the particles to agglomerate was studied in the same circulating bed with a different batch of particles with an initial mass of 97.95 g. In these experiments, the secondary gas used was always $N_2$ with a flowrate of 2.4 l/min, measured at 20°C and 1 bar, to maintain circulation. The primary gas flowrate was kept at 2.0 l/min (20°C and 1 bar). The durations and primary gas used in each experiment are summarised in Table 4-2. In experiments II.1, II.3 and II.5, agglomeration of the particles was not observed. The pressure drop across the bubbling section of the fluidised bed was relatively constant throughout the experiments, allowing for the slight changes in the mass of OC particles due to chemical reaction. However, agglomeration and de-fluidisation of the bed material was observed in experiments II.2 and II.4.

**Table 4-2 experimental conditions used to investigate agglomeration**

| *Experiment No.* | *Bed Temperature,* °C | *Primary gas* | *Duration, hours* | *De-fluidisation* |
|---|---|---|---|---|
| II.1 | 850 | air | 6.0 | no |
| II.2 | 850 | 5 vol% $H_2$ in $N_2$ | 7.1 | yes |
| | | air | 0.5 | |
| II.3 | 850 | air | 8.2 | no |
| | | 5 vol% $H_2$ in $N_2$ | 1.0 | |
| II.4 | 850 | 5 vol% $H_2$ in $N_2$ | 4.3 | yes |
| | | air | 4.5 | |
| II.5 | 900 | $N_2$ | 3.2 | no |
| | | air | 2.7 | |

The sequence of events in experiment II.4 is shown in Figure 4-5 as an example to illustrate the occurrence of de-fluidisation. During the first 260 minutes of the experiment when a reducing gas was used, the measured pressured drop decreased gradually as oxygen was removed from the OC until $t$ ~ 200 min when the reaction was complete. A mass balance on the oxygen available from the OC showed that if all of the $H_2$ supplied had reacted with the particles, the reaction would have finished at $t$ ~ 180 min, in good agreement with the experimental results. The circulation of the bed was confirmed several times during the course of the experiment and was found to be steady. At $t$ ~ 260 min, the fluidising gas was switched to air, marked by the sharp disturbance in pressure drop. The pressure drop in the bed increased slightly during the first 2 minutes after the gas switch, probably owing to the oxidation of the particles. However, the pressure drop decreased relatively quickly thereafter until $t$ ~270 min and remained constant after. It was confirmed visually that at $t$ ~270 min, the circulation of the particles had stopped. Unsuccessful attempts were made to restore fluidisation by

increasing the flowrate of air, manifested by the pressure fluctuations at *t* ~ 290 min: and the reactor was cooled down shortly after that time to retrieve the particles. Between *t* = 260 min and 270 min, a moderate increase in the temperature, of ~ 10°C, in the bed was observed and the temperature did not increase further after the pressure drop stabilised. Interestingly, most of the retrieved OC particles remained as single particles and only a small fraction was agglomerated, of which only two agglomerates of size larger than 650 µm were isolated. The large agglomerates were strong enough to survive sieving but when attempting to pick them up using a pair of tweezers, they disintegrated into smaller particles.

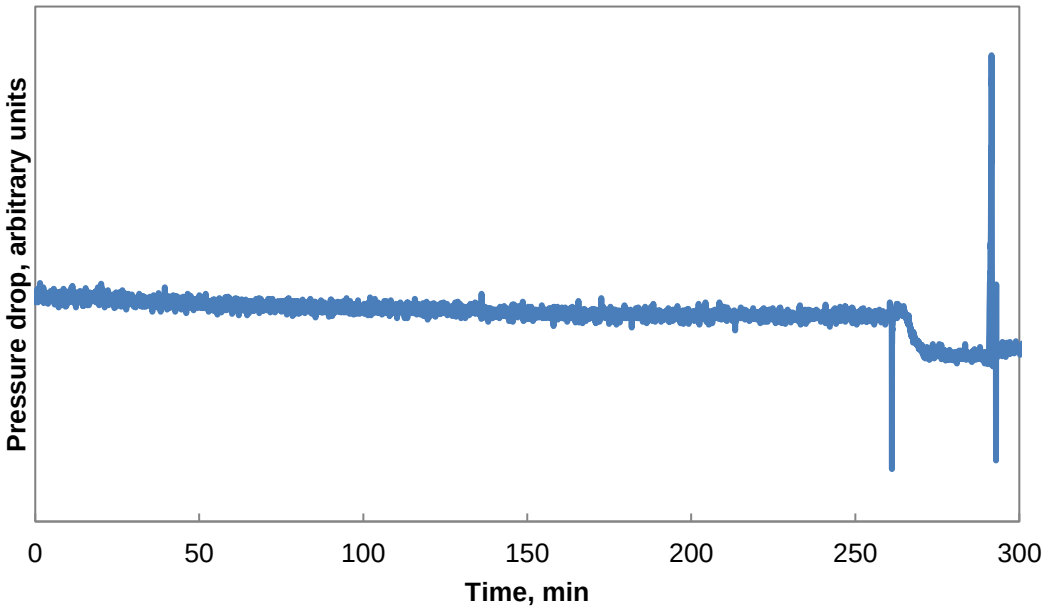


Figure 4-5 The pressure drop across the bubbling section of the fluidised bed in experiment II.4. De-fluidisation started after the primary gas switched from 5 vol% $H_2$ in $N_2$ to air at *t* = 260 min.

From the experimental results presented in Table 4-2, it can be concluded that stable fluidisation and circulation can be maintained regardless of the oxidation state of the OC particles. However, de-fluidisation occurred when fully-reduced particles were oxidised in air, the behaviour being reproducible and observable in both experiments II.2 and II.4. When the OC particles were being oxidised from $Cu_2O$ or reduced from CuO by $H_2$, no de-fluidisation was observed. Thus it appears that the de-fluidisation and agglomeration of the OC particles is associated with the oxidation of Cu. This result is consistent with other studies on Cu-based materials: various degrees of agglomeration in a fluidised bed were observed when the CuO content exceeded

10 wt% in the OC (de Diego *et al.*, 2005) but for CLOU operations, agglomeration was not observed with particles containing 40 wt% CuO on $ZrO_2$ or 60 wt% CuO on $MgAl_2O_4$ (Gayán *et al.*, 2012). The agglomeration of the particles could be due to the low melting point of metallic Cu and the exothermic oxidation of the Cu could raise the local temperature of the particle close to or even above the melting point of Cu, 1085°C. The temperature of the particles during oxidation was estimated as follows:

Consider the extreme case where the oxidation of the OC particles were so fast that the $O_2$ in the gas phase was consumed completely by a single layer of OC particles at the bottom of the fluidised bed. Assuming that transport processes were in steady state and the temperature inside the particles was uniform, the heat balance between the layer of particles and the fluidising gas is given by

$$n\pi d_p^{\,2}\frac{Nu\lambda_{air}}{d_p}\Delta T = \dot{N}_{O2}\Delta H_r \qquad 4\text{-}6$$

in which $n$ is the number of particles present in the layer such that the total surface area available for heat transfer is $n\pi d_p^2$; $\lambda_{air}$ is the thermal conductivity of air and $Nu$ is the Nusselt number for the convective heat transfer between the particles and the gas; $\dot{N}_{O2}$ is the molar flowrate of $O_2$ at the inlet; $\Delta H_r$ is the enthalpy of reaction of

$$4Cu + O_2 \rightarrow 2Cu_2O, \qquad 4\text{-}7$$

with a value of -334 kJ/mol at 850°C (NIST, 2011). If the direct oxidation of Cu to CuO was assumed, the magnitude of $\Delta H_r$ would be slightly lower, at -298 kJ/mol; $\Delta T$ is the temperature difference between the particle and the fluidising gas. Contribution from thermal radiation was neglected in equation 4-6 because the fluidising gas was either air or $N_2$, neither of which is active in the IR region. Assuming the Nusselt number takes the value of 2, *i.e.* for a single particle in an infinite medium, equation 4-6 can be rearranged as

$$\Delta T = \frac{\dot{N}_{O2}\Delta H_r}{2n\pi d_p\lambda_{air}}. \qquad 4\text{-}8$$

The value of n can be estimated from the cross sectional area of the reactor, $A_x$, assuming a particle coverage of 0.6, such that

$$n = \frac{0.6A_x}{\frac{1}{4}\pi d_p^{\,2}} \qquad 4\text{-}9$$

and the rise in temperature of the particles due to the oxidation reaction 4-7 was calculated to be ~ 112°C. Thus the particle temperature was ~ 970°C, approximately

100°C below the melting point of Cu. However, the actual temperature of the particles is expected to be lower owing to the assumptions made in this calculation. Thus it is unlikely that the metallic Cu melted during the oxidation and the mechanism of agglomeration of fully-reduced OC particles on re-oxidation remains unclear.

## *4.4. Discussion*

The OC particles synthesised by the wet-mixing method had extremely low internal surface area and pore volume, as measured by the nitrogen adsorption experiment. However, both the reduction and oxidation of the particles were reasonably fast when measured in a TGA. In fact, as shown in Chapter 7, complete decomposition of the OC particles to $Cu_2O$ could be achieved in < 20 s in a fluidised bed. As a result, simple mechanical mixing can be used for the preparation of the particles instead of the more complicated impregnation or co-precipitation techniques. This is important for the large scale production of OCs for CLC and CLOU operations because, for the process to be viable, the OCs must be produced in large quantities at low cost. The wet-mixing method employed in this work could be easily scaled up, as it only involves the mechanical mixing of the precursors in an aqueous environment with little control over pH, atmosphere or temperature *etc.* required.

The virgin particles exhibited excellent attrition resistance in a circulating fluidised bed. However, the pore structure of the cycled material was significantly different from that of the virgin material, as seen in Figure 4-2. As a result, the mechanical strength of the cycled particles might be lower than that of the virgin ones. This is certainly seen in other carriers, *e.g.* fresh ilmenite exhibits excellent mechanical strength but cycled ilmenite is significantly weaker (Rydén *et al.*, 2014), albeit a completely different chemical composition to that used in this Dissertation. It was difficult to assess the resistance to attrition of the cycled particles in the current apparatus because it was impractical to produce enough cycled material using available equipment for this investigation.

## *4.5. Summary*

In this chapter, an OC containing 60 wt% CuO supported on mayenite was prepared by the wet-mixing method. Characterisation of the particles was carried out using a variety of techniques and it was found that the OC particles exhibited excellent chemical and mechanical stability with a high oxygen capacity of 6 wt% for CLOU and 12 wt% for CLC. The particles did not agglomerate in a circulating fluidised bed unless

being oxidised from the fully-reduced form. As a result, it was concluded that this oxygen carrier is suitable for use in a CLOU process. Discussions of the thermodynamics and chemical kinetics of the carrier are deferred until Chapters 5 and 6.

# 5. The thermodynamic equilibrium of the CLOU reaction of the oxygen carrier

## *5.1. Introduction*

In this chapter, as well as in the following chapter, investigations into the chemical kinetics of the forward and backward reaction in

$$4CuO \underset{k_{-1}}{\overset{k_1}{\rightleftharpoons}} 2Cu_2O + O_2 \qquad 5\text{-}1$$

will be presented. In equation 5-1, the forward and backward rate constants are represented by $k_1$ and $k_{-1}$, respectively. Being an equilibrium process, it is straightforward that the equilibrium constant for the reaction is

$$K = \frac{P_{eq}}{1\,\text{bar}}, \qquad 5\text{-}2$$

assuming the activities of the solids are unity. Here, $P_{eq}$ is the equilibrium partial pressure of $O_2$ for the reaction. Since the equilibrium constant is related to the Gibbs free energy of reaction at standard conditions (*i.e.* at 1 bar), $\Delta G°$, its dependence on temperature can be written as

$$K(T) = \exp\left(\frac{-\Delta G°(T)}{RT}\right), \qquad 5\text{-}3$$

where the temperature, $T$, is in kelvin and $R$ is the universal gas constant, equal to 8.314 J/mol/K. Thus the value of $K$ and hence $P_{eq}$ can be obtained using values of $\Delta G°$ at the appropriate temperatures which can be obtained from standard thermodynamic databases. The equilibrium partial pressure plays an important role in the kinetics of reaction 5-1 as follows.

Because reaction 5-1 is a heterogeneous reaction between a gas and solid, the release or uptake of $O_2$ by the solid has to occur at the solid-gas interface. Hence the rate of production of $O_2$ per unit surface area available for the reaction can be represented as an $n^{th}$ order reaction

$$\frac{dN_{O2}}{dt} = k_1 - k_{-1}C_s{}^n \qquad 5\text{-}4$$

where $N_{O2}$ is the amount of $O_2$ produced per unit surface area; $k_1$ and $k_{-1}$ are the rate constants for the forward and backward reactions, respectively and $C_s$ denotes the molar concentration of the $O_2$ at the reaction interface. The absence of the dependence of the solid species in the rate expression is because the reactant, CuO, and the

product, $Cu_2O$, are not mutually soluble to any appreciable extent so that the activities of these species are constant and can be taken as unity by convention. When the system is at equilibrium, it is evident that

$$\frac{dN_{O2}}{dt} = 0 \qquad 5\text{-}5$$

so that

$$k_1 = k_{-1} C_{eq}^{\ n} \qquad 5\text{-}6$$

in which $C_{eq}$ is the equilibrium concentration of $O_2$ and is related to $P_{eq}$ *via*

$$C_{eq} = \frac{P_{eq}}{RT}. \qquad 5\text{-}7$$

Combining equations 5-6 and 5-4, one obtains an expression with only one rate constant, *viz.*

$$\frac{dN_{O2}}{dt} = k_{-1}\left(C_{eq}^{\ n} - C_s^{\ n}\right). \qquad 5\text{-}8$$

Of course, during the course of the reaction, the amount of the solid reactant changes and so does the total interfacial area available for the reaction. To account for the dependence of the observed rate of chemical reaction on this factor, a conversion function $f(X)$, depending only on the fractional conversion of the solid reactant, $X$, can be employed so that the rate expression becomes

$$\frac{dX}{dt} = k_{in}\left(C_{eq}^{\ n} - C_s^{\ n}\right) f(X) \qquad 5\text{-}9$$

where $k_{in}$ is the corresponding rate constant, which is proportional to $k_{-1}$. Clearly, for the rate expression to be valid, the function $f(X)$ must be positive and finite in the interval (0,1) with $f(1) = 0$. In some circumstances, the initial rate of the reaction, at $X = 0$, can be zero. Such behaviour is commonly observed in the kinetics of the phase transformation of solids where, for example, Avrami (1939, 1940, 1941) postulated that the conversion function should be

$$f(X) = a(1-X)\left(-\ln(1-X)\right)^{a-1/a} \qquad 5\text{-}10$$

where the constant $a$ takes only integer values 1, 2, 3 or 4, depending on the mechanism of crystallisation. In the special case where $a = 1$, the logarithmic term disappears and the conversion function becomes that of a first-order homogenous reaction throughout the solid.

Often, the diffusion of the gaseous species within the pores of the solid is rate limiting so that reaction is confined to a thin region on the outer surface of an unreacted,

shrinking core. The resulting conversion function in this case is (Kunii and Levenspiel 1991):

$$f(X) = \frac{3}{2}\left((1-X)^{-1/3} - 1\right). \qquad 5\text{-}11$$

In a similar case where the reactant is non-porous and the reaction is limited by the intrinsic kinetics at the surface, the conversion function is given by (Kunii and Levenspiel 1991)

$$f(X) = 3(1-X)^{2/3}. \qquad 5\text{-}12$$

Many other conversion functions have been proposed depending on different reaction models and, or, the physical set up of the particular problem as reviewed by Khawam and Flanagan (2006).

Returning to equation 5-9, it is clear that the rate of reaction depends on the kinetic rate constant $k_{in}$ as well as the difference between the concentration of $O_2$ at the surface of the solid and the equilibrium concentration. Thus the precise knowledge of the equilibrium concentration of $O_2$ at different temperatures is a crucial prerequisite for determining the reaction kinetics of the CLOU reaction.

However, the calculated values of the equilibrium partial pressure of $O_2$ can differ from each other, at the same conditions, by about 10% for the conversion between CuO and $Cu_2O$, depending on the thermodynamic data used, as seen in Figure 5-1. It should also be noted that, although the thermodynamic data available from literature are in good agreement, the original data were generally obtained from very pure systems ( *e.g.* Jacob and Alcock, 1975) to eliminate any potential influences from impurities. On the other hand, evidence from the work presented in Chapter 3 has shown that when the CuO is mixed with a support (mayenite), the support can alter the thermodynamics of CuO without incurring a phase change. Thus it is important always to measure the equilibrium partial pressure of $O_2$ for particular OCs whenever possible, especially when attempts are being made to measure the kinetics of the carrier. In this chapter, a method based on diffusion has been developed to measure the equilibrium of systems using the TGA. In addition, the effect of support and conversion on the equilibrium of the carrier is investigated further.

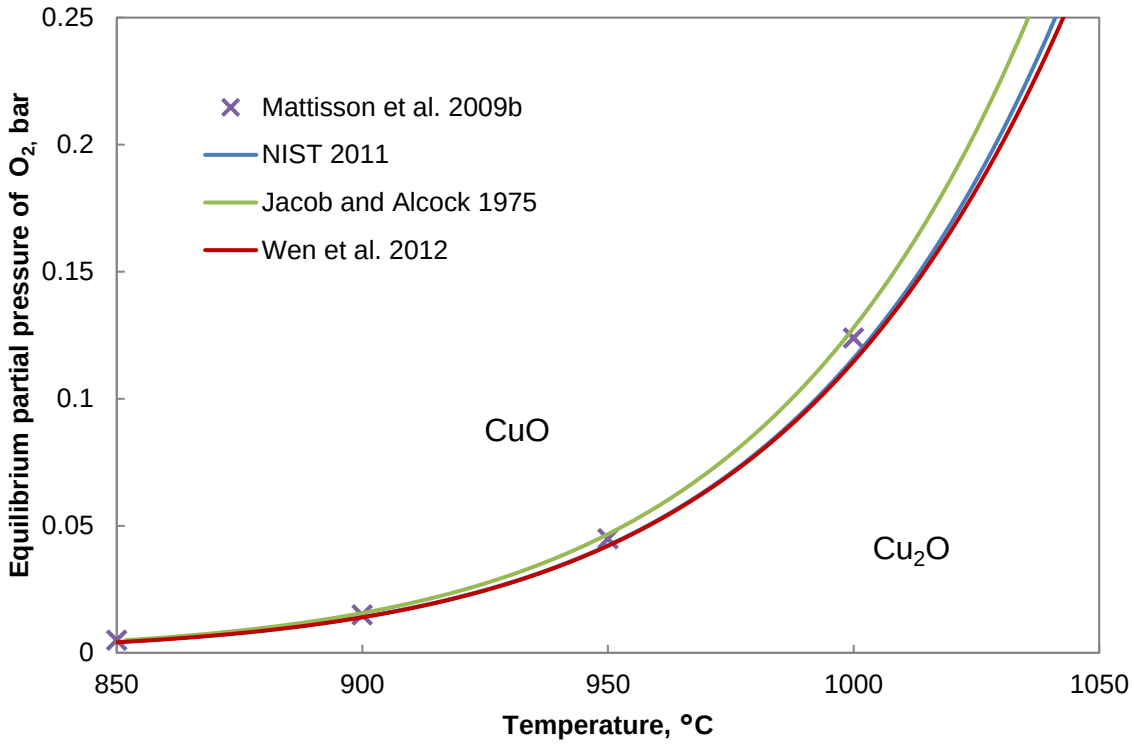


Figure 5-1 Some values of the equilibrium partial pressure of $O_2$ for the CuO/$Cu_2O$ system obtained from literature. Data presented by Jacob and Alcock (1975) were derived from their original experiment; Wen *et al.* (2012) fitted data obtained from Barin (2008) whilst the source of data in the work of Mattisson *et al.* (2009b) was not specified.

## *5.2. Experimental methods*

### *5.2.1. Temperature programmed reaction*

In Chapter 3, it was found that the OC supported on mayenite exhibited two different decomposition temperatures in a constant atmosphere and the portion of the material which decomposed at a higher temperature decreased with cycling. This behaviour was investigated further in this chapter by means of temperature programmed reaction with the aid of XRD analysis.

Firstly, ~ 7 mg of the fresh OC prepared using the wet mixing method (300-425 μm) was held at 850°C in the TGA for 10 minutes before the temperature was increased to 940°C with a steady heating rate of 10°C/min. The gas used was a mixture of air and Ar with a total flowrate of ~ 130 ml/min measured at 20°C and 1 bar. The mole fraction of $O_2$ was selected such that the decomposition and re-oxidation of the material would occur between 850°C and 1000°C (~2 vol% as estimated from the inlet gas flowrates, and the equilibrium temperature at this condition was 916°C according to the NIST database (NIST, 2011)).The sample was then maintained at 940°C for a

further 10 minutes before the temperature was increased again to 1000°C at the same rate of heating. Once the temperature of the sample had reached 1000°C, the furnace was cooled to 850°C at 10°C/min and held at that temperature for an additional 10 minutes. The same sample was subjected to the above temperature programme for 10 cycles to study the cyclic behaviour of the carrier and some reference materials (CuO powder as received and CuO powder calcined in air at 1000°C for 6 hours) were investigated using the same temperature programme for comparison.

Secondly, to investigate the dependence of the equilibrium temperature on the conversion of the material in a fixed atmosphere, approximately 6.1 mg of pre-treated OC (fully reduced and then re-oxidised at 850°C for 3 times in a fluidised bed) in the same size fraction (300-425 μm) was held at 850°C in a constant atmosphere (same as above, a mixture of air and Ar containing ~ 2 vol% $O_2$) for 20 minutes before being heated to 940°C at a rate of 10°C/min. For the first batch of samples, the temperature was maintained at 940°C for 10 minutes for the complete decomposition of CuO to $Cu_2O$. The samples were subsequently cooled from 940°C to 850°C with different, but constant, cooling rates ranging from 1°C/min up to 20°C/min. For the second batch of samples, the temperature was maintained at 920°C ($P_{eq}$ = 0.022 bar at this temperature (NIST, 2011)) for 20 minutes. At this temperature, the kinetics of decomposition were slow due to a low concentration driving force present, so the sample had only partly decomposed by the end of the isothermal period. The temperature was then cooled to 850°C at the same constant cooling rates as used for the first batch of samples. In addition, a sample was subjected to a similar temperature programme as the second batch with a final cooling rate of 5°C/min except that the end point of the heating period was changed from 940°C to 945°C to increase the conversion of the sample for comparison. For further confirmation, approximately 6.2 mg of the pre-treated OC was held at 900°C for 10 minutes in 2 vol% $O_2$ as before. Subsequently, the temperature of the sample was increased to 935°C and then decreased to 905°C and increased back to 935°C with the same rate of heating and cooling, 5°C/min, to determine the temperature at which detectable oxidation or reduction of the sample could be first observed.

### *5.2.2. The diffusion method*

A novel diffusion method developed in this chapter to measure the equilibrium partial pressure of the OC prepared by wet mixing containing 60 wt% CuO was as follows. A batch of the fresh OC, ~ 50 mg, with particle sieve sizes between 180 μm

and 300 μm, was fully reduced using 5% $H_2$ in $N_2$ as the reactive gas (~50 ml/min measured at 20°C and 1 bar) in a TGA at 900°C for 15 minutes and then fully oxidised in air (~50 ml/min at 20°C and 1 bar) at the same temperature for 10 minutes, such that no further change in mass was observed by the end of each segment. The cycle was repeated until the particles had been fully reduced 5 times; after this the sample was cooled to room temperature in the reducing environment to prevent any re-oxidation during cooling. Between 5.7 and 6.0 mg of the reduced OC was then used for the following investigation.

A cylindrical alumina crucible (Mettler Toledo, 70 μl nominal volume) was procured, having an i.d. of 4.95 mm and depth 4.00 mm. The crucible was equipped with a standard removable alumina lid with a hole in the centre (i.d. 0.90 mm) to limit the amount of gas diffusing in and out of the crucible. The mass of the sample was chosen so that the particles formed a monolayer at the base of the crucible. The atmosphere within the TGA was a mixture of Ar and air (total flowrate ~ 130 ml/min at 20°C and 1 bar) with the mole fraction of $O_2$ being ~1.5%. The temperature of the furnace of the TGA was maintained at 50°C to obtain a stable reading for the mass of sample, without any reaction. After 10 minutes, the set point was changed to a temperature between 700°C and 925°C so that the sample was oxidised by the $O_2$ present in the atmosphere. The mass transfer of gas within the alumina crucible with a lid is a purely diffusive process provided that the external rate of gas flow across the hole is not too fast. Assuming that the chemical reaction at the surface of the solid particles is fast compared to the rate of diffusion of gases within the crucible, then the concentration of gases at the surface of the particles would be equal to the equilibrium concentration, thus enabling the determination of the equilibrium concentration by measuring the rate of mass transfer inside the crucible, determined, in turn by the rate of change of mass of the sample.

While the above protocol was useful for the validation of the diffusion method, a significant portion of the sample was oxidised during transient heating period. To circumvent this problem, the protocol was improved for the determination of the equilibrium partial pressure of $O_2$ for the CLOU reaction between 850°C and 950°C, as follows. In each investigation, the sample was held in Ar (~120 ml/min at 20°C and 1 bar) at 50°C for 5 minutes before the set point changed to the reaction temperature. The sample was held for a further 5 minutes in Ar to allow the temperature of the sample to settle down before air was blended into the purge stream to create an

oxidising environment. The amount of air blended was such that the resulting atmosphere was slightly oxygen rich compared to the equilibrium so that it was sufficient to oxidise the sample fully at the specified temperature but the rate of reaction was relatively slow to limit the vertical flux into the crucible.

## 5.3. Theory

### 5.3.1. Diffusion in a cylindrical crucible

The multi-component diffusion process is governed by the Stefan-Maxwell equation (Maxwell, 1867; Stefan, 1871). For an isothermal system with a constant total pressure, the equation for the $i^{th}$ species in an $n$-component system is given by

$$\nabla y_i = \sum_{\substack{j \\ j \neq i}}^{n} \frac{y_i \underline{J}_j - y_j \underline{J}_i}{c D_{ij}} \qquad 5\text{-}13$$

where $y$ denotes the mole fraction of the species $i$ or $j$ depending on the subscript. Correspondingly, the diffusive flux of the species is denoted by $\underline{J}$. The total molar concentration of the gases is $c$ and $D_{ij}$ is the binary diffusion coefficient between the $i^{th}$ and $j^{th}$ components.

In the method described in section 5.2.2, both the isothermal and isobaric assumptions are justified since only a small amount of the sample was used so that the temperature variation was small. Also, the mole fraction of $O_2$ was small so that the change in the total pressure of the system could be ignored. Because gaseous systems are close to ideal at atmospheric pressure and high temperature, the binary diffusion coefficients are independent of the composition of the gas and can be estimated using (Fuller *et al.*, 1966):

$$D_{ij} = \frac{10^{-3} T^{1.75} \left( \frac{1}{M_i} + \frac{1}{M_j} \right)^{1/2}}{P \left[ \left( \sum V_i \right)^{1/3} + \left( \sum V_j \right)^{1/3} \right]^2} \times \frac{1}{10000}. \qquad 5\text{-}14$$

Here, $M$ is the relative molecular mass of the species concerned and the parameter $\Sigma V$ is known as the diffusion volume. The temperature $T$ is in kelvin and the total pressure, $P$, in atm. The conversion factor of $10^{-4}$ is used to convert the diffusion coefficient from the original units (in $cm^2/s$) to SI units.

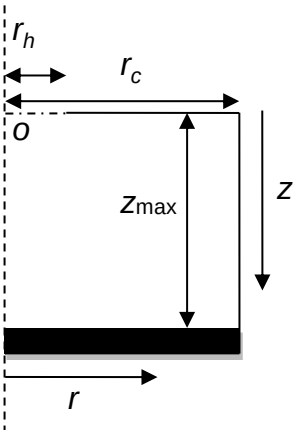

Figure 5-2 Side view of the right half of a cylindrical crucible

The geometry of the particular problem described in the previous section is axisymmetric so that the Stefan-Maxwell equations can be solved in 2-D cylindrical coordinate instead of the full 3-D case, as shown in Figure 5-2 with the radial coordinate *r* and vertical coordinate *z*. The radius of the hole in the lid is represented by $r_h$; the radius of the crucible is $r_c$ and the depth $z_{max}$. Here *z* is taken as positive into the crucible (downwards) since the origin, *o*, is taken at the centre of the lid. Thus there are a total of 3*n* variables from the Stefan-Maxwell equations (*n* in *y* and 2*n* in $\underline{J}$, *n* in each dimension). It is important to note that, for each dimension, only *n*-1 of the *n* equations are independent because at any point in space, the sum of mole fractions of all gaseous species must be unity, *i.e.*

$$\sum_{i=1}^{n} y_i = 1 \qquad 5\text{-}15$$

and hence

$$\sum_{i=1}^{n} \nabla y_i = 0. \qquad 5\text{-}16$$

As a result, the system of equations consists of 2*n*-2 independent Stefan-Maxwell equations, together with either equation 5-15 or 5-16. A further set of *n* equations can be obtained from the conservation of mass of each species throughout the space, *viz.*

$$c\frac{\partial y_i}{\partial t} + \nabla \bullet \underline{J}_i = S_i. \qquad 5\text{-}17$$

Here, $S_i$ is the source term of species *i* due to, *e.g.* a gas phase reaction within the space of interest. Hence one more equation, normally in terms of $\underline{J}_i$, is required to close the system.

For the specific case of CLOU in this set up, three gaseous species are involved, namely $O_2$, $N_2$ and Ar (denoted as species 1, 2 and 3 respectively for convenience), of

which only $O_2$ interacts with the solid at the base of the crucible. Since no reaction takes place within the crucible except at the surface of the solid, $S_i = 0$ everywhere and the generation or consumption of $O_2$ is manifested as a boundary condition. Furthermore, at steady state, both $N_2$ and Ar are stagnant inside the crucible, which is mathematically equivalent to

$$\underline{J}_i = 0 \quad \forall r, z \qquad i = 2 \text{ or } 3. \tag{5-18}$$

After the elimination of redundant equations, the system of equations at steady state reduces to

$$\nabla y_2 = \frac{y_2 \underline{J}_1}{cD_{12}} \tag{5-19}$$

$$\nabla y_3 = \frac{y_3 \underline{J}_1}{cD_{13}} \tag{5-20}$$

$$\nabla \bullet \underline{J}_1 = 0 \tag{5-21}$$

and it is clear that equations 5-19 and 5-20 only differ by the binary diffusion coefficient. In this case, $D_{12}$ and $D_{13}$ differ by approximately 5% according equation 5-14 so that $N_2$ and Ar could have been treated as one species to good approximation.

To solve the system of equations, only equations 5-20 and 5-21 need to be considered and equation 5-19 can be solved in the same way when coupled with equation 5-21. Substituting equation 5-20 into equation 5-21, one obtains

$$cD_{13} \nabla \bullet \nabla \ln y_3 = 0 \tag{5-22}$$

which in turn simplifies to the Laplace equation in $\ln(y_3)$

$$\nabla^2 \ln y_3 = 0 \tag{5-23}$$

and can be solved by the method of separation of variables.

Using the boundary conditions that the radial flux of $O_2$ must be zero at the centreline $r = 0$, due to symmetry, as well as at the side walls of the crucible, $r = r_c$, the general solution to equation 5-23 takes the form (see Appendix A for a brief derivation)

$$\ln y_3 = \kappa_1 \frac{z}{z_{\max}} + \kappa_2 + \sum_{n=1}^{\infty} B_{J,0}\left(\omega_n \frac{r}{r_c}\right)\left(\kappa_{3n} \exp\left(\omega_n \frac{z_{\max}}{r_c} \frac{z}{z_{\max}}\right) + \kappa_{4n} \exp\left(-\omega_n \frac{z_{\max}}{r_c} \frac{z}{z_{\max}}\right)\right) \tag{5-24}$$

where $B_{J,0}$ is the zeroth-order Bessel function of the first kind. The parameters $\omega_n$ are the $n^{\text{th}}$ root of the first-order Bessel function of the first kind, $B_{J,1}$. The constants $r_c$ and $z_{\max}$ correspond to the radius of the crucible and the distance from the lid to the surface

of the solid at the base of the crucible, respectively. The values of the constants $\kappa_1$, $\kappa_2$, $\kappa_{3n}$ and $\kappa_{4n}$ depend on additional boundary conditions imposed at the top and bottom surfaces of the crucible.

The first boundary condition applies to the top surface of the crucible just below the lid. It is obvious that the vertical flux of $O_2$ must be zero between $r_h \le r \le r_c$ in Figure 5-2. For $0 \le r < r_h$, the concentration of the gas is taken to be constant and the same as the bulk flow, given that the diffusive flux is sufficiently small.

At the gas-solid interface, $z = z_{\max}$, the partial pressure of $O_2$ can be taken as the equilibrium partial pressure, assuming the chemical reaction is must faster than the diffusion in the crucible. However, the exact value of the partial pressure of $O_2$ at the interface is unknown at this stage so that this boundary condition must be transformed. Since the partial pressure of $O_2$ is constant, the Dirichlet boundary condition is equivalent to a Neumann boundary condition: zero radial flux of $O_2$ at the bottom,$J_{r,1}(r,z_{\max})$, because

$$\left.\frac{dy_1}{dr}\right|_{z=z_{\max}} = -\left(\frac{y_2}{cD_{12}} + \frac{y_3}{cD_{13}}\right) J_{r,1}(r, z_{\max}) = 0. \qquad 5\text{-}25$$

Thus the boundary conditions can be expressed as:

$$\begin{cases} J_{z,1}(r,0) = 0 & r_h \le r \le r_c \\ y_3(r,0) = y_{3,bulk} & 0 \le r < r_h \\ J_{r,1}(r, z_{\max}) = 0 & \end{cases} \qquad 5\text{-}26$$

where $y_{3,bulk}$ denotes the mole fraction of species 3, Ar, in the bulk gas above the crucible. $J_{z,1}$ and $J_{r,1}$ are, respectively, the vertical and radial fluxes of species 1, *i.e.* $O_2$.

At this point, it is possible to solve the steady-state diffusion problem numerically. In this work, a pseudo-transient continuation method was applied to a method-of-lines solution of the system where both the special dimensions were discretised. However, it is worth considering an analytical solution to the problem. For the Laplace equation 5-23 with segmented boundary conditions consisting of both Dirichlet and Neumann boundary conditions, the analytical solution is much more difficult to obtain compared with the same equation coupled with either pure Dirichlet or pure Neumann boundary conditions and a special technique called the Wiener-Hopf method (Noble, 1988) is needed for a complete solution. Because the exact values of the unknown coefficients are of secondary interest for the current work, no attempt was made to undertake the

heavy mathematical exercise here. Instead, the nature of those coefficients is illustrated below, using some convenient proxies which can be obtained from the already-solved system.

Suppose that the vertical flux of $O_2$ at the top boundary just below the lid for the solved system is $J_{z,1}(r,0)$, the average flux based on the cross sectional area of the crucible can be expressed as

$$J_{ave} = \frac{\int_0^{r_c} 2\pi r J_{z,1}(r,0)\,dr}{\pi r_c^{\,2}} = \frac{\int_0^{r_h} 2\pi r J_{z,1}(r,0)\,dr}{\pi r_c^{\,2}} \qquad 5\text{-}27$$

since

$$J_{z,1}(r,0) = 0 \qquad\qquad r_h \le r \le r_c .$$

Furthermore, denoting the mole fraction of Ar at the gas-solid interface at the bottom of the crucible as $y_{3,s}$, it can be shown (see Appendix C) that

$$\begin{cases} \dfrac{\kappa_1}{z_{\max}} = \dfrac{J_{ave}}{cD_{13}} \\ \kappa_2 = \ln y_{3,s} - \kappa_1 \\ \kappa_{3n} = -\kappa_{4n} \exp\left(-\omega_n \dfrac{2z_{\max}}{r_c}\right) \\ \kappa_{4n} = -\dfrac{1}{1+\exp\left(-\omega_n \dfrac{2z_{\max}}{r_c}\right)} \dfrac{1}{cD_{13}} \dfrac{\int_0^{r_c} rB_{J,0}\left(\omega_n \dfrac{r}{r_c}\right) J_{z,1}(r,0)\,dr}{\dfrac{r_c\omega_n}{2} B_{J,2}^{\,2}\left(\omega_n \dfrac{r}{r_c}\right)} . \end{cases} \qquad 5\text{-}28$$

and $\kappa_1$ reflects the difference between the average values of ln $y_3$ at the top and bottom of the crucible; $\kappa_2$ is the average value of ln $y_3$ at the top of the crucible. The constants $\kappa_{3n}$ and $\kappa_{4n}$ depend only on the profile of the vertical flux at the inlet. In particular, if the crucible had no lid, then both $\kappa_{3n}$ and $\kappa_{4n}$ would be zero since $J_{z,1}(r,0)$ would be constant across the radius of the crucible and

$$\int_0^{r_c} rB_{J,0}\left(\omega_n \frac{r}{r_c}\right) dr = \left[ rB_{J,1}\left(\omega_n \frac{r}{r_c}\right) \right]_0^{r_c} = 0. \qquad 5\text{-}29$$

### *5.3.2. Numerical solution to the diffusion problem*

The diffusion problem can be solved numerically using a pseudo-transient continuation method. That is, instead of solving the steady state equation 5-21, the

time-dependent version (equation 5-17) is solved for some arbitrary initial conditions until the time $t$ is sufficiently large so that the steady-state profile is obtained. This method is chosen so that the problem can be discretised in both spatial dimensions, $r$ and $z$, to transform the system of PDEs (equations 5-13 and 5-17) into ODEs with $t$ as the only independent variable (known as the method of lines). In this way, the standard ODE solvers (*e.g.* ode15s in MATLAB®) can be used without the need for special PDE solvers.

The system of ODEs involving $t$ stems from equation 5-17. In 2-D cylindrical coordinate with no source term, the system of equations in vector form is

$$c\frac{\partial \underline{y}}{\partial t} = -\left(\frac{1}{r}\frac{\partial\left(r\,\underline{J_r}\right)}{\partial r} + \frac{\partial \underline{J_z}}{\partial z}\right) \qquad 5\text{-}30$$

where $\underline{y}$ is a column vector of the mole fractions of all the gas species involved, $\underline{J_r}$ and $\underline{J_z}$ are the radial and vertical fluxes of each species (not to be confused with $\underline{J_i}$ in equation 5-13, where the vector spans in two spatial dimensions rather than the gas species). Correspondingly, the Stefan-Maxwell equation 5-13 can be written in matrix form as

$$\frac{\partial \underline{y}}{\partial \xi} = \underline{\underline{M}}\,\underline{J_\xi} \qquad 5\text{-}31$$

In which $\xi$ represents either the $r$ or $z$ coordinate. The matrix $\underline{\underline{M}}$ is a square matrix with elements

$$\begin{cases} M_{ij} = \dfrac{y_i}{cD_{ij}} \\ M_{ii} = -\displaystyle\sum_j \frac{y_j}{cD_{ij}} \end{cases} \quad i \neq j\,. \qquad 5\text{-}32$$

Thus the problem can be solved by substituting equation 5-31 into equation 5-30 to eliminate the flux terms. However, the matrix $\underline{\underline{M}}$ is singular so that equation 5-31 cannot be solved by the pre-multiplication of its inverse, $\underline{\underline{M}}^{-1}$.

Nevertheless, in the special case where one gas species is stagnant, *i.e.* the flux of the species is zero everywhere (for convenience, this species is arranged as the last species in the system), the last column of $\underline{\underline{M}}$ is of no consequence because the corresponding flux is constantly zero. In addition, the last row of $\underline{\underline{M}}$ is redundant due to equation 5-16

$$\sum_{i=1}^{n} \nabla y_i = 0 .$$

As a result, for an *n*-component system with at least one stagnant species, only *n*-1 equations need to be considered in each dimension and the corresponding square matrix $\underline{\underline{M}}_{n-1}$, of rank *n*-1, is simply the submatrix of $\underline{\underline{M}}$ dropping the last row and column. Unlike $\underline{\underline{M}}$, $\underline{\underline{M}}_{n-1}$ is not singular so that it can be inverted to yield the flux vectors with *n*-1 components and the missing *n*th component is simply zero, *i.e.*

$$\underline{J_\xi} = \begin{bmatrix} \underline{\underline{M}}_{n-1}^{-1} & 0 \\ 0 & 0 \end{bmatrix} \frac{\partial \underline{y}}{\partial \xi} \qquad \text{5-33}$$

where the zeros are used as a short hand to indicate the last column and last row of the matrix contains only zero entries. Now equation 5-33 can be substituted into equation 5-30 to generate a system of ODEs containing only $y_i$ and *t*. To implement the method of lines, the spatial dimensions *r* and *z* are discretised into segments of appropriate sizes and the spatial derivatives are approximated using the central difference scheme outlined in Appendix D.

The system of ODEs with three components can be solved with the following boundary conditions

$$\begin{cases} J_{z,i}(r,0) = 0 & r_h \le r \le r_c & \text{BC1-1} \\ y_i(r,0) = y_{i,bulk} & 0 \le r < r_h & \text{BC1-2} \\ J_{r,i}(0,z) = 0 & & \text{BC2} \\ J_{r,i}(r_c,z) = 0 & & \text{BC3} \\ y_1(r,z_{\max}) = y_{1s} & & \text{BC4} \\ J_{z,2}(r,z_{\max}) = 0 & & \text{BC5} \end{cases} \qquad \text{5-34}$$

where $y_{i,bulk}$ and $y_{i,s}$ are the mole fractions of species *i* in the bulk gas outside the crucible and that at the gas-solid interface, respectively. The fact that $N_2$ (species 2) is also stagnant is reflect by the zero flux conditions normal to the centreline, side wall and bottom of the crucible (BCs 2, 3 and 5). In BC1-2, although there are three species involved, only one of the mole fractions is independent because the composition of air is fixed so that

$$\frac{y_{1,bulk}}{0.21} = \frac{y_{2,bulk}}{0.78} \qquad \text{5-35}$$

and the mole fraction of Ar at any point can be calculated from the balance

$$y_3 = 1 - y_1 - y_2. \quad \text{5-36}$$

Strictly speaking the BCs 4 and 5 are inaccurate during the transient period. However, this does not affect the steady-state solution because the BCs are exact at steady state. Since the transient profile is not of interest but just a means to acquire the steady-state solution, the choice of the time independent BCs can be justified. For the same reason, any arbitrary initial conditions can be used to calculate the steady-state solution. For convenience, a uniform concentration profile equal to that of the bulk condition throughout the space was used as the initial condition.

It can be easily shown from dimensional analysis that the time scale for diffusion is proportional to $L^2/D_{ij}$ where $L$ is the length scale of the problem. Here, the diameter and the depth of the crucible are both approximately $5\times10^{-3}$ m whereas the binary diffusion coefficients at the temperatures of interest are close to $2\times10^{-4}$ m$^2$/s so that the timescale for diffusion is of the order of 0.1 s. To ensure that the steady-state solution was obtained, the pseudo-transient continuation method was allowed to run until an arbitrarily chosen time, $t$ = 20 s, much larger than 0.1 s.

Since neither $y_{1,bulk}$ nor $y_{1,s}$ is known in general, two additional pieces of information were required experimentally or otherwise to specify the system fully. $y_{1,bulk}$ can be inferred if the flowrates of Ar and Air are known precisely. Alternatively, $y_{1,bulk}$ could be obtained from a calibration experiment in which $y_{1,s}$ was known, *e.g.* the oxidation of Cu to $Cu_2O$ ($y_{1,s} \approx 0$). If the uptake of $O_2$ by the solid at steady state can be measured, for example in a TGA, $y_{1,bulk}$ can be deduced by solving the system iteratively with different values of $y_{1,bulk}$ until the calculated $O_2$ uptake matches the experimental value. Once $y_{1,bulk}$ was obtained, $y_{1,s}$ for the desired reaction, the oxidation of $Cu_2O$ to CuO, could be calculated using a similar iterative method.

## *5.4. Results*

### *5.4.1. The effect of support on equilibrium*

In Section 3.3.2, it was seen that OCs supported on mayenite had two decomposition processes, evident from the two distinctive endothermic peaks as temperature increased, shown in Figure 3-5. This phenomenon is investigated further here. The temperature programmed reaction of fresh OC particles prepared by wet mixing is presented in Figure 5-3.

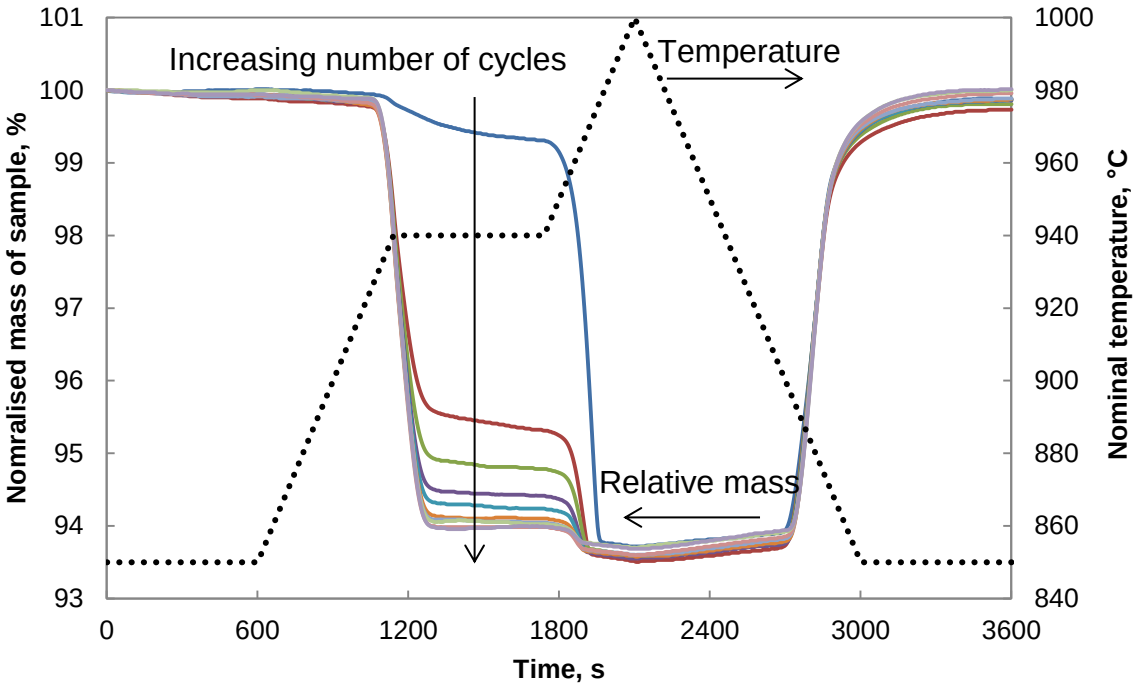


Figure 5-3 The temperature programmed reaction of the fresh OC prepared by wet mixing up to 10 cycles (solid lines). The data were normalised to the initial mass in each experiment for ease of comparison. The corresponding temperature programme is shown on the secondary axis (black dotted line).

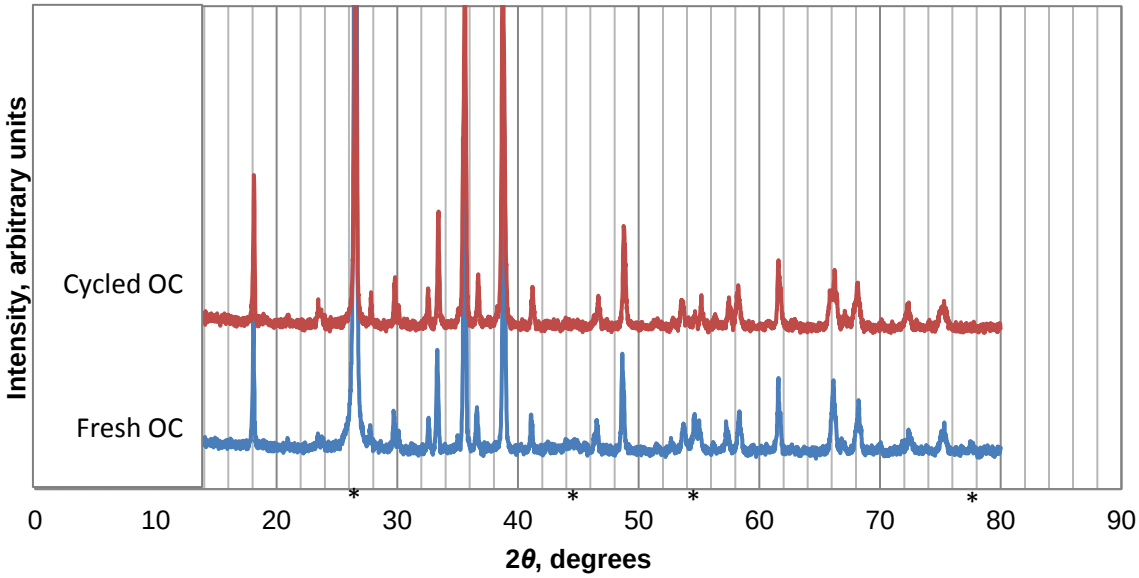


Figure 5-4 XRD patterns of fresh and cycled OCs, mixed with graphite powder as the reference material (with peaks at 26.5°, 54.5° and 77.4°, broad band centred at 44.3°, marked in asterisk (*)).

It is clear from the results that the first decomposition started at around 930°C and a second decomposition started around 950°C. During the isothermal section at 940°C ($t$ = 1200 s to 1800 s), no significant reaction was observed from the 3rd cycle onwards. Furthermore, the proportion of material decomposing at the lower temperature increased significantly over cycling and the proportion stabilised after 5 cycles of reaction. However, the change in decomposition temperature of the sample cannot be attributed to a phase change since the XRD patterns of the fresh and cycled OCs are identical and no extra phases could be identified in Figure 5-4.

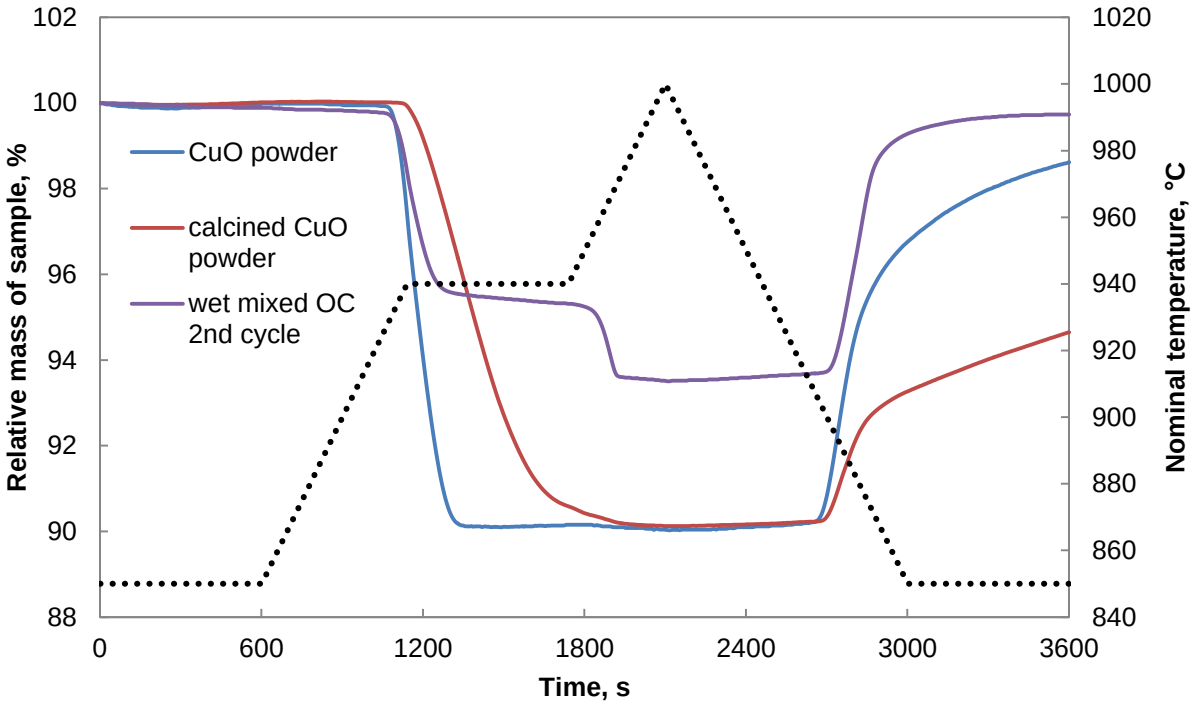


Figure 5-5 The temperature programmed reaction of calcined (red line) and un-calcined (blue line) CuO powder in comparison with the supported OC (purple line, data shown is from the 2nd cycle in Figure 5-4). The data were normalised to the initial mass in each experiment for ease of comparison. The corresponding temperature programme is shown on the secondary axis (black dotted line).

It is possible that the calcination of the OC at 1000°C annealed the material so that the defects in the CuO lattice were reduced significantly, causing the material to be more stable and therefore decomposed at a higher temperature. To verify whether this was the case, some as-received CuO powder was thermally treated in the same way as the supported OC - calcined at 1000°C for 6 hours in air – and the resulting powder subjected to the same temperature programme for comparison. Results are shown in Figure 5-5. Although the calcined CuO powder decomposed at a slightly higher temperature compared to the powder without the heat treatment, the material

decomposed completely during the isothermal section at 940°C and no secondary decomposition was observed. Thus, the behaviour cannot be explained by the annealing of material during calcination.

Another possible explanation for the shift in equilibrium temperature over cycling is that the CuO could interact with the support at the interface without a phase change and as a result the chemical potential of oxygen in the solid was altered slightly, causing a shift in equilibrium temperature.

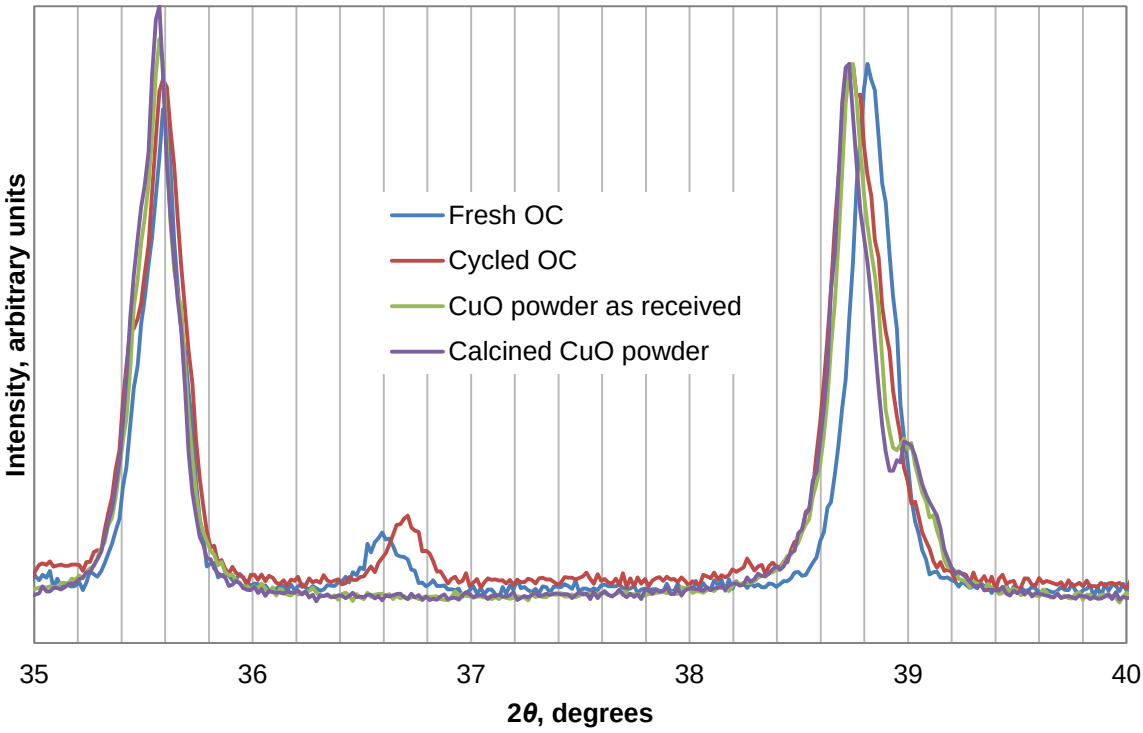


Figure 5-6 Section of the XRD patterns of different materials between 35° and 40° measured in 2$\theta$.

This explanation is partly supported by the XRD analysis when the relative peak positions of CuO from different materials (as-received CuO, calcined CuO, fresh OC prepared by wet mixing and cycled OC) were examined more closely, as shown in Figure 5-6. For better comparison, graphite powder was added to all the samples as a reference and the strong peak at 2$\theta$ = 26.5° was used to correct for systematic shifts in angle between experiments. After the correction, it was found that most of the major peaks of CuO present in different samples differ by one or two stepsizes (each stepsize was 0.0167°) in the experiments, and can be attributed to random errors alone. For example, in Figure 5-6 the major peak of CuO around 35.6° (corresponding to $(\bar{1}11)$ plane) from all the materials was located at either 35.57° or 35.59°, one step size away. However, the (111) peak of CuO from the fresh OC was seen at 38.82°, 5 steps away

from the corresponding peak from the other materials, which were detected within one step size of 38.73° (although the origin of the small peak close to $2\theta = 39°$ in the pure CuO samples is unclear). Similarly, the $(\bar{2}02)$ peak of the CuO from the fresh OC shifted to a lower value of $2\theta$ by about 0.15° compared to that from the as-received and calcined CuO powders whereas the same peak from the cycled OC shifted by about 0.04°, or 3 stepsizes, as shown in Figure 5-7.

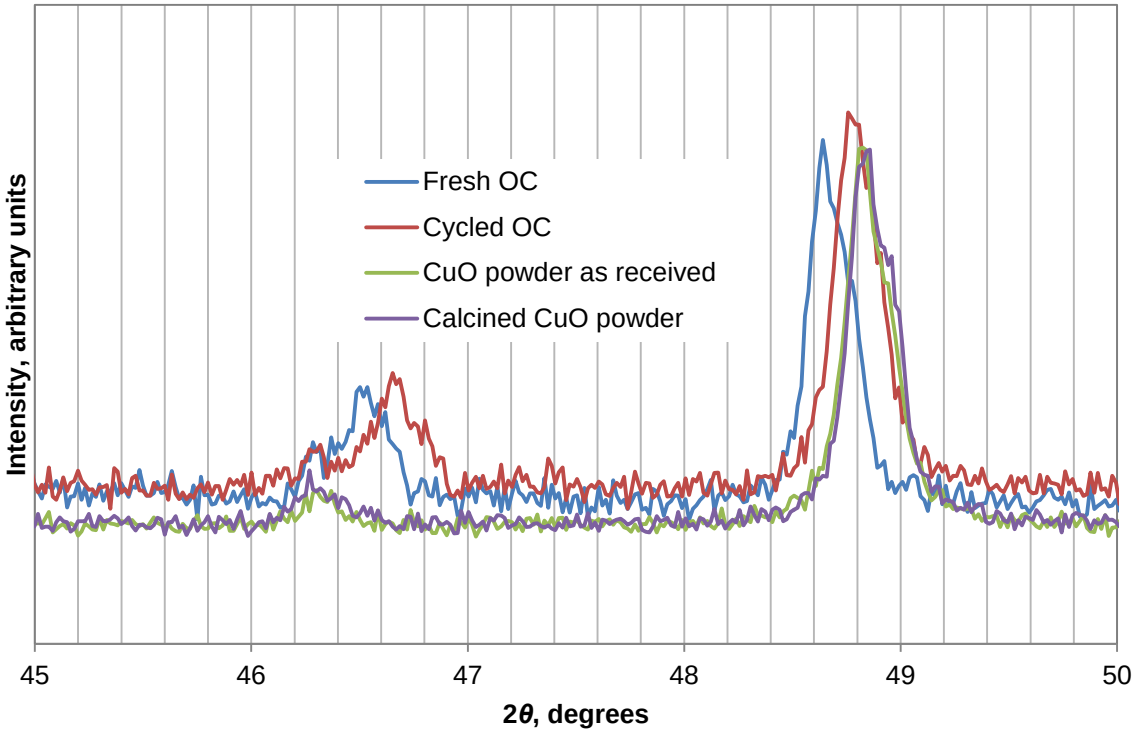


Figure 5-7 Section of the XRD patterns of different materials between 45° and 50° measured in $2\theta$.

These shifts are too large to be caused by random errors during measurements and only occur for particular peaks but not throughout the diffraction pattern and cannot be due to systematic errors. Therefore, it can be concluded with confidence that the shifts correspond to the contraction (in the case of the $(\bar{1}11)$ plane) or expansion (in the case of the $(\bar{2}02)$ plane) of the inter-planar distance of the CuO lattice in particular directions. The change in lattice parameters of the CuO phase in the fresh OC (but less so in the cycled OC) correlates well with the shift in equilibrium temperature and it is conceivable that there are causal links between these observations.

The shift in peak position can be further associated with the presence of calcium aluminates, most likely mayenite, because it is the major phase present in the OC. As seen in Figure 5-6 and Figure 5-7, the peaks associated with the mayenite phase

(around $2\theta$ = 36.6° and 46.6°) shifted towards higher values of $2\theta$ in the cycled OC and the difference increased with increasing values of $2\theta$ and thus was not due to systematic errors. This suggests that the unit cell of mayenite contracted in all directions after cycling. On the other hand, $Al_2O_3$ is not responsible for the peak shift since none was observed from the fresh and cycled OCs with $Al_2O_3$ as support investigated in Chapter 3 when the same analysis was performed; similarly, CuO samples doped with up to 5 mol% CaO did not show any peak shift in the CuO phase. Here, the doped samples were prepared by the addition of an appropriate amount of CuO powder to an aqueous solution of $Ca(CH_3COO)_2$ and stirred on a hotplate with a magnetic stirrer until dry. The resulting powder was calcined at 1000°C for 6 hours before the XRD analysis. In fact, at a doping level of 5 mol% CaO, additional peaks corresponding to $CaCu_2O_3$ was observed but the CuO phase was not affected.

### *5.4.2. The influence of solid conversion on equilibrium*

Since the fresh OC behaves differently from the cycled materials, a batch of OC was pre-treated (fully reduced in 5 vol% $H_2$ balance $N_2$ and then re-oxidised in air at 850°C for 3 times in a fluidised bed) so that the majority of the CuO present in the OC would decompose at the lower temperature, comparable to pure CuO and subsequent experiments were performed using the same batch of pre-treated OC.

For the first batch of samples where decomposition was complete before re-oxidation, exemplified by the experiment with a final cooling rate of 2°C/min shown in Figure 5-8, the temperature at which re-oxidation occurred was rather low, around 900°C as determined from the exothermic heat flow measurement (SDTA signal). The onset temperatures for re-oxidation of samples cooled at different rates are summarised in Table 5-1.

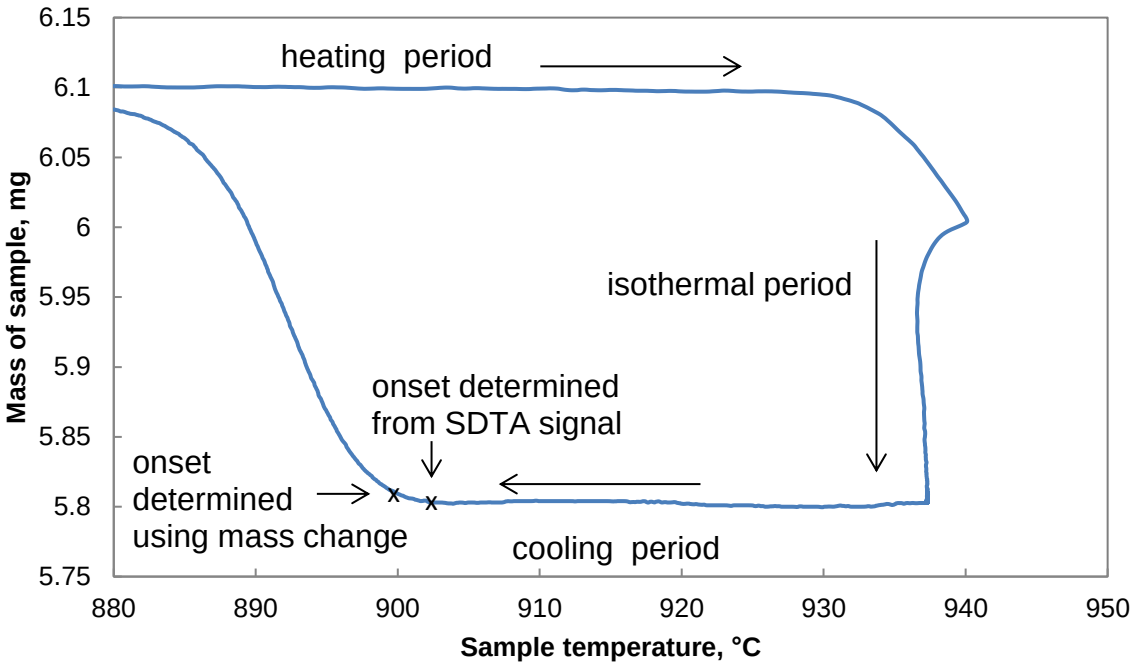


Figure 5-8 Temperature programmed reaction profile of the pre-treated OC. Sample fully decomposed followed by re-oxidation during cooling period with a rate of 2°C/min. The temperature programme is annotated in the figure.

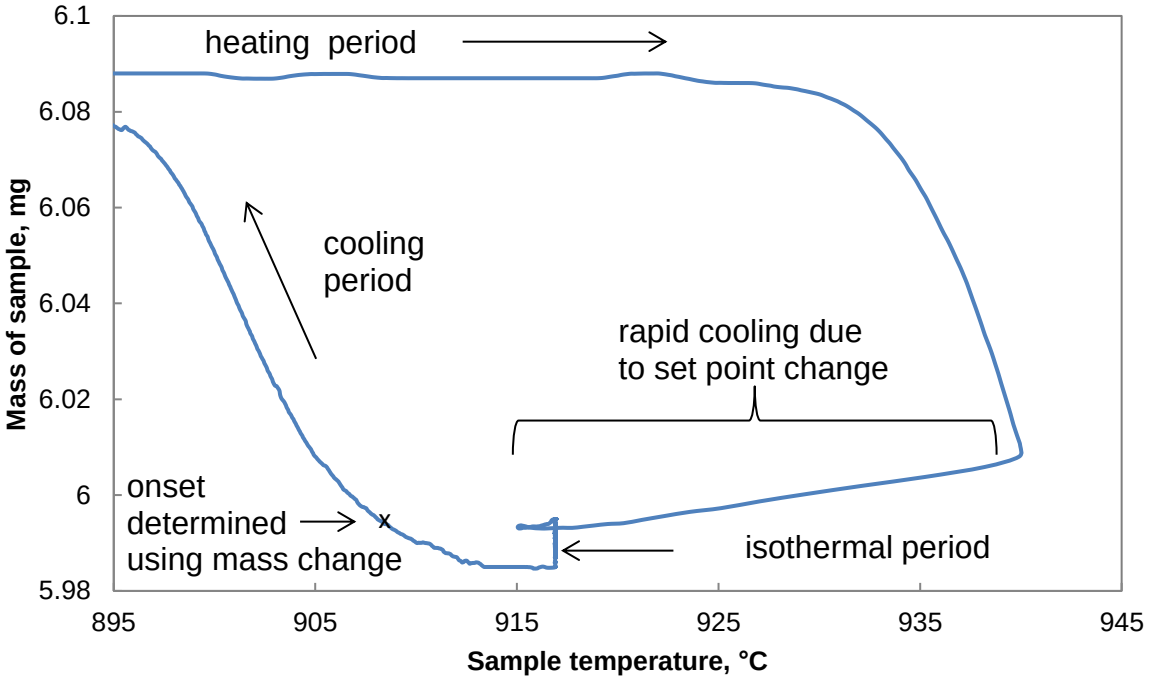


Figure 5-9 Temperature programmed reaction profile of the pre-treated OC. Sample partly decomposed followed by re-oxidation during cooling period with a rate of 2°C/min. The temperature programme is annotated in the figure.

For the second batch of samples which were only partly decomposed, the onset temperatures were found to be higher, as shown in Figure 5-9. Unfortunately, the onset temperatures cannot be determined by SDTA signal in this case since the amount of material available for re-oxidation was too little to cause a significant temperature change. Thus the onset temperatures were estimated as the sample temperature at which point the mass of the sample had increased by 0.010 mg compared to the mass of the sample at the end of the isothermal section. For comparison, the same method was applied to the data obtained from the first batch and presented in Table 5-1.

**Table 5-1 Estimates of the onset temperature of re-oxidation in a fixed atmosphere for fully decomposed and partly decomposed OC.**

| Cooling rate used, °C/min | Re-oxidation temperature for the fully decomposed batch determined from SDTA, °C | Re-oxidation temperature for the fully decomposed batch determined from mass change, °C | Re-oxidation temperature for the partly decomposed batch determined from mass change, °C |
|---|---|---|---|
| 1 | 904.5 | 902.5 | 911.5 |
| 2 | 902.5 | 899.5 | 908.5 |
| 5 | 902.5 | 896.5 | 905.0 |
| 10 | 895.0 | 889.5 | 902.0 |
| 20 | 891.0 | 884.5 | 896.0 |

Several conclusions can be drawn from the results in Table 5-1. Firstly, the onset temperatures of the partly decomposed batch were systematically higher than those of the fully decomposed batch by about 10°C across all cooling rates. Although a mass change threshold was necessary to determine the onset temperatures, meaning that the onset temperatures were inevitably underestimated, it can be expected that the true onset temperatures would differ to a similar extent, given the consistent difference in the estimates. Secondly, regardless of the methods used, the onset temperatures of re-oxidation decreased as the cooling rate increased. This observation is primarily due to the finite rate of reaction compared to the rate of change of temperature, especially close to the equilibrium position, and this is commonly encountered in thermal analysis. Thus, the results obtained using a lower ramp rate of temperature are more accurate. Lastly, the SDTA signals yielded a higher onset temperature. In conjunction with Figure 5-8, it would appear that the SDTA measurement produced a better estimate of the onset temperature: the mass of the sample remained largely constant before the determined point and started to change immediately after. Hence, when determining the onset temperature of a reaction, the SDTA signal should be used instead of mass changes whenever possible.

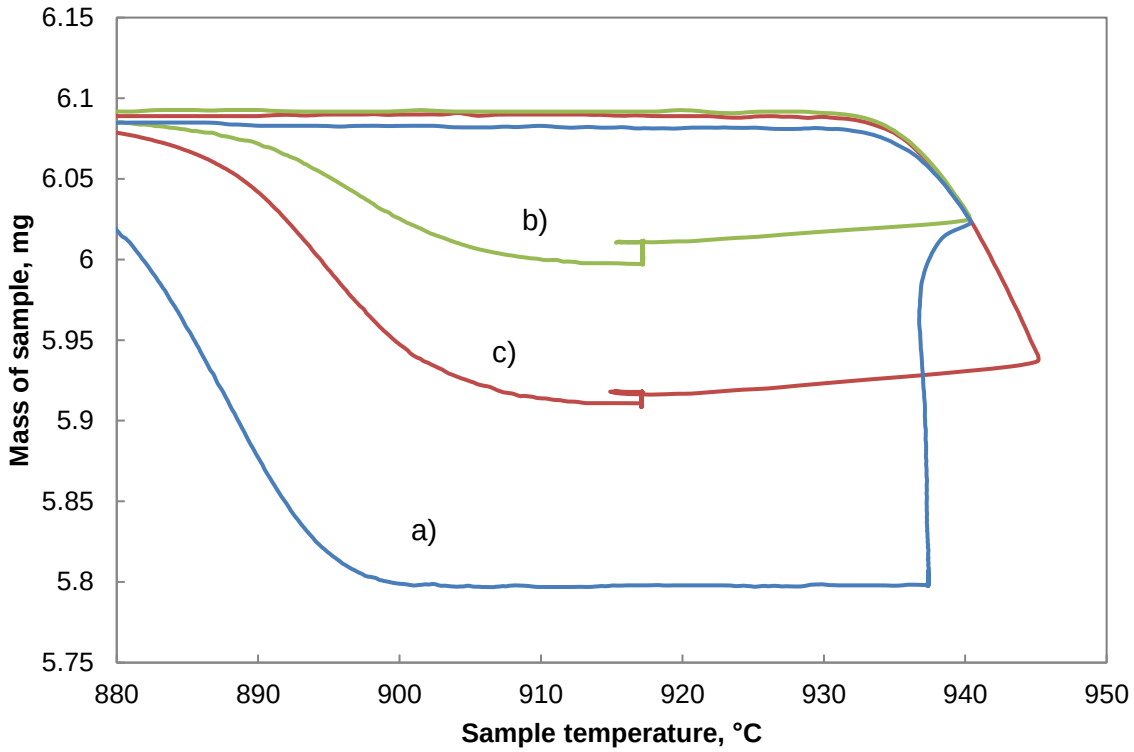


Figure 5-10 Temperature programmed reaction profile of the pre-treated OC. Samples decomposed to different extent before being re-oxidised in the cooling period with a rate of 5°C/min. a) fully decomposed (first batch, blue line); b) partly decomposed (second batch, green line); c) extent of decomposition is approximately half way between samples a) and b) (red line).

To investigate whether the degree of conversion has any effect on the onset temperature, a separate sample of the pre-treated OC was subjected to a similar temperature programme as the samples in the second batch except that the heating period terminated at 945°C instead to achieve a higher degree of decomposition. The re-oxidation was done with a cooling rate of 5°C/min and the onset temperature of the reaction was compared with the corresponding samples from the first and second batch of experiments, as shown in Figure 5-10.

The onset temperatures determined from the mass change using different threshold values are presented in Table 5-2. Despite the fact that the extent of decomposition of sample c) was approximately twice that of sample b), the onset temperatures of the re-oxidation was very close whereas the onset temperature of the completely decomposed sample a) was approximately 10°C lower irrespective of the threshold values chosen.

**Table 5-2 Onset temperatures for the re-oxidation of samples reduced to different extent**

| Sample number as used in Figure 5-10 | Onset temperature with threshold 0.010 mg, °C | Onset temperature with threshold 0.005 mg, °C | Onset temperature with threshold 0.003 mg, °C |
|---|---|---|---|
| a) | 896.5 | 898.0 | 899.0 |
| b) | 905.0 | 908.0 | 910.0 |
| c) | 906.5 | 908.5 | 910.5 |

Such behaviour can be explained in terms of nucleation. Whether the transformation of $Cu_2O$ to CuO occurs thermodynamically depends on the change in Gibbs free energy of the system. When the first nucleus of CuO forms within $Cu_2O$ the corresponding change in Gibbs free energy of the system is a combination of the Gibbs free energy of reaction 5-1 and the additional surface energy due to the creation of the CuO-$Cu_2O$ interface. The Gibbs free energy of reaction is proportional to the amount of CuO produced, which scales with the volume of CuO which in turn has a cubic dependence on the radius of the CuO crystal; whereas the total surface energy scales with the interfacial area which depends on the radius quadratically. As a result the contribution from surface energy is only significant at the initial stage of the transformation when the radius of the newly formed phase, CuO, is small.

Consequently, during the initial stage of the oxidation reaction where the starting phase is pure $Cu_2O$, a larger oversaturation, or concentration driving force of $O_2$ in this particular case, is required to initiate the reaction and the necessary concentration driving force can be lower if some CuO is present. In a temperature programmed reaction with a fixed $P_{O2}$, this means that the onset temperature for the oxidation will be lower if the OC was completely reduced to $Cu_2O$ prior to the oxidation compared to the case where the OC was only partly reduced.

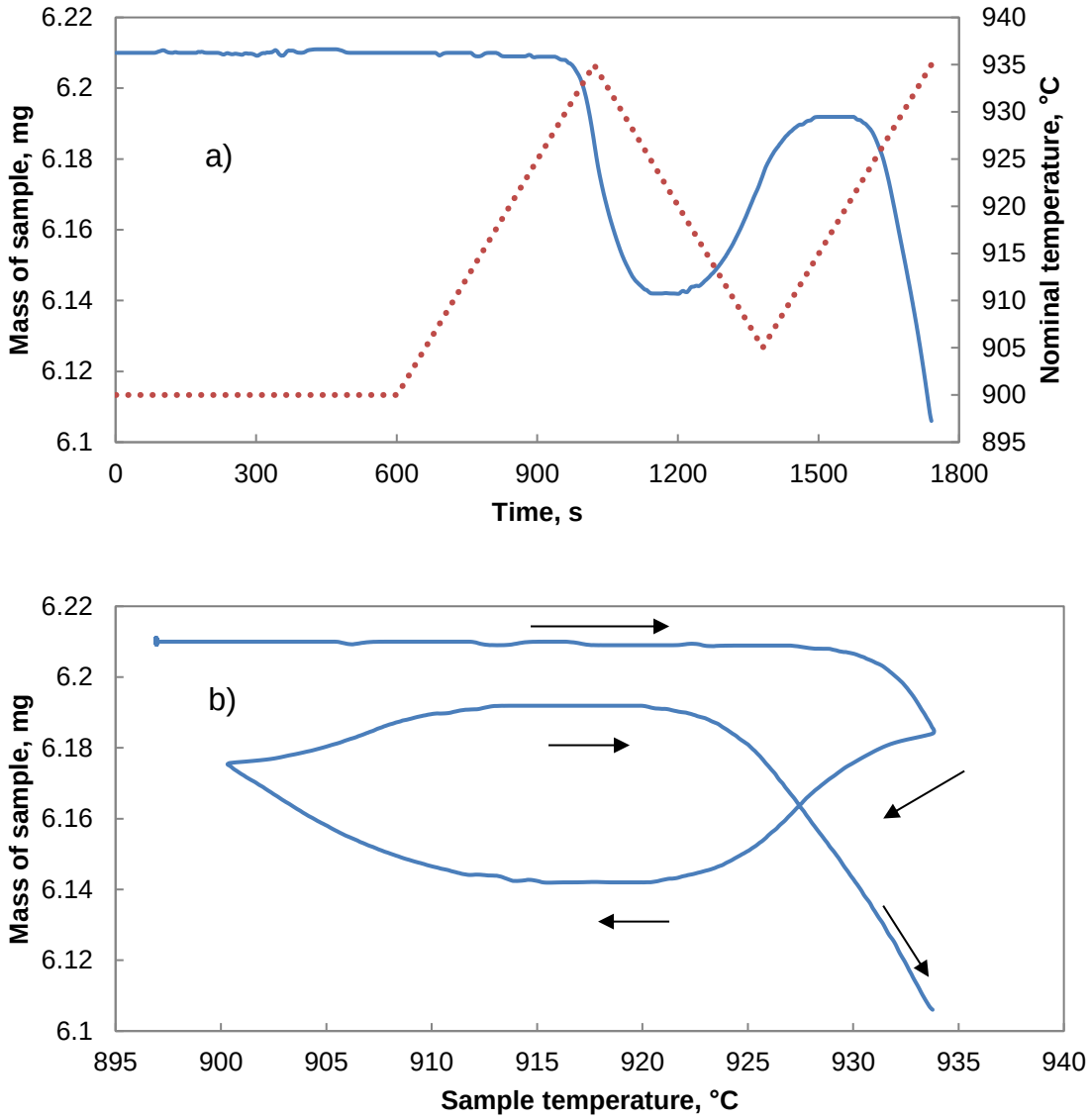


Figure 5-11 Temperature programmed reaction of pre-treated OC for partial redox reaction. a) The reaction profile plotted against time. Mass of the sample is represented by the blue solid line using the primary axis on the left; the temperature programme is shown as the red dotted line using the secondary axis. b) The same reaction profile plotted against sample temperature and the progression of the experiment with time is indicated by the arrows.

Conversely, the decomposition of CuO would occur at a higher temperature if only pure CuO were present compared to the case where both CuO and $Cu_2O$ were present. This was confirmed in the temperature programmed reaction shown in Figure 5-11 (b), where clearly the fully oxidised sample started to decompose at ~930°C but the decomposition did not stop until the sample was cooled to ~920°C. Furthermore, when the subsequent oxidation of the sample was incomplete (0.018 mg away from full oxidation, or 95.2% completion based on the nominal composition of the OC), the

onset of the decomposition was also ~920°C, comparable to the temperature at which point the previous decomposition stopped.

### 5.4.3. Isothermal investigations using the diffusion method

#### 5.4.3.1. Proof of concept

Firstly the oxidation of the reduced OC (cycled for 5 times prior to use) in a fixed atmosphere was investigated at different temperatures between 700°C to 925°C to validate the diffusion method described earlier in the chapter.

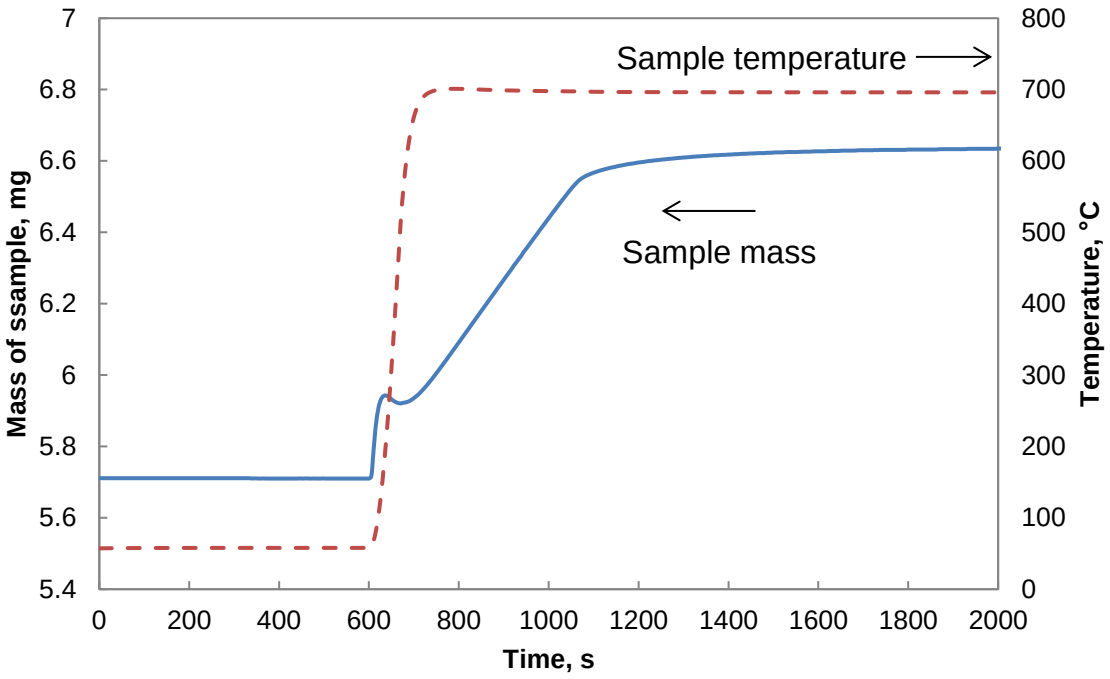


Figure 5-12 the reaction profile (blue solid line) of the oxidation of the reduced OC (in Cu form) at 700°C in a constant atmosphere. The atmosphere was a mixture of Ar and air containing approximately 1.5% $O_2$ by volume. The temperature of the sample was maintained at 50°C for 600 s followed by a set point change to 700°C. The sample temperature is shown on the secondary axis as the red dashed line.

The profile of the oxidation at 700°C is shown in Figure 5-12. The reduced sample was held at 50°C for 10 minutes prior to a set point change in temperature to 700°C. The disturbance of the mass of the sample shortly after the set point change ($t$ = 600 s) was the result of the changing buoyancy effect due to a change in temperature in combination. Also, there was some oxidation of the Cu to a small extent by the oxygen present inside the crucible as the sample temperature increased. About 200 s after the change in temperature, when the sample temperature was constant and a steady

diffusion profile had been established, the rate of mass change of the sample remained constant until the very last stage of the reaction where the rate of reaction was slow enough that the diffusion process within the crucible was no longer rate limiting.

The change in mass can be interpreted more easily when the buoyancy effect is corrected by means of a control experiment without the OC sample but otherwise identical to the actual experiment. The result is shown in Figure 5-13.

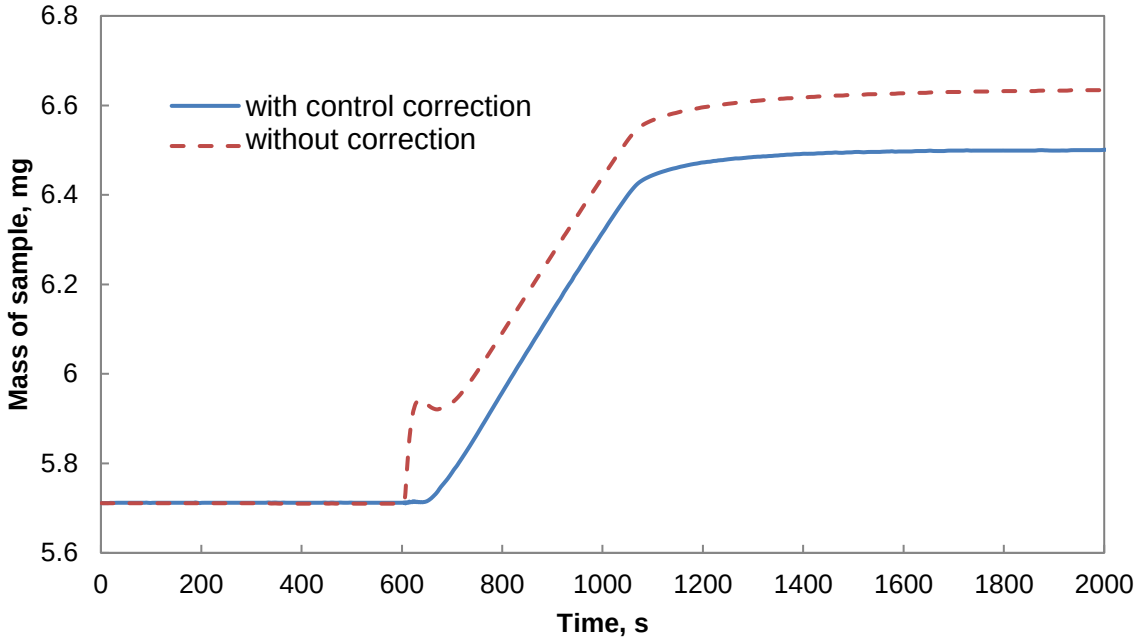


Figure 5-13 Control corrected reaction profile of the oxidation of the reduced OC (in Cu form) at 700°C in a constant atmosphere (blue solid line) compared to the profile without control correction (red dashed line).

The mass change calculated from the control experiment was 0.788 mg, in good agreement with the expected mass change for the full conversion of Cu to CuO based on the nominal composition of the carrier, calculated to be 0.778 mg. At this temperature, it was not possible to distinguish whether Cu was oxidised directly to CuO or to CuO *via* $Cu_2O$ as an intermediate. Since the equilibrium partial pressure of $O_2$, $P_{eq}$, for the reaction 5-1 is close to zero at temperatures below 800°C, in the mass transfer limit, no discernible change in the rate of reaction could be observed even if the intermediate step were involved, since the concentration driving force for the diffusion process remained largely unchanged.

However, at higher temperatures where $P_{eq}$ is significant, the stepwise oxidation of $Cu \rightarrow Cu_2O \rightarrow CuO$ becomes apparent. At 850°C, the reaction profile was similar to

that at 700°C except that two distinctive rates of reaction could be identified. As shown in Figure 5-14, the rate of oxidation slowed down abruptly from point *A* onwards. The mass changes before and after point *A* were 0.390 mg and 0.404 mg, or 49.1% and 50.9% of the total mass change, respectively. The fact that the mass change at point *A* was close to 50% suggests that the second segment of the oxidation was largely due to $Cu_2O$ with a small amount of unreacted Cu being oxidised, too, and the oxidation before point *A* can be attributed to the oxidation of Cu to $Cu_2O$.

Therefore, solving the diffusion problem outlined in Section 5.3 numerically, the mole fraction of $O_2$ in the bulk atmosphere could be calculated from the rate obtained from the first linear region, before point *A*, since the mole fraction of $O_2$ at the gas-solid interface can be taken as zero (due to the low value of $P_{eq}$ for the oxidation of Cu to $Cu_2O$) in the diffusion controlled limit. In turn, the equilibrium mole fraction of $O_2$ for the oxidation of $Cu_2O$, and by extension $P_{eq}$, can be calculated using the rate obtained from the second linear region once the bulk composition is known. The results are described in Section 5.4.3.2, below.

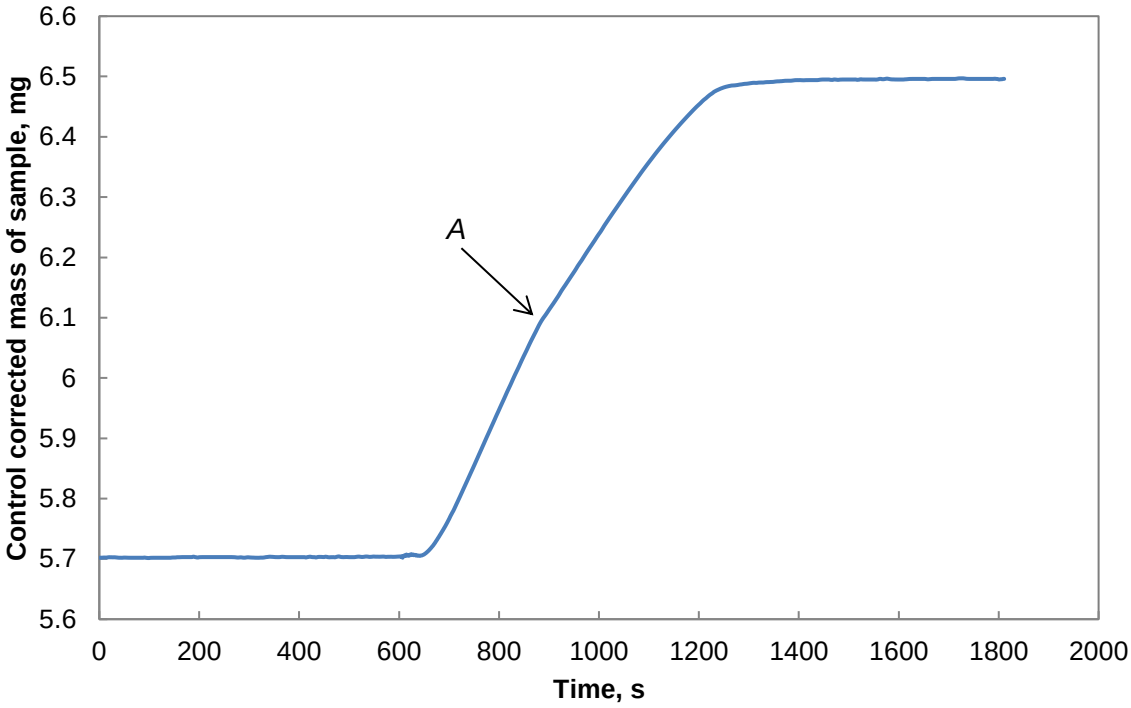


Figure 5-14 Control corrected reaction profile of the oxidation of the reduced OC (in Cu form) at 850°C in a constant atmosphere. The atmosphere was a mixture of Ar and air containing approximately 1.5% $O_2$ by volume.

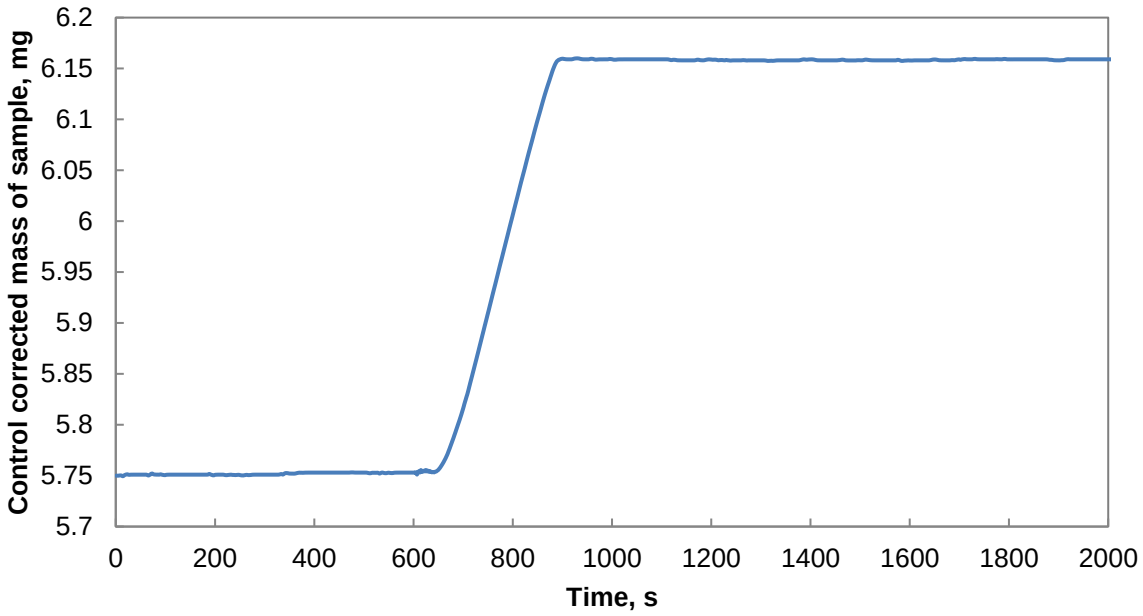


Figure 5-15 Control corrected reaction profile of the oxidation of the reduced OC (in Cu form) at 925°C in a constant atmosphere. The atmosphere was a mixture of Ar and air containing approximately 1.5% $O_2$ by volume.

At even higher temperatures, *e.g.* 925°C, $P_{eq}$ is higher than the partial pressure of $O_2$, $P_{O2}$, in the environment and Cu can only be oxidised to $Cu_2O$: the result is shown in Figure 5-15, which shows no changes in rate.

A subtle point which deserves attention is that the oxidation of Cu to $Cu_2O$ stopped abruptly at $t \approx 900$ s in Figure 5-15. In contrast, the reaction slowed down much more smoothly towards the end in previous cases where full oxidation was achieved. The difference suggests that the oxidation of Cu to $Cu_2O$ is probably zeroth order with respect to the solid, *i.e.* the conversion function $f(X)$ is constant and can be taken as unity whereas the oxidation of $Cu_2O$ does depend on conversion so that the rate of reaction slowed down at high values of $X$. Based on this hypothesis, it can be further deduced that a significant amount of $Cu_2O$ was present as the reaction intermediate during the oxidation of the OC at 700°C even though no change of rate was observed between the successive oxidations.

### *5.4.3.2. Quantitative determination of $P_{eq}$*

Whilst the above results suggest that the diffusion method can be used for the determination of $P_{eq}$, the experimental procedure was improved to obtain more accurate results for analysis, as described in this section. In particular, the value of $P_{O2}$

in the bulk atmosphere was kept constant in the initial investigations for convenience whereas it would be more sensible to adjust $P_{O2}$ according to temperature so that, at each temperature, the rate of oxidation of $Cu_2O$ to CuO was always low. Furthermore, it can be seen from Figure 5-12 that more than 200 s was needed for the sample to reach the reaction temperature from 50°C. Thus, for more consistent results, the sample was kept in an Ar atmosphere at the beginning of a new experiment and air was only introduced 5 minutes after the set point change in temperature to ensure that the sample temperature was not changing significantly during the reaction phase. The experimental arrangement was, otherwise, identical to that used in the initial investigations described above.

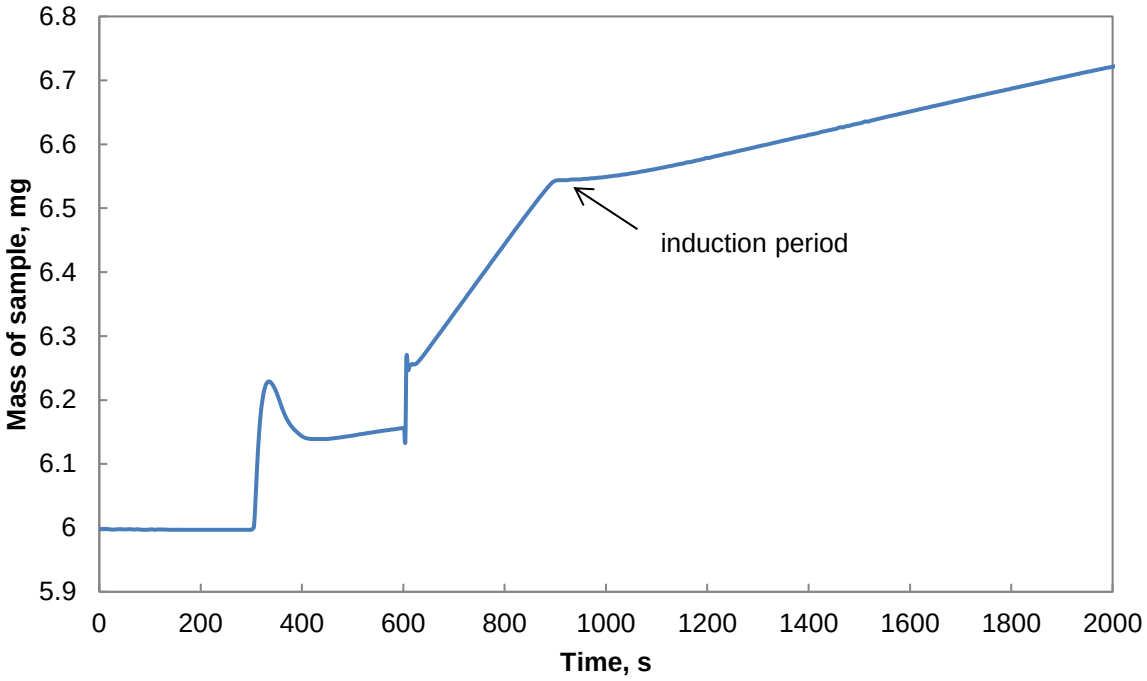


Figure 5-16 The reaction profile (without control subtraction) of the oxidation of the reduced OC (in Cu form) at 875°C. The temperature of the sample was maintained at 50°C in Ar for 300 s followed by a set point change to 875°C. Air was introduced into the purge gas stream at $t$ = 600 s.

The experiment performed at 875°C is presented in Figure 5-16 to illustrate the salient points of the experiments. Since the temperature of the sample would have settled down when air was introduced at $t$ = 600 s, unlike the previous experiments, the buoyancy effect due to change in temperature was not important and a control correction was not necessary. It can be seen from Figure 5-16 that oxidation occurred to a slight extent between $t$ = 500 and 600 s and this was due to a small amount of ambient air leaking into the furnace chamber, giving rise to a concentration of oxygen

up to 0.1 vol% in the furnace when inert gas was used – a known problem with the TGA/DSC1. The disturbance in the measured mass of sample at $t$ = 600 s was due to the added air stream, to supply oxygen for reaction, disturbing the microbalance. The rates of oxidation from Cu to $Cu_2O$ and from $Cu_2O$ to CuO were largely constant and the two rates were extracted to calculate the bulk mole fraction of $O_2$ in the vicinity of the hole in the crucible and $P_{eq}$, respectively, for each of the experiments. In contrast with the proof-of-concept experiments (*e.g.* Figure 5-14), an induction period, where the mass of the sample did not change significantly, was visible during the transition between the two oxidation reactions from $t$ = 900 s to 950 s. This induction period can be attributed to the relatively small driving force (or 'oversaturation') for the oxidation of $Cu_2O$ resulting in a slow nucleation process.

The equilibrium partial pressures, $P_{eq}$, calculated from the rates of oxidation obtained from the series of experiments are summarised in Table 5-3, below. Here, $T_{nominal}$ is the reference temperature used to set up the TGA programme, $T_{ave,1}$ and $T_{ave,2}$ are the measured sample temperatures averaged over the first and second linear regions (for a 60 s interval in each region) respectively; $y_{1,bulk}$ is the mole fraction of $O_2$ in the bulk gas calculated using the measured $T_{ave,1}$ and the corresponding mass gain. $y_{1,s}$ is the mole fraction of $O_2$ at the gas-solid interface calculated using the measured $T_{ave,2}$ and the corresponding mass gain, as well as the calculated value of $y_{1,bulk}$; $P_{eq}$ can be calculated by multiplying $y_{1,s}$ by the total pressure of the system, 1 atm or 1.01 bar.

**Table 5-3 Summary of the experimentally measured temperatures and calculated mole fraction of $O_2$ at points of interest**

| $T_{nominal}$, °C | $T_{ave,1}$, °C | *Calculated* $y_{1,bulk}$ | $T_{ave,2}$, °C | *Calculated* $y_{1,s}$ | $P_{eq}$, bar |
|---|---|---|---|---|---|
| 850 | 848.85±0.13 | 0.00740 | 848.13±0.01 | 0.00471 | 0.00477 |
| 875 | 874.21±0.18 | 0.00926 | 873.32±0.01 | 0.00770 | 0.00780 |
| 900 | 900.01±0.19 | 0.0134 | 898.40±0.01 | 0.0130 | 0.0132 |
| 925 | 925.74±0.09 | 0.0248 | 923.90±0.05 | 0.0209 | 0.0212 |
| 950 | 950.59±0.12 | 0.0416 | 948.26±0.11 | 0.0355 | 0.0360 |

It can be seen that the value of $P_{eq}$ for the CuO/$Cu_2O$ system changed by approximately one order of magnitude from 850°C to 950°C which implies that very precise control of temperature is required in practice to maintain stable operation. The rapid change of $P_{eq}$ with temperature is due to the relatively high enthalpy of reaction

for the oxidation reaction in the temperature range concerned since the value of $P_{eq}$ is equal to the equilibrium constant of the reaction, which in turn depends on the Gibbs free energy of the reaction (similar to equation 5-3). Assuming that the enthalpy and entropy of reaction remain constant in this temperature interval, equation 5-3 can be expressed as

$$P_{eq} = K = \exp\left(\frac{-\left(\Delta H_r - T\Delta S_r\right)}{RT}\right) = \exp\left(\frac{\Delta S_r}{R}\right)\exp\left(\frac{-\Delta H_r}{RT}\right) \qquad 5\text{-}37$$

where $\Delta H_r$ and $\Delta S_r$ denote the enthalpy and entropy of the *reduction reaction*, respectively. Equation 5-37 takes an Arrhenius form with $\Delta H_r$ being equivalent to the activation energy and $\Delta S_r$ being related to the pre-exponential factor. Thus the values of $\Delta H_r$ and $\Delta S_r$ can be estimated from a plot of $\ln P_{eq}$ against 1/T, as shown in Figure 5-17.

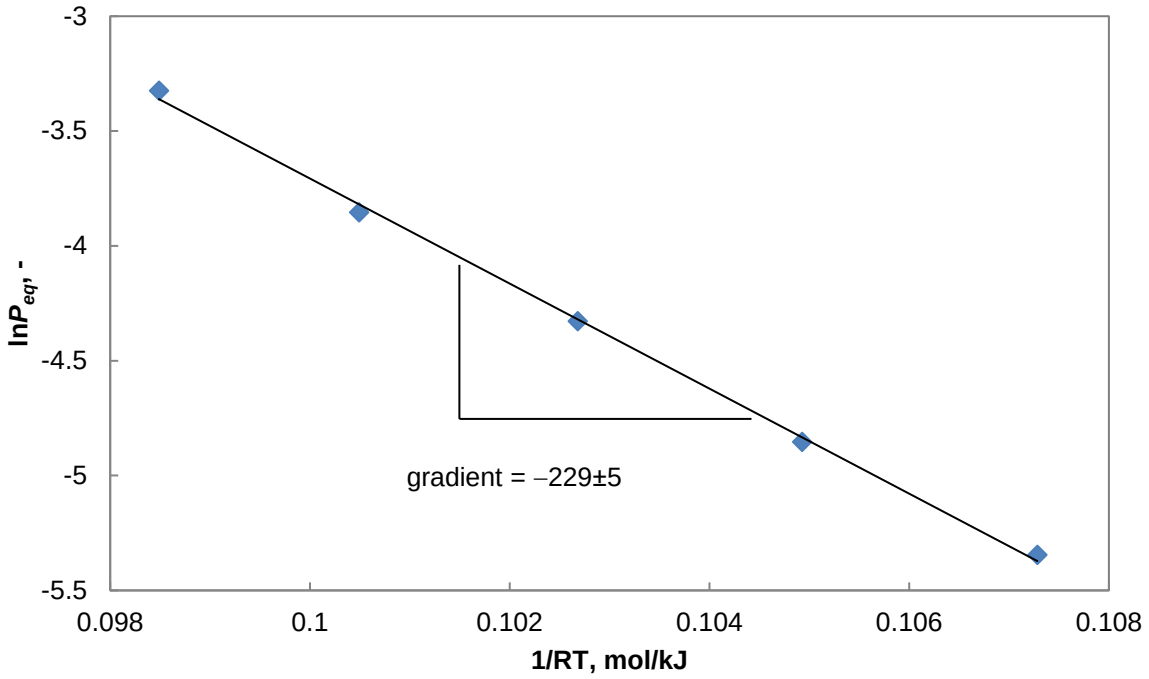


Figure 5-17 Plot of $\ln P_{eq}$ against 1/RT using data from Table 5-3. The gradient of the plot yields the negative of the enthalpy of reaction for the reduction of CuO to $Cu_2O$ in kJ/mol. The *y*-intercept of the plot yields $\Delta S_r/R$ from which the entropy of reaction can be calculated.

From a least-squares fit of the results, the value of $\Delta H_r$ was found to be 229 kJ/mol for the reduction with a standard error of 5 kJ/mol (equivalent to an enthalpy of reaction of -229 kJ/mol for the oxidation) and the corresponding value for $\Delta S_r$ was calculated to be 159 J/mol/K. In comparison, the values for pure CuO in the same

temperature range are 261 kJ/mol and 188 J/mol/s according to Jacob and Alcock (1975) and 263 kJ/mol and 188 J/mol/s from NIST database (NIST, 2011).

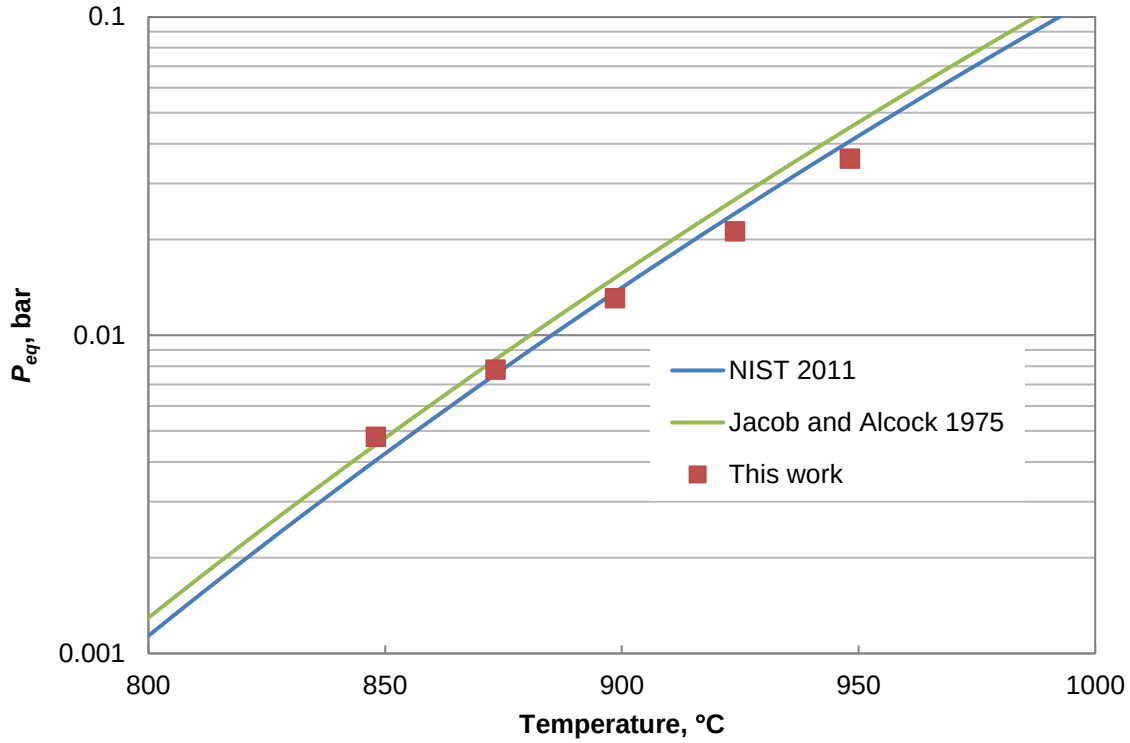


Figure 5-18 Comparison between the values of $P_{eq}$ measured in this work and values obtained from literature.

Both the $\Delta H_r$ and $\Delta S_r$ measured from this work are approximately 15% lower than the values commonly used for pure CuO. This is expected because the CuO sample used was not particularly pure (>98%) and the support in the OC might have influenced the oxygen chemical potential of the $CuO/Cu_2O$ to some extent. However, the measured $P_{eq}$ are close to the literature values in the temperature range investigated - especially so when compared with the NIST data - as can be seen from Figure 5-18. The discrepancy between the measured and reference values could be even smaller when the following factors are considered. Firstly, the rate of chemical reaction may not be sufficiently fast for the reaction to be fully mass transfer controlled, especially at the low temperature end. From the kinetic studies to be discussed in the following Chapter 6, it can be estimated that the rate of chemical reaction is approximately 10 times faster than the rate of mass transfer inside the crucible, thus the values of $P_{eq}$ calculated in Table 5-3 would have overestimated the true values by approximately a tenth of the concentration driving force. This overestimate is more significant at low

temperature since the value of $P_{eq}$ is comparable to the concentration difference between the bulk gas and the surface of the OC particles in this case whereas at higher temperatures, such as 950°C, the value of $P_{eq}$ is much higher than the concentration difference so that the percentage error is much smaller. Secondly, the calculated value of $y_{1,bulk}$ was assumed to be constant throughout the reaction. This assumption is only valid if the diffusion of gas into the crucible is negligible compared to the flow of gas outside the crucible and the assumption gets worse as temperature increases because the bulk concentration increases exponentially. Hence the rate of diffusion during the oxidation of Cu to $Cu_2O$ can be rather fast at higher temperatures. On the other hand, the oxidation of $Cu_2O$ to CuO was controlled to be relatively slow at all temperatures. As a result, at 950°C, and even 925°C, the value of $y_{1,bulk}$ measured from the first oxidation would underestimate the true value during the second oxidation, leading to an underestimate of $y_{1,s}$ and $P_{eq}$. When taking these factors into account, it is expected that the true values of $P_{eq}$ for the OC would be closer to those of pure CuO than as presented in Figure 5-18 and the data from the NIST database can therefore be used to calculate $P_{eq}$ of the OC for practical purposes without excessive error.

## *5.5. Discussion*

It is evident from the results presented above that the equilibrium concentration of $O_2$, $P_{eq}$, of the reversible reaction 5-1,

$$4CuO \underset{k_{-1}}{\overset{k_1}{\rightleftharpoons}} 2Cu_2O + O_2,$$

depends not only on temperature but also on the conversion of the material. This behaviour is consistent with many homogeneous crystallisation processes where a significant oversaturation is required to initiate the reaction. On the other hand, the degree of oversaturation reduces drastically if seed nuclei are present, analogous to a partly reacted mixture of CuO and $Cu_2O$. A consequence is that the initial rate of reaction is slower than that at a higher conversion, leading to an apparent auto-catalytic reaction profile. One of the most commonly-used models to describe such behaviour was developed by Avrami (1941, 1940, 1939), derived originally for isothermal conditions so that the oversaturation was constant during the reaction. Consequently, the rate of nucleation and the rate of growth of nuclei can be taken to be constant. Depending on the relative magnitude of the two rates as well as the growth characteristic (linear, planar or polyhedral), the index *a* in the Avrami equation 5-10

takes integer values between 1 and 4. In the case of CLOU, however, the situation is more complicated because the oversaturation also depends on the partial pressure of oxygen in the bulk gas, $P_{O2}$. Thus the relative rate of nucleation and growth may be different at different values of $P_{O2}$ which could lead to different reaction profiles. Indeed this is observed here: when the value of $P_{O2}$ is close to $P_{eq}$, the rate of nucleation is slow so that an induction period is observed , as in Figure 5-16, but when $P_{O2} >> P_{eq}$ (Figure 5-14), the induction period is absent, suggesting that nucleation is sufficiently fast for the reaction to be controlled by crystal growth only. In light of this additional complication, extreme caution must be exercised when the Avrami model is applied in similar situations. Furthermore, because the rate of reaction depends on the concentration driving force in addition to temperature, it is generally insufficient to determine the apparent activation energy of the reaction using an Arrhenius plot, *i.e.* plotting the logarithm of reaction rate *vs*. 1/T. It is possible, however, to use the Arrhenius plot in two special cases: 1) the value of $P_{O2}$ in the environment is much higher than $P_{eq}$ so that their difference remains largely unchanged over the range of temperature investigated or, 2) the value $P_{O2}$ is close to zero so that the difference is approximately $P_{eq}$, which can be written in a form similar to the Arrhenius equation (equation 5-37) so that it can be incorporated in to the apparent rate constant. Otherwise the apparent activation energy may appear to be negative, resulting in potentially misleading interpretations of the rate of reaction (Zhu *et al.*, 2004).

It was noted earlier that the rapid change in the value of $P_{eq}$ over the temperature range investigated was related to the relatively high enthalpy of reaction. In view that it is difficult to eliminate temperature gradients within a reactor in large scale operations, it would be desirable to develop OCs having a lower enthalpy of reaction for CLOU processes so that less stringent temperature control can be used. From equation 5-37, it can be seen that the ratio of $P_{eq}$ at different temperatures is related to the enthalpy of reaction by

$$\frac{P_{eq,T_1}}{P_{eq,T_2}} = \exp\left(\frac{-\Delta H_r}{R}\left(\frac{1}{T_1}-\frac{1}{T_2}\right)\right). \qquad 5\text{-}38$$

Taking $T_1$= 1223 K (950°C) and $T_2$ = 1123 K (850°C), a value of $\Delta H_r$ = 184 kJ/mol would limit the ratio to approximately 5 and a value of 79 kJ/mol would lower the ratio to 2. In addition, a smaller value of $\Delta H_r$ is beneficial since the temperature change of

the OC would be smaller during reactions so that the effect of thermal stress could be reduced thereby improving the performance of the OC in terms of diminished attrition.

To date, many studies exist with respect to the CLOU reaction of different materials, most notably Cu-based oxides (*e.g.* Adánez-Rubio *et al.*, 2014; Arjmand *et al.*, 2012b; Clayton and Whitty, 2014; Clayton *et al.*, 2014) and perovskite materials (*e.g.* Abad *et al.*, 2015; de Diego *et al.*, 2014). Two approaches are commonly employed for such studies: 1) Assuming a simple rate expression, *i.e.*

$$\frac{dX}{dt} = k_{app} C_s^{\,n} f(X), \qquad 5\text{-}39$$

where the apparent activation energy of reaction, $k_{app}$, is modelled by the Arrhenius equation. The influence of the thermodynamic driving force is effectively incorporated into the fitted kinetic parameters without separate consideration. 2) Assume a rate expression similar to equation 5-9,

$$\frac{dX}{dt} = k_{in}\left(C_{eq}^{\,n} - C_s^{\,n}\right) f(X)$$

to account for the thermodynamic driving force explicitly and obtain a kinetic parameter due to reaction kinetics alone. While both methods can be used to fit the experimental results for practical use, the second method should be the preferred choice since the dependence of reaction rate on the thermodynamic driving force is not always compatible with the Arrhenius expression, as outlined earlier. When using the second approach, most studies rely on thermodynamic databases for the values of equilibrium oxygen concentration. From the current work, it can be seen that for Cu-based materials where the support does not interact with the CuO significantly, the equilibrium oxygen concentrations of the OC are within ~ 10% of the database values (based on NIST database) so that using database values would not influence the calculated kinetic parameters greatly.

On the other hand, with more effort directed towards novel perovskite materials, such thermodynamic data may no longer be available. In these cases, the diffusion method employed in this work can be effective in determining the thermodynamic parameters of the novel systems, given that the rate of chemical reaction is sufficiently fast in the temperature range of interest. The diffusion method can also capture the change in thermodynamic equilibrium with respect to conversion (or degree of oxygen deficiency) easily since the TGA measure the mass of the sample with respect to time directly so that the reaction rate and conversion can be calculated directly, whereas in fluidised-bed based methods, the conversion has to be estimated using the gas

concentration measured at the outlet which may increase the uncertainty of the results since mass balance from gas analysers are not always easily closed due to background drift *etc*. Furthermore, the diffusion method requires materials of the order of milligrams, whereas fluidised bed requires materials at least on the gram-level. Hence it is more advantageous to test novel materials using the TGA since a minimal amount of synthesis is needed.

In addition, the diffusion method can be used to determine steady state kinetics not necessarily limited by thermodynamics. For instance, it has been of interest to determine the ratio of $CO/CO_2$ near the surface of a carbon particle in a combustion process (*e.g.* Arthur, 1951; Hayhurst and Parmar, 1998; Scala, 2011; Tognotti *et al.*, 1991) and one of the difficulties was to account for the oxidation of CO away from the solid surface before the gas was analysed. Since the diffusion method measures the weight of sample directly and does not rely on further gas analysers, the $CO/CO_2$ ratio could be calculated from the rate of mass loss of the solid sample. Assuming the reaction is in the mass transfer limited regime, the surface concentration of $O_2$ is close to zero and not affected by the product ratio. Hence, for the same flux of $O_2$ entering the crucible, the mass loss would be approximately twice as high if the product were solely CO, compared with the case where the product were solely $CO_2$, due to the reaction stoichiometry. In this case any secondary reaction outside the crucible does not affect the results at all and the reaction within the crucible is limited due to the small size.

## *5.6. Summary*

In this chapter, the thermodynamic equilibrium of the OC was investigated and a method based on diffusion was developed for the measurement of equilibrium processes, in particular the oxidation of Cu and $Cu_2O$ respectively.

It was found that the fresh OC exhibited different equilibria for the decomposition of CuO to $Cu_2O$ with a first decomposition step close to that of pure CuO and a second step occurring at a much higher temperature. However, this behaviour was only transient and after a few redox cycles, the majority of the OC decomposed at the lower temperature. The higher decomposition temperature of the fresh material was attributed to the stabilisation of the CuO phase in the presence of the supporting mayenite after being thermally treated over long period of time (during calcination). For the cycled OC, the equilibrium was different between unconverted and partly converted

OCs but the degree of conversion was not important except at very low and very high conversions where surface energy had a more significant influence on the Gibbs free energy of reaction.

Quantitative measurements of the equilibrium concentration of $O_2$, $P_{eq}$, for the $Cu_2O$/CuO transition of the cycled OC were undertaken between 850°C and 950°C, the temperature range relevant for CLOU with Cu-based materials, using a novel diffusion method developed in this chapter. The measured values of $P_{eq}$ are in agreement with the standard results for pure $Cu_2O$/CuO systems obtained from NIST database, within ~ 10% over the temperature range. However, the average enthalpy and entropy of reaction was found to be slightly lower than the documented values.

It was also found that the initial behaviour in the oxidation of $Cu_2O$ to CuO was dependent on the partial pressure of $O_2$ in the environment. Specifically, when $P_{O2}$ was close to $P_{eq}$, an induction period was observed before significant reaction took place. This was attributed to the slow rate of nucleation in such conditions. When $P_{O2}$ was significantly higher than $P_{eq}$, no induction period was observed.

Lastly the advantages of the diffusion method were discussed. This method could be used to determine the thermodynamics of systems where the equilibrium shifts during the course of reaction under isothermal conditions, or to measure the ratio of two products in steady state, such as the combustion products near the surface of char particles.

# 6. The kinetics of oxygen uncoupling

## *6.1. Introduction*

In Chapter 5, it was proposed that the rate law for the reaction 5-1,

$$4CuO \rightleftharpoons 2Cu_2O + O_2,$$

when expressed in terms of rate of change of conversion of the solid (forward direction being positive), should take the form of equation 5-9, *i.e.*

$$\frac{dX}{dt} = k_{in}\left(C_{eq}{}^{n} - C_s{}^{n}\right) f(X).$$

In this equation, the kinetic contribution is represented by the rate constant $k_{in}$, which can be characterised by an activation energy $E_a$ and a pre-exponential factor $k_{in,0}$, using the Arrhenius equation

$$k_{in} = k_{in,0} \exp\left(\frac{-E_a}{RT}\right). \qquad 6\text{-}1$$

The concentration driving force, ($C_{eq}{}^{n} - C_s{}^{n}$), is characterised by the order of reaction with respect to $O_2$, $n$. Chuang *et al.* (2010) found that the value of $n$ (for the oxidation) was close to 1 when the concentration of $O_2$, $C_s$, was ≤ ~0.4 mol/m$^3$ between 400°C and 800°C for Cu-based OC co-precipitated with $Al_2O_3$. The order was found to decrease at higher values of $C_s$. However, it was noted that with higher $C_s$, the response time of the gas analyser became significant compared to the duration of the experiment so that the measured initial rate probably underestimated the true value, thereby leading to an apparent decrease in the order of reaction. Chuang *et al.* (2010) also acknowledged that at temperatures above 600°C, the reaction was partly controlled by external mass transfer and this may have led to an apparent order of reaction of unity, characteristic of the transport process rather than the chemical reaction. It is worth noting that the authors considered the oxidation reaction to be irreversible at these conditions but this assumption does not affect the conclusion since at such low temperatures $C_{eq}$ is practically zero. Clayton *et al.* (2014) studied the oxidation in a TGA of two Cu-based OCs, starting from $Cu_2O$, and reported the order of reaction with respect to $O_2$ to be 1.3. However, in a separate investigation, on the decomposition, in $N_2$, of the same carriers in the fully-oxidised form, the order of reaction was found to be ~ 1 (Clayton and Whitty, 2014).

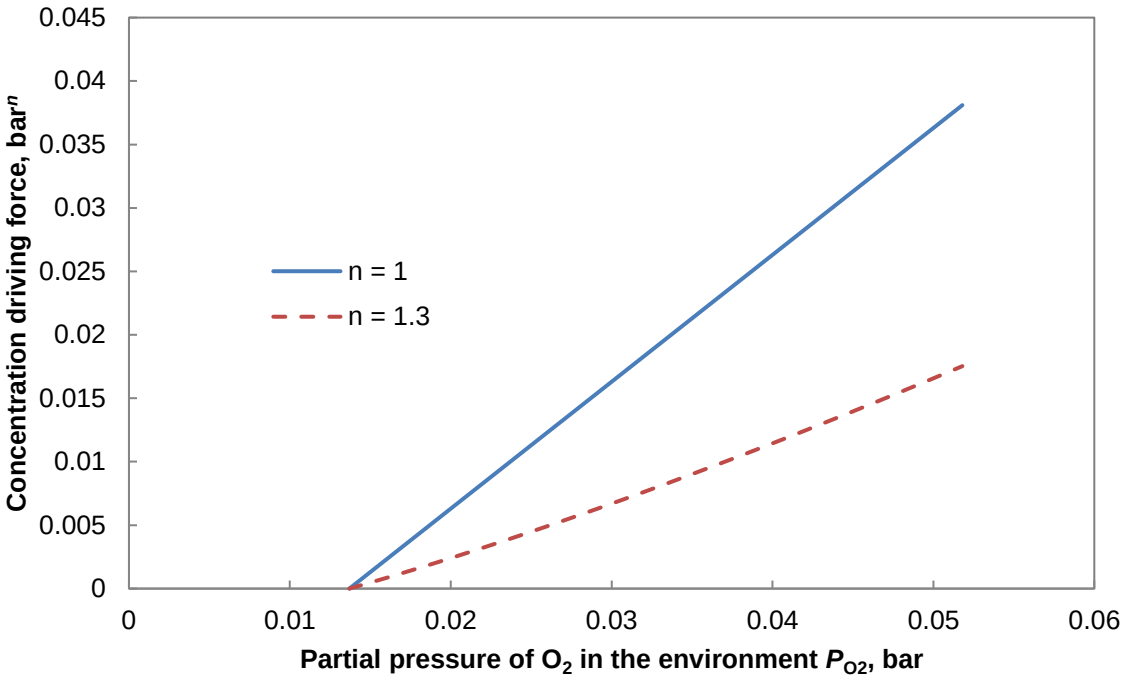


Figure 6-1 The concentration driving force for the CuO/$Cu_2O$ transformation with different orders of reaction. A value of $P_{eq}$ = 0.0137 bar was used as an example here. It can be seen that for $n$ = 1.3 (red dashed line), the dependence is approximately linear, but having a lower gradient compared to the truly linear case of $n$ = 1 (blue solid line).

Whilst the apparent difference in the order of reaction between oxidation and reduction can be attributed to different reaction mechanisms, it should be recognised that at for small values of $C_s$, or equivalently $P_{O2}$, the concentration driving force can be approximated by a first-order reaction with a different constant of proportionality as illustrated in Figure 6-1. Hence a reaction model with apparent order 1.3 is almost equivalent to a model with order 1 but having a different pre-exponential factor.

It thus appears that using a first order reaction model to account for the concentration driving force is adequate to describe the transformation between CuO and $Cu_2O$ and $n$ is taken to be unity in this Dissertation to take advantage of its simplicity, especially when combined with mass transfer modelled as will be discussed later in the chapter.

The dependence of the rate of reaction on the conversion of the solid, $f(X)$, can take different forms depending on the solid reaction model used (Khawam and Flanagan, 2006). Various studies have proposed different reaction models for the decomposition of CuO to $Cu_2O$, including zeroth order reaction (Clayton and Whitty,

2014), first order reaction (Sahir *et al.*, 2012), Avrami-Erofeev kinetics (equation 5-10) with $a$ = 2 (Arjmand *et al.*, 2012b) or $a$ = 3 (Wang *et al.*, 2013) and non-integer values such as $a$ = 4/3 (Adánez-Rubio *et al.*, 2014). It should be noted that in many studies, the discrimination between different reaction models was done by comparing the coefficient of determination of the fits of the theoretical models to the experimental results, with the model yielding the highest coefficient of determination adopted as the rate expression (Adánez-Rubio *et al.*, 2014; Arjmand *et al.*, 2012b; Song *et al.*, 2012). However, sometimes the coefficients of determination for different models were found to be very close to each other, indicating that several models might describe the experimental results equally well, thus requiring further discrimination.

The determination of the parameters in equation 5-9, such as the rate constant, $k_{in}$ ,and the form of $f(X)$ has normally been undertaken in either a fluidised bed (*e.g.* Arjmand *et al.*, 2012b; Sahir *et al.*, 2012) or a TGA (*e.g.* Adánez-Rubio *et al.*, 2014; Clayton and Whitty, 2014; Clayton *et al.*, 2014). In either apparatus, care must be taken to account for effects other than chemical reaction, such as analyser response time, and external and internal mass transfer, because these factors might influence the observed rate of reaction. For instance, Chuang *et al.* (2010) found that the oxidation of co-precipitated particles containing Cu and $Al_2O_3$ in the sieve size fraction 355-500 µm obeyed a shrinking core mechanism because of the relatively slow rate of mass transfer of $O_2$ within the particles compared to the rate of chemical reaction. Similarly, external mass transfer effects often influence the observed rate of release of $O_2$ from materials for CLOU this can be exploited to measure the equilibrium partial pressure of the reaction (Arjmand *et al.*, 2011; Wen *et al.*, 2012) rather than the kinetics.

In this Chapter, the kinetics of decomposition of the wet-mixed Cu-based OC from CuO to $Cu_2O$ were determined using a TGA and the effect of external mass transfer was accounted for using an approach based on the diffusion method described in Section 5.3.1. Some of the results presented in this Chapter appear in Hu *et al.* (2016).

## 6.2. Experimental method

The decomposition of the OC was investigated isothermally at given temperatures between 850°C and 950°C in a TGA. Chapter 5 demonstrated that the virgin particles behaved differently from cycled ones; all particles used in this Chapter were pre-treated, *i.e.* fully reduced in 5% $H_2$ with balance $N_2$ and then re-oxidised in air at 850°C for 3 times in a fluidised bed. The particles used were in the sieve size fraction 300-425 µm except in one experiment where a smaller fraction, 100-160 µm, was employed to investigate the effect of internal mass transfer. In a typical isothermal experiment, between 6 and 20 mg of the pre-treated OC was placed in a standard 70 µl alumina crucible without a lid. The samples were held at the reaction temperature, between 850°C and 950°C with air as the reactive gas (50 ml/min at 20°C and 1 bar) so that the sample did not decompose. At a prescribed time, the reactive gas was switched off, leaving only the Ar from the purge and protective streams (~120 ml/min in total at 20°C and 1 bar) to start the decomposition.

To determine the kinetics accurately, ~ 6.1 mg of the pre-treated particles were placed in a shallow platinum crucible with an i.d. of 5.5 mm and depth 2.1 mm instead of the standard alumina crucible (i.d. 4.9 mm, depth 4.0 mm) to improve the rate of external mass transfer further. The sample was first heated in air (with Ar as the purge and protective gas, as before) to 900°C. When the temperature had stabilised, the air was switched off and the decomposition reaction was allowed to proceed to completion with the TGA purged with Ar. The sample was then re-oxidised in air and the process was repeated five times to confirm that the behaviour of the particles was similar over cycles. Subsequently the particles were brought to 875°C, 925°C, 950°C and 850°C for a further redox cycle at each temperature to determine the rate of reaction at those temperatures respectively.

## 6.3. Coupling particle kinetics with external mass transfer

In Chapter 5, the solution to the diffusion problem within a cylindrical crucible with a lid containing a hole in the centre was presented. The same method can be used to solve the diffusion problem without a lid, using appropriate boundary conditions. Here, the problem is only 1-D without the lid because the concentration of the gas is now constant across the top surface so that the radial flux disappears and the problem resembles that of the Stefan tube.

For a 1-D binary diffusion case ($O_2$-Ar), the Stefan-Maxwell equations become

$$\frac{dy_1}{dz} = -\frac{dy_2}{dz} = \frac{y_1 J_2 - y_2 J_1}{cD}, \qquad 6\text{-}2$$

where the subscripts 1 and 2 denote $O_2$ and Ar respectively; $y$ denotes the mole fraction of the gas species and $J_i$ the diffusive flux of the species $i$; the spatial dimension $z$ is measured vertically downwards with origin at the top of the crucible. The total concentration of gas is denoted by $c$ and the binary diffusion coefficient is given by $D$, which can be estimated using equation 5-14 (Fuller *et al.*, 1966). Since Ar is inert, the flux $J_2$ is zero, assuming pseudo-steady-state and hence equation 6-2 can be integrated to give

$$J_1 = \frac{cD}{z_{\max}} \ln\left(\frac{1 - y_{1.bulk}}{1 - y_{1,s}}\right), \qquad 6\text{-}3$$

in which $y_{1,bulk}$ and $y_{1,s}$ represent the mole fractions of $O_2$ at the top of the crucible and at the surface of the OC particles (because only a monolayer of particles were used) respectively and $z_{\max}$ represents the length of the crucible, following the same notation in Figure 5-2. When $y_{1,bulk}$ and $y_{1,s}$ are sufficiently small, the natural logarithm can be linearised using the Taylor expansion, so that equation 6-3 becomes

$$\begin{aligned} J_1 &\approx \frac{cD}{z_{\max}}\left(y_{1,s} - y_{1,bulk}\right) \\ &= \frac{D}{z_{\max}}\left(C_s - C_b\right), \end{aligned} \qquad 6\text{-}4$$

where $C_s$ and $C_b$ denote the concentration of $O_2$ in mol/m$^3$ at the surface of the particles and the top of crucible, respectively, and a mass transfer coefficient can be defined, for convenience, to be

$$k_g = \frac{D}{z_{\max}}. \qquad 6\text{-}5$$

Under the pseudo-steady-state assumption, the rate of mass transfer of $O_2$ from the surface of the particles to the top of the crucible must be the same as the rate of production of $O_2$ in the decomposition reaction. Hence the diffusive flux $J_1$ is related to the rate of chemical reaction, using equation 5-9, by

$$\pi r_c^{\,2} J_1 = \frac{m_{O2}}{32} k_{in}\left(C_{eq} - C_s\right) f(X), \qquad 6\text{-}6$$

where $r_c$ is the radius of the crucible, $C_{eq}$ is the equilibrium concentration of $O_2$ at the given temperature. The total mass of oxygen available in the OC within the crucible, for the purpose of CLOU, is represented by $m_{O2}$ and the constant 32 is the molar mass of $O_2$, which serves to convert the right-hand-side of the equation to a molar basis to

be compatible with the left-hand-side. Substituting equations 6-4 and 6-5 into 6-6, the surface concentration, $C_s$, can be isolated to give

$$C_s = \frac{k_{in}'f(X)}{k_{in}'f(X)+k_g}(C_{eq}-C_b)+C_b, \qquad 6\text{-}7$$

where the new constant $k_{in}'$ is related to $k_{in}$ by

$$k_{in}' = \frac{m_{O2}}{32\pi r_c^{\,2}}k_{in}. \qquad 6\text{-}8$$

Equation 6-7 can be used to eliminate the unknown $C_s$ in equation 6-4, leading to

$$J_1 = \frac{k_{in}'f(X)k_g}{k_{in}'f(X)+k_g}(C_{eq}-C_b). \qquad 6\text{-}9$$

Taking reciprocals allows the separation of the kinetic term and mass transfer term,

$$\frac{1}{J_1} = \frac{1}{(C_{eq}-C_b)}\left(\frac{1}{k_{in}'f(X)}+\frac{1}{k_g}\right), \qquad 6\text{-}10$$

and a plot of $1/J_1$ against $1/f(X)$ can be used to extract $k_{in}'(C_{eq} - C_b)$ and $k_g(C_{eq} - C_b)$ from the gradient and $y$-intercept of the graph, respectively, using a suitable $f(X)$. If $C_{eq}$ and $C_b$ are known, at this point, the rate constant $k_{in}$ can be calculated directly. More generally, the concentrations might not be known precisely, as in the present work, because the TGA was not perfectly air-tight and a small concentration of $O_2$ might well have been present in the bulk gas, thus affecting the accuracy of the result at low temperatures. In such case, the ratio between the $y$-intercept and the gradient, $k_{in}'/k_g$, is independent of the concentration driving force, eliminating the influence of the thermodynamic equilibrium concentration. This approach works best when the values of $k_{in}'$ and $k_g$ are comparable (within one order of magnitude or so). If the value of $k_g$ is much greater than $k_{in}'$, the mass transfer has negligible effect on the measured rate of reaction and equation 6-9 can be approximated by

$$J_1 = k_{in}'f(X)(C_{eq}-C_b), \qquad 6\text{-}11$$

and the analysis would be redundant. On the other hand, if the value of $k_g$ is too small, the reaction would be entirely limited by external mass transfer in the beginning until a conversion high enough such that $k_{in}'f(X)$ becomes comparable to $k_g$, leaving only a few data points useful for the extraction of the kinetic information, leading to large errors.

## 6.4. Results

### 6.4.1. The effect of particle size on the rate of reaction

While Section 6.3 considered the influence of external mass transfer on the measured rate of reaction, the mass transfer within the OC particles may be important, too, especially with large particles (*e.g.* Sahir *et al.*, 2012). To investigate the effect of particle size on the rate of reaction, two samples of about 10 mg each were decomposed at 900°C under identical conditions in the TGA. The first sample contained particles with sizes between 300-425 µm, whereas the second sample contained particles with sizes between 100-160 µm. The reaction profiles of the two experiments are shown in Figure 6-2. It can be seen that the profiles of rate against conversion were very similar for the two samples, and the time taken for complete conversion was comparable. In addition, the rate of mass change in both cases was almost constant between up to $X$= 0.6 indicating that the reaction was largely limited by external mass transfer to that point. As the conversion increased beyond 0.6, the value of $f(X)$ was small enough that $k_{in}'f(X)$ became comparable with $k_g$ and the chemical reaction started to influence the observed rate of mass change. The fact that the reaction profile was not influenced by particle size suggests that with a particle size up to 425 µm, the effect of internal mass transfer was not significant. Had both batches been in the regime of significant intraparticle mass transfer, there would have been a difference in rate, because the effectiveness factors would have been different for the two sizes. Also, evidence from determining the activation energy, discussed in Section 6.4.3 below, is strongly in favour of the particles operating without substantial intraparticle mass transfer.

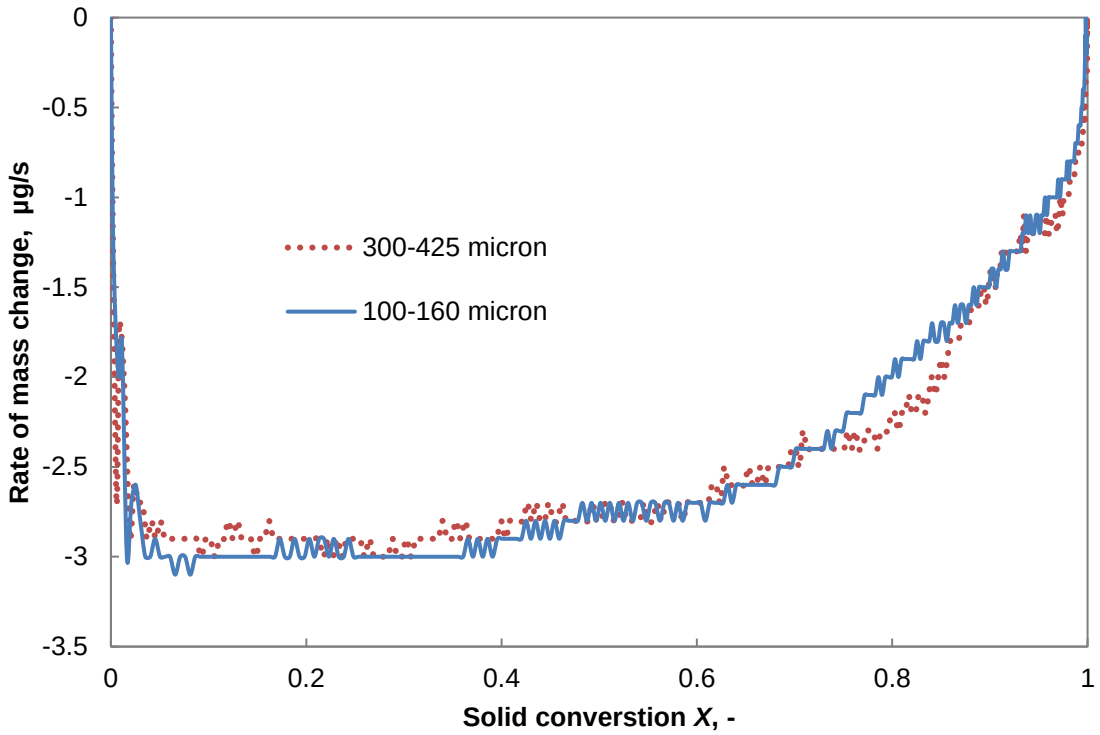


Figure 6-2 Rate of oxygen release of two samples with comparable mass but different particle sizes in Ar at 900°C. An alumina crucible with depth 4 mm and diameter 4.9 mm was used. 300-425 µm sample: 10.4 mg, time for completion: 280 s; 100-160 µm sample: 9.8 mg, time for completion: 270 s.

### *6.4.2. Effect of particle-particle interaction*

To minimise the influence of neighbouring particles, care was taken to ensure that a monolayer of oxygen carrier particles was used for experiments. To confirm that the presence of other oxygen carrier particles in the vicinity did not influence the reaction of a single particle significantly, two samples (300-425 µm) of similar mass (6.58 mg *vs.* 6.28 mg) were decomposed in argon at 900°C under identical conditions in the TGA except that the first sample was mixed with quartz sand particles of the same size fraction to increase the inter-particle spacing. As shown in Figure 6-3, the reaction profiles of the two experiments were found to be almost identical. In addition, the time taken for complete reaction was found to be 198 s and 200 s respectively. Thus it was concluded that neighbouring particles do not have a significant effect on the reaction of a single particle.

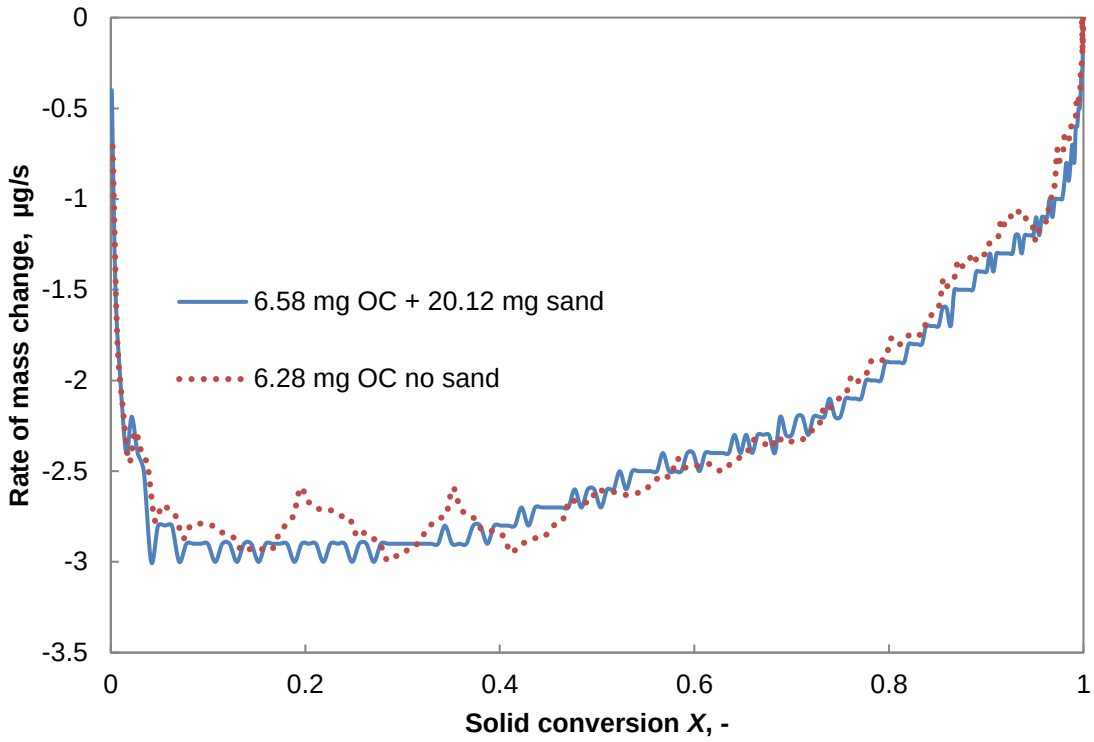


Figure 6-3 Rate of oxygen release of two samples with comparable mass in Ar at 900°C. One sample was mixed with quartz sand (blue solid line) and the other consisted of the OC particles alone (red dotted line).

### 6.4.3. Determination of the kinetic parameters

In order to obtain accurate kinetic results, the rate of external mass transfer should be as fast as possible compared with the rate of chemical reaction. This was achieved by 1) using a shallow crucible with a height of just 2.11 mm to increase the value of $k_g$ and 2) using as small amount of OC as possible to reduce $m_{O2}$ and hence $k_{in}'$. The mass of OC used was approximately 6 mg so that $m_{O2}$ was about 360 µg. A lower mass was not used to ensure a good signal to noise ratio, because the accuracy of the TGA balance was limited to about ±1 µg.

#### 6.4.3.1. Effect of cycling

The experiment was designed such that the same batch of particles was used at different temperatures in a sequential manner. Thus it is necessary to establish that cycling does not have a significant effect on the rate of reaction. To confirm this, the sample was decomposed and re-oxidised at 900°C for 5 cycles to compare the rate of decomposition in different cycles.

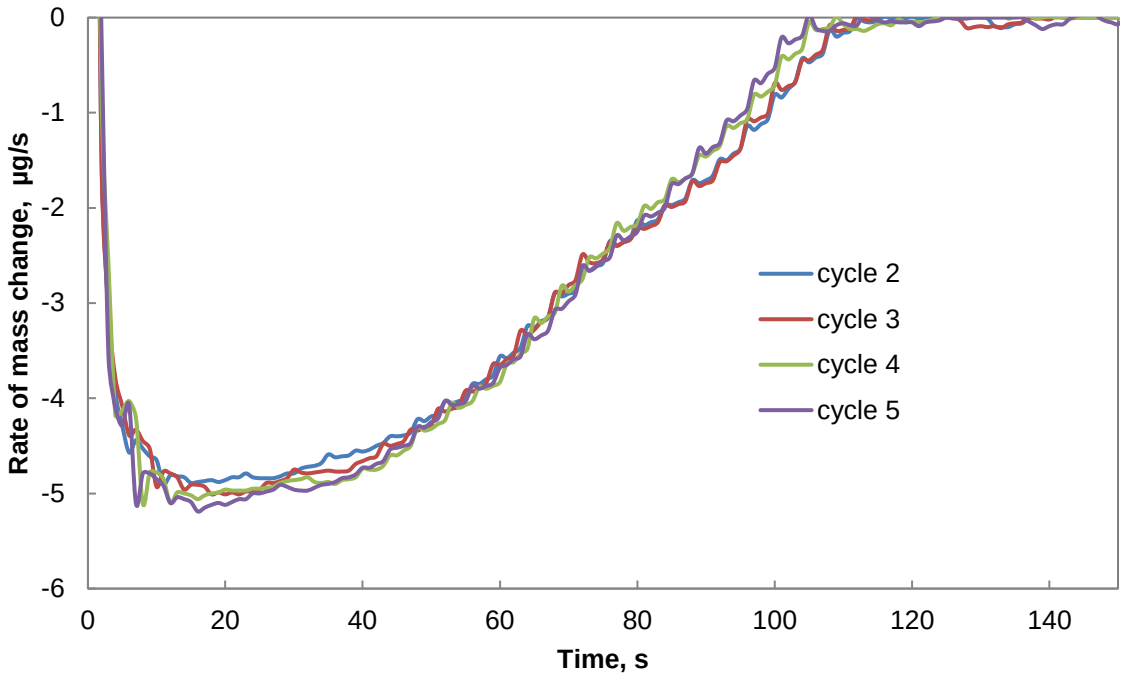


Figure 6-4 The rate of oxygen release of the OC particles in successive cycles in a TGA at 900°C.

It is clear from the highly reproducible reaction profiles shown in Figure 6-4 that the rate of decomposition of the carrier did not change in cycles 2 to 5 and hence the sequential nature of the experiment should not affect the kinetic parameters extracted at different temperatures. Furthermore, it should be noted that the maximum rate of decomposition was ~ 5 µg/s, about 1.7 times higher than the maximum rate observed using similar amount of OC particles in a taller crucible as shown in Figure 6-3, indicating that external mass transfer influences the apparent rate of reaction significantly.

### *6.4.3.2. The choice of f(X)*

In order to make use of equation 6-10, an appropriate conversion function, $f(X)$, must be used. It is obvious from the reaction profiles shown earlier that the rate of decomposition is a non-constant function of the conversion of the solid; hence the zeroth-order model can be ruled out. Other commonly-used reaction models including $n^{th}$ order reaction kinetics, the Avrami-Erofeev model and the shrinking core model were considered. It should be noted that although it was confirmed in Section 6.4.1 that mass transfer within the OC particles did not influence the rate of reaction, shrinking core kinetics might still be applicable due to the preparation method used. Since an OC particle consists of fine CuO grains approximately 10 µm, evenly

distributed throughout the particle, it is possible that the mass transfer effect is negligible on the particle scale but significant on the grain scale, due to different diffusivities between the particle and the grains. Thus locally at each grain, the reaction could proceed *via* the shrinking core mechanism and this would be independent of the size of the OC particle.

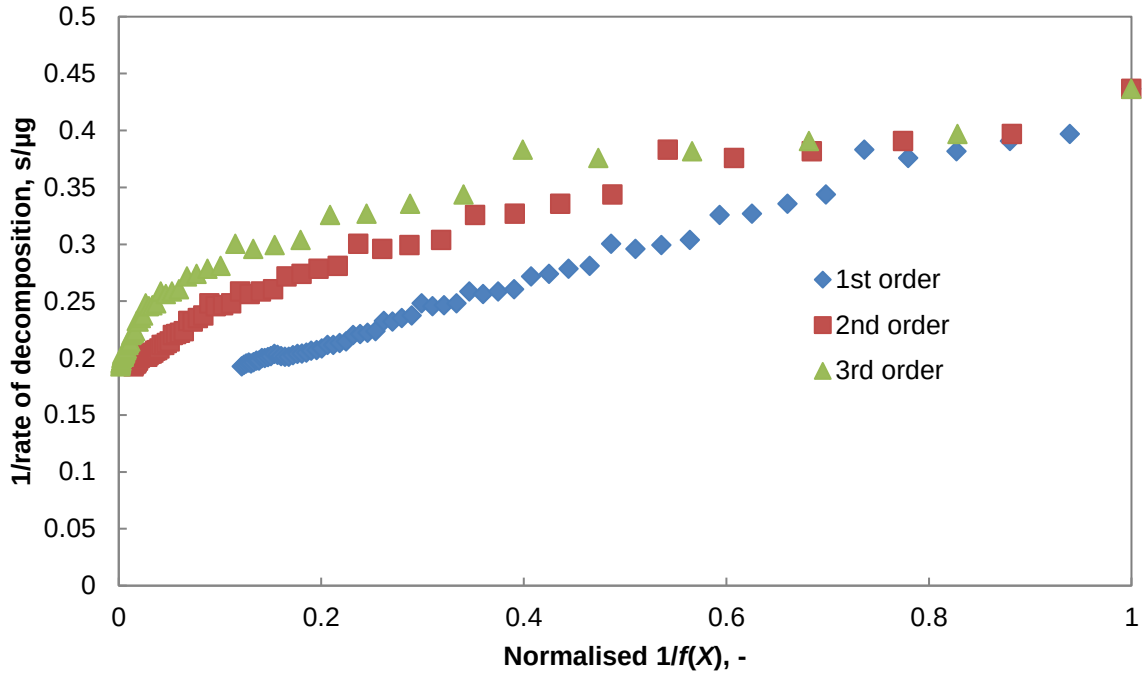


Figure 6-5 1/rate of the decomposition reaction as a function of 1/$f(X)$ for an $n^{th}$ order reaction model with $n$ = 1, 2 or 3. The abscissa is normalised by the largest value of 1/$f(X)$ used in the construction of the graph for ease of comparison. The results were obtained from the experimental reaction profile at 900°C with a range of $X$ between 0.2 and 0.9.

Figure 6-5 presents the corresponding plots derived from equation 6-10 using an $n^{th}$ order reaction model with $n$ = 1, 2 or 3. The corresponding conversion functions, $f(X)$, are $(1 - X)^n$. Here, the values of 1/$f(X)$ are normalised against the highest value in each case, for the ease of comparison, and this does not affect the linearity of the plots. The rate of decomposition is recorded simply as the negative of the rate of mass change measured from the TGA experiment. It can be seen from Figure 6-5 that, of the three curves shown, only the first-order reaction model produced a straight line and the linearity decreased as the order of reaction increased. Correspondingly, the coefficient of determination for a linear least-squares fitting of these curves decreased from 0.993 for the first order model to 0.824 for the 3$^{rd}$ order model.

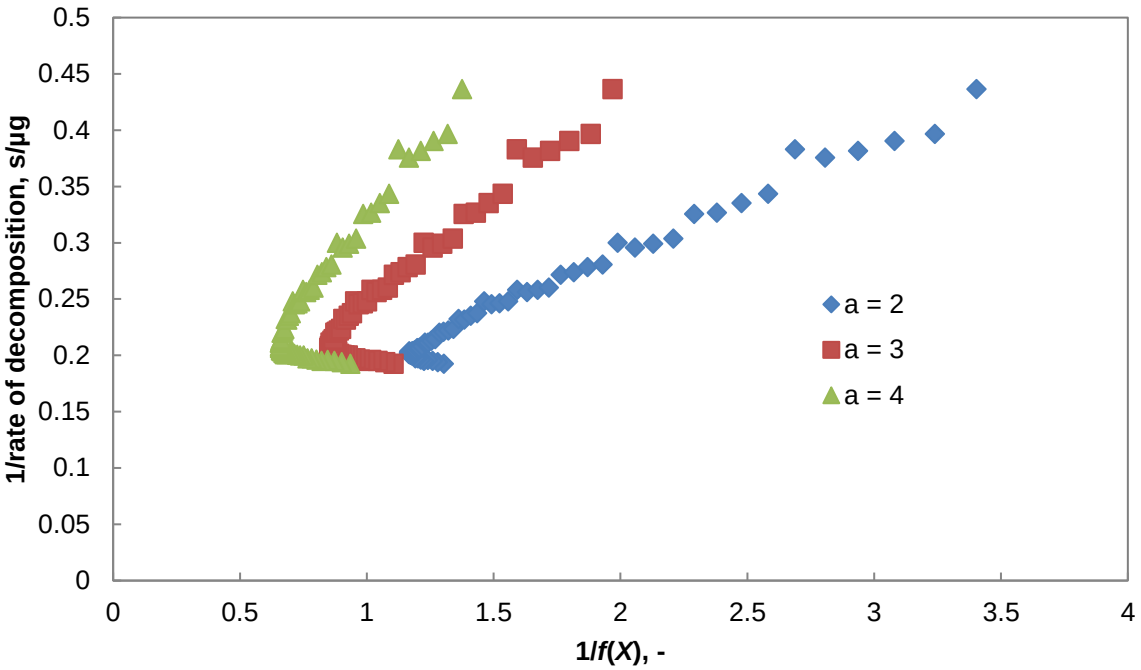


Figure 6-6 1/rate of the decomposition reaction as a function of 1/$f(X)$ for $a^{th}$ order Avrami-Erofeev model with $a$ =2, 3 or 4. The results were obtained from the experimental reaction profile at 900°C with a range of $X$ between 0.2 and 0.9.

Next, the Avrami-Erofeev model with the form

$$f(X) = (1-X)(-\ln(1-X))^{a-1/a} \qquad 6\text{-}12$$

was considered. When $a$ = 1, the expression is identical to the first-order reaction model. When $a$ takes higher integer values between 2 and 4, a linear plot cannot be obtained, as shown in Figure 6-6. The functional form of the Avrami-Erofeev model dictates that the rate of reaction would reach a maximum at the conversion

$$X_c = 1-\exp\left(\frac{1-a}{a}\right), \qquad 6\text{-}13$$

and the maximum point should not change when external mass transfer effects are taken into account. The point $X_c$ corresponds to the left-most points on each of the plots shown in Figure 6-6. As a result, the value of 1/$f(X)$ should decrease as $X$ increases until the point $X_c$ and then start to increase, unlike the $n^{th}$ order reaction model in which the value of 1/$f(X)$ increases monotonically as $X$ increases. In Figure 6-6, it can be seen that when $X > X_c$, the curves are reasonably linear, irrespective of the order $a$. However, when $X < X_c$, the rate of reaction did not decrease as expected from the models as $X$ decreased but remained almost constant in this region instead. This systematic deviation cannot be accounted for by experimental error alone and

thus it appears that the Avrami-Erofeev model does not describe the decomposition of the OC adequately despite the fact that a relatively high value of the coefficient of determination (0.982) can be obtained for the case when $a$ = 2.

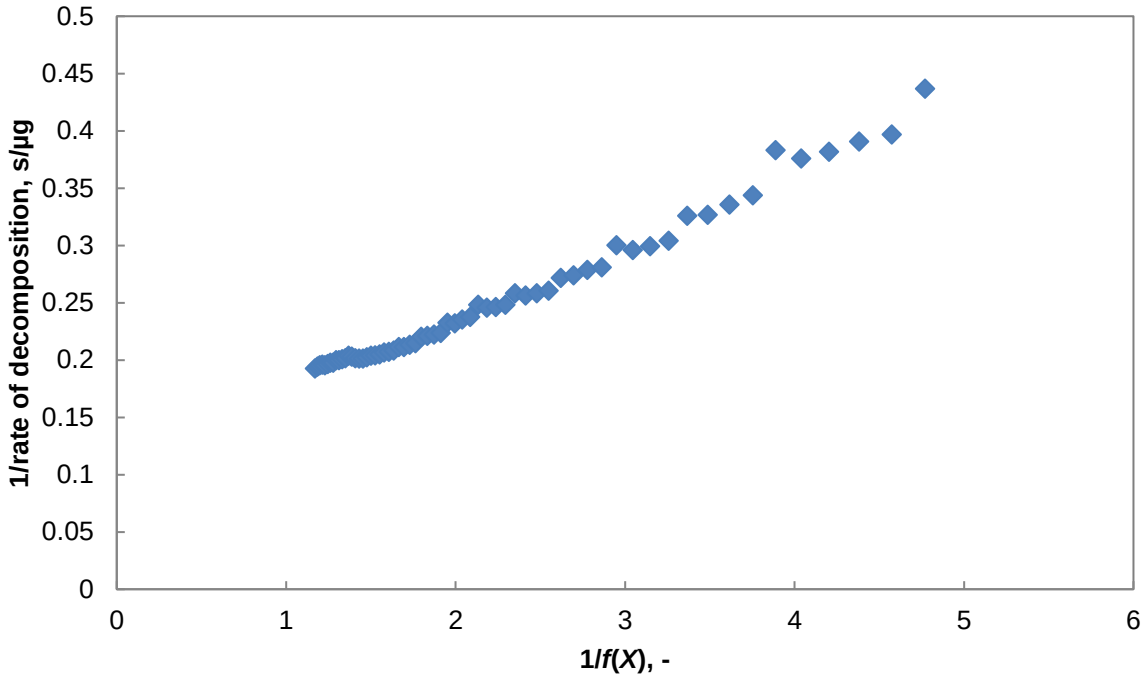


Figure 6-7 1/rate of the decomposition reaction as a function of 1/$f(X)$ for the shrinking core model. The results were obtained from the experimental reaction profile at 900°C with a range of $X$ between 0.2 and 0.9.

Lastly, the plot obtained using a shrinking grain model where the reaction only proceeds at the surface of each individual non-porous grain of CuO,

$$f(X) = (1 - X)^{2/3}, \qquad 6\text{-}14$$

is presented in Figure 6-7 and good linearity was obtained with a coefficient of determination of 0.985.

Hence the first-order reaction model and the shrinking grain model are used separately to obtain the corresponding kinetic parameters.

### *6.4.3.3. Calculation of the rate constant*

The experimental results shown in Figure 6-8 were produced using the first order reaction model. It can be seen that while all the plots were linear in the temperature range investigated, those obtained at 850°C were scattered considerably, especially at high values of $X$ > 0.75. The very slow rate of decomposition, less than 1 µg/s, was

responsible for the large scatter at this temperature. On the other hand, the number of data points usable for the extraction of the kinetic parameters at 950°C was only 25 due to the short duration of the reaction at the temperature. As a result, it was not possible to widen the temperature range of the investigation further.

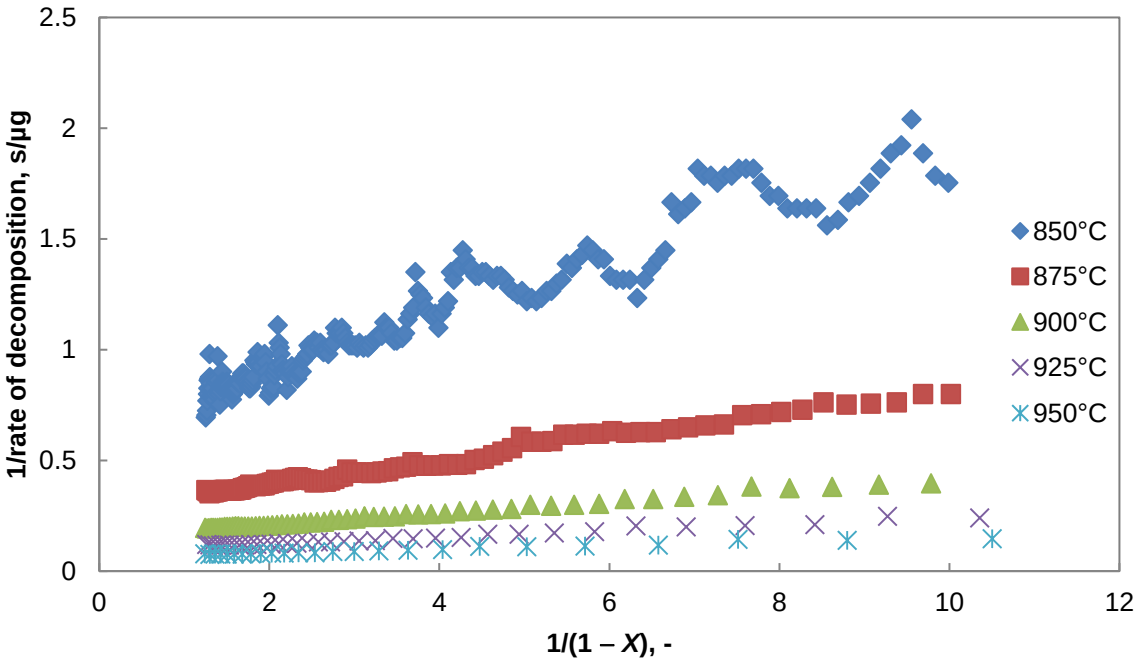


Figure 6-8 Plots of 1/rate of the decomposition reaction as a function of 1/(1–$X$) *i.e.* using the first-order reaction model at various temperatures with a range of $X$ between 0.2 and 0.9.

Despite the fact that the observed rate of reaction increased by more than 10-fold over a temperature difference of 100°C, the ratio $k_{in}'/k_g$, calculated using the method outlined in Section 6.3, only increased from 5.0 at 850°C to 7.4 at 950°C, a very modest change. Considering that $k_g$ only depends on temperature weakly, through the binary diffusion coefficient, $D$, the rate constant could not have changed by 10-fold in the temperature range. In fact, as discussed in Section 5.5, this large difference in the rate of reaction was due largely to the thermodynamics of the reaction, *i.e.* the relatively high enthalpy of reaction. Therefore, it can be seen that the activation energy of the reaction must be much smaller than the enthalpy change of the reaction. A consequence of this result is that, if the thermodynamic contribution were not eliminated by taking the ratio $k_{in}'/k_g$, the activation energy would be dwarfed by the enthalpy of reaction and a small percentage deviation of the enthalpy change of reaction used for the calculation (either measured experimentally as in Chapter 5, or

using literature values) from the true value would influence the value of the activation energy greatly, leading to potentially erroneous results.

Once the ratio $k_{in}'/k_g$ was obtained from the least-squares fittings of the plots in Figure 6-8, the activation energy was estimated as follows. Using equations 6-1, 6-5 and 6-8, it can be shown that

$$\frac{k_{in}'}{k_g} \propto \frac{k_{in}}{D_{12}} \propto \frac{\exp\left(-\frac{E_a}{RT}\right)}{T^{1.75}}. \qquad 6\text{-}15$$

Hence a plot of $\ln(T^{1.75}\, k_{in}'/k_g)$ against $1/RT$ should yield a straight line with a gradient $-E_a$.

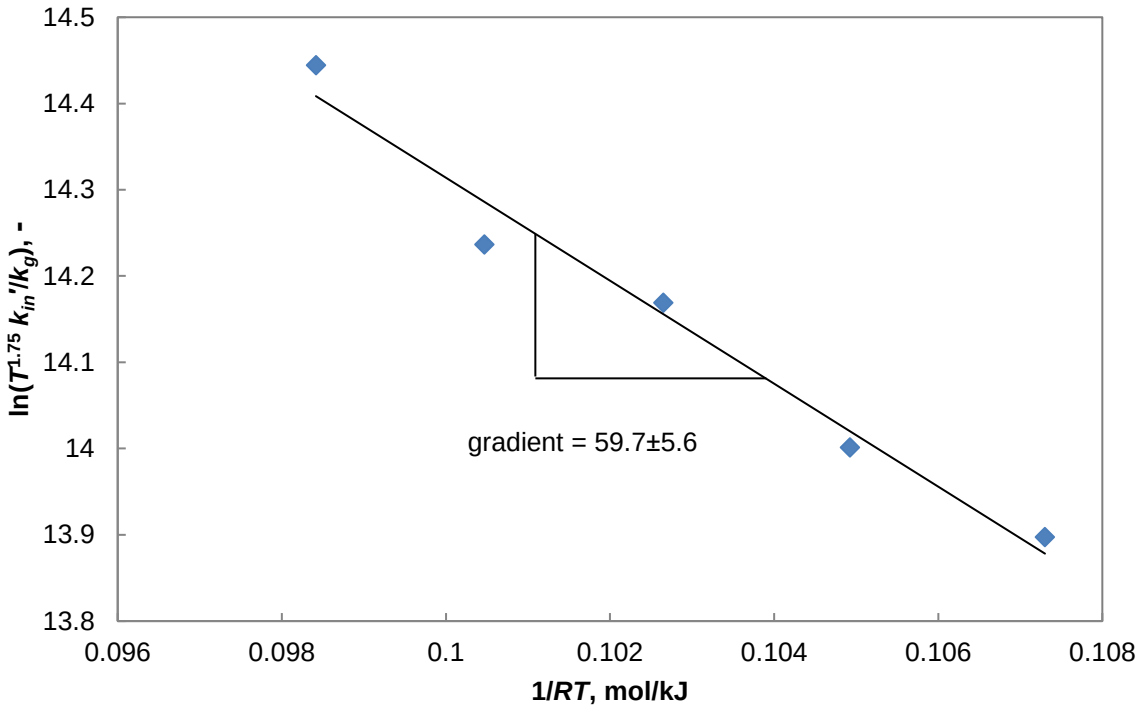


Figure 6-9 Modified Arrhenius plot for data obtained at 850°C, 875°C, 900°C, 925°C and 950°C, values of $k_{in}'$ and $k_g$ are extracted using data between 20% and 90% conversion at each temperature, as shown in Figure 6-8. The activation energy was found to be 59.7±5.6 kJ/mol, with a coefficient of determination of 0.974.

Figure 6-9 shows the determination of the activation energy. It can be seen that the results form a reasonable linear trend on the modified Arrhenius plot, from which the activation energy of the decomposition of CuO was found to be 59.7 kJ/mol with a standard error of 5.6 kJ/mol. The corresponding pre-exponential factor was calculated from the *y*-intercept as 632 $m^3$/mol/s.

When the shrinking grain model was used instead, the modified Arrhenius plot yielded an activation energy of 79.2±2.8 kJ/mol with a corresponding pre-exponential factor of 1350 $m^3$/mol/s. Both models fit the experimental results well. However, the shrinking grain model produces smaller values of $k_{in}$ compared to the first order reaction model when the activation energy and pre-exponential factor are used to back-calculate the rate constant.

### *6.4.3.4. Discrimination between the reaction models*

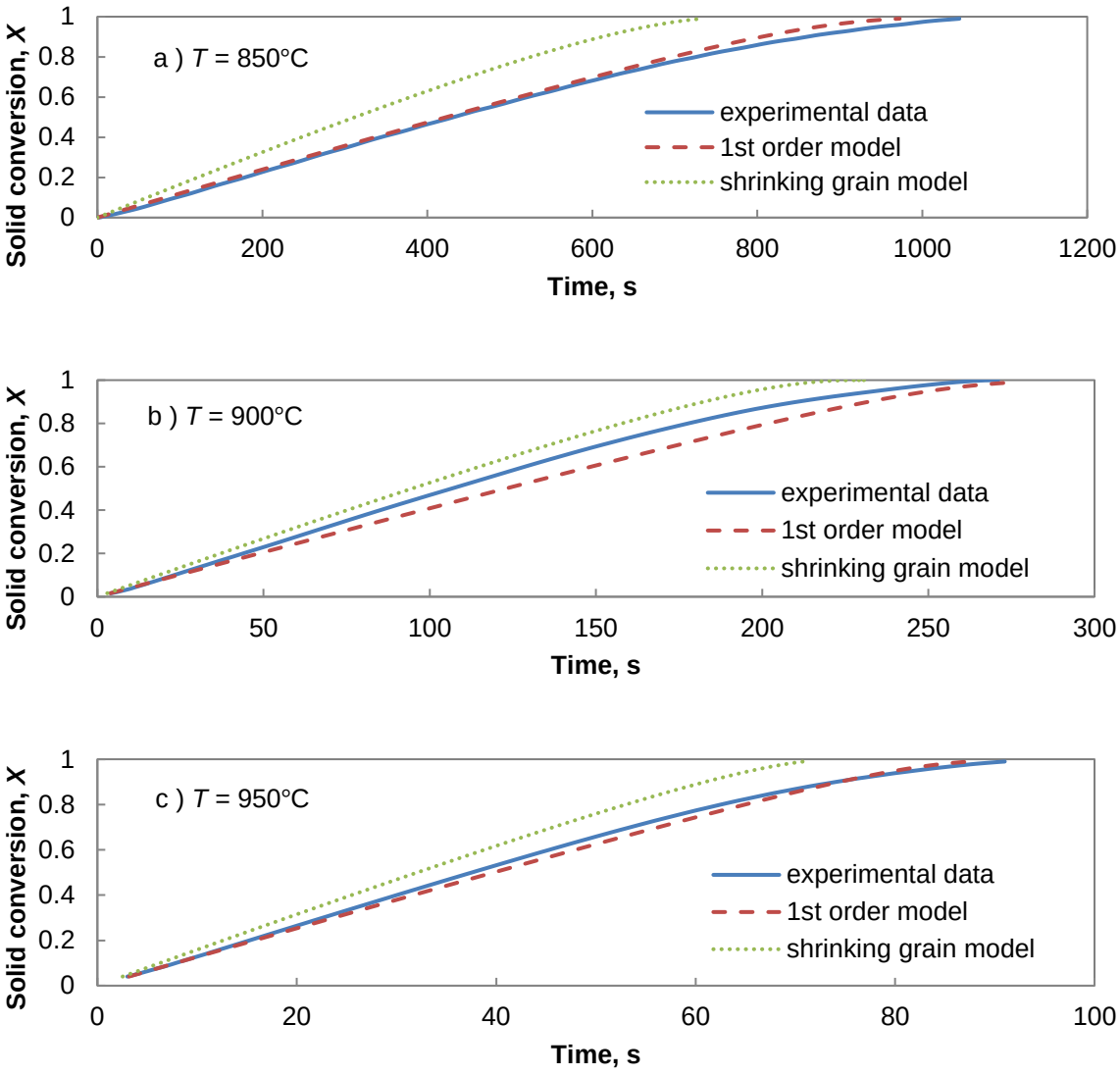


Figure 6-10 Model predictions for experiments in a taller crucible, hence lowered external mass transfer coefficient. Particle size 300-425 µm, sample mass 9.84 mg, reaction temperature a) 850°C, b) 900°C and c) 950°C.

To distinguish between the first order reaction model and the shrinking grain model, the kinetic parameters obtained in the previous section were used to model the reaction profile in the deeper alumina crucible with a height of 4 mm. The mass transfer

coefficient $k_g$ was modified to account for the change in the depth of the crucible and the model results are shown in Figure 6-10. It can be seen from Figure 6-10 that the first order reaction model provides better predictions over the temperature range of interest, between 850°C and 950°C, compared to the shrinking grain model although the goodness of fit varies considerably between different temperatures. Thus the first order reaction model appears to be superior to the shrinking grain model. However, it is worth noting that, as one might expect, the model results are much more sensitive to the rate of mass transfer than the rate of chemical reaction in this case and it would have been better to have validated the kinetic parameters in situations where the rate of mass transfer is fast – this will be discussed further in Chapter 7.

## *6.5. Discussion*

In this work, the activation energy of the OC was found to be 59.7 kJ/mol. In comparison, the activation energy of similar Cu-based OCs supported on $TiO_2$ and $ZrO_2$ were reported to be 58 kJ/mol and 67 kJ/mol, respectively (Clayton and Whitty, 2014), very close to the value found here. Interestingly, Clayton and Whitty (2014) also determined the apparent activation energy of the decomposition reaction in $N_2$, by taking the natural logarithm of the measured rate against 1/*T*. The apparent activation energies were found to be 264 kJ/mol and 284 kJ/mol respectively (and a similar apparent activation energy of 270 kJ/mol was found for a carrier consisting of 60 wt% CuO and 40 wt% $MgAl_2O_4$ (Adánez-Rubio *et al.*, 2014)). Following the argument presented earlier, this value of apparent activation energy should simply be the sum of the true activation energy due to the kinetics and the enthalpy of reaction for the decomposition, assuming the rate of reaction is first order with respect to the concentration of $O_2$. If the enthalpy of decomposition is taken from the literature, ~ 260 kJ/mol (Jacob and Alcock, 1975; NIST, 2011), the true activation energy would appear to be between 4 kJ/mol and 24 kJ/mol, significantly lower than that quoted by Clayton and Whitty (2014). In fact, this approach of subtracting $\Delta H_r$ from the apparent activation energy was adopted by Sahir *et al.* (2012) who reported a value of 20 kJ/mol as the activation energy for a similar OC supported on $ZrO_2$. In view of the results from Clayton and Whitty (2014), it is possible that the true value of $\Delta H_r$ for the decomposition of the OC used by Sahir *et al.* (2012) was lower than the literature value for pure CuO due to the interaction with support and other impurities, which would be consistent with the observation made in Chapter 5, so that the activation energy was underestimated.

On the other hand, very different results were found by Arjmand *et al.* (2012b). In their study, 0.1 g of wood char was introduced to a fluidised bed containing 1 g of OC mixed with 10 g of quartz sand in a constant flow of $N_2$ and it was argued that the wood char reacted quickly with the released $O_2$ to maintain a low oxygen partial pressure in the bed, eliminating the thermodynamic limitations. Using this approach, Arjmand *et al.* (2012b) found the apparent activation energy of the decomposition of the OC was 139 kJ/mol, significantly lower than the values found by Clayton and Whitty (2014). In the same study, Arjmand *et al.* (2012b) also measured the equilibrium concentration of $O_2$ at different temperatures for the carrier and from the graphical results presented, it can be estimated that the enthalpy of reaction for the decomposition of this particular carrier was ~ 225 kJ/mol, higher than the apparent activation energy reported. This peculiar result can be explained by the presence of internal mass transfer resistance within the OC particles, as recognised by the authors. The OC particles had a high BET surface area but relatively low porosity (Arjmand *et al.*, 2012b) so that the average pore diameter was very small, approximately 20 nm, based on the equivalent surface-volume diameter and even smaller if a cylindrical pore model were used. This contrasts with the OC particles used for the current study which have a low BET surface area and a relatively high porosity. As a result, the particles used by Arjmand *et al.* (2012b) exhibited significant internal mass transfer resistance despite their smaller size, compared to the particles used in this work. To a first approximation, the apparent activation energy of a chemical reaction is half the true value if the reaction is limited by internal mass transfer (Levenspiel, 1999). Using this result, the true activation energy of the decomposition of the OC carrier studied by Arjmand *et al.* (2012b) would be ~ 280 kJ/mol including the enthalpy of reaction and ~ 55 kJ/mol excluding $\Delta H_r$.

In conjunction with the information available from the literature, it appears that the activation energy associated with the kinetic rate constant is approximately 60 kJ/mol for CuO based OCs irrespective of the supporting material, so long as the support does not form a new phase with the CuO. At the same time, it also appears that if the equilibrium partial pressure of $O_2$ were to be fitted with an Arrhenius-type expression, the average value of $\Delta H_r$ for supported CuO is somewhat lower than the corresponding value for pure CuO (Jacob and Alcock, 1975; NIST, 2011). However, the magnitude of the rate of reaction at different temperatures depends also on the pre-exponential factor and a similar generalisation could not be made here, primarily due to the different models of $f(X)$ involved in different investigations.

## 6.6. Summary

In this chapter, the kinetics of the decomposition of the wet-mixed OC in an inert environment was investigated. From a theoretical approach, it was recognised that in order to obtain accurate kinetics parameters, the effect of thermodynamic equilibrium must be accounted for appropriately. This was done here by coupling the chemical kinetics with external mass transfer effect with suitable models to fit the experimental results and extract the chemical reaction term $k_{in}'(C_{eq} - C_b)$ and the mass transfer term $k_g(C_{eq} - C_b)$ separately. The effect of thermodynamic equilibrium, in the form of a concentration driving force, $(C_{eq} - C_b)$, can then be eliminated by taking the ratio of the two terms, hence isolating the rate constant. From the available experimental data, it was found that among the commonly used conversion functions, $f(X)$, describing the dependence of the rate of chemical reaction on the degree of conversion of the solid reactant, the first order reaction model, *i.e.* $f(X) = 1 - X$ was most appropriate. The final rate expression of the decomposition of the OC was found to be

$$\frac{dX}{dt} = 632\exp\left(-\frac{59.7 \pm 5.6}{RT}\right)(1-X)(C_{eq} - C_s), \qquad \text{6-16}$$

with $C_s$ representing the concentration of $O_2$ at the surface of the particles.

Following a critical analysis of the literature on the investigation of the kinetics of the decomposition of Cu-based carriers, it was concluded that the activation energy of the reaction, *i.e*. the temperature dependence of the rate constant, is approximately 60 kJ/mol for many carriers studied, irrespective of the preparation method or the nature of the support material, provided that the support did not form a new phase with the CuO. Thus this value could be used as a first approximation in the design of CLOU reactors with CuO in general. However, a common value for the pre-exponential factor could not be found, due to the different reaction models proposed and further work is required to verify whether there exists a universal rate expression for Cu-based OCs.

# 7. Verification of the chemical kinetics

## *7.1. Introduction*

In the previous chapter, the first-order reaction model and the shrinking grain model were found to fit the experimental results well. However, the first-order model was able to predict the reaction profile better in the situation where the mass transfer resistance external to each particle was higher. It should be noted, however, that the validation experiments were largely limited by external mass transfer and thus the observed kinetics were very sensitive to the external coefficient of mass transfer rather than to the rate constant of the chemical reaction. Thus, it was not possible to confirm with sufficient confidence that one or other model applied. In the present chapter, the kinetics of the same OC was investigated in a laboratory-scale fluidised bed, which exhibited faster external mass transfer characteristics than the TGA, thus enabling further discrimination between the two reaction models.

As noted in Chapter 6, to date, the kinetic studies conducted on OCs for CLOU have been done either in a TGA (*e.g.* Adánez-Rubio *et al.*, 2014; Clayton and Whitty, 2014; Clayton *et al.*, 2014) or a fluidised bed (*e.g.* Arjmand *et al.*, 2012b; Sahir *et al.*, 2012). Investigations utilising both the TGA and the fluidised bed (*e.g.* Gayán *et al.*, 2012; Xu *et al.*, 2013) often characterised different aspects of the OC in each apparatus. Of course, if the kinetic parameters reported in the literature corresponded to the rate of chemical reaction as desired, the parameters would be applicable in all situations; however this has not been formally confirmed so far. The aim of this chapter is to use the kinetic parameters obtained from the TGA studies described in Chapter 6 with appropriate models describing the transport processes in a bubbling fluidised bed to produce a reactor model for the CLOU reaction. The intention here was a) to provide further information on the validity of the two reaction models considered in Chapter 6, and b) to confirm experimentally whether the kinetic parameters obtained are, indeed, associated with the kinetics of the chemical reaction rather than, as yet unknown, transport or other effects. Parts of this chapter have been published in Hu *et al.* (2016).

## 7.2. Experimental

The laboratory-scale fluidised bed used for this study was described in Section 2.5.1. In a typical experiment, the fluidised bed with an i.d. of 17 mm was set up as shown in Figure 7-1 on the right. The temperature of the bed was kept at a constant value between 850°C and 950°C and approximately 8 g of silica sand in the size fraction 300-355 µm was fluidised in a stream of $N_2$. The flowrate varied between 0.6 l/min up to 2.2 l/min as measured at 20°C and 1 bar across the experiments but in each experiment, the flowrate was kept constant. The resulting superficial gas velocity in the fluidised bed was between 5 and 18 times that of the minimum fluidisation velocity estimated using the correlation by Wen and Yu, (1966). The temperature of the fluidised bed was measured using a type K thermocouple and the off gas was sampled by the UEGO sensor (described in Section 2.5.1) *via* a 1/16 inch stainless steel tube located in the freeboard. A slight vacuum was maintained in the UEGO sensor in normal operation so that no auxiliary equipment was required for gas sampling. When a constant reading from the UEGO sensor was obtained, a small batch of the pre-treated OC (fully reduced in 5 vol% $H_2$ in $N_2$ and then re-oxidised in air at 850°C for 3 times in a fluidised bed, as before) in the size fraction 300-425 µm, and mass between 5 mg and 20 mg, was dropped into the fluidised bed from the top of the reactor. The concentration of $O_2$ in the off gas was measured by the UEGO sensor until the reading dropped to the same constant level before the experiment, marking the end of

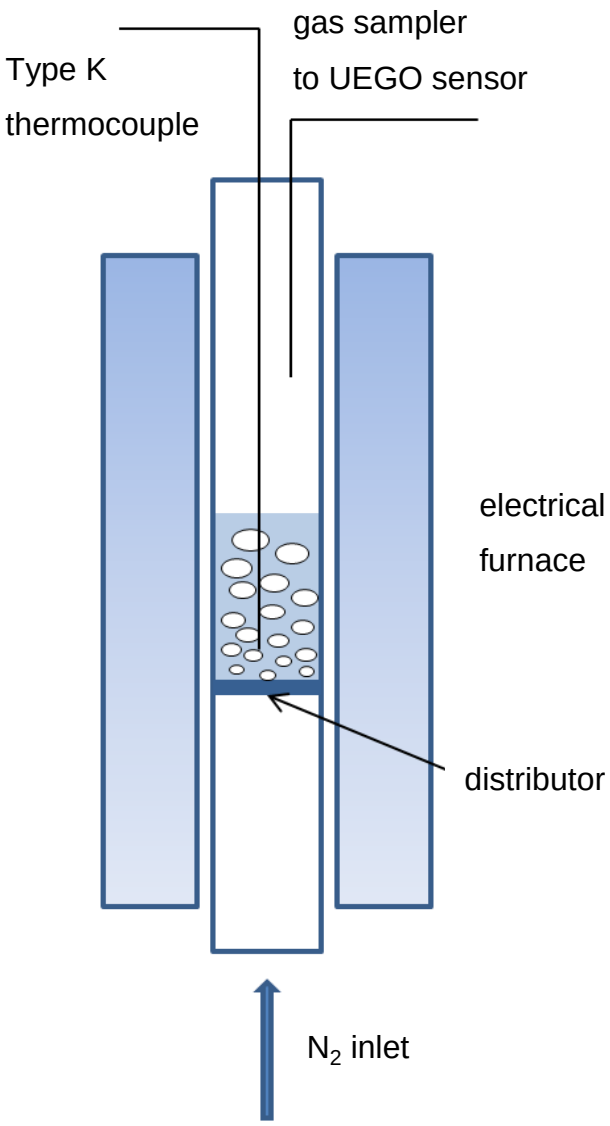


Figure 7-1 An illustration of the batch bubbling fluidised bed reactor.

the reaction. The reacted OC particles were not recovered from the bed before subsequent experiments because $O_2$ released by the carriers would result in a concentration always less than 10% of the corresponding value at equilibrium and hence the reduced particles from previous batches would not be able to re-oxidise in such an environment and would have no effect on subsequent experiments.

## *7.3. Modelling approach*

### *7.3.1. Fluidised bed model*

The following model of the bubbling fluidised bed, depicted in Figure 7-2, is based on the two phase theory of fluidisation (Davidson and Harrison, 1963; Kunii and Levenspiel, 1991). In this theory, the bubbling bed is assumed to consist of two separate phases – a particulate phase, or emulsion phase, which contains all the particles and just enough gas to maintain minimum fluidisation, and a bubble phase carrying the remaining gas. The particulate phase was assumed to be well mixed and maintained at the minimum fluidisation conditions with a superficial gas velocity $U_{mf}$ and a corresponding voidage $\varepsilon_{mf}$. The bubble phase gas was assumed to be in plug flow and in constant contact with the particulate phase to allow for the exchange of gases but not particles. Here, it was assumed that the fluidised bed was isothermal and isobaric throughout the reaction. The volume of each phase was also assumed to be constant since the amount of $O_2$ released during the reaction was small compared to the volume of the bed. The mass transfer of gases between the bubble phase and particulate phase can be estimated using an interphase mass transfer coefficient, $k_{gt}$, (Sit and Grace, 1981)

$$k_{gt} = \frac{U_{mf}}{3} + \sqrt{\frac{4D\varepsilon_{mf}u_b}{\pi d_b}}\,. \qquad 7\text{-}1$$

The minimum fluidisation velocity, $U_{mf}$, was estimated using the correlation of Wen and Yu, (1966), as outlined in Section 2.5.1 and the binary diffusion coefficient, $D$, for $N_2$ and $O_2$, was calculated using the Fuller-Schettler-Giddings equation (Fuller *et al.*, 1966). The bubble velocity, $u_b$, was related to the bubble diameter $d_b$ *via* (Davidson and Harrison, 1963)

$$u_b = 0.711\sqrt{gd_b} + U_0 - U_{mf}\,, \qquad 7\text{-}2$$

where $g$ is the gravitational acceleration and $U_0$ is the superficial gas velocity through the bed. Cai *et al.* (1994) proposed the following correlation for the bubble diameter, $d_b$, as a function of the vertical distance of the bubble from the distributor, $H$:

$$d_b = 0.38H^{0.8}\left(U_0 - U_{mf}\right)^{0.42} \times \exp\left(-1.4\times10^{-4} - 0.25\left(U_0 - U_{mf}\right)^2 - 0.1\left(U_0 - U_{mf}\right)\right). \qquad 7\text{-}3$$

The total volume of the fluidised bed, $V_t$, was taken as the product of the cross-sectional area of the reactor and the height of the fluidised bed, $H_{\max}$, which can be calculated using the following correlation (Babu *et al.*, 1978)

$$\frac{H_{\max}}{H_{mf}} = 1 + \frac{14.3\left(U_0 - U_{mf}\right)^{0.738} d_p^{\,1.006}\,\rho_p^{\,0.376}}{\left(U_{mf}\right)^{0.937}\rho^{0.126}}\,, \qquad 7\text{-}4$$

where $d_p$ and $\rho_p$ denote the diameter and density of the solid particles, respectively, and $\rho$ is the density of the fluidising gas. Also, $H_{mf}$ is the height of the fluidised bed at minimum fluidisation. It is straightforward to calculate the volume of the particulate phase, $V_{em}$, knowing the mass, particle size, density and voidage of the sand particles used and the volume of the bubble phase, $V_b$, is the difference between the total volume and the volume of the particulate phase and the bubble fraction in the fluidised bed is given by

$$\varepsilon_b = \frac{V_b}{V_t}\,. \qquad 7\text{-}5$$

Hence the volumetric flowrates of the gas through the particulate phase and the bubble phase are given by $U_{mf}\,A_x(1-\varepsilon_b)$ and $U_0A_x - U_{mf}\,A_x(1-\varepsilon_b)$, respectively, with $A_x$ being the cross sectional area of the fluidised bed.

To calculate the rate of gas mass transfer between the particulate and the bubble phases, it was further assumed that the bubble phase occupies a constant cross sectional area at any height in the bed, $\varepsilon_bA_x$. The bubble phase was modelled as $n$ well-mixed segments in series in the vertical direction, each segment in contact with the particulate phase for the purpose of gas exchange. All the bubbles were assumed to be spherical so that the interfacial area for mass transfer in each segment, $A_i$, was

$$A_i = \frac{6V_b}{d_b n}. \qquad 7\text{-}6$$

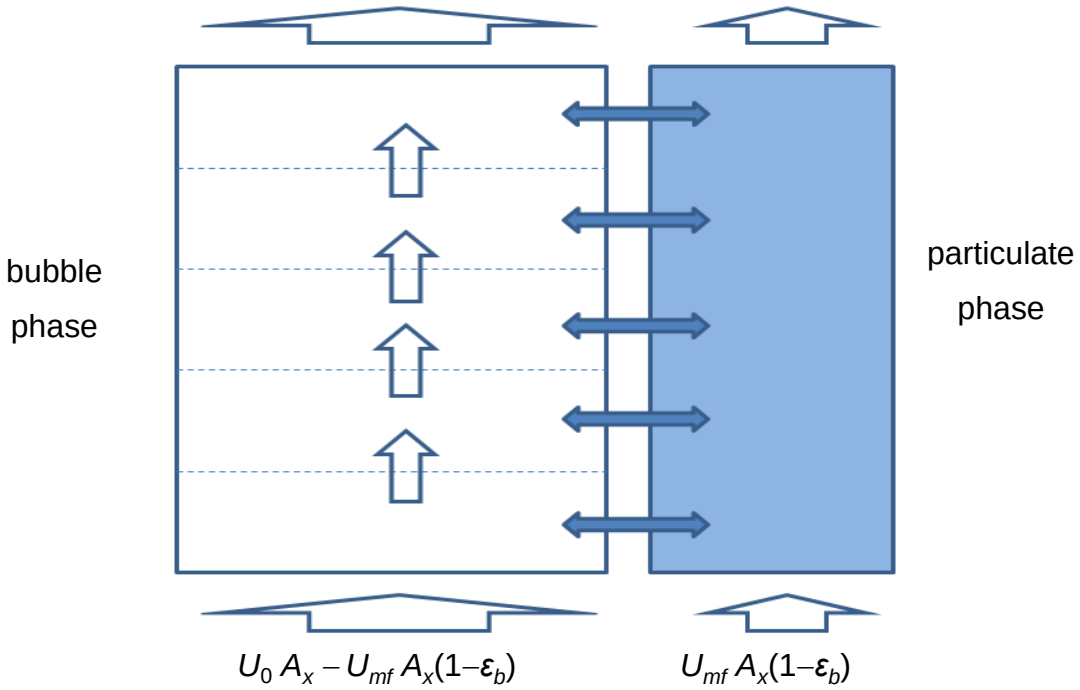


Figure 7-2 A graphical representation of the implementation of the two phase theory of fluidisation for a bubbling fluidised bed.

Lastly, it was assumed that once the gas leaves the two-phase region of the fluidised bed and enters the freeboard, the two streams mix immediately to form a single well mixed stream and the resulting concentration of $O_2$ is the model equivalent to the concentration measured using the UEGO sensor.

### *7.3.2. Single particle model*

Since only a small mass of OC particles was dropped into the fluidised bed in any given experiment, it was assumed that the particles mixed into the particulate phase instantaneously and the OC particles were sufficiently far apart from each other for their being treated as a collection of single particles in an infinite medium.

In Chapter 6, it was concluded that the rate of internal mass transfer was fast compared to the rate of decomposition of the OC investigated. Nevertheless, a single particle model accounting for internal mass transfer was constructed so that a) the conclusion could be investigated with a detailed, numerical model and b) the model could be used to describe the behaviour of larger particles in which the internal mass transfer might become significant. In addition, the effect of heat transfer was also considered.

In constructing the single particle model, it was assumed that the particle concerned was spherical and uniform in composition, porosity, *etc*. It was further assumed that the atmosphere surrounding the particle was uniform in all directions so that the problem was spherically symmetric. Since only $N_2$ and $O_2$ were present and the concentration of $O_2$ was low, Fick's law, rather than the Stefan-Maxwell formulation, was used to describe the diffusion of gases within the particle for simplicity. The modelling approach for a single particle is presented below.

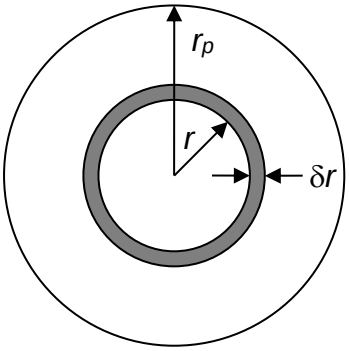


Figure 7-3 A general element (spherically-symmetric shell) considered within a spherical particle.

Consider a general element in the shape of a shell at distance $r$ from the centre of the particle with thickness $\delta r$, as shown in Figure 7-3. The conservation of mole of gas phase $O_2$ within the element, using Fick's second law, gives, in terms of the concentration of $O_2$, $C$, and the local conversion of the solid within the element, $X$:

$$\varepsilon_p \frac{\partial C}{\partial t} = \frac{1}{r^2}\frac{\partial}{\partial r}\left(r^2 D_{eff}\frac{\partial C}{\partial r}\right) + \frac{\rho_m}{4}\frac{dX}{dt}, \qquad 7\text{-}7$$

in which $\varepsilon_p$ represents the porosity of the OC particle; $\rho_m$ represents the molar density of CuO for the given particle, *i.e.* the number of moles of CuO per unit volume of the OC particle and the factor 4 comes from the stoichiometry of the decomposition, reflecting the fact that the molar ratio of CuO to the produced $O_2$ is 4:1; $D_{eff}$ is the effective diffusion coefficient inside the particle and was estimated using

$$D_{eff} = \frac{D\varepsilon_p}{\tau^2} \qquad 7\text{-}8$$

where $D$ is the binary diffusion coefficient for $O_2$ and $N_2$. Here, $\tau$ is the tortuosity factor accounting for the additional length the gas molecules must travel when diffusing through the tortuous pore network within the particle, compared to a straight-line distance. A typical value of 2 is used for $\tau^2$ for the estimation of the effective diffusivity.

It should be noted that Knudsen diffusion is not considered here because the OC particles used were macro-porous, evident from the very small BET surface area (0.810 $m^2/g$) and rather large porosity of 0.66, so that the Knudsen diffusion did not apply.

Similarly, the energy equation applied to the system, assuming Fourier's law, is given by

$$c_p \frac{\partial T}{\partial t} = \frac{1}{r^2}\frac{\partial}{\partial r}\left(r^2 \lambda_s \frac{\partial T}{\partial r}\right) + \frac{\rho_m}{4}\frac{dX}{dt}\left(-\Delta H_r\right), \qquad 7\text{-}9$$

where $c_p$ is the volumetric heat capacity of the solid, $T$ is the thermodynamic temperature at position $r$ and $\lambda_s$ is the thermal conductivity in the solid. $\Delta H_r$ is the enthalpy of reaction per mole of $O_2$ produced from the decomposition reaction, as before. The value of $c_p$ can be approximated using the Dulong-Petit law (Dulong and Petit, 1819) as $3R$ per mole of atoms and the contribution from gases present in the pores of the particle has been neglected since the number density of the gas molecules is negligible compared to that of the solid atoms. The thermal conductivity for the particle was taken to be 0.5 W/m/K, a typical value for porous ceramic materials (Litovsky *et al.*, 1996).

Both the first-order reaction model and the shrinking grain model obtained from Chapter 6 can be used for the reaction term in equations 7-7 and 7-9 and the goodness of fit of the results obtained from each model to the experimental results was used to verify the validity of the models.

In order to solve equations 7-7 and 7-9, it was assumed that the OC particles were fully oxidised when dropped into the fluidised bed and all the residual gaseous $O_2$ initially present within the pores of the particles had been flushed out before the particles reached the dense bed. Also, the particles only started to heat up when they were mixed into the particulate phase. These initial conditions can be represented mathematically as

$$\begin{cases} X(0,r) = 0 & (a) \\ C(0,r) = 0 & (b) \\ T(0,r) = 293\,\mathrm{K} & (c) \end{cases}. \qquad 7\text{-}10$$

The boundary conditions of the problem are given by

$$\begin{cases} \dfrac{\partial C}{\partial r}(t,0)=0 & (a) \\ \dfrac{\partial T}{\partial r}(t,0)=0 & (b) \\ -D_{eff}\left.\dfrac{\partial C}{\partial r}\right|_{r=r_p}=\dfrac{Sh\times D}{2r_p}\left(C\big|_{r=r_p}-C_{em}\right) & (c) \\ -\lambda_s\left.\dfrac{\partial T}{\partial r}\right|_{r=r_p}=\dfrac{Nu\times\lambda_{N2}}{2r_p}\left(T\big|_{r=r_p}-T_{em}\right)+5.67\times10^{-8}\varepsilon\left(T\big|_{r=r_p}{}^4-T_{em}{}^4\right) & (d) \end{cases}. \qquad 7\text{-}11$$

The BCs 7-11 (*a*) and (*b*) reflect the spherically-symmetric nature of the particles being modelled and BCs 7-11 (*c*) and (*d*) match the mass and heat fluxes, respectively, entering the particle to the corresponding values leaving the particulate phase of the fluidised bed. In equation 7-11 (*c*), $C_{em}$ is the concentration of $O_2$ in the particulate phase and *Sh* is the Sherwood number, obtained using the following correlation (Avedesian and Davidson, 1973; La Nauze, 1985):

$$Sh = 2\varepsilon_{mf} + 0.69\left(\frac{d_p U_{mf}}{\varepsilon_{mf}\nu}\right)^{1/2}\left(\frac{\nu}{D}\right)^{1/3}, \qquad 7\text{-}12$$

where $\nu$ is the kinematic viscosity of the fluidising gas and $d_p$ is the diameter of the particle . In equation 7-11 (*d*), $T_{em}$ is the temperature of the particulate phase; $\lambda_{N2}$ is the thermal conductivity of $N_2$ gas. The Nusselt number for convective heat transfer, *Nu* was estimated using a correlation similar to equation 7-12 by virtue of the analogy between heat and mass transfer (*e.g.* Scott *et al.*, 2004):

$$Nu = 2 + 1.0\left(\frac{d_p U_{mf}}{\nu}\right)^{0.6}\left(\frac{d_p}{d_{sand}}\right)^{0.26}. \qquad 7\text{-}13$$

The correlation yielded a Nu ~2. The black body assumption was used in the numerical solution, i.e. $\varepsilon = 1$.

### *7.3.3. Solution*

To obtain the solution, the single particle model must be coupled with the fluidised bed model. Since the amount of OC particles is small, compared to the fluidised bed of sand, in coupling the two models, it was assumed that the temperature of the fluidised bed remains constant at $T_{em}$. Furthermore, it was assumed that the volume of the bubble phase and that of the particulate phase did not change during the course of reaction. This is not strictly true since gaseous $O_2$ is produced from the OC particles; however it is a good approximation since the equilibrium concentration of $O_2$ at the reaction temperatures between 850°C to 950°C is below 0.5 mol/m$^3$, about 5 vol% of

the total gas and the actual concentration measured in all experiment was lower than 0.15 mol/m$^3$ so that the change in volume of the gas was insignificant.

Since all the OC particles reside within the particulate phase of the fluidised bed, the release of $O_2$ from the OC can be considered as the source of $O_2$ to the particulate phase. Thus the mass balance of $O_2$ in the particulate phase is given by

$$\begin{aligned}&\sum_{i=1}^{n} k_{gt} A_i \left(C_i - C_{em}\right) + \frac{Sh \times D}{2r_p}\left(C\big|_{r=r_p} - C_{em}\right) \times 4\pi {r_p}^2 n_p \\ &= U_{mf} A_x \left(1-\varepsilon_b\right) C_{em} + V_{em}\varepsilon_{mf} \frac{dC_{em}}{dt}\end{aligned}, \qquad 7\text{-}14$$

where the summation represents the amount of $O_2$ transferred from the bubble phase and the concentration of $O_2$ in each small segment of the bubble phase is represented by $C_i$. $n_p$ is the total number of OC particles in the fluidised bed. The mass balance of $O_2$ in the $i^{th}$ segment of the fluidised bed is

$$\left(U_0 A_x - U_{mf} A_x \left(1-\varepsilon_b\right)\right)\left(C_{i-1} - C_i\right) = k_{gt} A_i \left(C_i - C_{em}\right) + \frac{V_b}{n}\frac{dC_i}{dt}, \qquad 7\text{-}15$$

and for the first segment, $C_0 = 0$ since only $N_2$ is entering the fluidised bed.

Equations 7-14 and 7-15 can be solved simultaneously with equations 7-7 and 7-9 using the method of lines, *i.e.* discretising the particle in the radial direction to transform equations 7-7 and 7-9 into a system of differential equations with respect to time only. For example, if a particle were discretised into thin shells of thickness $\delta r$, as shown in Figure 7-3 earlier, the spatial derivative at position $r_i$ in equation 7-9 can be approximated using the central difference as

$$\frac{\partial}{\partial r}\left(r^2 \frac{\partial T}{\partial r}\right)\bigg|_{r=r_i} \approx \frac{\left(r + \frac{\partial r}{2}\right)^2 \frac{T_{i+1} - T_i}{\delta r} - \left(r + \frac{\partial r}{2}\right)^2 \frac{T_i - T_{i-1}}{\delta r}}{\delta r}, \qquad 7\text{-}16$$

where $T_{i+1}$, $T_i$ and $T_{i-1}$ are the temperatures of the $i$+1$^{th}$, $i^{th}$ and $i$–1$^{th}$ element, respectively. The resulting system of ODEs with respect to $t$ can be solved using the standard ODE solver ode15s available in MATLAB®. Once the equations have been solved, the concentration of $O_2$ in the gas leaving the fluidised bed, $C_{out}$, was calculated using the weighted average

$$C_{out} = \frac{\left(U_0 A_x - U_{mf} A_x \left(1-\varepsilon_b\right)\right) C_n + U_{mf} A_x \left(1-\varepsilon_b\right) C_{em}}{U_0 A_x}. \qquad 7\text{-}17$$

Accordingly, the profile of $C_{out}$ could be compared with the experimental results.

## 7.4. Results

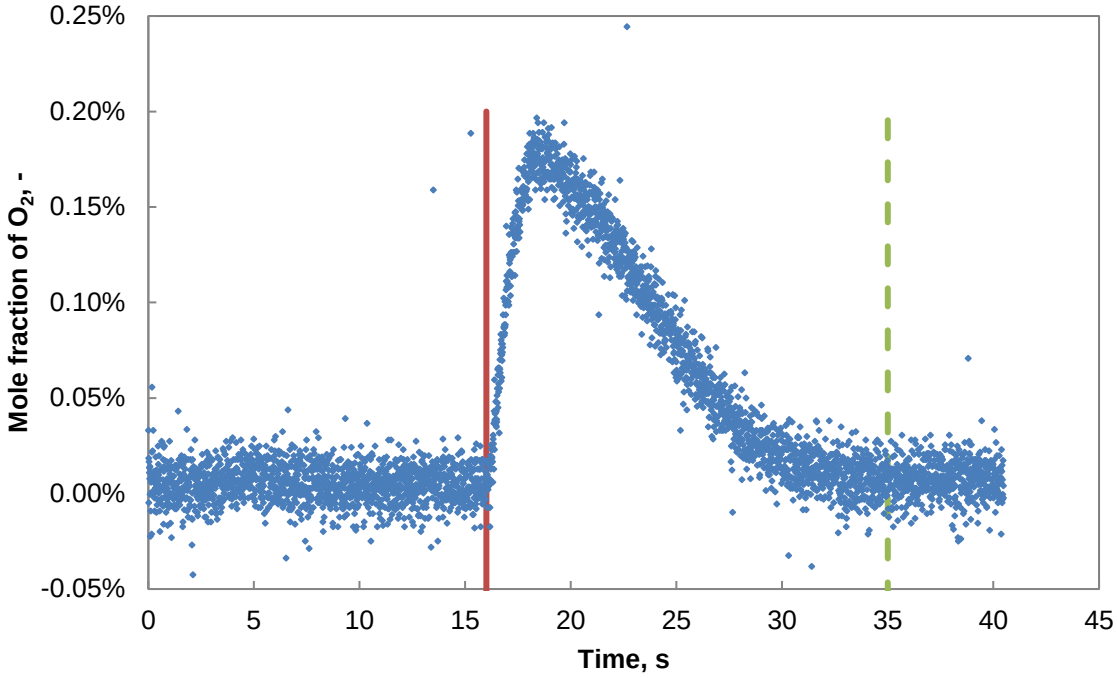


Figure 7-4 A typical reaction profile of the decomposition of the OC in a fluidised bed. Mass of OC used: 4.9 mg; bed temperature: 904°C; fludising gas flowrate: 1.0 l/min of $N_2$, measured at 20°C and 1 bar ($U_0/U_{mf} \approx 11$). The start of the reaction is marked by the red solid vertical line and the end by the green dashed vertical line.

A typical concentration profile of $O_2$, measured experimentally, is shown in Figure 7-4. It can be seen that the rate of decomposition increased to a maximum shortly after the sample was dropped into the fluidised bed and then gradually diminished to zero as the reaction proceeded. The oxygen released, as measured by integrating the concentration profile between the start and end point of the experiment, was 1.08 times the amount expected from the amount and composition of the OC used. The slight error in the mass balance is most likely due to the fact that the baseline value of the mole fraction of $O_2$ was slightly positive, as can be seen between 35 and 40 s in Figure 7-4. It is worth noting that the maximum mole fraction of $O_2$ measured during the experiment was approximately 0.17%, far below the corresponding value at equilibrium, 1.54% (NIST, 2011), so that it can be expected that the reaction was largely limited by kinetics rather than by approaching chemical equilibrium.

In the following section, the effect of gas flowrate and the mass of OC particles used on the reaction profile will be discussed.

### 7.4.1. *Effect of gas flowrate and mass of OC*

Although the measured mole fraction of $O_2$ was small compared to the equilibrium value, as exemplified by Figure 7-4, it is theoretically possible that the rate of mass transfer between the particulate and the bubble phases was slow so that the concentration of $O_2$ was close to equilibrium in the particulate phase gas but the overall concentration of the off gas measured from the freeboard appeared to be low due to dilution by the bubble phase. This issue was discussed by Chuang *et al.* (2010). In addition, the mixing of particles within the fluidised bed could also influence the rate of reaction. To establish the importance of these factors, experiments were conducted at the same bed temperature, 904°C, with different gas flowrates and masses of the OC.

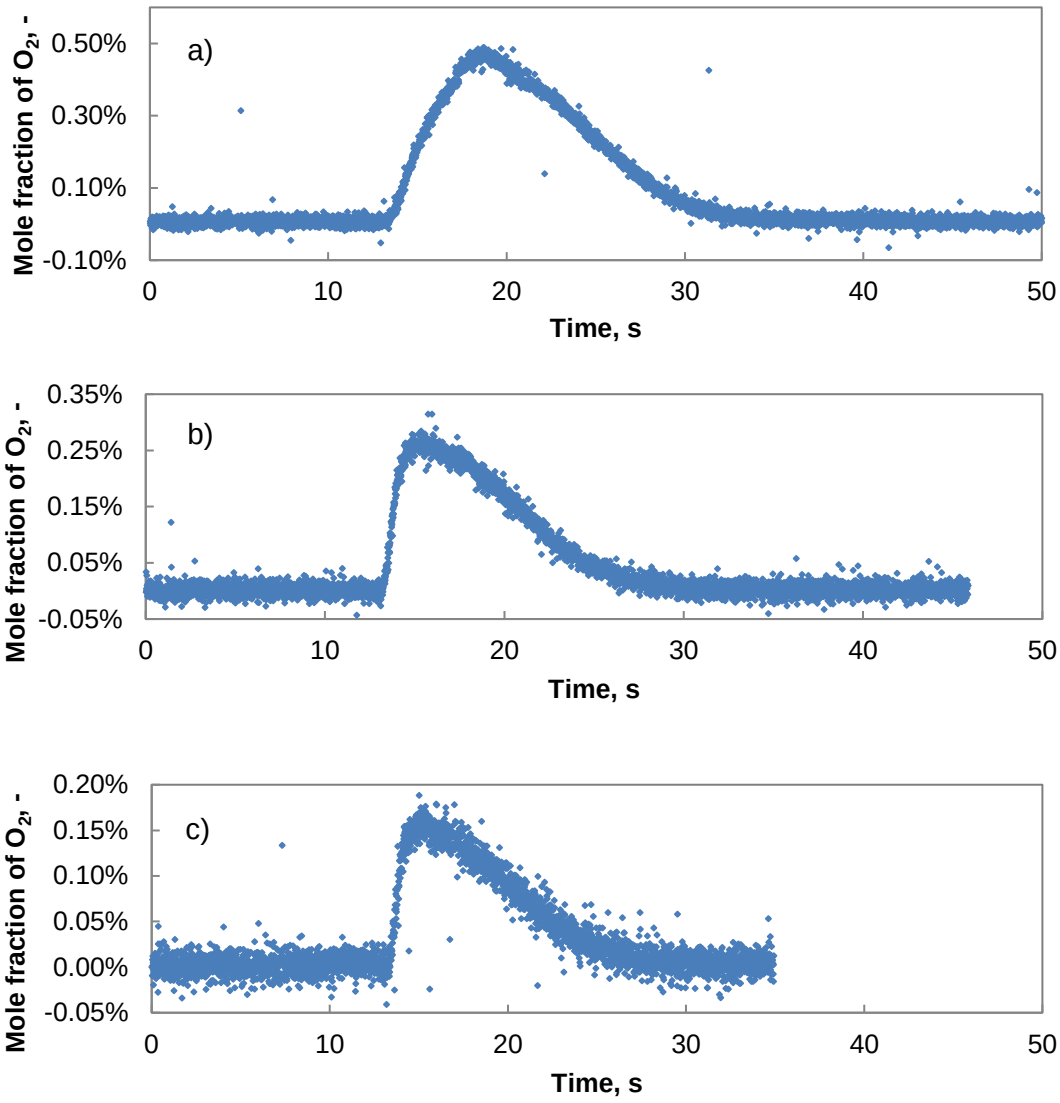


Figure 7-5 Reaction profiles at 904°C using different gas flowrate. a) sample mass 9.5 mg, gas flowrate 0.6 l/min ($U_0/U_{mf} \approx 5$); b) sample mass 10.2 mg, gas flowrate 1.4 l/min ($U_0/U_{mf} \approx 11$); c) sample mass 10.0 mg, gas flowrate 2.2 l/min ($U_0/U_{mf} \approx 18$).

First, the effect of gas flowrate was investigated. As shown in Figure 7-5, with the sample mass ~ 10 mg, the experiment with a gas flowrate of 0.6 l/min took longer to complete compared to the experiments with higher fluidising flowrates whereas no significant difference in the time for complete reaction could be seen between the experiments with higher flowrates (1.4 l/min and 2.2 l/min). Furthermore, the shape of the reaction profile with the lowest flowrate appeared different from the others. Specifically, the initial rate of rise of the rate of reaction occurred much more slowly than in other cases. A possible explanation for the difference in shape seen in Figure 7-5 a) is that at lower gas flowrates, it would take longer for the OC particles to mix completely with the sand in the particulate phase when dropped into the fluidised bed at low gas flowrates. Consequently, a significant $O_2$ concentration could have built up within the volume containing the dispersing OC particles, limiting the rate of release of $O_2$ initially by affecting the concentration driving force for decomposition. Clearly, this effect would diminish once the particles were dispersed within the particulate phase. Hence the rate of reaction in Figure 7-5 a) was slow initially, but the reaction profile after the maximum was reached appeared similar to the reaction profiles in Figure 7-5 b) and c). The radial dispersion coefficient for particles estimated using the correlation of Shi and Fan (1984)

$$D_{SL} = (U_0 - U_{mf}) H_{mf} \times 0.46 \times \left( \frac{(U_0 - U_{mf}) d_p}{\nu} \right)^{-0.21} \left( \frac{H_{mf}}{d_p} \right)^{0.24} \left( \frac{\rho_p - \rho}{\rho} \right)^{-0.43}, \qquad 7\text{-}18$$

was 1.05 x $10^{-4}$ $m^2/s$ for the case Figure 7-5 a) and the time constant for radial mixing was estimated to be 2.8 s from $L^2/D_{SL}$, where $L$ was taken as the diameter of the fluidised bed, 1.7 cm. The time constants for cases in Figure 7-5 b) and c) are 1.3 s and 0.9 s, respectively. The decreasing time constants calculated are in agreement with the decreasing time taken for the rate of reaction to reach the maximum value in Figure 7-5. However, it should be noted that although the above correlation fitted experimental results with $U_0/U_{mf}$ between 1.5 and ~20 well, the diameter and height of the fluidised beds used were much larger than those used in this work (Shi and Fan, 1984). Hence, the estimated values of $D_{SL}$ might be in error. In addition, the maximum concentration reached in the fluidised bed was higher with a smaller flowrate as seen in Figure 7-5. Therefore the concentration driving force for the decomposition reaction would be lowered – in fact the maximum concentration reached in Figure 7-5 a) was about 30% of the equilibrium value whereas the maximum seen in Figure 7-5 c) was

only about 10%. It thus appears that the reaction is more likely to be limited by chemical kinetics using a higher gas flowrate.

Secondly, the effect of sample mass was investigated. As shown in Figure 7-6, the reaction profiles were not affected by the mass of sample used, within experimental error, and the maximum concentration of $O_2$ measured in each experiment was found to be proportional to the mass of sample added. This result confirms that interphase mass transfer within the fluidised bed is not a significant factor because if the reaction were limited by interphase mass transfer, the time for complete reaction would be approximately proportional to the mass of sample added and the maximum concentration measured would be independent of the sample mass. Furthermore, results from the numerical modelling also support this conclusion. As shown in Figure 7-7, the concentration of $O_2$ in the bubble phase matches that in the particulate phase closely at a given time during the reaction except at positions close to the distributor where the concentration in the bubble phase is primarily determined by the inlet condition. It is also seen that the concentration in the bubble phase exceeds that in the particulate phase higher, this is because the concentration of $O_2$ in the gas in the particulate phase was decreasing with time at this instance and the plug flow nature of the bubble phase implies that at higher heights the concentration of the bubble phase lags behind that of the particulate phase and hence higher.

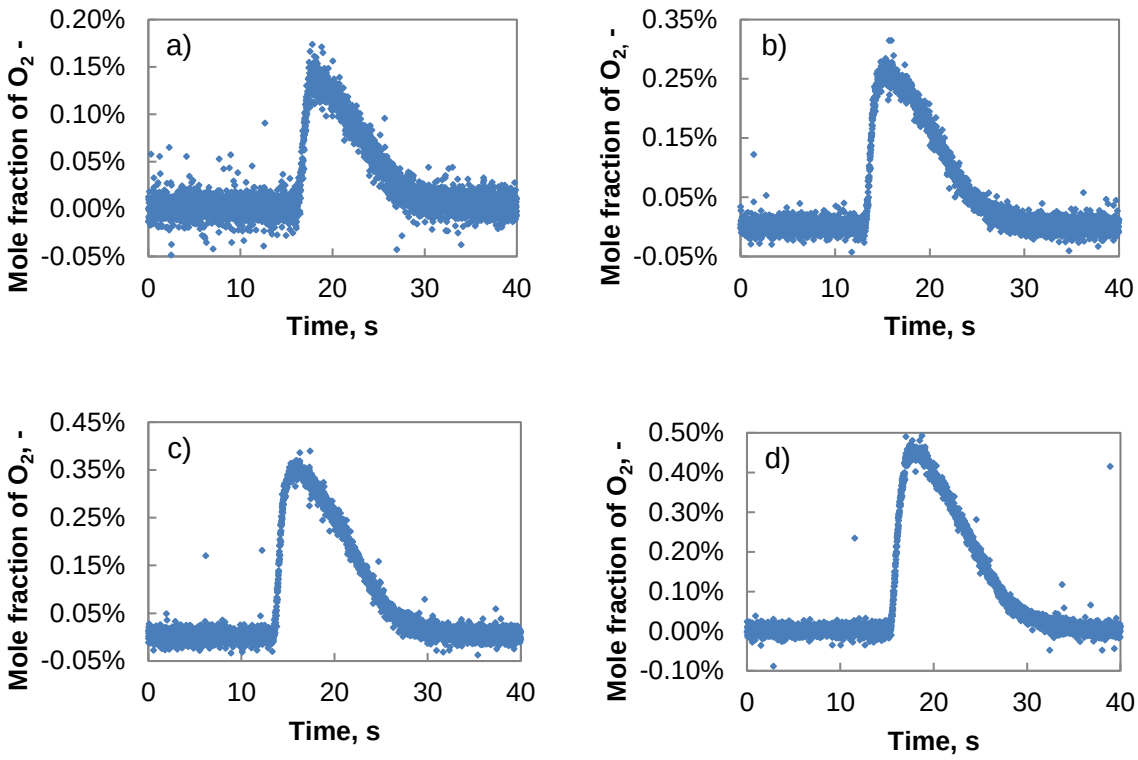


Figure 7-6 Reaction profiles at 904°C using different sample mass, with a gas flowrate of 1.4 l/min ($U_0/U_{mf} \approx 11$). Sample mass used: a) 5.4 mg; b) 10.2 mg; c) 15.0 mg; d) 19.2 mg.

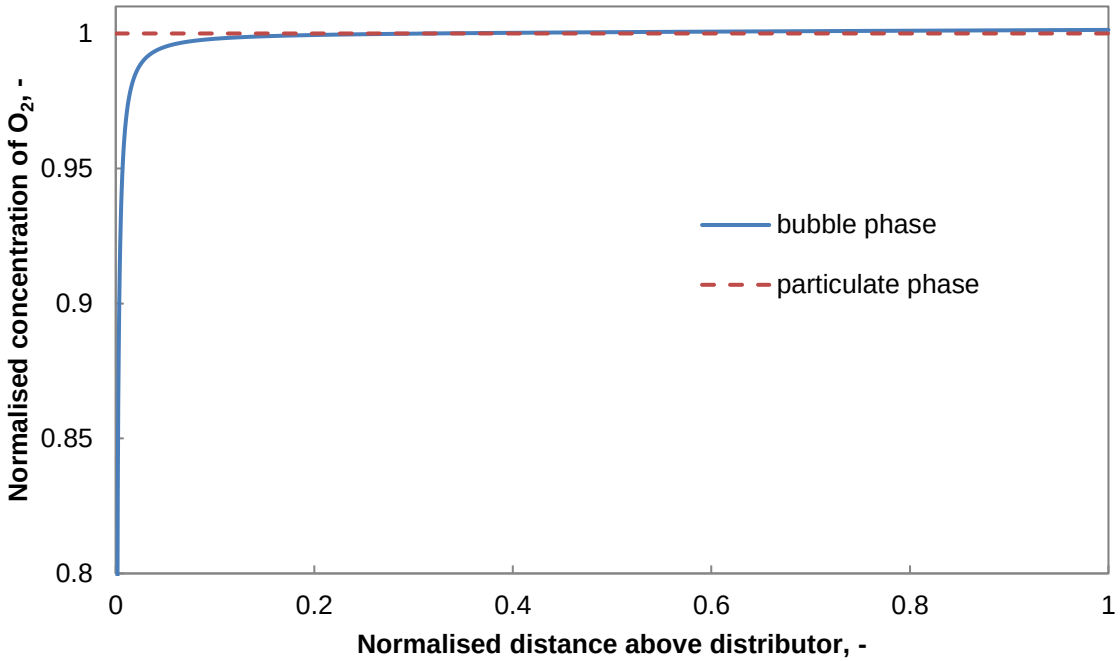


Figure 7-7 the concentration profiles in the bubble phase and particulate phase obtained from the numerical modelling. Input parameters: Temperature 904°C, mass of sample: 19.2 mg, gas flowrate: 1.4 l/min. The profiles are taken at $t$ = 1.3 s after the

reaction started. The concentrations are normalized against that in the particulate phase.

### *7.4.2. Validation of the numerical model*

In view of the fact that mixing within the particulate phase becomes important at low gas flowrates, the model results were validated against experiments performed with high gas flowrates.

The concentration profile of $O_2$ measured by the UEGO sensor in one such experiment is shown in Figure 7-8, together with the model results produced using the first order reaction model and the shrinking grain model, respectively. The input parameters to the model are the temperature of the fluidised bed, measured as 904°C, the mass of OC particles used, 10 mg and the flowrate of the fluidising $N_2$, 2.2 l/min at 20°C and 1 bar.

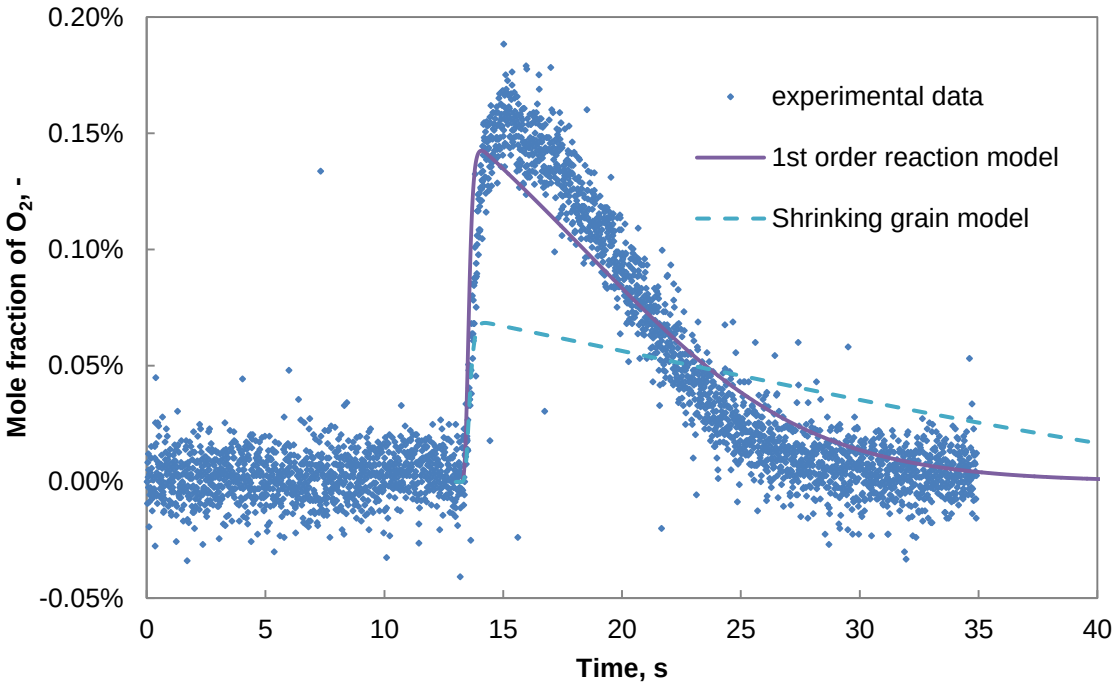


Figure 7-8 Reaction profile of a typical experiment conducted at 904°C in a fluidised bed with a $N_2$ flowrate of 2.2 l/min (20°C and 1 bar). The initial mass of the OC particles was 10.0 mg.

It can be seen from Figure 7-8 that the results obtained using the first-order reaction model slightly underestimated the rate of reaction. In particular, the maximum concentration calculated from the model was ~10% lower than the measured value. On the other hand, the shrinking grain model produced results significantly different from the experiment and similar results were observed in other experiments with

different sample masses, gas flowrates and temperatures. Consequently, it was concluded that the first-order reaction model and the associated kinetic parameters should be used for the decomposition of the OC instead of the shrinking grain model. It is also worth noting that, while the mass of sample used in the fluidised bed experiment was almost twice as much as that used in the TGA experiment presented in Chapter 6, the reaction was completed in < 20 s in the fluidised bed compared to > 100 s in the TGA (*cf.* Figure 6-4 and Figure 7-8). This is strong evidence that external rates of mass transfer were relatively slow in the TGA despite efforts made to minimise its influence. The fact that the reaction proceeded ~ 5 times faster in the fluidised bed is also consistent with the finding that the rate of chemical reaction was about 5–7 times faster than the rate of external mass transfer in the TGA, if the first-order reaction model were used.

Comparing the first-order reaction model with the experimental results, it can be seen that the numerical model predicted a faster rise in the rate of reaction in the beginning of the reaction and there are several reasons to account for this discrepancy. First of all, as discussed in Chapter 5, the rate of decomposition of the fully oxidised OC could be significantly slower in the initial stages due to nucleation effects, that is, extra energy is required to overcome the surface energy due to the creation of a new phase and this was not allowed for in the numerical model. Second, since the rate of reaction is very sensitive to temperature, it is possible that the heat transfer from the fluidised bed to the particles was overestimated. This will be discussed further in Section 7.5. Third, the numerical model assumed that no $O_2$ was present in the pores of the OC particles initially. However, given that the temperature of the particle increased from room temperature to the reaction temperature in ~ 1 s, it is likely that the $O_2$ could not be flushed out of the pores within this time scale so that the initial rate of reaction would have been lower due to the residual $O_2$ present in the pore network. Fourth, although the initial mixing of the OC particles into the particulate phase is improved with higher gas flowrates, it is possible that the mixing still required a time constant of the order of 1 s or so, which could lead to a reduced rate of decomposition. However, this is difficult to verify experimentally. Lastly, the response time of the UEGO sensor was between 10 ms - 100 ms depending on the operating condition and given that the concentration of $O_2$ rose to a maximum in ~2 s, the sensor response time might have a slight influence on the measured results.

Figure 7-9 shows the comparison between the experimental results and the corresponding model results at 950°C and 850°C, respectively. Similar to the results at 900°C, the model predicted a slightly slower rate of reaction at 950°C. In fact, the maximum rate obtained from the model was approximately 10% lower than the observed maximum rate in both cases. While the maximum rate from the model is comparable with the experimental result at 850°C, it should be pointed out that a relatively low gas flowrate was used at this temperature and the experimental rate could be lower than expected due to the solid mixing issue discussed earlier. It was not possible to obtain reliable results with higher gas flowrates because the signal was too weak to produce a satisfactory mass balance on oxygen. Considering the fact that the numerical model underestimated the reaction rate across the temperature range investigated and the deviation was comparable at 900°C and 950°C, while the experimental results at 850°C could have been higher without the influence of solid mixing, it is likely that the activation energy obtained from Chapter 6 is reasonably accurate whilst the pre-exponential factor is lower than the true value.

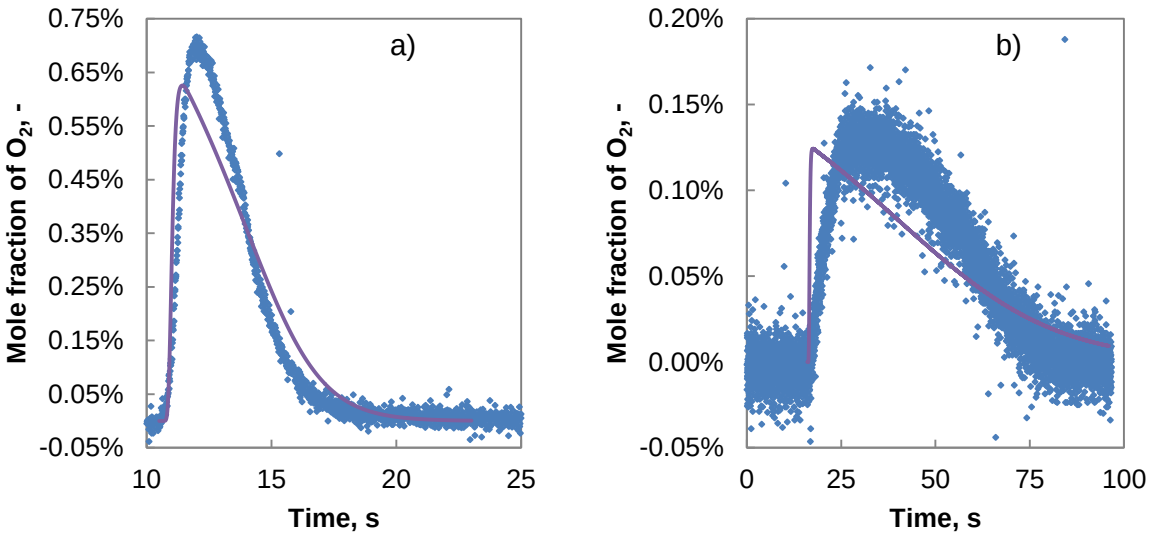


Figure 7-9 The reaction profiles of the decomposition of the OC at different temperatures. The experimental results are shown in blue points and the model results are shown by the purple solid lines. a) reaction temperature 950°C, sample mass 10.0 mg, gas flowrate 1.2 l/min; b) reaction temperature 850°C, sample mass 10.6 mg, gas flowrate 0.6 l/min. All gas flowrates measured at 20°C, 1 bar.

Lastly, the assumption of negligible internal mass transfer resistance in the particles used in the calculation of the kinetic parameters in Chapter 6 was checked against the single particle model developed here. As shown in Figure 7-10, the

simulated result indicates that at some arbitrary, intermediate overall conversion, the local conversion of the particle does vary with its radius to a limited extent, from ~ 0.495 at the centre to ~ 0.581 at the surface. Hence the rate constant determined in Chapter 6 could be an underestimate of the intrinsic rate of chemical reaction, due to the additional, small but significant, mass transfer resistance unaccounted for. In fact, the effectiveness factor for a spherical particle (Thiele, 1939),

$$\eta = \frac{3}{\phi}\left(\frac{1}{\tanh\phi} - \frac{1}{\phi}\right) \qquad 7\text{-}19$$

was found to be 0.89 based on the initial rate of chemical reaction at the bed temperature, calculated from the input model parameters at 904°C. Here, the Thiele modulus, $\phi$, is given by

$$\phi = r_p \sqrt{\frac{\frac{\rho_m}{4}\left.\frac{dX}{dt}\right|_{X=0}}{D_{eff}}} \,. \qquad 7\text{-}20$$

Of course, as the reaction proceeds, the rate of chemical reaction decreases so that the effectiveness factor would increase accordingly.

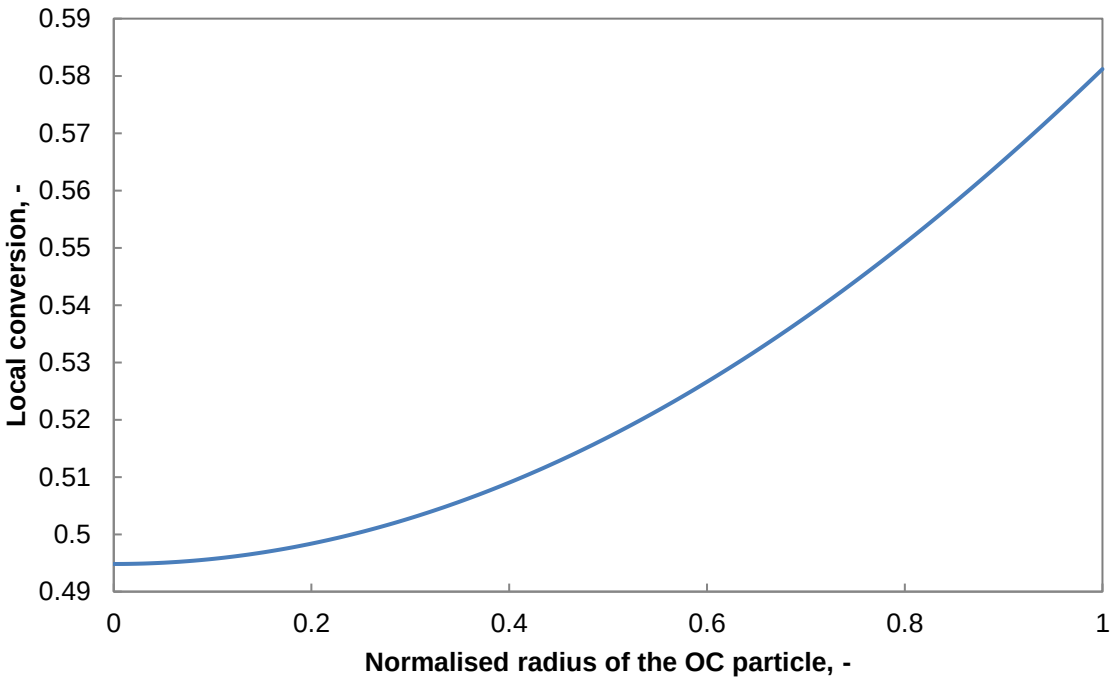


Figure 7-10 Model result of local conversion vs. normalised radius of a single particle. Reaction temperature 904°C, sample mass 5.4 mg, gas flowrate 1.4 l/min; time for reaction $t$ = 6 s.

As a result, it appears that the rate of chemical reaction measured in Chapter 6 included a small contribution from internal mass transfer and was an underestimate of the intrinsic rate of chemical reaction.

## 7.5. Discussion

In this section, the sensitivity of the numerical simulation to some important input parameters is discussed.

### 7.5.1. Rate of mass transfer

In this work, the Sherwood number, *Sh*, used for the mass transfer between the OC particles and the particulate phase was obtained from equation 7-12. Since the correlation relates the Sherwood number to properties at minimum fluidisation only *via* $\varepsilon_{mf}$ and $U_{mf}$, the Sherwood number depends on the temperature of the fluidised bed but not the gas flowrate used. At 904°C, the value of *Sh* calculated is 1.11, a rather low value. As pointed out by Hayhurst (2000), equation 7-12 is strictly applicable when the active particle is much larger than the particles constituting the majority of the fluidised bed. In the other limit where the active particle is much smaller than the bulk bed material, the term $2\varepsilon_{mf}$ in equation 7-12 should be replace by 2, yielding

$$Sh = 2 + 0.69\left(\frac{2r_p U_{mf}}{\varepsilon_{mf}\nu}\right)^{1/2}\left(\frac{\nu}{D}\right)^{1/3}, \qquad 7\text{-}21$$

which gives *Sh* = 2.27, *i.e.* a rate of mass transfer twice the value. In the present case, the size of the active particles is comparable to the inert sand particles so that the Sherwood number can be expected to lie between these two values. It can be seen from Figure 7-11 that with an increasing Sherwood number up to an unrealistic, arbitrarily large value of 10, the simulated reaction profile does not change significantly. With *Sh* = 2.27, the maximum rate was approximately the same as the experimental result and 9.7% higher than the base case with *Sh* = 1.11, and with *Sh* = 10, the maximum rate was only 18% higher than the base case. Thus it can be concluded that external mass transfer does not influence the model results greatly although the choice of the equation 7-12 may have underestimated the mass transfer between the particles and the particulate phase.

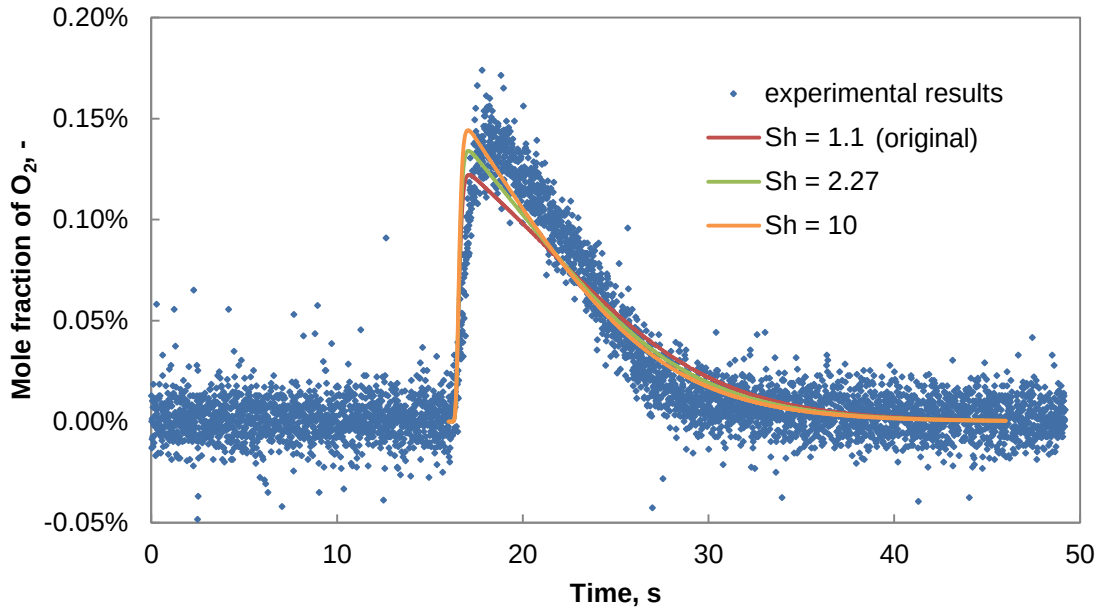


Figure 7-11 The effect of Sherwood number on the numerical simulation, with the corresponding experimental results overlaid for comparison. Reaction temperature 904°C, sample mass 5.4 mg, gas flowrate 1.4 l/min (20°C, 1 bar).

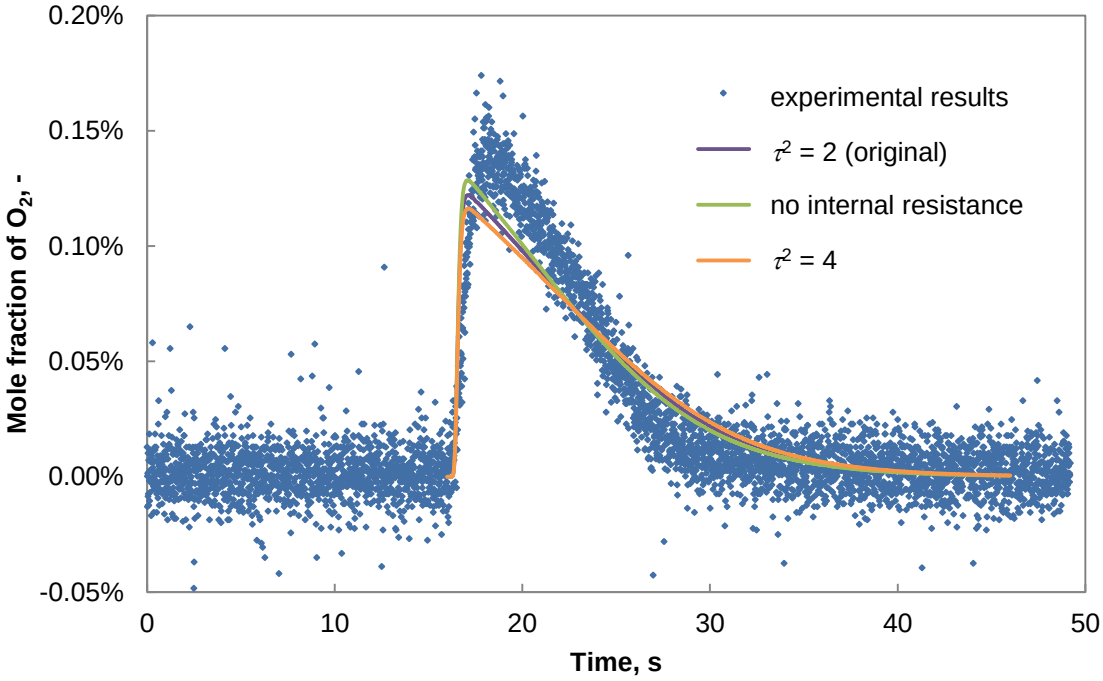


Figure 7-12 The effect of internal mass transfer resistance on the numerical simulation, with the corresponding experimental results overlaid for comparison. Reaction temperature 904°C, sample mass 5.4 mg, gas flowrate 1.4 l/min (20°C, 1 bar).

The uncertainties in the internal mass transfer resistance are largely due to the uncertainty in the tortuosity, $\tau^2$. However, as can be seen from Figure 7-12, the numerical model is not very sensitive to the choice of tortuosity. The maximum rate of reaction was 5.2% higher than the base case when the internal mass transfer resistance was ignored and 4.8% lower when $\tau^2$ was doubled. This observation is consistent with the assumption associated with the first-order reaction model used in Chapter 6 that internal mass transfer does not have a significant effect on the rate of reaction.

### *7.5.2. Rate of heat transfer*

With the thermal conductivity of the single particle estimated as 0.5 W/m/K, the model showed that the heat transfer within the particle was fast and the temperature of the particle was essentially uniform along the radius. Increasing the value of $\lambda_s$ had no effect on the simulated reaction profile. In fact, the temperature gradient within the particle was insignificant even when the thermal conductivity was reduced to 0.05 W/m/K and had little effect on the rate of reaction, as shown in Figure 7-13. The maximum rate of reaction obtained with this extremely low thermal conductivity was merely 7.5% lower than the base case. Thus the large uncertainty in the thermal conductivity should not have affected the results from the model.

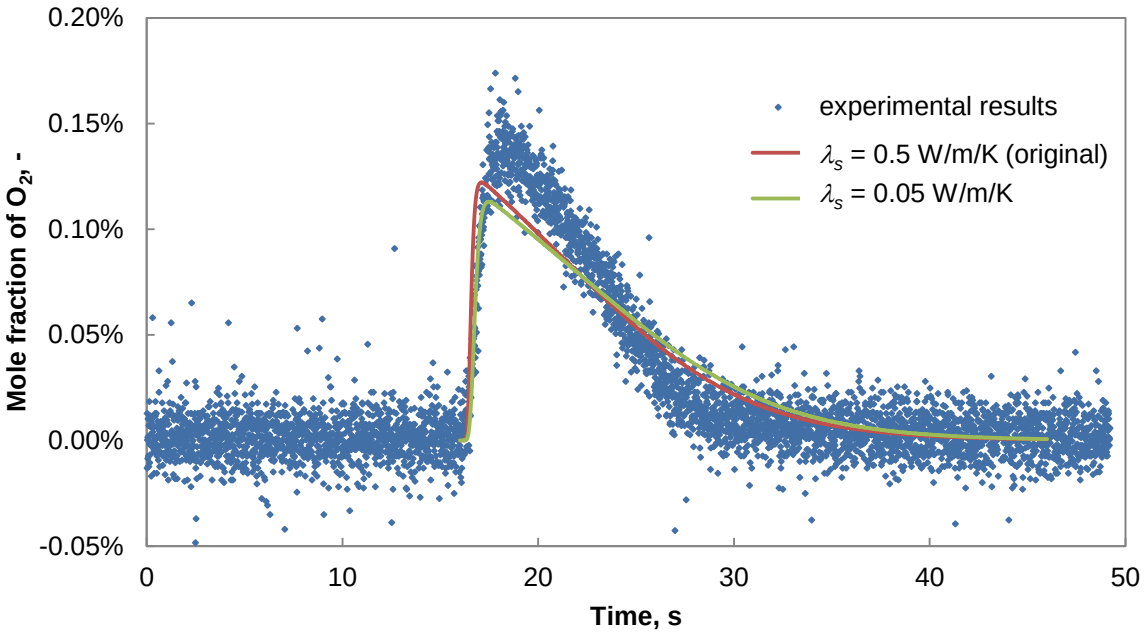


Figure 7-13 The effect of solid thermal conductivity on the numerical simulation, with the corresponding experimental results overlaid for comparison.

In comparison, the numerical model is reasonably sensitive to parameters associated with the heat transfer from the fluidised bed to the OC particles. From equation 7-11 (d), it can be seen that the Nusselt number and the emissivity are the main contributors to the uncertainties in the quantification of external heat transfer whereas the thermal conductivity of $N_2$ can be obtained with high accuracy from *e.g.* NIST (2011). The surface temperature of the OC particle over time is presented in Figure 7-14. It can be seen that ~1 s after the particle was dropped into the fluidised bed, the temperature of the particle increased to ~ 896°C. The temperature increased relatively slowly after that due to the moderately endothermic decomposition of the OC and the bed temperature, 904°C was only reached towards the end of the reaction. It is expected that the temperature difference between the surface of the particle and the fluidised bed depends critically on the Nusselt number and the emissivity of the bed material.

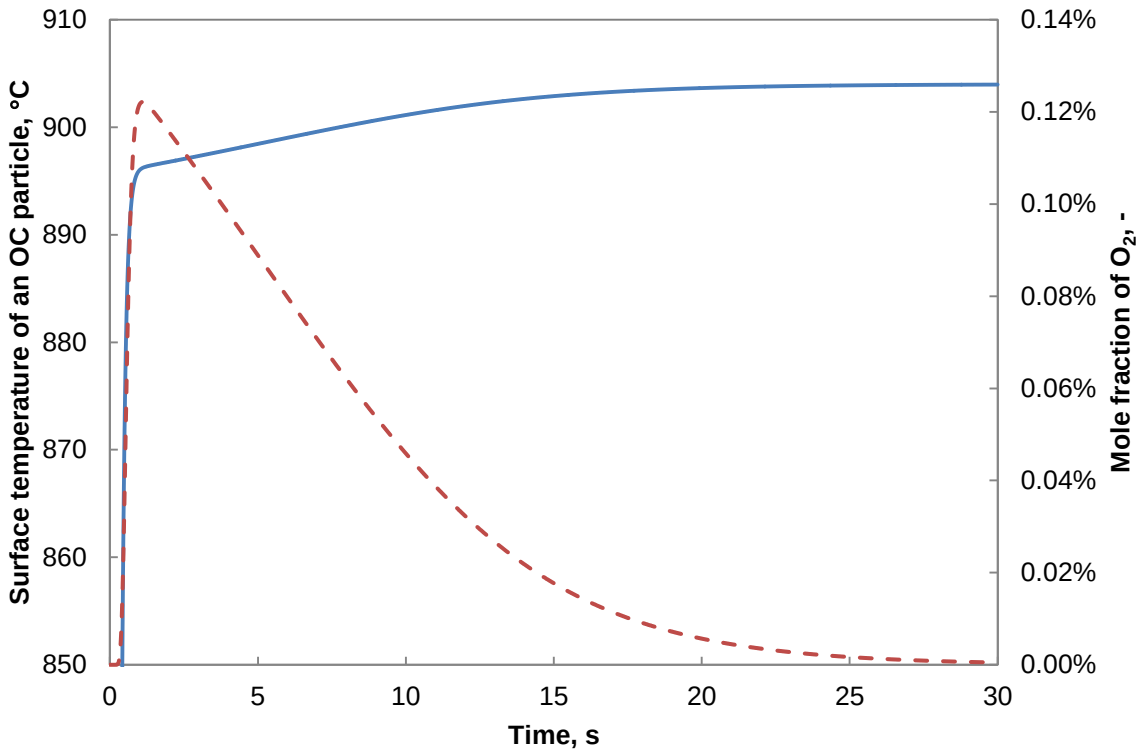


Figure 7-14 Simulated evolution of the surface temperature of an OC particle (blue solid line) and the corresponding concentration profile of $O_2$ (red dashed line). Bed temperature 904°C, sample mass 5.4 mg, gas flowrate 1.4 l/min (20°C, 1 bar).

As shown in Figure 7-15, When both *Nu* and $\varepsilon$ were halved, corresponding to a reduction of the rate of external heat transfer by a factor of 2, the maximum rate calculated decreased by 15% but when either the value of *Nu* or $\varepsilon$ was halved, the

reaction profile did not change substantially and the maximum rate calculated was lowered by 6.1% and 5.2%, respectively. Figure 7-16 presents the contribution to external heat transfer from convection and radiation, respectively. At temperatures above 800°C, the heat transfer due to convection and radiation is very similar in value but convective heat transfer dominates at lower particle temperature. Since the CLOU reaction is only appreciable above 800°C, it is reasonable to assume that both modes of heat transfer contribute almost equally. The upper bound of the rate of external heat transfer was estimated with *Nu* = 4 and in this case the maximum rate of reaction was 6.9% higher than the base case as shown in Figure 7-15. In the extreme case with no external heat transfer resistance, by fixing the surface temperature of the OC particles at the bed temperature, the maximum rate could increase by 23%.

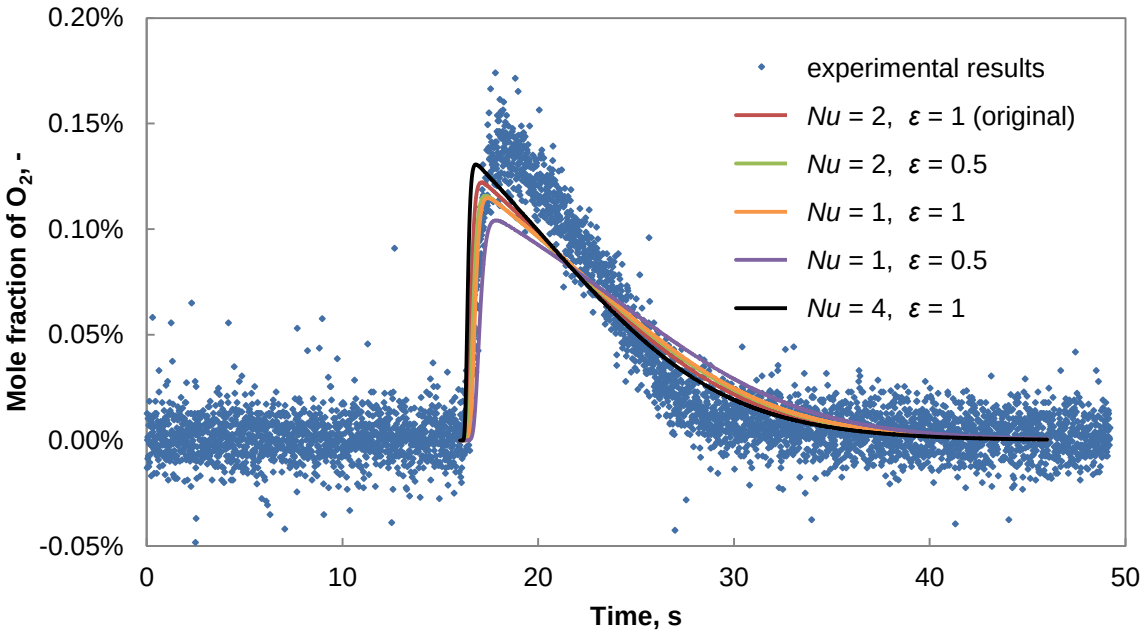


Figure 7-15 The effect of external heat transfer on the numerical simulation, with the corresponding experimental results overlaid for comparison.

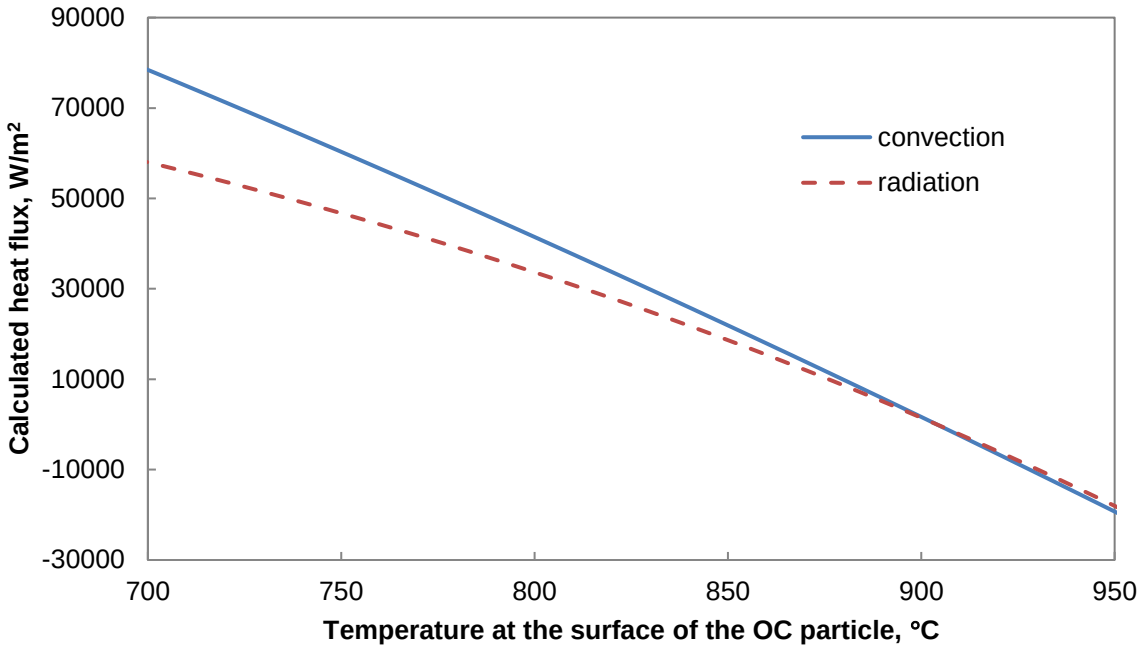


Figure 7-16 Calculated heat flux from the particulate phase to the surface of an OC particle due to convection (blue solid line) and radiation (red dashed line). Temperature of the particulate phase was taken to be constant at 904°C.

### *7.5.3. Rate of chemical reaction*

Lastly, the sensitivity of the model to the rate of chemical reaction is presented in Figure 7-17. The results were obtained by changing the value of the pre-exponential factor in the rate expression rather than the activation energy. At a given temperature, the two approaches are equivalent. However, as discussed in Section 7.4.2, since the model results are able to predict the temperature dependence of the reaction profile adequately, the value of activation energy used in the model is likely to be accurate. As shown in Figure 7-17, the reaction profile obtained from the simulation depends strongly on the rate of chemical reaction used: when the rate constant was doubled or halved, the maximum rate of reaction calculated from the model deviated from the original value by more than 30% in each case. More importantly, the time for completion of the reaction was visibly different between the cases investigated, which was not seen by varying other parameters of the model.

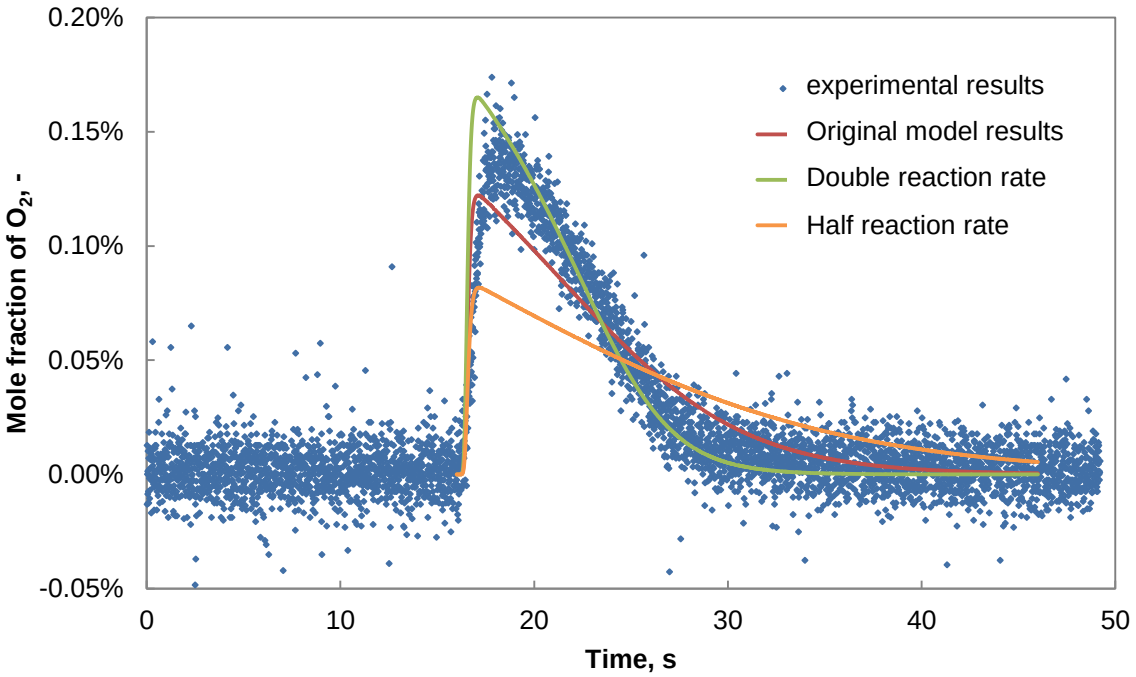


Figure 7-17 The effect of the rate of chemical reaction on the numerical simulation, with the corresponding experimental results overlaid for comparison.

Thus it appears that the numerical model is most sensitive to the rate of chemical reaction whereas uncertainties in external heat and mass transfer have very modest influence on the results. Hence, the model is effective in validating the rate parameters for the decomposition of the OC particles obtained from Chapter 6 using the TGA. Given that the model reaction profile is close to the experimental results within ~ 10-15% between 850°C and 950°C, it can be concluded that the kinetic parameters obtained experimentally are reasonably accurate.

## *7.6. Summary*

In this chapter, the kinetic parameters obtained in Chapter 6 have been investigated further using a batch fluidised bed. By appropriate modelling of the fluidised bed, it was shown that the kinetic parameters obtained from the TGA were also applicable in a fluidised bed, despite the large difference in mass transfer effects between the two set-ups. Experimental results as well as the sensitivity analysis carried out on the numerical model showed that in a batch fluidised bed, the decomposition of the OC particles with a size fraction of 300-425 µm is primarily controlled by the chemical reaction rather than transport processes.

The deviation of the modelled reaction profile from the experimental results was more severe with low gas flowrates or high mass of OC particles used and the mixing

of OC particles in the particulate phase was thought to be responsible for this behaviour. However, further work is required to test this hypothesis.

# 8. Conclusion

The purpose of this Dissertation was to develop a suitable OC for CLOU which could have the potential to be used at a large scale. From the literature surveyed in Chapter 1, it was decided that Cu-based materials are the most promising for CLOU, amongst the OCs so far investigated, owing to the high oxygen carrying capacity per unit mass of starting oxide and a suitable equilibrium partial pressure of $O_2$ for oxygen release and uptake around 900°C. However, pure CuO cannot be used as an OC because it rapidly deactivates when cycled between a fully-reduced and fully-oxidised form and, generally, it has to be supported, *e.g.* on a refractory oxide, to maintain its activity and offer resistance to attrition. In this work, mechanical mixing was adopted for the preparation of the supported OCs because of its simplicity and potential ease of scale up.

From the investigations presented in Chapter 3, it was found that $Al_2O_3$, a commonly-used support material, can be used to improve the stability of CuO with respect to its reactivity. An OC containing 70 wt% CuO and 30 wt% $\alpha$-$Al_2O_3$ prepared using the dry-mixing method was found to be stable over repeated redox cycling. However, it is possible for the CuO to react with $Al_2O_3$ to form copper aluminates, which do not release oxygen at an appreciable rate and cannot be used for CLOU. It was found that the tendency to form copper aluminates depended on the temperature at which the OCs were calcined, as well as the form of $Al_2O_3$ used for the synthesis of the OC. The difference in the reactivity between different polymorphs of $Al_2O_3$ was attributed to their structural differences and it was concluded that $\gamma$-$Al_2O_3$ should not be used as a support for a Cu-based OC for the purpose of CLOU and $\alpha$-$Al_2O_3$ supported particles should not be employed above 950°C to avoid loss of oxygen capacity of the OC. The problem can be avoided when some CaO is mixed with the $Al_2O_3$ to form a calcium aluminate support. In particular, the calcium aluminate mayenite, $12CaO \cdot 7Al_2O_3$, was found to be more inert than $\alpha$-$Al_2O_3$ and did not form any compounds with CuO when calcined at 1000°C. Furthermore, mayenite was found to be more effective at stabilising the reactivity of CuO compared to $Al_2O_3$ with the same mass fraction. Thus mayenite was chosen as a suitable support material for the OC to be investigated in greater detail.

As presented in Chapter 4, it was found that the powders produced from the dry-mixing method could not form particles, by granulation, with sufficient strength for

fluidisation. However, a wet-mixing method using $Ca(OH)_2$ and $Al(OH)_3$ instead of mayenite was able to produce the mayenite support after calcination and the particles prepared from this route were robust enough for use in a fluidised bed. The OC particles synthesised using this method were macro-porous with a porosity ~ 0.66. The fact that the OC particles possessed little BET surface area means that the related BJH pore volume is not a fair reflection of the internal structure of the particles since these measurements are for pore diameters ≤ 200 nm. It was found that the rate of attrition of the calcined particles in a small-scale circulating fluidised bed at high temperature was relatively high during the first 50 hours of operation and stabilised afterwards at a constant value of ~ 0.01 wt%/h. By comparing the size distribution of the particles before and after the experiment, it was concluded that the primary mechanism of attrition of these particles was through abrasion rather than fragmentation. Similar experiments performed with different fluidising gases (air, 5% $H_2$ in $N_2$, or 100% $N_2$) indicated that circulation and fluidisation of the particles were stable over several hours, irrespective of the degree of reduction of the particles, but when the particles were oxidised from the fully reduced form (containing metallic Cu), rapid agglomeration and de-fluidisation occurred within ~ 10 minutes. On the other hand, no de-fluidisation was observed when the particle was oxidised from the $Cu_2O$ form, which is relevant in CLOU operation. Hence it was concluded that the particles synthesised through the wet-mixing method with a nominal composition of 60 wt% CuO, 23 wt% $Al_2O_3$ and 17 wt% CaO gave a suitable OC for the CLOU process.

A theoretical analysis of the rate of reaction for the $CuO/Cu_2O$ system, *i.e.* $4CuO \rightleftharpoons 2Cu_2O+O_2$, revealed that the rate of reaction depends on both the intrinsic kinetics and the thermodynamics of the system, in the following form

$$\frac{dX}{dt} = k_{in}\left(C_{eq}{}^{n} - C_{s}{}^{n}\right) f(X),$$

and these two factors must be studied in isolation in order to obtain a reliable rate expression. Hence the thermodynamics and the kinetics of the OC particles were investigated separately and results are presented in Chapters 5 and 6, respectively.

In Chapter 5, a novel method was developed to measure the equilibrium concentration of $O_2$ for the oxidation of the carrier at various temperatures in a TGA. It was found that the virgin particles had a different thermodynamic equilibrium compared to the particles which had been cycled several times. Careful examination of the XRD patterns of the virgin and cycled materials revealed that the CuO lattice of the virgin

particles was slightly distorted whereas that of the cycled particles was similar to pure CuO. This distortion was attributed, by a process of elimination, to the interaction with the mayenite support during the calcination step of the particle synthesis and subjecting the particles to several redox cycles eliminated this distortion. The equilibrium concentration of $O_2$ in $4CuO \rightleftharpoons 2Cu_2O+O_2$ measured from the oxidation of the cycled OC particles was found to be similar to the standard values available in the literature for pure CuO. However, the enthalpy of reaction estimated from the experimental results was approximately 15% lower than the standard values. Furthermore, a nucleation-and-growth behaviour was observed during the oxidation of the OC particles when a small concentration driving force was used. However, such behaviour was absent when a larger concentration driving force was used. The difference in reaction kinetics was attributed to the dependence of the rate of nucleation on the concentration driving force. The measurement of the equilibrium concentration of $O_2$ of the relatively simple $CuO/Cu_2O$ served as a proof of concept, demonstrating that the diffusion method developed in this Dissertation could be used to measure the thermodynamic equilibrium as well as steady state kinetics of a range of reactions reliably, provided that the rate of the gas-solid reaction is fast compared to the rate of diffusion of gases.

In Chapter 6, the kinetics of the decomposition of the OC particles was investigated. By careful analysis of the experimental results, aided by theoretical modelling of the transport processes, it was found that the rate of decomposition of CuO could follow either a first-order reaction with respect to the solid or a shrinking grain reaction model. A preliminary discrimination between the two models was made by increasing the external mass transfer resistance. Accordingly, it was found that the first-order reaction model performed better. Following a critical analysis of the literature regarding the rate of decomposition of CuO, it was found that the activation energy of the reaction for CuO-based OCs supported on different materials were comparable to each other, around 60 kJ/mol, in excellent agreement with the value obtained in this work, 59.6 $\pm$5.6 kJ/mol. However, a similar comparison could not be made for the pre-exponential factor owing to the various, different reaction models assumed in the literature.

Lastly, the kinetics of the decomposition of the OC particles were measured in a laboratory-scale fluidised bed to verify the applicability of the kinetic parameters obtained in the TGA in a different system with faster rate of external mass transfer. A

fluidised bed model, based on the two-phase theory of fluidisation, was coupled with a single particle model with internal diffusion, and was used to describe the fluidised bed system. It was found that using the kinetic parameters obtained from the TGA experiment, the numerical model was able to produce a reaction profile in good agreement with the experimental results. However, the numerical rate of reaction was slightly underestimated by the model. A sensitivity analysis of the numerical model with respect to mass transfer, heat transfer and rate of chemical reaction revealed that the numerical model was most sensitive to the rate of chemical reaction and external heat and mass transfer had moderate impact on the model results. Thus it appeared that the measured kinetics parameters in a TGA, with appropriate consideration of mass transfer effects, can be extended to fluidised bed systems with reasonable accuracy.

In summary, a Cu-based oxygen carrier containing 60 wt% CuO and 40 wt% calcium aluminate support primarily consisted of mayenite was developed for use in CLOU processes. The work presented in this Dissertation encompassed a comprehensive characterisation of the developed oxygen carrier, including the chemical and mechanical stability of the carrier in a circulating fluidised bed environment as well as the detailed investigation of the thermodynamics and kinetics of the reactions associated with the CLOU process. A novel method and appropriate models were developed during these investigations to extend the capability of TGA work to determine kinetics and these methods can be extended to related studies in the future. On the basis of the results presented in this Dissertation, the oxygen carrier developed is worthy of investigation at the pilot scale.

# 9. Future work

The virgin OC particles demonstrated excellent resistance to attrition when circulated in a fluidised bed for more than 200 hours. However, it was not possible to investigate the attrition resistance of the particles which had been subjected to repeated redox cycling due to the lack of such material. Since the virgin and cycled materials sometimes behave differently with respect to attrition (Rydén *et al.*, 2014), the attrition resistance of the cycled particles should be measured as well.

It was observed that the mechanism of the oxidation of $Cu_2O$ depended on the concentration driving force. It would be of academic, as well as practical, interest to investigate this dependence further, so that a complete description of the reaction mechanism can be developed. It was also observed, from the results presented in Chapter 5, that the enthalpy of reaction for $4CuO \rightleftharpoons 2Cu_2O+O_2$ was somewhat lower than values available from standard databases; related work in the literature supports this observation to some extent. However, the underlying reason for this discrepancy is unclear and further investigation is needed.

In Chapter 6, a first-order reaction model was found to be appropriate for the decomposition of CuO. However, in light of the fact that the reaction mechanism may well be different depending on the concentration driving force, the kinetics of the carriers should be investigated further with a broad range of concentration driving force to develop a more comprehensive model.

Lastly, in Chapter 7, it was seen that the model results always predicted a faster rise of the rate of reaction in the initial stage of the decomposition reaction, attributed to the incomplete mixing of the OC particles. While this explanation is supported by some experimental evidence, the direct measurement of the solid mixing times in the fluidised bed was not possible due to the high temperature involved. This needs further investigation in a suitably-designed apparatus. It is also clear that the coefficient of external mass transfer might be affected by the size of fluidised bed, at the laboratory scale. Given the ubiquitous use of these reactors, further research is needed on this topic. Notably, magnetic resonance imaging offers the potential to measure the solid mixing directly at room temperature (Fennell *et al.* 2005) at small time scales and can be valuable for future investigations.

# 10.Appendix

## *A. Solution to the 2-D Laplace equation*

The differential equation 5-23 in two dimensions can be solved using the substitution $\ln y_3 = f(r)g(z)$. The treatment yields

$$\frac{1}{r}f'g + f''g + fg'' = 0 \qquad 10\text{-}1$$

where *f* ′ represent the first derivative of *f* w.r.t *r* and so on. The equation can be rearranged as

$$\frac{1}{r}\frac{f'}{f} + \frac{f''}{f} = -\frac{g''}{g} = \pm\alpha^2 \qquad 10\text{-}2$$

for some non-negative $\alpha$.

Now consider the function involving only *g*(*z*):

$$g'' \pm \alpha^2 g = 0, \qquad 10\text{-}3$$

the positive case yields oscillatory solution and is clearly not physically sound since the mole fraction or its natural logarithm is not expected to oscillate with increasing value of *z*. Thus the right hand side of equation 10-2 should take the negative form, which gives

$$g(z) = p_{1,\alpha}\exp(\alpha z) + p_{2,\alpha}\exp(-\alpha z) \qquad 10\text{-}4$$

when $\alpha \neq 0$. When $\alpha = 0$, the solution becomes

$$g(z) = p_{1,0}z + p_{2,0}. \qquad 10\text{-}5$$

Here $p_{1,\alpha}$ and $p_{2,\alpha}$ are constants to be determined, depending on the value of $\alpha$.

Correspondingly, the part of equation 10-2 involving only *f* is the Bessel's differential equation of order zero:

$$r^2 f'' + rf' + r^2 \times \alpha^2 f = 0 \qquad 10\text{-}6$$

which has the general solution in the form

$$f(r) = q_{1,\alpha}B_{J,0}(\alpha r) + q_{2,\alpha}B_{Y,0}(\alpha r) \qquad 10\text{-}7$$

for a particular value of $\alpha$. Here, $B_{J,0}(\alpha r)$ and $B_{Y,0}(\alpha r)$ are, respectively, the Bessel Function of the first and second kind with order zero and the coefficients $q_{1,\alpha}$ and $q_{2,\alpha}$ are to be determined.

Since the Bessel function of the second kind has a singularity as $r \to 0$, the coefficients $q_{2,\alpha}$ must be zero for all values of $\alpha$ in order for the solution to converge at the centerline of the crucible. Furthermore, since the Laplace equation is

homogeneous, the general solution comprises of a linear combination of all possible solutions (generated from different values of $\alpha$), which forms an infinite series, *i.e.*

$$\ln y_3 = q_{1,0}p_{1,0}z + q_{1,0}p_{2,0} + \sum_{\substack{\alpha \\ \alpha\neq 0}}^{\infty} q_{1,\alpha}B_{J,0}(\alpha r)\left(p_{1,\alpha}\exp(\alpha z) + p_{2,\alpha}\exp(-\alpha z)\right). \qquad 10\text{-}8$$

The possible values $\alpha$ can take in equation 10-8 are constrained by the second boundary condition: zero radial flux at the wall.

Combining with equation 5-20

$$\nabla y_3 = \frac{y_3 \underline{J}_1}{cD_{13}},$$

the boundary condition yields

$$cD_{13}\left.\frac{\partial \ln y_3}{\partial r}\right|_{r=r_c} = J_{r,1}\big|_{r=r_c} = 0. \qquad 10\text{-}9$$

Therefore, differentiate equation 10-8 w.r.t. $r$ and evaluate at $r = r_c$ gives

$$0 = -\sum_{\substack{\alpha \\ \alpha\neq 0}}^{\infty} \alpha q_{1,\alpha}B_{J,1}(\alpha r_c)\left(p_{1,\alpha}\exp(\alpha z) + p_{2,\alpha}\exp(-\alpha z)\right), \qquad 10\text{-}10$$

using the identity

$$\frac{d}{dy}B_{J,0}(y) = -B_{J,1}(y). \qquad 10\text{-}11$$

By inspection of equation 10-10, it is obvious that non-trivial solutions only exist if the term $\alpha r_c$ is a zero of $B_{J,1}$. Denoting the $n^{\text{th}}$ zero of $B_{J,1}$ by $\omega_n$ and combining some coefficients, the equation 10-8 can now be simplified and non-dimensionalised to equation 5-24

$$\ln y_3 = \kappa_1 \frac{z}{z_{\max}} + \kappa_2 + \sum_{n=1}^{\infty} B_{J,0}\left(\omega_n \frac{r}{r_c}\right)\left(\kappa_{3n}\exp\left(\omega_n \frac{z_{\max}}{r_c}\frac{z}{z_{\max}}\right) + \kappa_{4n}\exp\left(-\omega_n \frac{z_{\max}}{r_c}\frac{z}{z_{\max}}\right)\right).$$

## B. The orthogonality and normalisation relations of Bessel functions

The combined expression for the orthogonality and normalisation relations of Bessel functions of the same order in the normalised form is generally written as

$$\int_0^1 y B_{J,n}(\alpha_i y) B_{J,n}(\alpha_j y)\,dy = \frac{1}{2} B_{J,n+1}{}^2(\alpha_i y)\delta_{ij} \qquad 10\text{-}12$$

where $\alpha_i$ and $\alpha_j$ are the $i^{\text{th}}$ and $j^{\text{th}}$ zeros of $B_{J,n}$, respectively. The function $\delta_{ij}$ is the Kronecker's delta – that is, the value of the function is zero everywhere except for $i = j$ where the function takes the value of unity. The proof of the orthgonality relation can be obtained as follows:

It is known that the Bessel function $u = B_{J,n}(\alpha_i)$ with the arbitrary constant $\alpha_i$ satisfies the differential equation

$$y^2 \frac{d^2u}{dy^2} + y\frac{du}{dy} + \left(\alpha_i{}^2 y^2 - n^2\right)u = 0 \qquad 10\text{-}13$$

and similarly $v = B_{J,n}(\alpha_j y)$ satisfies

$$y^2 \frac{d^2v}{dy^2} + y\frac{dv}{dy} + \left(\alpha_j{}^2 y^2 - n^2\right)v = 0\,. \qquad 10\text{-}14$$

Now, multiplying equation 10-13 by $v$ and 10-14 by $u$ and taking the difference of the results yields:

$$y(yu'' + u')v - y(yv'' + v')u + y^2 uv\left(\alpha_i{}^2 - \alpha_j{}^2\right) = 0\,. \qquad 10\text{-}15$$

Using the identity

$$\begin{aligned}\frac{d}{dy}(yu'v - yv'u) &= u'v + y(u''v + u'v') - v'u - y(v''u + v'u') \\ &= (yu'' + u')v - (yv'' + v')u\end{aligned}, \qquad 10\text{-}16$$

equation 10-15 can be simplified to

$$\frac{d}{dy}(yu'v - yv'u) = -yuv\left(\alpha_i{}^2 - \alpha_j{}^2\right). \qquad 10\text{-}17$$

Integrating equation 10-17 gives

$$\int_0^1 yB_{J,n}(\alpha_i y)B_{J,n}(\alpha_j y)dy = \frac{\left[yB_{J,n}{}'(\alpha_i y)B_{J,n}(\alpha_j y) - yB_{J,n}(\alpha_i y)B_{J,n}{}'(\alpha_j y)\right]_0^1}{-\left(\alpha_i{}^2 - \alpha_j{}^2\right)}$$
$$= \frac{\alpha_j B_{J,n}(\alpha_i)B_{J,n}{}'(\alpha_j) - \alpha_i B_{J,n}{}'(\alpha_i)B_{J,n}(\alpha_j)}{\alpha_i{}^2 - \alpha_j{}^2}. \qquad 10\text{-}18$$

It is clear from equation 10-18 that for $i \neq j$, the integral is zero if $\alpha_i$ and $\alpha_j$ are zeros of $B_{J,n}$, corresponding to the general orthogonality relation. Furthermore, if $\alpha_i$ and $\alpha_j$ are zeros of the derivative of $B_{J,n}$, the integral is also zero. For the 2-D cylindrical case discussed in Appendix A, the Bessel functions involved are of order zero ($n = 0$) and since

$$B_{J,0}{}'(\alpha_i y) = -\alpha_i B_{J,1}(\alpha_i y), \qquad 10\text{-}19$$

It follows that

$$\int_0^1 yB_{J,0}(\omega_i y)B_{J,0}(\omega_j y)dy = 0 \qquad i \neq j \qquad 10\text{-}20$$

where $\omega_i$ and $\omega_j$ are zeros of $B_{J,1}$ as defined earlier. When $i = j$, the normalisation relation 10-12 in this case is slightly different. Using integration by parts with the fact that

$$\frac{d}{dy}\left(yB_{J,1}(y)\right) = yB_{J,0}(y), \qquad 10\text{-}21$$

The normalisation relation becomes

$$\begin{aligned}
&\int_0^1 yB_{J,0}(\omega_i y)B_{J,0}(\omega_i y)dy \\
&= \left[\frac{1}{\omega_i} yB_{J,1}(\omega_i y)B_{J,0}(\omega_i y)\right]_0^1 - \int_0^1 yB_{J,1}(\omega_i y)\left(-B_{J,1}(\omega_i y)\right)dy \\
&= \int_0^1 yB_{J,1}(\omega_i y)B_{J,1}(\omega_i y)dy \\
&= \frac{1}{2}B_{J,2}{}^2(\omega_i).
\end{aligned} \qquad 10\text{-}22$$

The last step of equation 10-22 follows from the general normalisation relation since $\omega_i$ is a zero of $B_{J,1}$.

## *C. Determination of the coefficients of the Fourier-Bessel series*

Let the vertical flux of $O_2$ at the top surface of the crucible (shown in Figure 5-2) just below the lid be $J_{z,1}(r,0)$, the boundary condition yields

$$\begin{aligned} J_{z,1}(r,0) &= cD_{13}\left.\frac{d\ln y_3}{dz}\right|_{z=0} \\ &= cD_{13}\left(\frac{\kappa_1}{z_{\max}} + \sum_{n=1}^{\infty}\frac{\omega_n}{r_c}B_{J,0}\left(\omega_n\frac{r}{r_c}\right)\left(\kappa_{3n}-\kappa_{4n}\right)\right). \end{aligned} \qquad 10\text{-}23$$

Transforming the equation to utilise the orthogonality relation from Appendix B gives

$$\begin{aligned} \int_0^{r_c} rB_{J,0}\left(\omega_i\frac{r}{r_c}\right)\frac{J_{z,1}(r,0)}{cD_{13}}dr &= \int_0^{r_c} rB_{J,0}\left(\omega_i\frac{r}{r_c}\right)\frac{\kappa_1}{z_{\max}}dr \\ &+ \sum_{n=1}^{\infty}\frac{\omega_n}{r_c}\left(\kappa_{3n}-\kappa_{4n}\right)\int_o^{r_c} rB_{J,0}\left(\omega_i\frac{r}{r_c}\right)B_{J,0}\left(\omega_n\frac{r}{r_c}\right)dr. \end{aligned} \qquad 10\text{-}24$$

For $i = 0$, $\omega_0 = 0$, only the constant term survives, hence

$$\frac{\kappa_1}{z_{\max}} = \frac{1}{cD_{13}}\frac{\int_0^{r_c} rJ_{z,1}(r,0)dr}{\int_0^{r_c} rdr} = \frac{1}{cD_{13}}\frac{\int_0^{r_c} 2\pi rJ_{z,1}(r,0)dr}{\pi r_c^{\,2}}. \qquad 10\text{-}25$$

The term $\dfrac{\int_0^{r_c} 2\pi rJ_{z,1}(r,0)dr}{\pi r_c^{\,2}}$ corresponds to the vertical flux of $O_2$ averaged over the cross-sectional area of the crucible, $J_{ave}$, therefore the constant $\dfrac{\kappa_1}{z_{\max}}$ reflects the average value of $\dfrac{d\ln x_3}{dz}$ inside the crucible, *i.e.*

$$\frac{\kappa_1}{z_{\max}} = \frac{J_{ave}}{cD_{13}}. \qquad 10\text{-}26$$

For higher values of $\omega$, the constant term $\kappa_{3n}$-$\kappa_{4n}$ can be calculated in a similar manner as

$$\kappa_{3n}-\kappa_{4n} = \frac{r_c}{\omega_n}\frac{1}{cD_{13}}\frac{\int_0^{r_c} rB_{J,0}\left(\omega_n\frac{r}{r_c}\right)J_{z,1}(r,0)dr}{\int_o^{r_c} rB_{J,0}^{\,2}\left(\omega_n\frac{r}{r_c}\right)dr}. \qquad 10\text{-}27$$

At $z = z_{\max}$, the second boundary condition translates to

$$
\begin{aligned}
0 &= J_{r,1}\Big|_{z=z_{\max}} \\
&= \frac{d\ln x_3}{dr} \\
&= -\sum_{n=1}^{\infty} \frac{\omega_n}{r_c} B_{J,1}\left(\omega_n \frac{r}{r_c}\right)\left(\kappa_{3n} \exp\left(\omega_n \frac{z_{\max}}{r_c}\right) + \kappa_{4n} \exp\left(-\omega_n \frac{z_{\max}}{r_c}\right)\right)
\end{aligned}
\qquad \text{10-28}
$$

which must hold for all values of *r*. Therefore the coefficient term must satisfy

$$
\kappa_{3n} \exp\left(\omega_n \frac{z_{\max}}{r_c}\right) + \kappa_{4n} \exp\left(-\omega_n \frac{z_{\max}}{r_c}\right) = 0 \qquad \text{10-29}
$$

For all $\omega_n$ so that

$$
\kappa_{3n} = -\kappa_{4n} \exp\left(-\omega_n \frac{2z_{\max}}{r_c}\right). \qquad \text{10-30}
$$

Substituting equation 10-30 into equation 10-27 and using the normalisation relation 10-22 gives

$$
\begin{aligned}
\kappa_{4n} &= -\frac{r_c}{\omega_n} \frac{1}{cD_{13}} \frac{\int_0^{r_c} rB_{J,0}\left(\omega_n \frac{r}{r_c}\right) J_{z,1}(r,0)dr}{\int_o^{r_c} rB_{J,0}{}^2\left(\omega_n \frac{r}{r_c}\right)dr} \frac{1}{1+\exp\left(-\omega_n \frac{2z_{\max}}{r_c}\right)} \\
&= -\frac{r_c}{\omega_n} \frac{1}{cD_{13}} \frac{\int_0^{r_c} rB_{J,0}\left(\omega_n \frac{r}{r_c}\right) J_{z,1}(r,0)dr}{\frac{r_c^2}{2} B_{J,2}{}^2\left(\omega_n \frac{r}{r_c}\right)} \frac{1}{1+\exp\left(-\omega_n \frac{2z_{\max}}{r_c}\right)} \\
&= -\frac{1}{1+\exp\left(-\omega_n \frac{2z_{\max}}{r_c}\right)} \frac{1}{cD_{13}} \frac{\int_0^{r_c} rB_{J,0}\left(\omega_n \frac{r}{r_c}\right) J_{z,1}(r,0)dr}{\frac{r_c\omega_n}{2} B_{J,2}{}^2\left(\omega_n \frac{r}{r_c}\right)}.
\end{aligned}
\qquad \text{10-31}
$$

It is worth noting that for an infinitely long cylinder, *i.e.* $z_{\max} \to \infty$, $\kappa_{3n} \to 0$ and the positive exponential term diminishes as expected.

Lastly, since the mole fraction of $O_2$ is constant along the radius of the crucible, the mole fractions of $N_2$ and Ar must be constant as well. Denoting the mole fraction of Ar at the interface as $y_{3,s}$, the boundary condition yields

$$
\kappa_2 = \ln y_{3,s} - \kappa_1. \qquad \text{10-32}
$$

## *D. Discretisation of the PDEs for the method of lines*

In Chapters 5 and 7, the method of lines was used to discretise all other dimensions of the PDEs apart from the temporal one in order to transform them into ODEs with respect to time only.

In both cases, the PDEs to be discretised were second order in the respective dimensions.

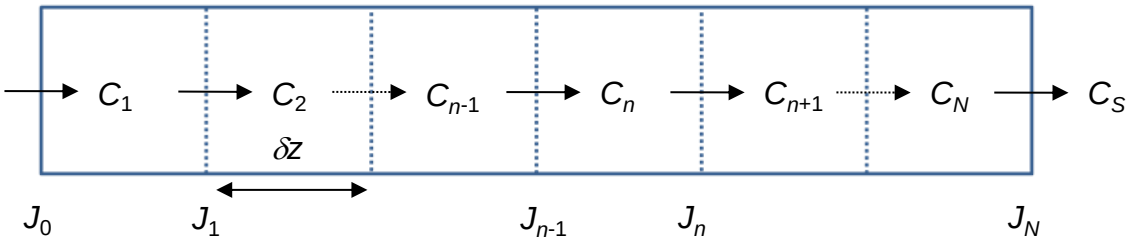


Figure 10-1 An illustration of discretised elements in one dimension.

Taking the diffusion problem in one dimension as an example, shown in Figure 10-1, the problem is discretised into cells of length $\delta z$. The flux from the $n^{th}$ cell to the $n$+1$^{th}$ cell is given by the difference

$$J_n = -D\left.\frac{\partial C}{\partial z}\right|_n \approx -D\frac{C_{n+1}-C_n}{\delta z}, \qquad 10\text{-}33$$

assuming Fickian diffusion for simplicity. The flux $J_n$ is located at position $n\delta z$. The derivative of $J$ evaluated at position ($n$-0.5)$\delta z$, coincides with the position of $C_n$, is given by

$$\begin{aligned}\left.\frac{dJ}{dz}\right|_{n-0.5} &= -D\left.\frac{\partial^2 C}{\partial z^2}\right|_{n-0.5} \\ &\approx -D\frac{\left(\frac{C_{n+1}-C_n}{\delta z}-\frac{C_n-C_{n-1}}{\delta z}\right)}{\delta z}, \\ &= -D\frac{C_{n+1}-2C_n+C_{n-1}}{\delta z^2}\end{aligned} \qquad 10\text{-}34$$

*i.e.* a central difference scheme. In the radial direction, the corresponding expression is

$$\left.\frac{1}{r}\frac{\partial\left(r\underline{J_r}\right)}{\partial r}\right|_{n-0.5} \approx -D\frac{1}{(n-0.5)\delta r}\frac{\left(n\partial r\frac{C_{n+1}-C_n}{\delta r}-(n-1)\partial r\frac{C_n-C_{n-1}}{\delta r}\right)}{\delta r} \qquad 10\text{-}35$$
$$= -D\frac{(n)C_{n+1}-(2n-1)C_n+(n-1)C_{n-1}}{(n-0.5)\delta r^2}$$

When the Stefan-Maxwell formulation is used instead, the relationship between $J$ and $C$ is more complicated but the scheme can still be used with the values of $J_n$ evaluated half an element ahead of the position of the corresponding $C_n$.

# List of abbreviations and symbols

## *Abbreviations*

| | |
|---|---|
| AR4/5 | The fourth/fifth assessment report by the IPCC |
| BC | Boundary condition |
| BET | Brunauer–Emmett–Teller |
| BJH | Barrett-Joyner-Halenda |
| CCS | Carbon capture and storage |
| CFB | Circulating fluidised bed |
| CLC | Chemical-looping combustion |
| CLOU | Chemical-looping with oxygen uncoupling |
| DSC | Differential scanning calorimetry |
| EOR | Enhanced oil recovery |
| FCC | Fluid catalytic cracking |
| FWHM | Full width at half maximum |
| i.d. | Internal diameter |
| ICSD | Inorganic Crystal Structure Database |
| IEA | International Energy Agency |
| IPCC | Intergovernmental Panel on Climate Change |
| NIST | National Institute of Standards and Technology, USA |
| NOAA | National Oceanic and Atmospheric Administration, United States Department of Commerce |
| NPL | National Physical Laboratory, UK |
| OC | Oxygen carrier |
| SDTA | Simultaneous differential thermal analysis |
| TGA | Thermogravimetric analysis/analyser |
| XRD | X-Ray (powder) diffraction |
| YSZ | Yttrium stabilised zirconia |
| IC | Initial condition |

## *Symbols*

| Symbol | | units |
|---|---|---|
| $a$ | Exponent in the Avrami equation, taking integer values 1,2,3 or 4 | - |
| $A_i$ | Interfacial area in each segment of the bubble phase | $m^2$ |
| $Ar_p$ | Archimedes number | - |
| $A_x$ | Cross sectional area of the fluidised bed | $m^2$ |
| $B_{J,n}$ | $n$th order Bessel function of the first kind | - |
| $B_{Y,n}$ | $n$th order Bessel function of the second kind | - |

| | | |
|---|---|---|
| $c$ | Total gas concentration of the system | $mol/m^3$ |
| $C_{\mu,2}$ | Constant in Sutherland's formula | $Pa\ s/K^{1/2}$ |
| $C_{\mu,2}$ | Constant in Sutherland's formula | K |
| $C_b$ | Concentration of $O_2$ of the bulk gas in the reactor | $mol/m^3$ |
| $C_d$ | Drag coefficient | - |
| $C_{em}$ | Concentration of $O_2$ in the particulate phase | $mol/m^3$ |
| $C_{eq}$ | Equilibrium concentration of $O_2$ for the CLOU reaction | $mol/m^3$ |
| $C_i$ | Concentration of $O_2$ in each segment of the bubble phase | $mol/m^3$ |
| $C_{out}$ | Concentration of $O_2$ at the outlet of fluidised bed | $mol/m^3$ |
| $c_p$ | volumetric heat capacity of the solid | $J/m^3/K$ |
| $C_s$ | Concentration of $O_2$ at the surface of particles | $mol/m^3$ |
| $d_b$ | Bubble diameter | m |
| $D_{ij}$ | Binary diffusion coefficient between species *i* and *j* | $m^2/s$ |
| $d_p$ | Diameter of the solid particles | m |
| $d_{riser}$ | Diameter of the riser in the circulating fluidised bed | m |
| $d_{sand}$ | Diameter of sand | m |
| $D_{SL}$ | Lateral dispersion coefficient for solid in a fluidised bed | $m^2/s$ |
| $E_a$ | Activation energy in the Arrhenius equation | kJ/mol |
| $g$ | Gravitational acceleration | $m/s^2$ |
| $H$ | Vertical distance of a bubble from the distributor | - |
| $H_{max}$ | Height of the fluidised bed | m |
| $H_{mf}$ | Height of the fluidised bed at minimum fluidisation | m |
| $i$ | Generic index denoting independent variables of the same measure *e.g.* species, dimensions or dimensionless numbers | - |
| $j$ | Generic index denoting independent variables of the same measure *e.g.* species, dimensions or dimensionless numbers | - |
| $J_{ave}$ | The vertical flux of $O_2$ into the crucible averaged by its cross-sectional area | $mol/m^2/s$ |
| $\underline{J_i}$ | Diffusive flux vector of species *i* | $mol/m^2/s$ |
| $J_{r,i}$ | The radial flux of the *i*th species in the system | $mol/m^2/s$ |
| $J_{z,i}$ | The vertical flux of the *i*th species in the system | $mol/m^2/s$ |
| $K$ | Equilibrium constant for a reaction | - |
| $k_1$ | Forward rate constant for reaction 5-1 | $mol/m^2/s$ |
| $k_{-1}$ | Backward rate constant for reaction 5-1 | $m^{3n-2}\ /mol^{n-1}/s$ |
| $k_{app}$ | Apparent rate constant | various |
| $k_g$ | Mass transfer coefficient | m/s |

| | | |
|---|---|---|
| $k_{gt}$ | Interphase mass transfer coefficient | m/s |
| $k_{in}$ | Rate constant for reaction 5-1 in terms of solid conversion (equation 5-9) | $m^{3n}/mol^{n}/s$ |
| $k_{in,0}$ | Pre-exponential factor in the Arrhenius equation | Various |
| $K_{Sh}$ | shape factor in the Scherrer equation | - |
| $K_{\alpha}$ | X-Ray terminology for emission due to 2p→1s relaxation (weighted average) | - |
| $K_{\alpha 1}$ | X-Ray terminology for emission due to $2p_{(3/2)}$→1s relaxation | - |
| $K_{\alpha 2}$ | X-Ray terminology for emission due to $2p_{(1/2)}$→1s relaxation | - |
| $L$ | Length scale for dimensional analysis | m |
| $M$ | Relative molecular mass | - |
| $\underline{\underline{M}}$ | The coefficient matrix for the n-component Stefan-Maxwell equation | - |
| $\underline{\underline{M}}_{n\text{-}1}$ | The submatrix of $\underline{\underline{M}}$ dropping the last column and row | - |
| $m_{O2}$ | Total mass of oxygen available for CLOU | g |
| $m_{red}$ | Mass of the fully reduced sample | g |
| $m_t$ | Mass of sample at time $t$ | g |
| $n$ | Generic index denoting independent variables of the same measure *e.g.* species, dimensions or dimensionless numbers | - |
| $N_{O2}$ | Amount of $O_2$ produced per unit area of CuO | $mol/m^2$ |
| $\dot{N}_{O2}$ | Molar flowrate of $O_2$ | mol/s |
| $n_p$ | Number of OC particles in a fluidised bed | - |
| $Nu$ | Nusselt number | - |
| $o$ | Origin of a coordinate system | - |
| $P$ | Total pressure of the system | atm |
| $p_{1,\alpha}$ | Arbitrary constant in the $z$-dependent solution of the Laplace equation | $m^{-1}$ for $\alpha = 0$ dimensionless otherwise |
| $p_{2,\alpha}$ | Arbitrary constant in the $z$-dependent solution of the Laplace equation | - |
| $P_{eq}$ | Equilibrium partial pressure of $O_2$ | bar |
| $P_{O2}$ | Partial pressure of $O_2$ of the specific atmosphere | bar |
| $q_{1,\alpha}$ | Arbitrary constant in the $r$-dependent solution of the Laplace equation | - |
| $q_{2,\alpha}$ | Arbitrary constant in the $r$-dependent solution of the Laplace equation | - |
| $R$ | Universal gas constant | kJ/mol/K |
| $r$ | Radial coordinate | m |
| $r_c$ | Radius of the crucible (internal) | m |

| | | |
|---|---|---|
| $Re_{mf}$ | Reynolds number based on minimum fluidisation velocity | - |
| $Re_t$ | Reynolds number based on terminal velocity of paritcles | - |
| $r_h$ | Radius of the hole in the lid | m |
| $Sh$ | Sherwood number | - |
| $S_i$ | Source term for species $i$ | mol/m$^3$/s |
| $t$ | Time | s |
| $T$ | Temperature | K or °C |
| $T_{em}$ | Temperature of the particulate phase | K |
| $u$ | Generic symbol for arbitrary functions | - |
| $U_0$ | Superficial gas velocity in a fluidised bed | m/s |
| $u_b$ | Bubble velocity | m/s |
| $U_{mf}$ | Minimum fluidisation velocity | m/s |
| $U_t$ | Terminal velocity of a single particle | m/s |
| $U_{gr}$ | Terminal velocity of a group of particles | m/s |
| $v$ | Generic symbol for arbitrary functions | - |
| $V_b$ | Volume of the bubble phase | m$^3$ |
| $V_{em}$ | Volume of the particulate phase | m$^3$ |
| $V_t$ | Total volume of the fluidised bed | m$^3$ |
| $X$ | Conversion | - |
| $X_c$ | The conversion at which a maximum rate is observed using the Avrami-Erofeev model | - |
| $y$ | Dummy variable | |
| $y_i$ | Mole fraction of gas species $i$ | - |
| $y_{i,bulk}$ | The mole fraction of species $i$ in the bulk gas outside the crucible | - |
| $y_{i,s}$ | The mole fraction of species $i$ at the gas-solid interface | - |
| $z$ | Vertical coordinate | m |
| $z_{\max}$ | Depth of the crucible, measured from the lid to the surface of the solid content at the base of the crucible | m |

| Greek symbols | | |
|---|---|---|
| $\alpha$ | Parameter used in the method of separation of variables | 1/m |
| $\beta$ | Full width at half maximum for a diffraction peak | radian |
| $\Delta G$ | Gibb's free energy of reaction | kJ/mol |
| $\Delta G°$ | Standard Gibbs free energy of reaction | kJ/mol |
| $\Delta H_r$ | Enthalpy of reaction | kJ/mol |
| $\Delta H_r°$ | Standard enthalpy of reaction | kJ/mol |
| $\Delta m$ | Expected change in mass | g |
| $\Delta S_r$ | Entropy of reaction | J/mol/K |
| $\Delta T$ | Temperature difference | °C |
| $\varepsilon$ | Emissivity (for radiative heat transfer) | - |
| $\varepsilon_{mf}$ | Voidage at minimum fluidisation | - |
| $\varepsilon_p$ | Porosity of the OC particle | - |
| $\phi$ | Thiele modulus | - |
| $\eta$ | Effectiveness factor | - |
| $\kappa_1$ | Constant in the general solution of the Laplace equation in 2-D cylindrical coordinate | - |
| $\kappa_2$ | Constant in the general solution of the Laplace equation in 2-D cylindrical coordinate | - |
| $\kappa_{3n}$ | Constant in the general solution of the Laplace equation in 2-D cylindrical coordinate | - |
| $\kappa_{4n}$ | Constant in the general solution of the Laplace equation in 2-D cylindrical coordinate | - |
| $\lambda$ | wavelength | m |
| $\lambda_i$ | Thermal conductivity of species *i* ($N_2$ or air) | W/m/K |
| $\lambda_s$ | Thermal conductivity of the OC particle | W/m/K |
| $\mu$ | Viscosity of the fluidising gas | Pa s |
| $\nu$ | Kinematic viscosity of a gas | $m^2/s$ |
| $\theta$ | Bragg Angle | radian |
| $\rho$ | Density of the fluidising gas | $kg/m^3$ |
| $\rho_m$ | Molar density of CuO in the OC particle | $mol/m^3$ |
| $\rho_p$ | Density of the OC particle | $kg/ m^3$ |
| $\Sigma V$ | Diffusion volume used in the Fuller-Schettler-Giddings equation | - |
| $\tau$ | Tortuosity factor | - |
| $\omega_n$ | The *n*th zero of $B_{J,1}$, a parameter in the general solution of the Laplace equation in 2-D cylindrical coordinate | - |
| $\xi$ | Generic spatial coordinate | - |

# References


Abad, A., Adánez-Rubio, I., Gayán, P., García-Labiano, F., de Diego, L.F., Adánez, J., 2012. Demonstration of chemical-looping with oxygen uncoupling (CLOU) process in a 1.5kWth continuously operating unit using a Cu-based oxygen-carrier. Int. J. Greenh. Gas Control 6, 189–200. doi:10.1016/j.ijggc.2011.10.016

Abad, A., García-Labiano, F., Gayán, P., de Diego, L.F., Adánez, J., 2015. Redox kinetics of $CaMg_{0.1}Ti_{0.125}Mn_{0.775}O_{2.9-\delta}$ for Chemical Looping Combustion (CLC) and Chemical Looping with Oxygen Uncoupling (CLOU). Chem. Eng. J. 269, 67–81. doi:10.1016/j.cej.2015.01.033

Adánez, J., Abad, A., Garcia-Labiano, F., Gayan, P., de Diego, L.F., 2012. Progress in chemical-looping combustion and reforming technologies. Prog. Energy Combust. Sci. doi:10.1016/j.pecs.2011.09.001

Adánez, J., Cuadrat, A., Abad, A., Gayán, P., de Diego, L.F., García-Labiano, F., 2010. Ilmenite Activation during Consecutive Redox Cycles in Chemical-Looping Combustion. Energy & Fuels 24, 1402–1413. doi:10.1021/ef900856d

Adánez, J., de Diego, L.F., García-Labiano, F., Gayán, P., Abad, A., Palacios, J.M., 2004. Selection of Oxygen Carriers for Chemical-Looping Combustion. Energy & Fuels 18, 371–377. doi:10.1021/ef0301452

Adánez, J., García-Labiano, F., de Diego, L.F., Gayán, P., Celaya, J., Abad, A., 2006a. Nickel−Copper Oxygen Carriers To Reach Zero CO and $H_2$ Emissions in Chemical-Looping Combustion. Ind. Eng. Chem. Res. 45, 2617–2625. doi:10.1021/ie050558l

Adánez, J., Gayán, P., Celaya, J., de Diego, L.F., García-Labiano, F., Abad, A., 2006b. Chemical Looping Combustion in a 10 kW th Prototype Using a $CuO/Al_2O_3$ Oxygen Carrier: Effect of Operating Conditions on Methane Combustion. Ind. Eng. Chem. Res. 45, 6075–6080. doi:10.1021/ie060364l

Adánez-Rubio, I., Gayán, P., Abad, A., de Diego, L.F., García-Labiano, F., Adánez, J., 2012. Evaluation of a Spray-Dried $CuO/MgAl_2O_4$ Oxygen Carrier for the Chemical Looping with Oxygen Uncoupling Process. Energy & Fuels 26, 3069–3081. doi:10.1021/ef3002229

Adánez-Rubio, I., Gayán, P., Abad, A., García-Labiano, F., de Diego, L.F., Adánez, J., 2014. Kinetic analysis of a Cu-based oxygen carrier: Relevance of temperature and oxygen partial pressure on reduction and oxidation reactions rates in Chemical Looping with Oxygen Uncoupling (CLOU). Chem. Eng. J. 256, 69–84. doi:10.1016/j.cej.2014.06.102

Arjmand, M., Azad, A.-M., Leion, H., Lyngfelt, A., Mattisson, T., 2011. Prospects of $Al_2O_3$ and $MgAl_2O_4$-Supported CuO Oxygen Carriers in Chemical-Looping Combustion (CLC) and Chemical-Looping with Oxygen Uncoupling (CLOU). Energy & Fuels 25, 5493–5502. doi:10.1021/ef201329x

Arjmand, M., Azad, A.-M., Leion, H., Mattisson, T., Lyngfelt, A., 2012a. Evaluation of $CuAl_2O_4$ as an Oxygen Carrier in Chemical-Looping Combustion. Ind. Eng. Chem. Res. 51, 13924–13934. doi:10.1021/ie300427w

Arjmand, M., Hedayati, A., Azad, A.-M., Leion, H., Rydén, M., Mattisson, T., 2013. $Ca_xLa_{1-x}Mn_{1-y}M_yO_{3-\delta}$(M = Mg, Ti, Fe, or Cu) as Oxygen Carriers for Chemical-Looping with Oxygen Uncoupling (CLOU). Energy & Fuels 27, 4097–4107. doi:10.1021/ef3020102

Arjmand, M., Keller, M., Leion, H., Mattisson, T., Lyngfelt, A., 2012b. Oxygen Release and Oxidation Rates of $MgAl_2O_4$ -Supported CuO Oxygen Carrier for Chemical-Looping Combustion with Oxygen Uncoupling (CLOU). Energy & Fuels 26, 6528–6539. doi:10.1021/ef3010064

Arjmand, M., Leion, H., Mattisson, T., Lyngfelt, A., 2012c. Evaluation of different manganese ores in chemical- looping combustion ( CLC ) for solid fuels 26–28.

Arthur, J.R., 1951. Reactions between carbon and oxygen. Trans. Faraday Soc. 47, 164. doi:10.1039/tf9514700164

Avedesian, M.M., Davidson, J.F., 1973. Combustion of carbon particles in a fluidised bed. Trans. Inst. Chem. Eng. 51, 121–131.

Avrami, M., 1941. Granulation, Phase Change, and Microstructure Kinetics of Phase Change. III. J. Chem. Phys. 9, 177–184. doi:10.1063/1.1750872

Avrami, M., 1940. Kinetics of Phase Change. II Transformation-Time Relations for Random Distribution of Nuclei. J. Chem. Phys. 8, 212–224. doi:10.1063/1.1750631

Avrami, M., 1939. Kinetics of Phase Change. I General Theory. J. Chem. Phys. 7, 1103–1112. doi:10.1063/1.1750380

Babu, S.P., Shah, B., Talwalkar, A., 1978. Fluidization correlations for coal gasification materials — minimum fluidization velocity and fluidized bed expansion ratio. AIChemE Symp. Ser. 74, 176–186.

Bao, J., Li, Z., Cai, N., 2013. Promoting the Reduction Reactivity of Ilmenite by Introducing Foreign Ions in Chemical Looping Combustion. Ind. Eng. Chem. Res. 52, 6119–6128. doi:10.1021/ie400237p

Barin, I., 2008. Cl-Cu2Te, in: Thermochemical Data of Pure Substances. Wiley-VCH Verlag GmbH, Weinheim, Germany, pp. 524–634. doi:10.1002/9783527619825.ch12f

Barrett, E.P., Joyner, L.G., Halenda, P.P., 1951. The Determination of Pore Volume and Area Distributions in Porous Substances. I. Computations from Nitrogen Isotherms. J. Am. Chem. Soc. 73, 373–380. doi:10.1021/ja01145a126

Berguerand, N., Lyngfelt, A., 2008a. Design and operation of a 10kWth chemical-looping combustor for solid fuels – Testing with South African coal. Fuel 87, 2713–2726. doi:10.1016/j.fuel.2008.03.008

Berguerand, N., Lyngfelt, A., 2008b. The use of petroleum coke as fuel in a 10kWth chemical-looping combustor. Int. J. Greenh. Gas Control 2, 169–179. doi:10.1016/j.ijggc.2007.12.004

Bode, S., Jung, M., 2006. Carbon dioxide capture and storage—liability for non-permanence under the UNFCCC. Int. Environ. Agreements Polit. Law Econ. 6, 173–186. doi:10.1007/s10784-006-9004-4

Bohn, C.D., Müller, C.R., Cleeton, J.P., Hayhurst, A.N., Davidson, J.F., Scott, S.A., Dennis, J.S., 2008. Production of Very Pure Hydrogen with Simultaneous Capture of Carbon Dioxide using the Redox Reactions of Iron Oxides in Packed Beds. Ind. Eng. Chem. Res. 47, 7623–7630. doi:10.1021/ie800335j

Bolt, P.H., Habraken, F.H.P.M., Geus, J.W., 1998. Formation of Nickel, Cobalt, Copper, and Iron Aluminates from $\alpha$- and $\gamma$-Alumina-Supported Oxides: A Comparative Study. J. Solid State Chem. 135, 59–69. doi:10.1006/jssc.1997.7590

Boot-Handford, M.E., Abanades, J.C., Anthony, E.J., Blunt, M.J., Brandani, S., Mac Dowell, N., Fernández, J.R., Ferrari, M.-C., Gross, R., Hallett, J.P., Haszeldine, R.S., Heptonstall, P., Lyngfelt, A., Makuch, Z., Mangano, E., Porter, R.T.J., Pourkashanian, M., Rochelle, G.T., Shah, N., Yao, J.G., Fennell, P.S., 2014. Carbon capture and storage update. Energy Environ. Sci. 7, 130–189. doi:10.1039/C3EE42350F

Brunauer, S., Emmett, P.H., Teller, E., 1938. Adsorption of Gases in Multimolecular Layers. J. Am. Chem. Soc. 60, 309–319. doi:10.1021/ja01269a023

Cai, P., Schiavetti, M., De Michele, G., Grazzini, G.C., Miccio, M., 1994. Quantitative estimation of bubble size in PFBC. Powder Technol. 80, 99–109. doi:10.1016/0032-5910(94)02834-6

Cho, P., Mattisson, T., Lyngfelt, A., 2004. Comparison of iron-, nickel-, copper- and manganese-based oxygen carriers for chemical-looping combustion. Fuel 83, 1215–1225. doi:10.1016/j.fuel.2003.11.013

Chuang, S., Dennis, J., Hayhurst, A., Scott, S., 2008. Development and performance of Cu-based oxygen carriers for chemical-looping combustion. Combust. Flame 154, 109–121. doi:10.1016/j.combustflame.2007.10.005

Chuang, S.Y., Dennis, J.S., Hayhurst, A.N., Scott, S.A., 2010. Kinetics of the Oxidation of a Co-precipitated Mixture of Cu and $Al_2O_3$ by $O_2$ for Chemical-Looping Combustion. Energy & Fuels 24, 3917–3927. doi:10.1021/ef1002167

Clayton, C.K., Sohn, H.Y., Whitty, K.J., 2014. Oxidation Kinetics of $Cu_2O$ in Oxygen Carriers for Chemical Looping with Oxygen Uncoupling. Ind. Eng. Chem. Res. 53, 2976–2986. doi:10.1021/ie402495a

Clayton, C.K., Whitty, K.J., 2014. Measurement and modeling of decomposition kinetics for copper oxide-based chemical looping with oxygen uncoupling. Appl. Energy 116, 416–423. doi:10.1016/j.apenergy.2013.10.032

Collings, N., Hegarty, K., Ramsander, T., 2012. Steady-state modelling of the universal exhaust gas oxygen (UEGO) sensor. Meas. Sci. Technol. 23, 085108. doi:10.1088/0957-0233/23/8/085108

Cuadrat, A., Abad, A., García-Labiano, F., Gayán, P., de Diego, L.F., Adánez, J., 2011. Ilmenite as oxygen carrier in a chemical looping combustion system with coal. Energy Procedia 4, 362–369. doi:10.1016/j.egypro.2011.01.063

Davidson, J.F., Harrison, D., 1963. Fluidised particles. Cambridge Univeristy Press, Cambridge.

Davies, R., Dinsdale, A., Gisby, J., Robinson, J., Martin, S., 2002. MTDATA - thermodynamic and phase equilibrium software from the national physical laboratory. Calphad 26, 229–271. doi:10.1016/S0364-5916(02)00036-6

Davies, R.H., Dinstale, A.T., Chart, T.G., Barry, T.I., H., R.M., 1990. Application of MTDATA to the Modeling of Multicomponent Equilibria, in: Hastie, J.W. (Ed.), Materials Chemistry at High Temperatures. Humana Press, Totowa, NJ, NJ, pp. 251–262. doi:10.1007/978-1-4612-0481-7

De Diego, L.F., Abad, A., Cabello, A., Gayán, P., García-Labiano, F., Adánez, J., 2014. Reduction and Oxidation Kinetics of a $CaMn_{0.9}Mg_{0.1}O_{3-\delta}$ Oxygen Carrier for Chemical-Looping Combustion. Ind. Eng. Chem. Res. 53, 87–103. doi:10.1021/ie4015765

De Diego, L.F., García-Labiano, F., Adánez, J., Gayán, P., Abad, A., Corbella, B.M., María Palacios, J., 2004. Development of Cu-based oxygen carriers for chemical-looping combustion. Fuel 83, 1749–1757. doi:10.1016/j.fuel.2004.03.003

De Diego, L.F., Gayán, P., García-Labiano, F., Celaya, J., Abad, A., Adánez, J., 2005. Impregnated $CuO/Al_2O_3$ Oxygen Carriers for Chemical-Looping Combustion: Avoiding Fluidized Bed Agglomeration. Energy & Fuels 19, 1850–1856. doi:10.1021/ef050052f

Dennis, J.S., Pacciani, R., 2009. The rate and extent of uptake of $CO_2$ by a synthetic, CaO-containing sorbent. Chem. Eng. Sci. 64, 2147–2157. doi:10.1016/j.ces.2009.01.051

Dennis, J.S., Scott, S.A., Hayhurst, A.N., 2006. In situ gasification of coal using steam with chemical looping: a technique for isolating $CO_2$ from burning a solid fuel. J. Energy Inst. 79, 187–190.

Dlugokencky, E., Tans, P., 2015. ESRL Global Monitoring Division - Global Greenhouse Gas Reference Network [WWW Document]. URL http://www.esrl.noaa.gov/gmd/ccgg/trends/global.html (accessed 6.1.15).

Donat, F., Hu, W., Scott, S.A., Dennis, J.S., 2015. Characteristics of Copper-based Oxygen Carriers Supported on Calcium Aluminates for Chemical-Looping Combustion with Oxygen Uncoupling (CLOU). Ind. Eng. Chem. Res. 54, 6713–6723. doi:10.1021/acs.iecr.5b01172

Dulong, P., Petit, A., 1819. Recherches sur quelques points importans de la theorie de la Chaleur. Ann. Chim. Phys. 10, 395–413.

Eagleson, M., 1993. Copper (II) Oxide. Concise Encycl. Chem.

Fan, L.-S., Zhu, C., 2005. Principles of Gas-Solid Flows. Cambridge University Press.

Fennell, P., Anthony, B. (Eds.), 2015. Calcium and Chemical Looping Technology for Power Generation and Carbon Dioxide ($CO_2$) Capture: Solid Oxygen- and $CO_2$-Carriers. Elsevier Science.

Fennell, P. S., Davidson, J. F., Dennis, J. S., Gladden, L. F., Hayhurst, A. N., Mantle, M. D., Müller, C. R., Rees, A. C., Scott, S. A., Sederman, A. J., 2005. A study of the mixing of solids in gas-fluidized beds, using ultra-fast MRI. Chem. Eng. Sci. 60, 2085-2088. doi:10.1016/j.ces.2004.11.040

Forero, C.R., Gayán, P., García-Labiano, F., de Diego, L.F., Abad, A., Adánez, J., 2011. High temperature behaviour of a $CuO/\gamma Al_2O_3$ oxygen carrier for chemical-looping combustion. Int. J. Greenh. Gas Control 5, 659–667. doi:10.1016/j.ijggc.2011.03.005

Fuller, E.N., Schettler, P.D., Giddings, J.C., 1966. New method for prediction of binary gas-phase diffusion coefficients. Ind. Eng. Chem. 58, 18–27. doi:10.1021/ie50677a007

Galinsky, N., Mishra, A., Zhang, J., Li, F., 2015. $Ca_{1-x}A_xMnO_3$ (A=Sr and Ba) perovskite based oxygen carriers for chemical looping with oxygen uncoupling (CLOU). Appl. Energy. doi:10.1016/j.apenergy.2015.04.020

Gayán, P., Abad, A., de Diego, L.F., García-Labiano, F., Adánez, J., 2013. Assessment of technological solutions for improving chemical looping combustion of solid fuels with $CO_2$ capture. Chem. Eng. J. 233, 56–69. doi:10.1016/j.cej.2013.08.004

Gayán, P., Adánez-Rubio, I., Abad, A., de Diego, L.F., García-Labiano, F., Adánez, J., 2012. Development of Cu-based oxygen carriers for Chemical-Looping with Oxygen Uncoupling (CLOU) process. Fuel 96, 226–238. doi:10.1016/j.fuel.2012.01.021

Geldart, D., 1972. The effect of particle size and size distribution on the behaviour of gas-fluidised beds. Powder Technol. 6, 201–215. doi:10.1016/0032-5910(72)83014-6

Grida, I., Evans, J.R.G., 2003. Extrusion freeforming of ceramics through fine nozzles. J. Eur. Ceram. Soc. 23, 629–635. doi:10.1016/S0955-2219(02)00163-2

Gu, H., Shen, L., Xiao, J., Zhang, S., Song, T., 2011. Chemical Looping Combustion of Biomass/Coal with Natural Iron Ore as Oxygen Carrier in a Continuous Reactor. Energy & Fuels 25, 446–455. doi:10.1021/ef101318b

Gu, H., Shen, L., Xiao, J., Zhang, S., Song, T., Chen, D., 2012. Iron ore as oxygen carrier improved with potassium for chemical looping combustion of anthracite coal. Combust. Flame 159, 2480–2490. doi:10.1016/j.combustflame.2012.03.013

Hallstedl, B., 1990. Assessment of the $CaO$-$Al_2O_3$ System. J. Am. Ceram. Soc. 73, 15–23. doi:10.1111/j.1151-2916.1990.tb05083.x

Hayashi, K., Hirano, M., Hosono, H., 2005. Thermodynamics and kinetics of hydroxide ion formation in $12CaO \cdot 7Al_2O_3$. J. Phys. Chem. B 109, 11900–6. doi:10.1021/jp050807j

Hayhurst, A.N., 2000. The mass transfer coefficient for oxygen reacting with a carbon particle in a fluidized or packed bed. Combust. Flame 121, 679–688. doi:10.1016/S0010-2180(99)00178-9

Hayhurst, A.N., Parmar, M.S., 1998. Does solid carbon burn in oxygen to give the gaseous intermediate CO or produce $CO_2$ directly? Some experiments in a hot bed of sand fluidized by air. Chem. Eng. Sci. 53, 427–438. doi:10.1016/S0009-2509(97)00334-5

Hotta, A., 2010. Foster Wheeler's Solutions for Large Scale CFB Boiler Technology: Features and Operational Performance of Łagisza 460 MWe CFB Boiler. Proc. 20th Int. Conf. Fluid. Bed Combust. 59–70.

Hu, W., Donat, F., Scott, S.A., Dennis, J.S., 2016. Kinetics of oxygen uncoupling of a copper based oxygen carrier. Appl. Energy. 161, 92-100. doi: 10.1016/j.apenergy.2015.10.006

IEA, 2014a. Key World Energy Statistics 2014. OCED publishing, Paris. doi:10.1787/22202811

IEA, 2014b. World Energy Outlook 2014. IEA, Paris. doi:10.1787/20725302

Imtiaz, Q., Broda, M., Müller, C.R., 2014. Structure–property relationship of co-precipitated Cu-rich, $Al_2O_3$- or $MgAl_2O_4$-stabilized oxygen carriers for chemical looping with oxygen uncoupling (CLOU). Appl. Energy 119, 557–565. doi:10.1016/j.apenergy.2014.01.007

Imtiaz, Q., Kierzkowska, A.M., Müller, C.R., 2012. Coprecipitated, copper-based, alumina-stabilized materials for carbon dioxide capture by chemical looping combustion. ChemSusChem 5, 1610–8. doi:10.1002/cssc.201100694

IPCC, 2014. Climate Change 2014: Synthesis Report. Contribution of Working Groups I, II and III to the Fifth Assessment Report of the Intergovernmental Panel on Climate Change. Geneva.

IPCC, 2007. Climate Change 2007: Mitigation of Climate Change. Cambridge University Press, New York.

Ishida, M., Jin, H., 1997. $CO_2$ recovery in a power plant with chemical looping combustion. Energy Convers. Manag. 38, S187–S192. doi:10.1016/S0196-8904(96)00267-1

Ishida, M., Jin, H., 1994. A novel combustor based on chemical-looping reactions and its reaction kinetics. J. Chem. Eng. JAPAN 27, 296–301. doi:10.1252/jcej.27.296

Ishida, M., Jin, H., Okamoto, T., 1998. Kinetic Behavior of Solid Particle in Chemical-Looping Combustion: Suppressing Carbon Deposition in Reduction. Energy & Fuels 12, 223–229. doi:10.1021/ef970041p

Ishida, M., Zheng, D., Akehata, T., 1987. Evaluation of a chemical-looping-combustion power-generation system by graphic exergy analysis. Energy 12, 147–154. doi:10.1016/0360-5442(87)90119-8

Jacob, K.T., Alcock, C.B., 1975. Thermodynamics of $CuAlO_2$ and $CuAl_2O_4$ and Phase Equilibria in the System Cu2O-CuO-Al2O3. J. Am. Ceram. Soc. 58, 192–195. doi:10.1111/j.1151-2916.1975.tb11441.x

Jin, H., Ishida, M., 2004. A new type of coal gas fueled chemical-looping combustion. Fuel 83, 2411–2417. doi:10.1016/j.fuel.2004.06.033

Jin, H., Okamoto, T., Ishida, M., 1998. Development of a Novel Chemical-Looping Combustion: Synthesis of a Looping Material with a Double Metal Oxide of CoO−NiO. Energy & Fuels 12, 1272–1277. doi:10.1021/ef980080g

Källén, M., Rydén, M., Dueso, C., Mattisson, T., Lyngfelt, A., 2013. $CaMn_{0.9}Mg_{0.1}O_{3-\delta}$ as Oxygen Carrier in a Gas-Fired 10 kW th Chemical-Looping Combustion Unit. Ind. Eng. Chem. Res. 52, 6923–6932. doi:10.1021/ie303070h

Khawam, A., Flanagan, D.R., 2006. Solid-state kinetic models: basics and mathematical fundamentals. J. Phys. Chem. B 110, 17315–28. doi:10.1021/jp062746a

Kunii, D., Levenspiel, O., 1991. Fluidization Engineering, 2nd ed. Elsevier.

La Nauze, R.D., 1985. Fundamentals of coal combustion in fluidised beds. Chem. Eng. Res. Des. 63, 3–33.

Lambert, A., Briault, P., Comte, E., 2011. Spinel mixed oxides as oxygen carriers for chemical looping combustion. Energy Procedia 4, 318–323. doi:10.1016/j.egypro.2011.01.057

Leion, H., Jerndal, E., Steenari, B.-M., Hermansson, S., Israelsson, M., Jansson, E., Johnsson, M., Thunberg, R., Vadenbo, A., Mattisson, T., Lyngfelt, A., 2009. Solid fuels in chemical-looping combustion using oxide scale and unprocessed iron ore as oxygen carriers. Fuel 88, 1945–1954. doi:10.1016/j.fuel.2009.03.033

Leion, H., Lyngfelt, A., Johansson, M., Jerndal, E., Mattisson, T., 2008a. The use of ilmenite as an oxygen carrier in chemical-looping combustion. Chem. Eng. Res. Des. 86, 1017–1026. doi:10.1016/j.cherd.2008.03.019

Leion, H., Mattisson, T., Lyngfelt, A., 2008b. Solid fuels in chemical-looping combustion. Int. J. Greenh. Gas Control 2, 180–193. doi:10.1016/S1750-5836(07)00117-X

Leion, H., Mattisson, T., Lyngfelt, A., 2007. The use of petroleum coke as fuel in chemical-looping combustion. Fuel 86, 1947–1958. doi:10.1016/j.fuel.2006.11.037

Leonidova, E.I., Leonidov, I.A., Patrakeev, M. V., Kozhevnikov, V.L., 2011. Oxygen non-stoichiometry, high-temperature properties, and phase diagram of $CaMnO_{3-\delta}$. J. Solid State Electrochem. 15, 1071–1075. doi:10.1007/s10008-010-1288-1

Levenspiel, 1999. Chemical Reaction Engineering, 3rd ed. Wiley India Pvt. Limited.

Levin, I., Brandon, D., 2005. Metastable Alumina Polymorphs: Crystal Structures and Transition Sequences. J. Am. Ceram. Soc. 81, 1995–2012. doi:10.1111/j.1151-2916.1998.tb02581.x

Li, Z., Cai, N., Huang, Y., Han, H., 2005. Synthesis, Experimental Studies, and Analysis of a New Calcium-Based Carbon Dioxide Absorbent. Energy & Fuels 19, 1447–1452. doi:10.1021/ef0496799

Linderholm, C., Abad, A., Mattisson, T., Lyngfelt, A., 2008. 160h of chemical-looping combustion in a 10kW reactor system with a NiO-based oxygen carrier. Int. J. Greenh. Gas Control 2, 520–530. doi:10.1016/j.ijggc.2008.02.006

Linderholm, C., Lyngfelt, A., Cuadrat, A., Jerndal, E., 2012. Chemical-looping combustion of solid fuels – Operation in a 10kW unit with two fuels, above-bed and in-bed fuel feed and two oxygen carriers, manganese ore and ilmenite. Fuel 102, 808–822. doi:10.1016/j.fuel.2012.05.010

Linderholm, C., Mattisson, T., Lyngfelt, A., 2009. Long-term integrity testing of spray-dried particles in a 10-kW chemical-looping combustor using natural gas as fuel. Fuel 88, 2083–2096. doi:10.1016/j.fuel.2008.12.018

Litovsky, E., Shapiro, M., Shavit, A., 1996. Gas Pressure and Temperature Dependences of Thermal Conductivity of Porous Ceramic Materials: Part 2, Refractories and Ceramics with Porosity Exceeding 30%. J. Am. Ceram. Soc. 79, 1366–1376. doi:10.1111/j.1151-2916.1996.tb08598.x

Liu, W., 2013. The Production of Hydrogen Using Chemical Looping. University of Cambridge.

Lyngfelt, A., 2011. Oxygen Carriers for Chemical Looping Combustion - 4 000 h of Operational Experience. Oil Gas Sci. Technol. – Rev. d'IFP Energies Nouv. 66, 161–172. doi:10.2516/ogst/2010038

Mantzavinos, D., Hartley, A., Metcalfe, I.S., Sahibzada, M., 2000. Oxygen stoichiometries in $La_{1-x}Sr_xCo_{1-y}FeyO_{3-\delta}$ perovskites at reduced oxygen partial pressures. Solid State Ionics 134, 103–109. doi:10.1016/S0167-2738(00)00718-9

Markström, P., Linderholm, C., Lyngfelt, A., 2013. Chemical-looping combustion of solid fuels – Design and operation of a 100kW unit with bituminous coal. Int. J. Greenh. Gas Control 15, 150–162. doi:10.1016/j.ijggc.2013.01.048

Mattisson, T., Leion, H., Lyngfelt, A., 2009a. Chemical-looping with oxygen uncoupling using $CuO/ZrO_2$ with petroleum coke. Fuel 88, 683–690. doi:10.1016/j.fuel.2008.09.016

Mattisson, T., Lyngfelt, A., Cho, P., 2001. The use of iron oxide as an oxygen carrier in chemical-looping combustion of methane with inherent separation of $CO_2$. Fuel 80, 1953–1962. doi:10.1016/S0016-2361(01)00051-5

Mattisson, T., Lyngfelt, A., Leion, H., 2009b. Chemical-looping with oxygen uncoupling for combustion of solid fuels. Int. J. Greenh. Gas Control 3, 11–19. doi:10.1016/j.ijggc.2008.06.002

Maxwell, J. C., 1867. On the dynamical theory of gases. Philos. Trans. R. Soc. 157, 49–88.

Mizusaki, J., Mori, N., Takai, H., Yonemura, Y., Minamiue, H., Tagawa, H., Dokiya, M., Inaba, H., Naraya, K., Sasamoto, T., Hashimoto, T., 2000. Oxygen nonstoichiometry and defect equilibrium in the perovskite-type oxides $La_{1-x}Sr_xMnO_{3+d}$. Solid State Ionics 129, 163–177. doi:10.1016/S0167-2738(99)00323-9

NIST, 2011. NIST Standard Reference Database Number 69, in: NIST Chemistry WebBook.

Noble, B., 1988. Methods based on the Wiener-Hopf technique for the solution of partial differential equations. Chelsea Publishing Company, New York.

Patterson, A., 1939. The Scherrer Formula for X-Ray Particle Size Determination. Phys. Rev. 56, 978–982. doi:10.1103/PhysRev.56.978

Pires, J.C.M., Martins, F.G., Alvim-Ferraz, M.C.M., Simões, M., 2011. Recent developments on carbon capture and storage: An overview. Chem. Eng. Res. Des. 89, 1446–1460. doi:10.1016/j.cherd.2011.01.028

Readman, J.E., Olafsen, A., Larring, Y., Blom, R., 2005. $La_{0.8}Sr_{0.2}Co_{0.2}Fe_{0.8}O_{3-\delta}$ as a potential oxygen carrier in a chemical looping type reactor, an *in-situ* powder X-ray diffraction study. J. Mater. Chem. 15, 1931. doi:10.1039/b416526h

Regitz, S., Collings, N., 2008. Fast response air-to-fuel ratio measurements using a novel device based on a wide band lambda sensor. Meas. Sci. Technol. 19, 075201. doi:10.1088/0957-0233/19/7/075201

Richardson, J. F., Zaki, W. N., 1954. Sedimentation and fluidisation : Part I. Trans. Inst. Chem. Eng. 32, 35–55.

Richter, H.J., Knoche, K.F., 1983. Reversibility of Combustion Processes, in: Gaggioli, R.A. (Ed.), Efficiency and Costing, ACS Symposium Series. American Chemical Society, Washington, D.C., pp. 71–85. doi:10.1021/bk-1983-0235

Robertson, A., Goidich, A., Fan, Z., 2010. 1300°F 800 MWe USC CFB Boiler Design Study. Proc. 20th Int. Conf. Fluid. Bed Combust. 125–131. doi:10.1007/978-3-642-02682-9

Ropp, R.C., 2013. Group 13 (B, Al, Ga, In and Tl) Alkaline Earth Compounds, in: Encyclopedia of the Alkaline Earth Compounds. Elsevier, pp. 481–635. doi:10.1016/B978-0-444-59550-8.00006-5

Roth, R.S., Hwang, N.M., Rawn, C.J., Burton, B.P., Ritter, J.J., 1991. Phase Equilibria in the Systems CaO-CuO and CaO-$Bi_2O_3$. J. Am. Ceram. Soc. 74, 2148–2151. doi:10.1111/j.1151-2916.1991.tb08274.x

Rubin, E.S., Mantripragada, H., Marks, A., Versteeg, P., Kitchin, J., 2012. The outlook for improved carbon capture technology. Prog. Energy Combust. Sci. 38, 630–671. doi:10.1016/j.pecs.2012.03.003

Rydén, M., Lyngfelt, A., Mattisson, T., 2011. $CaMn_{0.875}Ti_{0.125}O_3$ as oxygen carrier for chemical-looping combustion with oxygen uncoupling (CLOU)—Experiments in a continuously operating fluidized-bed reactor system. Int. J. Greenh. Gas Control 5, 356–366. doi:10.1016/j.ijggc.2010.08.004

Rydén, M., Moldenhauer, P., Lindqvist, S., Mattisson, T., Lyngfelt, A., 2014. Measuring attrition resistance of oxygen carrier particles for chemical looping combustion with a customized jet cup. Powder Technol. 256, 75–86. doi:10.1016/j.powtec.2014.01.085

Ryu, H.-J., Lim, N.-Y., Bae, D.-H., Jin, G.-T., 2003. Carbon deposition characteristics and regenerative ability of oxygen carrier particles for chemical-looping combustion. Korean J. Chem. Eng. 20, 157–162. doi:10.1007/BF02697202

Sahir, A.H., Sohn, H.Y., Leion, H., Lighty, J.S., 2012. Rate Analysis of Chemical-Looping with Oxygen Uncoupling (CLOU) for Solid Fuels. Energy & Fuels 26, 4395–4404. doi:10.1021/ef300452p

Saucedo, M.A., Lim, J.Y., Dennis, J.S., Scott, S.A., 2014. $CO_2$-gasification of a lignite coal in the presence of an iron-based oxygen carrier for chemical-looping combustion. Fuel 127, 186–201. doi:10.1016/j.fuel.2013.07.045

Scala, F., 2011. Fluidized-Bed Combustion of Single Coal Char Particles: An Analysis of the Burning Rate and of the Primary $CO/CO_2$ Ratio. Energy & Fuels 25, 1051–1059. doi:10.1021/ef101182s

Schilling, A., Cantoni, M., Guo, J.D., Ott, H.R., 1993. Superconductivity above 130 K in the Hg–Ba–Ca–Cu–O system. Nature 363, 56–58. doi:10.1038/363056a0

Schmidt-Whitley, R.D., Martinez-Clemente, M., Revcolevschi, A., 1974. Growth and microstructural control of single crystal cuprous oxide $Cu_2O$. J. Cryst. Growth 23, 113–120. doi:10.1016/0022-0248(74)90110-9

Scott, S.A., Davidson, J.F., Dennis, J.S., Hayhurst, A.N., 2004. Heat Transfer to a Single Sphere Immersed in Beds of Particles Supplied by Gas at Rates above and below Minimum Fluidization. Ind. Eng. Chem. Res. 43, 5632–5644. doi:10.1021/ie0307380

Scott, S.A., Dennis, J.S., Hayhurst, A.N., Brown, T., 2006. In situ gasification of a solid fuel and $CO_2$ separation using chemical looping. AIChE J. 52, 3325–3328. doi:10.1002/aic.10942

Shen, L., Wu, J., Xiao, J., 2009a. Experiments on chemical looping combustion of coal with a NiO based oxygen carrier. Combust. Flame 156, 721–728. doi:10.1016/j.combustflame.2008.08.004

Shen, L., Wu, J., Xiao, J., Song, Q., Xiao, R., 2009b. Chemical-Looping Combustion of Biomass in a 10 kW th Reactor with Iron Oxide As an Oxygen Carrier. Energy & Fuels 23, 2498–2505. doi:10.1021/ef900033n

Shi, Y.F., Fan, L.T., 1984. Lateral mixing of solids in batch gas-solids fluidized beds. Ind. Eng. Chem. Process Des. Dev. 23, 337–341. doi:10.1021/i200025a026

Siriwardane, R., Tian, H., Richards, G., Simonyi, T., Poston, J., 2009. Chemical-Looping Combustion of Coal with Metal Oxide Oxygen Carriers. Energy & Fuels 23, 3885–3892. doi:10.1021/ef9001605

Sit, S.P., Grace, J.R., 1981. Effect of bubble interaction on interphase mass transfer in gas fluidized beds. Chem. Eng. Sci. 36, 327–335. doi:10.1016/0009-2509(81)85012-9

Song, H., Shah, K., Doroodchi, E., Wall, T., Moghtaderi, B., 2012. Evaluation of suitable oxygen carriers for Chemical Looping Air Separation ( CLAS ) for large scale oxygen production 26–28.

Song, Q., Xiao, R., Deng, Z., Shen, L., Xiao, J., Zhang, M., 2008a. Effect of Temperature on Reduction of $CaSO_4$ Oxygen Carrier in Chemical-Looping Combustion of Simulated Coal Gas in a Fluidized Bed Reactor. Ind. Eng. Chem. Res. 47, 8148–8159. doi:10.1021/ie8007264

Song, Q., Xiao, R., Deng, Z., Zheng, W., Shen, L., Xiao, J., 2008b. Multicycle Study on Chemical-Looping Combustion of Simulated Coal Gas with a $CaSO_4$ Oxygen Carrier in a Fluidized Bed Reactor. Energy & Fuels 22, 3661–3672. doi:10.1021/ef800275a

Stefan, J., 1871. Über das Gleichgewicht und die Bewegung insbesondere die Diffusion von Gasgemengen. Sitzungsber. Akad. Wiss. Wien 63, 63–124.

Ströhle, J., Orth, M., Epple, B., 2014. Design and operation of a 1MWth chemical looping plant. Appl. Energy 113, 1490–1495. doi:10.1016/j.apenergy.2013.09.008

Subramanian, M.A., Torardi, C.C., Calabrese, J.C., Gopalakrishnan, J., Morrissey, K.J., Askew, T.R., Flippen, R.B., Chowdhry, U., Sleight, A.W., 1988. A New High-Temperature Superconductor: Bi2Sr3-x Cax Cu2O8+y. Science 239, 1015–7. doi:10.1126/science.239.4843.1015

Sutherland, W., 1893. The viscosity of gases and molecular force. Philos. Mag. Ser. 5 36, 507–531.

Suzuki, R.O., Bohac, P., Gauckler, L.J., 1994. Thermodynamics and Phase Equilibria in the Ca-Cu-O System. J. Am. Ceram. Soc. 77, 41–48. doi:10.1111/j.1151-2916.1994.tb06955.x

Teraoka, Y., Zhang, H.-M., Furukawa, S., Yamazoe, N., 1985. Oxygen permeation through perovskite-type oxides. Chem. Lett. 1743–1746. doi:10.1246/cl.1985.1743

Terayama, K., Ikeda, M., 1983. Study on Thermal Decomposition of $MnO_2$ and $Mn_2O_3$ by Thermal Analysis. Trans. Japan Inst. Met. 24, 754–758. doi:10.2320/matertrans1960.24.754

Thiele, E.W., 1939. Relation between Catalytic Activity and Size of Particle. Ind. Eng. Chem. 31, 916–920. doi:10.1021/ie50355a027

Tian, H., Guo, Q., Chang, J., 2008. Investigation into Decomposition Behavior of $CaSO_4$ in Chemical-Looping Combustion. Energy & Fuels 22, 3915–3921. doi:10.1021/ef800508w

Tilton, J. N., 2007. Fluid and particle dynamics, In: Perry, R.H., Green, D.W. (Eds), Perry's Chemical Engineers' Handbook ($8^{th}$ edition). McGraw-Hill, 52.

Tognotti, L., Longwell, J.P., Sarofim, A.F., 1991. The products of the high temperature oxidation of a single char particle in an electrodynamic balance. Symp. Combust. 23, 1207–1213. doi:10.1016/S0082-0784(06)80382-6

Tsang, C.-F., Meen, J.K., Elthon, D., 1995. Phase Equilibria of the Calcium Oxide-Copper Oxide System in Oxygen at 1 atm. J. Am. Ceram. Soc. 78, 1863–1868. doi:10.1111/j.1151-2916.1995.tb08901.x

Wang, J., Anthony, E.J., 2008. Clean combustion of solid fuels. Appl. Energy 85, 73–79. doi:10.1016/j.apenergy.2007.07.002

Wang, K., Yu, Q., Qin, Q., 2013. Reduction Kinetics of Cu-Based Oxygen Carriers for Chemical Looping Air Separation. Energy & Fuels 27, 5466–5474. doi:10.1021/ef401241r

Wen, C.Y., Yu, Y.H., 1966. A generalized method for predicting the minimum fluidization velocity. AIChE J. 12, 610–612. doi:10.1002/aic.690120343

Wen, Y., Li, Z., Xu, L., Cai, N., 2012. Experimental Study of Natural Cu Ore Particles as Oxygen Carriers in Chemical Looping with Oxygen Uncoupling (CLOU). Energy & Fuels 26, 3919–3927. doi:10.1021/ef300076m

Worrell, E., Price, L., Martin, N., Hendriks, C., Meida, L.O., 2001. Carbon dioxide emissions from the global cement industry 1. Annu. Rev. Energy Environ. 26, 303–329. doi:10.1146/annurev.energy.26.1.303

Xiao, R., Song, Q., Zhang, S., Zheng, W., Yang, Y., 2010. Pressurized Chemical-Looping Combustion of Chinese Bituminous Coal: Cyclic Performance and Characterization of Iron Ore-Based Oxygen Carrier. Energy & Fuels 24, 1449–1463. doi:10.1021/ef901070c

Xu, L., Wang, J., Li, Z., Cai, N., 2013. Experimental Study of Cement-Supported CuO Oxygen Carriers in Chemical Looping with Oxygen Uncoupling (CLOU). Energy & Fuels 27, 1522–1530. doi:10.1021/ef301969k

Yang, H., Yang, S., Chi, X., Evans, J.R.G., 2006. Fine ceramic lattices prepared by extrusion freeforming. J. Biomed. Mater. Res. B. Appl. Biomater. 79, 116–21. doi:10.1002/jbm.b.30520

Yang, S., Kim, K., Baek, J.-I., Kim, J.-W., Lee, J.B., Ryu, C.K., Lee, G., 2012. Spinel $Ni(Al,Fe)_2O_4$ Solid Solution as an Oxygen Carrier for Chemical Looping Combustion. Energy & Fuels 26, 4617–4622. doi:10.1021/ef300712u

Zhang, X., Han, W., Hong, H., Jin, H., 2009. A chemical intercooling gas turbine cycle with chemical-looping combustion. Energy 34, 2131–2136. doi:10.1016/j.energy.2008.09.014

Zhu, Y., Mimura, K., Isshiki, M., 2004. Oxidation Mechanism of $Cu_2O$ to CuO at 600-1050°C. Oxid. Met. 62, 207–222. doi:10.1007/s11085-004-7808-6